

DECARBURIZATION KINETICS OF LIQUID Fe-  
C DROPLETS IN OXIDIZING SLAG

FUNDAMENTAL STUDY OF  
DECARBURIZATION BEHAVIOR OF LIQUID  
Fe-C DROPLETS IN OXIDIZING SLAG

By

Jayasree Biswas, B.E., M.Tech.

A Thesis

Submitted to the School of Graduate Studies

In Partial Fulfillment of the Requirements

For the Degree

Doctor of Philosophy

McMaster university

©Copyright by Jayasree Biswas, October 2021

DOCTOR OF PHILOSOPHY (2021)      McMaster University  
Materials Science and Engineering      Hamilton, Ontario

TITLE: Fundamental Study of Decarburization Behavior of  
Liquid Fe-C Droplets in Oxidizing Slag

AUTHOR: Jayasree Biswas, M. Tech (IIT Bombay, India)

SUPERVISOR: Professor Kenneth Coley

Number of Pages: xxx, 270

## ABSTRACT

Bloating of metal droplets in emulsion is an important phenomenon in BOF steelmaking in controlling the kinetics of refining. This bloating controls the kinetics by mainly increasing the residence time (from  $\sim 1/4$ th of a second to  $\sim 10$ - $15$  seconds) of the droplets in emulsion and the slag/metal surface ( $\sim 5$ - $6$  times) area. The bloating behavior is determined by the decarburization kinetics. This work aims to develop fundamental understanding of the bloating phenomena through series of experiments and mathematical modeling to explore various factors affecting the kinetics of decarburization.

An experimental study on varying the droplet carbon concentration, slag FeO concentration and basicity evidenced mixed controlled kinetics including transport of oxygen in the slag, interfacial (slag/metal) chemical reaction, nucleation and growth of CO bubbles. A mathematical model including these kinetic steps was developed. The model was able to demonstrate the partitioning of oxygen at the slag/metal interface into external (at the slag/metal interface) and internal (within droplet) decarburization in presence of the surface-active element sulfur. The model was developed using a single data set and validated for a wide range of experimental conditions. The model showed excellent agreement with experimental data for most of the reaction period but failed to predict a premature shutdown for droplets reacting with low conductivity slag.

In order to understand this discrepancy, the slag ionic and electronic conductivity were varied which showed a premature shutdown of decarburization reaction with low conductivity slag and continuation of the reaction to the thermodynamic limit with high

conductivity slag. A mechanism of generation of local electric field by accumulation of charge at the slag/metal interface was proposed to explain the premature shutdown of the reaction for low basicity slags. In all experiments with low conductivity slag sulfur was observed to delay the onset of internal decarburization. However, this effect was diminished or disappeared completely with high conductivity slag. This observation motivated additional experiments to study the competitive adsorption of oxygen and sulfur at the slag/metal interface both through experiments and modelling. It was shown that for low conductivity slag, sulfur poisoning inhibited reaction at the surface whereas for the high conductivity slags the faster transport of oxygen allowed oxygen to compete with sulfur for adsorption sites creating pathways for oxygen into the droplet. By including the possibility of competitive adsorption in the model it was possible to predict the behavior of high sulfur droplets in conductivity slags where the only modification to the model was to change the mass transfer coefficient as appropriate to the higher conductivity. Extension of this study to include silicon in the droplet showed significant effect on decarburization both in delaying bloating as well as increasing peak rate of decarburization.

## ACKNOWLEDGEMENTS

Foremost, I would like to express my sincere gratitude to my supervisor Dr. Kenneth Coley for his throughout guidance and continuous support. I have had the privilege to be supervised by such a great leader who always stands by his students in any academic or nonacademic issues and gives boundless freedom to explore. Throughout the Ph.D. period, he has guided me to cultivate the approach of deep thinking and analyzing with minute details patiently, which would be the best thing I am going to carry forward in future. The brainstorming technical discussions with him for last four years have prepared me to work with any other pyrometallurgical systems in future. I will miss his funny comments during paper corrections.

Besides my advisor, I would also like to thank my committee members Dr. Neslihan Dogan and Dr. Oleg Rubel for their valuable suggestion and guidance for supporting me to reach to my destination.

I would like to thank to each one from the department of materials science and engineering for creating such a welcoming and motivating environment for graduate students. I have to specially mention about Ed McCaffery, Dr. Xiaogang Li, Doug Culley without whom running high temperature experiments would have been impossible. I wish to express my thanks to Marry-Anne for her constant support. I am highly indebted to our highly motivated group members – Dr. Muhammed Nabeel, Dr. Mukesh Sharma, Dr. Aliyeh Rafiei, Dr. Brian Jamieson, Dr. Michelia Alba, Keyan Miao, Angshuman Podder and a special thanks to Dr. Kezhuan Gu for training me to become a true experimentalist. I would

like to thank to my friends mainly Arunima, Dipankar and Vinay for those discussions about each other's problems of Ph.D. life and motivating each other.

Last but not the least, I am very fortunate to have a supporting family like my mother, my sisters Pampa and Rumpa who sacrificed a lot for continuation of my higher studies. In memory of my father: your blessings are always with me. I would like to thank to my uncle who has always given me the assurance that everything is fine here, and you continue your study. I dedicate my thesis to my parents: Jayanti Biswas and Late Nilmoni Biswas.

## TABLE OF CONTENTS

|  |    |
|--|----|
| Chapter 1 .....                                  | 1  |
| 1. Introduction .....                            | 1  |
| 1.1. Research Background.....                    | 1  |
| 1.2. Thesis Outline.....                         | 4  |
| Chapter 2.....                                   | 7  |
| 2. Literature Review.....                        | 7  |
| 2.1. History of Steelmaking.....                 | 7  |
| 2.2. Basic Oxygen Steelmaking Process.....       | 9  |
| 2.2.1. Droplet Generation Rate.....              | 10 |
| 2.2.2. Residence Time.....                       | 14 |
| 2.2.3. Decarburization Reaction Kinetics.....    | 15 |
| 2.2.4. Nucleation Theory.....                    | 37 |
| 2.2.5. Slag Structure & Electrical Property..... | 52 |
| 2.3. Summary and Knowledge Gaps.....             | 58 |
| References.....                                  | 60 |
| Chapter 3.....                                   | 67 |



|   |     |
|---|-----|
| 3. Decarburization of Bloated Droplets: An Experimental Study to Understand the Kinetics of Decarburization of Metallic Iron Droplets in FeO Containing CaO-SiO <sub>2</sub> Slags..... | 67  |
| 3.1. Introduction.....  | 68  |
| 3.2. Experimental Procedure.....  | 72  |
| 3.2.1. Experimental Setup.....  | 72  |
| 3.2.2. Sample Preparation.....  | 72  |
| 3.2.3. Experimental Procedure.....  | 75  |
| 3.3. Experimental Results.....  | 77  |
| 3.3.1. The Effect of Carbon Concentration and Mass on Decarburization of Droplets.....  | 77  |
| 3.3.2. The Effect of Slag FeO Concentration on Decarburization of Droplets....  | 82  |
| 3.3.3. The Effect of Slag Basicity on Decarburization.....  | 84  |
| 3.4. Discussion.....  | 86  |
| 3.4.1. Decarburization of Droplets; Effect of Carbon Concentrations and Droplet Mass.....   | 86  |
| 3.4.2. Decarburization of Droplets Reacting with Slag at Different FeO Concentrations.....  | 102 |

|   |     |
|---|-----|
| 3.4.3. Decarburization of Droplets Reacting with Slags of Different Basicity... | 104 |
| 3.5. Conclusions.....   | 106 |
| 3.6. References.....  | 107 |
| Chapter 4.....  | 112 |
| 4. A Decarburization Model for a Fe-C Droplet Reacting in Oxidizing Slag.....   | 112 |
| 4.1.Introduction.....   | 113 |
| 4.2. Model Formulation.....   | 118 |
| 4.2.1. External Decarburization.....  | 121 |
| 4.2.2. Internal Decarburization.....  | 125 |
| 4.2.3. Escape of Bubbles.....   | 129 |
| 4.3.Results & Discussion.....   | 134 |
| 4.3.1. Effect of Sulfur on Decarburisation.....                                 | 134 |
| 4.3.2. Effect of Temperature.....   | 141 |
| 4.3.3. Effect of Droplet Size.....  | 142 |
| 4.3.4. Effect of Droplet Carbon Content.....                                    | 144 |
| 4.4. Sensitivity Analysis.....  | 147 |
| 4.5. Error Analysis.....  | 152 |
| 4.6. Conclusion.....  | 154 |
| 4.7. References.....  | 160 |
| Chapter 5.....  | 165 |

|  |     |
|--|-----|
| 5. Decarburization of Iron Carbon Droplets with Oxidizing Slag: An Experimental Study to Understand the Effect of Ionic and Electronic Conductivity on Decarburization Kinetics..... | 165 |
| 5.1.Introduction.....  | 166 |
| 5.2.Experimental Technique.....  | 169 |
| 5.2.1. Sample Preparation.....   | 169 |
| 5.2.2. Apparatus.....  | 172 |
| 5.2.3. Procedure.....  | 173 |
| 5.3.Results.....   | 174 |
| 5.3.1. Ferric Fraction Variation.....  | 174 |
| 5.3.2. Slag $Fe_2O_3$ Variation at Different Ferric Ratios.....  | 177 |
| 5.3.3. Slag Basicity Variation at Different Ferric Ratios.....   | 178 |
| 5.4.Discussion.....  | 179 |
| 5.4.1. Rate Controlling Step Analysis.....   | 180 |
| 5.4.2. Kinetic Model.....  | 185 |
| 5.4.3. Proposed Mechanism for Premature Shutdown.....  | 194 |
| 5.5.Conclusion.....  | 199 |
| 5.6.References.....  | 203 |
| Chapter 6.....   | 208 |
| 6. Consideration of the Competitive Adsorption of Oxygen and Sulfur on Droplet Decarburization and Bloating Kinetics.....  | 208 |

|   |     |
|---|-----|
| 6.1.Introduction.....   | 209 |
| 6.2.Experimental Procedure.....   | 211 |
| 6.2.1. Material Preparation.....  | 211 |
| 6.2.2. Experimental Setup.....  | 212 |
| 6.2.3. Procedure.....   | 214 |
| 6.3.Results.....  | 214 |
| 6.3.1. Decarburization for Droplets with 0.011 wt% Sulfur.....                          | 215 |
| 6.3.2. Decarburization for Droplets with 0.016 wt% Sulfur.....                          | 216 |
| 6.3.3. Decarburization for Droplets with 0.129 wt% Sulfur.....                          | 217 |
| 6.4. Discussion.....  | 219 |
| 6.4.1. Theoretical Framework.....   | 220 |
| 6.4.2. Case for 0.011 wt% Sulfur.....   | 224 |
| 6.4.3. Case for 0.016 wt% Sulfur.....   | 229 |
| 6.4.4. Case for 0.129 wt% Sulfur.....   | 235 |
| 6.5.Conclusion.....   | 239 |
| 6.6.References.....   | 240 |
| Chapter 7.....  | 243 |
| 7. Kinetics of Simultaneous Reactions Between Fe-C-Si Droplets and Oxidizing Slags..... | 243 |
| 7.1.Introduction.....   | 244 |

|   |     |
|---|-----|
| 7.2. Experimental Technique.....  | 248 |
| 7.2.1. Experimental Setup.....  | 248 |
| 7.2.2. Materials Preparation.....   | 249 |
| 7.2.3. Experiment Procedure.....  | 250 |
| 7.3. Results.....   | 251 |
| 7.3.1. Effect of Silicon Concentration.....                               | 251 |
| 7.3.2. Effect of Temperature Variation.....                               | 254 |
| 7.4. Discussion.....  | 256 |
| 7.4.1. Desiliconization Kinetic Analysis.....                             | 256 |
| 7.4.2. Kinetic Model Including Multiple Reaction Steps and Reactants..... | 261 |
| 7.4.3. Droplet Fragmentation.....   | 263 |
| 7.4.4. Industrial Significance.....                                       | 265 |
| 7.5. Conclusion.....  | 266 |
| 7.6. References.....  | 267 |
| Chapter 8.....  | 265 |
| 8. Conclusion.....  | 272 |
| 8.1. Concluding Remarks.....  | 272 |
| 8.2. Overall Conclusions.....   | 274 |
| 8.3. Future Work.....   | 276 |

## LIST OF FIGURES

### Chapter 2

|  |    |
|--|----|
| Figure 2.1: Schematic of BOF with three reaction zones .....   | 10 |
| Figure 2.2: Two modes of droplet generation (a) dropping (b) swarming <sup>[9]</sup> .....   | 12 |
| Figure 2.3: Effect of carbon content on decarburization rate of metal droplet with pure CO <sub>2</sub> <sup>[15]</sup> .....  | 18 |
| Figure 2.4: Illustration of change in reaction mechanism by varying temperature <sup>[18]</sup> .....  | 21 |
| Figure 2.5: Oxidation kinetics of Fe based alloy drops with and without carbon. (a) variation of Fe, (b) variation of P and (c) variation of C with time <sup>[19]</sup> ..... | 22 |
| Figure 2.6: Supersaturation limits for nucleation of CO bubbles in Fe-C-O at 1600°C <sup>[20]</sup> .....  | 23 |
| Figure 2.7: Effect of temperature and sulfur content on decarburization rate <sup>[31]</sup> .....   | 25 |
| Figure 2.8: Decarburization observed of Fe-C droplet in 20% FeO containing slag <sup>[12]</sup> .....  | 34 |
| Figure 2.9: Rate of CO evolution with respect to (a) slag FeO content and (b) droplet sulfur content <sup>[38]</sup> .....   | 35 |
| Figure 2.10: Droplet size effect on measured and predicted CO evolution <sup>[38]</sup> .....  | 36 |
| Figure 2.11: Bubble nucleation model for Fe-C-O system as suggested by Levine <sup>[39]</sup> .....  | 45 |

|  |    |
|--|----|
| Figure 2.12: Possible pathway to bubble nucleation via a blob of dissolved gas (Schematic) <sup>[51]</sup> .....   | 47 |
| Figure 2.13: Schematic drawings and silicate chain with bridging O (O <sup>0</sup> ) shown in blue, nonbridging O(O <sup>-</sup> ) shown as pink and free O <sup>2-</sup> shown as maroon and cations in green <sup>[55]</sup> ... | 53 |
| Figure 2.14: Comparison between measured and calculated electronic conductivity using $r_0^* = 3.87 \text{ \AA}$ <sup>[68]</sup> .....   | 58 |

### Chapter 3

|  |    |
|--|----|
| Figure 3.1: Schematic of experimental set up.....  | 75 |
| Figure 3.2: Total CO generation with time (a), (b), (c), (d) and normalized retained volume variation with time (e), (f), (g), (h) at different carbon concentration and at different droplet masses ..... | 82 |
| Figure 3.3: Total CO generation with time (a) and normalized retained volume profile with time (b) on varying FeO wt% .....  | 84 |
| Figure 3.4: Total CO generation with time (a) and normalized retained volume profile with time (b) on varying Slag V-ratio .....   | 86 |
| Figure 3.5: Circuit analogy of the decarburization system .....  | 90 |
| Figure 3.6: Simplified circuit of decarburizing droplets .....   | 91 |
| Figure 3.7: Total CO(t)/A <sub>avg(t)</sub> , Total CO (t) /V <sub>metal</sub> variation with time for droplets with 4.4 wt% Carbon in (a), (b) respectively .....   | 96 |

|  |     |
|--|-----|
| Figure 3.8: Total CO(t)/A <sub>avg(t)</sub> , Total CO(t) /V <sub>metal</sub> variation with time for droplets with 2.5 wt% Carbon in (a), (b) respectively .....  | 96  |
| Figure 3.9: Total CO(t)/A <sub>avg(t)</sub> , Total CO (t) /V <sub>metal</sub> variation with time at 1.5 wt% Carbon level in (a), (b) respectively .....  | 97  |
| Figure 3.10: Total CO(t)/A <sub>avg(t)</sub> , Total CO(t) /V <sub>metal</sub> variation with time at 0.5 wt% Carbon level in (a), (b)respectively .....   | 97  |
| Figure 3.11: End Point Carbon Concentration variation on varying slag FeO wt% and slag basicity (V-ratio = CaO/SiO <sub>2</sub> ) in (a) and (b) respectively .....  | 104 |
| <b>Chapter 4</b>   |     |
| Figure 4.1: A ‘Bloated Droplet’ reacting in the emulsion in Basic Oxygen Furnace.....  | 115 |
| Figure 4.2: Schematic of sequence of events happening when a droplet enters into oxidising slag. ....  | 120 |
| Figure 4.3: Schematic of the workflow of decarburisation model .....   | 121 |
| Figure 4.4: Schematic of the transition from dense slag state to foamy slag state (a) droplet in dense slag (b) bloated droplet in foamy slag (c) droplet coming back in the dense slag at the end.....                                  | 133 |
| Figure 4.5: (a) Total CO gas generation in moles with time from model and experiment <sup>[16]</sup> and (b) fraction of moles from external and internal decarburisation with time for 1g droplet with 2.62% C 0.007% S at 1580°C ..... | 138 |



|   |     |
|---|-----|
| Figure 4.6: (a) Total CO gas generation in moles with time from model and experiment <sup>[16]</sup> and (b) fraction of moles from external and internal decarburisation with time for 1g droplet with 2.62% C-0.014% S at 1580°C .....  | 138 |
| Figure 4.7: (a) Total CO gas generation in moles with time from model and experiment <sup>[16]</sup> and (b) fraction of moles from external and internal decarburisation with time for 1g droplet with 2.62% C-0.021% S at 1580°C .....  | 139 |
| Figure 4.8: Variation of carbon concentration of droplet with reaction time for different sulfur and with thermodynamic and supersaturation limit .....   | 139 |
| Figure 4.9: Total CO generation with time from model and experiment <sup>[30]</sup> for 1 g droplet with 0.007% S at 1580°C (a) and 1640°C (b). The fraction of external and internal decarburisation for droplet at 1580°C (c) and 1640°C(d) respectively .....  | 142 |
| Figure 4.10: Total CO gas generation profile with time from model and experiment <sup>[53]</sup> for droplets with 2.62% C on varying droplet mass (a) 0.5 g (b) 1.0 g (c) 1.5 g respectively..   | 143 |
| Figure 4.11: Total CO generation with time from model and experiment <sup>[45]</sup> on varying carbon concentration in (a), (b) and (c) for 1.5% C, 2.5% C and 4.5% C respectively. The contribution in mole fraction from external decarburisation internal nucleation and growth with time for (d) 1.5% C (e) 2.5% C and (f) 4.5% C respectively. .... | 146 |
| Figure 4.12: Total CO generation with time on varying model parameters as (a) slag mass transfer coefficient, (b) forward reaction rate constant of FeO dissociation, (c) surface tension modifier, (d) growth rate constant .....  | 150 |

Figure 4.13: Variation of fraction of contribution from internal nucleation and growth in total CO generation by varying  $\psi$  parameter,  $k_O$  in (a) and (b) respectively.....151

Figure 4.14: Variation of resistances due to slag transport, chemical reaction and internal nucleation-growth of bubbles with time for 0.007%S(a), 0.014%S(b) and 0.021%S(c) droplets .....152

## Chapter 5

Figure 5.1: Schematic of experimental set up.....172

Figure 5.2: (a) Total CO gas generation with time and (b) Peak rate variation on varying ferric fraction in the slag .....176

Figure 5.3: Normalized retained volume profile variation with time on varying ferric fraction in the slag .....176

Figure 5.4: Variation in the peak decarburization rate on varying slag  $Fe_2O_3$  concentration at three ferric ratios .....178

Figure 5.5: Variation in the decarburization profile on varying slag basicity concentration at three ferric ratio 0, 0.5 and 1 in (a), (b), (c) respectively .....179

Figure 5.1: Prediction of total CO generation profiles for (a) ferric fraction 0.1 and (b) ferric fraction 0.25 (c) ferric fraction 0.5 (d) ferric fraction 0.75 and (b) ferric fraction 0.8 cases.....183

|   |     |
|---|-----|
| Figure 5.7: ‘Peak decarburization rate’ plotted against the calculated ‘D*’ for a range of Ferric fractions at 16% Fe <sub>t</sub> O concentration in slag .....  | 189 |
| Figure 5.8: ‘Peak decarburization rate’ plotted against the calculated ‘D*’ for a range of Fe <sub>t</sub> O concentration in the slag at ferric fraction 0, 0.5 and 1 in (a), (b), (c) respectively... | 191 |
| Figure 5.9: ‘Peak decarburization rate’ plotted against the calculated ‘D*’ for a range of basicity in the slag at ferric fraction 0 and 1 in (a), (b) respectively .....                               | 192 |
| Figure 5.10: ‘Peak decarburization rate’ plotted against the calculated ‘D <sub>1</sub> *’ for a range of ferric fractions at 16% Fe <sub>t</sub> O concentration in slag .....                         | 194 |

## **Chapter 6**

|   |     |
|---|-----|
| Figure 6.1: Schematic of experimental setup .....   | 214 |
| Figure 6.2: Total CO generation with time (a) and the droplet volume variation with time (b) for 2.5 wt%C - 0.011 wt%S droplets ..... | 216 |
| Figure 6.3: Total CO generation with time (a) and the droplet volume variation with time (b) for 2.5 wt%C - 0.016 wt%S droplets.....  | 217 |
| Figure 6.4: Total CO generation with time (a) and the droplet volume variation with time (b) for 3.9 wt%C - 0.129 wt%S droplets ..... | 219 |
| Figure 6.5: Total CO generation profile for 3.9 wt%C - 0.129 wt%S for initial 100 seconds.....  | 219 |

|  |     |
|--|-----|
| Figure 6.6: Equilibrium fraction of adsorption sites variation with activity of oxygen for 2.5 wt%C - 0.011 wt%S .....   | 226 |
| Figure 6.7: Model predicted total CO generation profile for 2.5%C - 0.011%S droplets in (a) B=0.9 with $Fe^{3+}/Fe = 0$ , (b) B=0.9 with $Fe^{3+}/Fe = 0.5$ , (c) B=2.0 with $Fe^{3+}/Fe = 0$ .....                    | 228 |
| Figure 6.8: Variation of fraction of surface area covered by oxygen and sulfur with three different slags: (a) B=0.9 with $Fe^{3+}/Fe = 0$ , (b) B=0.9 with $Fe^{3+}/Fe = 0.5$ , (c) B=2.0 with $Fe^{3+}/Fe = 0$ ..... | 229 |
| Figure 6.9: Competition in adsorption between sulfur and oxygen at the slag/metal interface with (a) low conductivity slag (b) high conductivity slag for Fe - 2.5%C - 0.016%S droplets.....                           | 231 |
| Figure 6.10: Equilibrium fraction of adsorption sites variation with activity of oxygen for 2.5 wt%C - 0.016 wt%S .....  | 232 |
| Figure 6.11: Model predicted total CO generation profile for 2.5 wt%C - 0.016 wt%S droplets in (a) B=0.9 and $Fe^{3+}/Fe = 0$ , (a) B=0.9 and $Fe^{3+}/Fe = 0.5$ , (c) B=2.0 and $Fe^{3+}/Fe = 0$ .....                | 233 |
| Figure 6.12: Variation of fraction of surface area covered by oxygen and sulfur with three different slags (a) B=0.9 with $Fe^{3+}/Fe = 0$ , (b) B=0.9 with $Fe^{3+}/Fe = 0.5$ , (c) B=2.0 with $Fe^{3+}/Fe = 0$ ..... | 235 |
| Figure 6.13: Equilibrium fraction of adsorption sites variation with activity of oxygen for 3.9 wt%C - 0.129 wt%S .....  | 237 |

Figure 6.14: Model predicted total CO generation profile for 3.9wt%C - 0.129wt%S droplets in (a) B=0.9 and  $Fe^{3+}/Fe = 0$ , (a) B=0.9 and  $Fe^{3+}/Fe = 0.5$ , (c) B=2.0 and  $Fe^{3+}/Fe = 0$ .....238

Figure 6.15: Variation of fraction of surface area covered by oxygen and sulfur with three different slags (a) B=0.9 with  $Fe^{3+}/Fe = 0$ , (b) B=0.9 with  $Fe^{3+}/Fe = 0.5$ , (c) B=2.0 with  $Fe^{3+}/Fe = 0$  .....239

## Chapter 7

Figure 7.1: Schematic of experimental set up.....249

Figure 7.2: Total CO generation profile with time with varying silicon in (a) and the corresponding bloated droplet volume in (b) .....253

Figure 7.3: The change of Si concentration with time for droplets with different initial concentration: 0.25 wt% Si in (a) and 0.5 wt% Si in (b).....254

Figure 7.4: Total CO generation profile with time in (a) and the dynamic volume of bloated droplets in (b) .....255

Figure 7.5: Silicon removal Profile for Fe - 4.5%C - 0.011%S - 0.5% Si droplets with oxidizing slag at 1465°C and 1505°C in (a) and (b) respectively.....256

Figure 7.6: Silicon removal data replotted according to equation 4 at 1505°C in (a) and at 1465°C in (b) .....258

Figure 7.7: The time instant at which droplet volume is greater than 2 times of original droplet volume is plotted against the initial silicon concentration of droplets in (a) and the

|  |     |
|--|-----|
| variation of peak rate of decarburization is plotted against initial silicon concentration in (b).....   | 260 |
| Figure 7.8: Droplet temperature profile for droplets (a) Fe - 0.5%Si - 4.6%C (b) Fe - 0.25%Si - 4.4%C in oxidizing slag .....  | 261 |
| Figure 7.9: Total CO generated profile with time in (a) and the silicon removal profile in (b) for Fe - 4.6 wt%C - 0.5 wt%Si with oxidizing slag at 1505°C .....               | 263 |
| Figure 7.10: Total CO generated profile with time in (a) and the silicon removal profile in (b) for Fe - 4.6 wt%C - 0.25 wt%Si with oxidizing slag at 1505°C .....             | 263 |
| Figure 7.11: X-ray image of crucible with metal droplet and slag at reaction time 1s (a) and 85 s(b) for Fe - 4.4%C 2 g droplet in CaO/SiO <sub>2</sub> = 2, 16% FeO slag..... | 264 |
| Figure 7.12: Small individual droplets separated from slag in (a) and (b) size distribution of broken droplet pieces .....   | 265 |

## LIST OF TABLES

|  |     |
|--|-----|
| Table 2.1: Heterogeneous nucleation possibilities.....   | 40  |
| Table 3.1: Metal composition used in experiments.....  | 73  |
| Table 3.2: Slag composition used in set of experiments.....  | 74  |
| Table 3.3: Droplet melting time(s) before dropping into the slag .....   | 76  |
| Table 3.4: Comparison of $K_b^{nuc}$ value calculated and found experimentally.....  | 99  |
| Table 3.5: Initial and Final carbon content in droplet before and after the decarburization reaction with 16wt% FeO slag (V-ratio 0.9) ..... | 101 |
| Table 4.1: RMSE error of model prediction on varying wt% S of 1 g droplet at 1580°C.....   | 153 |
| Table 4.2: RMSE error of model prediction on varying droplet mass with 2.62% C – 0.007% S at 1640°C.....                                     | 154 |
| Table 4.3: RMSE error of model prediction on varying carbon concentration of 1.0 g droplet at 1580°C.....                                    | 154 |
| Table 5.1: Expected ferric fraction based on FeO, Fe <sub>2</sub> O <sub>3</sub> mass ratio vs measured value..                              | 171 |
| Table 5.2: Comparison of peak decarburization rate with possible gas/slag reaction rate.....   | 184 |
| Table 6.1. Droplet and slag composition(wt%) .....   | 212 |
| Table 7.1. Metal droplet composition (wt%) .....   | 250 |

## LIST OF ABBREVIATIONS AND SYMBOLS

BOF Basic Oxygen Furnace

EAF Electric Arc Furnace

[wt%*i*] Weight percentage of *i* in metal phase

(wt%*i*) Weight percentage of *i* in slag phase

$M_i$  Molecular Weight of *i*

$X_i$  Mole fraction of *i*(-)

$f_i$  Henrian activity coefficient of species *i*

$a_i$  Activity of species *i*

$J_i$  Flux of species *i* (mol/m<sup>2</sup>-s)

$t_i$  Transference number of charged species *i* (-)

$z_i$  Charge no of species *i* (-)

$\mu_i$  Chemical Potential of species *i* in slag(J/mol)

$\overrightarrow{k_1}, \overrightarrow{k_2}, \overrightarrow{k_3}$  and  $\overleftarrow{k_1}, \overleftarrow{k_2}, \overleftarrow{k_3}$  Forward and backward reaction Rate constants

$\frac{\dot{n}}{A}$  Rate of CO generation per unit area (mol/m<sup>2</sup>)

$\dot{n}_{Si}$  Rate of transfer of silicon (mole/s)



$p_{O_2}$  Oxygen potential(atm)

$h_C$  and  $h_O$  Henrian activity coefficient of C and O(-)

$A_{A\eta}$  and  $A_{W\eta}$  Preexponential Factor of viscosity correlation (Pa/s)

$A_{avg}(t)$  Time averaged area(m)

$A_{g-m}(t)$  Total gas/metal surface area within the metal droplet at time instant  $t(m^2)$

$A_s$  and  $A_m$  slag-gas and gas-metal interfacial area ( $m^2$ )

$A_{s-m}(t)$  instantaneous slag-metal surface area ( $m^2$ )

$B_A$  and  $B_W$  Activation energy term in viscosity correlation(K)

$C_{FeO}$  Concentration of FeO ( $mol/m^3$ )

$C_{Si}$  and  $C_{Si}^i$  Concentration of silicon in the bulk and at the slag/metal interface( $m^3/s$ )

$C_i$  Concentration of mobile ion  $i$ ,( $mol/m^3$ )

$C_p$  Specific Heat of liquid iron

$D_i$  Tracer diffusion coefficient of  $i$  ion ( $m^2/s$ )

$E_1$  and  $E_2$  Activation energies (J/mol)

$E^{crit}$  Electric Field at the critical point of reaction shut down (V/m)

$F_G$  Volumetric flow rate ( $Nm^3/s$ )

$J_s$  Rate of nucleation (number of nuclei/ $m^3$ -s)

$K_1$  Equilibrium constant for  $FeO + CO = Fe + CO_2$

$K_{CO}$  Thermodynamic equilibrium constant for C/CO reaction

$K_{CO}, K_{FeO_{eq}}$  Equilibrium constant of CO formation and FeO dissociation reaction (-)

$K_S$  Sulfur Adsorption Constant

$K_a, K_b^{nuc}$  and  $K_b^{gr}$  Rate Constants

$K_j$  Adsorption coefficient of species  $j$ , where  $j$  are [S] and [O] (-)

$N_0$  Number concentration of CO embryos in liquid (/m<sup>3</sup>)

$N_A$  Avogadro's number (/mol)

$N_B$  Blowing number (-)

$N_g$  Number of gas molecules in the gas bubble (-)

$P_L, P_{ve}$  Liquid pressure and the pressure in the vapor bubble equilibrium respectively (Pa)

$P_d$  Dipole moment (C-m)

$P_e$  Equilibrium pressure of the gas molecule in the liquid (Pa)

$P_g$  and  $P_l$  Pressure within the gas bubble and the liquid respectively (Pa)

$R_1, R_2, R_3$  Rate of Reactions

$R_B$  Droplet generation rate (kg/m<sup>3</sup>)

$R_{CO}, R_{FeO}$  Rate of CO formation and FeO dissociation at the slag/metal interface (mol/s)

$R_{Ov}$ ,  $R_I$ ,  $R_{II}$ ,  $R_{III}$ ,  $R_{IV}$ ,  $R_V$ ,  $R_{VI}$  and  $R_{VII}$  Resistances in the circuit analogy of decarburization

$R_g$  CO generation rate(mol/s)

$U^s$  Electrostatic Energy (J)

$V_0$  Original droplet volume(m<sup>3</sup>)

$V_{CO}(t)^{nuc}$ ,  $V_{CO}(t)^{gr}$  Volume of CO bubbles which are generated from nucleation and growth respectively at time  $t$  (m<sup>3</sup>)

$V_{CO}(t)$  Volume of the CO bubbles remaining in the droplet at time  $t$  (m<sup>3</sup>)

$V^{esc}(t)$  Volume of bubbles which are escaping from the bloated droplet at time  $t$  (m<sup>3</sup>)

$V_g$  Volume of gas bubble(m<sup>3</sup>)

$V_m$  Volume of liquid metal (m<sup>3</sup>)

$W_m$  Mass of the metal droplet (kg)

$W_{slag}^{dense}$  Mass of dense slag (kg)

$W_{slag}^{foamy}$  Mass of foamy slag (kg)

$W_{slag}^{tot}$  Total slag mass (kg)

$Z_2$  Valency of Oxygen (-)

$\frac{d\phi}{dx}$  Electrical Potential Gradient (V/m)

$d_{limit}$  Limiting diameter of the drop corresponding to  $R= 0.1$  pct(m)

$f_C$  and  $f_O$  Henrian activity coefficient of carbon and oxygen with respect to 1 wt% Henrian standard state (-)

$\vec{k}$  Forward reaction rate constant of FeO dissociation (mol/m<sup>2</sup>-s)

$k_1$  and  $k_2$  Specific rate constants from chemical reaction and slag transport respectively

$k_{CO_2}$  Rate constant of the CO<sub>2</sub> dissociation reaction

$k_o$  Overall Rate constant (mol/s)

$k_{eff}$  Effective slag mass transfer coefficient (m/s)

$k_{gr}$  Growth rate constant (mol/m<sup>2</sup>-s)

$k_m$  Mass transfer coefficient in metal phase (m/s)

$k_r$  Forward reaction rate constant of CO formation (kg/m<sup>2</sup>-s)

$k_s$  Mass transfer coefficient in slag (m/s)

$m_g$  and  $m_s$  Mass transfer coefficient in slag and in gas phase (m/s)

$n_c$  Number of molecules in critical cluster (-)

$n_{CO}$  Number of moles of CO in a bubble of radius  $r$ (mol)

$n_e$  Number of molecules in an embryo (-)

$n_r$  Number of moles in blob (mol)

$p_{O_2}$  Oxygen potential in the slag (Pa)

$r^0$  Hopping distance between  $Fe^{2+}$ - $Fe^{3+}$  ions (m)

$r_0^*$  Maximum hopping distance between  $Fe^{2+}$ - $Fe^{3+}$  ions (m)

$r^{crit}$  Critical radius of CO bubble in liquid metal (m)

$r_n$  Radius of bubble containing n molecules (m)

$r_t$  Radius of a bubble at t times step (m)

$u_G$  Critical gas velocity (m/s)

$v_m$  Volume of cluster ( $m^3$ )

$y_t^{Model}$  Model predicted data point at time t (mol)

$y_t^{exp}$  Experimentally found data point at time t (mol)

$\Omega_g$  Molar volume of the gas( $m^3$ )

$\gamma_{FeO}$  Activity coefficient of FeO of the bulk slag concentration (-)

$\theta_S$  Fraction of site blocked by surface active species sulfur (-)

$\theta_j$  Fraction of surface area blocked due to poisoning (-)

$\nu_{ph}$  Phonon frequency (/s)

$\rho_G$  and  $\rho_L$  Density of blown gas and liquid metal( $kg/m^3$ )

$\rho_d(t)$  Density of droplet at time t ( $kg/m^3$ )

$\sigma_{0_{blob}}$  and  $\sigma_{0_{bubble}}$  Surface tension of blob and bubble respectively (N/m)

$\sigma_0$  Surface tension of liquid metal (N/m)

$\sigma_c$  Total electrical conductivity of Slag (S/m)

$\sigma_{el}$  Electronic Conductivity of slag (S/m)

$\sigma_{ion}$  Ionic Conductivity of slag (S/m)

$\sigma_{tot}$  Total conductivity of slag (S/m)

$\Delta C_{FeO}$  Difference between interface and bulk concentration of FeO in the slag (mol/m<sup>3</sup>)

$\Delta G_{crit}$  Critical Gibbs Free energy (J/mol)

$\Delta\mu^*$ ,  $\Delta F^*$ ,  $r^*$  Chemical potential, Helmholtz free energy change at the critical radius  $r^*$

$\Delta F$  Helmholtz Free energy change (J/mol)

$\Delta H$  Heat of formation of CO molecule (J/mol)

$\Delta x$  Boundary layer thickness (m)

$D$  diffusivity of species in the metal (m<sup>2</sup>/s)

$d$  Sieve of diameter (m)

$F$  Faraday Constant(C/mol)

$R$  Cumulative wt (in pct) retained on the sieve (%)

$T$  Temperature (K)

$W$  activation energy of hopping process (J)

$N$  Number concentration of nucleation sites per unit volume ( $/m^3$ )

$R$  Universal Gas Constant (J/mol-K)

$V(t)$  Volume of droplet at time  $t$  ( $m^3$ )

$Z$  Zeldovich Factor (-)

$k$  Boltzmann Constant (J/K)

$m$  Mass of single molecule of CO (Kg)

$n$  Number of molecules in a cluster (-)

$r$  Radius of gas bubble(m)

$y$  Ferric Fraction ( $\frac{Fe^{3+}}{Fe^{2+}+Fe^{3+}}$ ) in the slag (-)

$y$  Fraction of  $Fe^{3+}$  ions ( $Fe^{3+}/Fe$ ) in the slag

$\beta$  Diffusive flux ( $mol/m^2-s$ )

$\eta$  Viscosity (Pa/s)

$\theta$  and  $\theta_0$  Contact Angles (Rad)

$\tau$  Surface concentration of adsorbed oxygen atoms (No of atoms/ $m^2$ )

$\psi$  Surface tension modifying parameter (-)

# **Chapter 1**

## **1. Introduction**

### **1.1. Research Background**

Steel has played a major role in the transformation of the global economy since industrialization. Several times in history, artificial demands for steel were created to boost the economy from post-World War I to post covid. In the post covid world, the infrastructure heavy stimulus packages announced by the Chinese Government (4 trillion) and the US government (2 trillion) will create huge demand<sup>[1]</sup> for steel. Although there is research underway worldwide on hydrogen-based steelmaking, until there is a breakthrough in technology to reduce the cost of electricity or special incentives are provided by the government on fossil fuel free steel products, it is not a feasible technology for large steel producers. In 2020, 1.8 billion tonnes of crude steel were produced globally, of which China produced more than 50%. In China, more than 90% of the crude steel is produced using oxygen steelmaking, and globally that number is 70%. With the growing demand for high quality steel with stringent composition requirements, optimization of the process is becoming more and more important.

In oxygen steelmaking, there are three primary reaction zones: the impact zone, the slag/metal bath interface, and the gas/slag/metal emulsion. Whilst all these zones play a significant role, the emulsion is the most significant for refining phosphorus and a major contributor to the refining of carbon. For this reason, it is essential to include the emulsion



in any model used to optimize steelmaking. The current work focuses on the decarburization behavior of droplets in the emulsion because of the importance of that reaction. The mechanism of decarburization controls the residence time of droplets in the emulsion, thereby impacting other refining reactions in the emulsion.

When the oxygen jet at supersonic velocity strikes the metal bath, many metal droplets are created and undergo refining in the emulsion. The extent of refining of these droplets is determined by the slag/metal interfacial area, composition of slag, and the residence time, i.e., the time spent by these individual droplets in the emulsion. The two most important parameters for refining, i.e., reaction area and the residence time, are determined respectively by the generation rate of droplets and the kinetics of the decarburization process. Decarburization generates CO bubbles within the droplets, causing swelling, often referred to as bloating. Due to bloating, the residence time of the droplets increases from a quarter of a second expected for dense droplets to up to 120 seconds. Bloating will also increase the reaction surface area by several times. Previous work<sup>[2]</sup> in the author's laboratory has shown that the swelling rate is strongly dependent on the rate of CO generation within the droplet. The major impurities, such as phosphorus, are removed only in the emulsion. Previous studies at McMaster University<sup>[3]</sup> have shown that the dephosphorization kinetics of droplets in oxidizing slag is enhanced mainly due to stirring introduced by CO bubbles formed inside the droplet. It is crucial to understand the decarburization kinetics and the bloating behavior of individual droplets not only to control carbon content in the steel but to control residence time. The primary motivation of this

study is to provide fundamental kinetic data and develop a model to predict and quantify the decarburization kinetics and the bloating behavior.

This project is a part of a larger project to develop a global model for basic oxygen steelmaking. The decarburization kinetics being the main controlling factor of refining in the emulsion, which is reported to contribute 60% of the total refining of the metal bath, it is important to develop a detailed physicochemical model of decarburization which can predict the bloating behavior as well as the overall rate of carbon removal.

To develop an effective decarburization model, there is a need to understand the way in which reaction kinetics are affected by variations of slag and metal composition. For this purpose, a detailed set of experiments were performed varying slag and metal compositions.

The detailed objective of this project can be summarized as follows:

1. Develop a decarburization model for a liquid metal droplet in oxidizing slag, including the partitioning of oxygen at the slag/metal interface and under mixed control involving all critical reaction steps:
  - a. Mass transport of FeO in the slag
  - b. Dissociation of FeO at the slag/metal interface
  - c. Formation of CO at the slag/metal interface
  - d. Transport of oxygen into the bulk metal
  - e. Nucleation & growth of CO bubble inside the droplet
  - f. Poisoning of the slag/metal interface and the bubble surface by sulfur

2. Develop an understanding of the decarburization kinetics and bloating behavior on varying droplet carbon concentration in the range of 0.5% to 4.4% in oxidizing slag, droplet slag basicity from 0.9 to 2, slag FeO concentration from 2.5% to 16%
3. Investigate the effect of slag electronic and ionic conductivity on the kinetics of decarburization, which is essential not only for oxygen steelmaking but also for any other pyrometallurgical refining reactions
4. Develop an insight into the interplay between the two adsorbing elements sulfur and oxygen on decarburization kinetics in which oxygen itself is a reactant.
5. Understand the competition in the removal reactions of silicon with carbon and the effect of silicon on the decarburization kinetics and bloating behavior of metal droplets in oxidizing slag.

## **1.2. Thesis Outline**

Chapter 1: Introduction: This chapter presents a brief background of this research work followed by the motivation of this research and mentions the different directions in which the project is explored.

Chapter 2: Literature Review: This chapter starts with a brief history of steelmaking covering the layout of an integrated steel plant, slag structure, details about the BOF process, and then a thorough review of the previous researches on decarburization kinetics both in oxidizing gas and slag is presented. In the later section of this chapter, a brief review of the classical nucleation theory and alternate nucleation theories for bubble nucleation is covered. In the end, spontaneous emulsification is discussed.

Chapter 3: *'Decarburization of Bloated Droplets: An experimental study to understand the kinetics of decarburization of metallic iron droplets in FeO containing CaO-SiO<sub>2</sub> slags'*:

This chapter discusses the experimental study performed for various carbon concentration droplets in oxidizing slag. A kinetics analysis has been presented based on a mixed controlled kinetic model, including slag mass transport, interfacial chemical reaction, and CO gas bubble nucleation. The study further confirms the need for a comprehensive decarburization model. A sudden shut down of decarburization reactions for all ranges of droplet carbon concentrations irrespective of the supply of reactants is discussed. This work has been accepted and in the process of publication. DOI: 10.1007/s11663-021-02344-x.

Chapter 4: *'A Decarburization Model for a Fe-C Droplet Reacting in Oxidizing Slag'*: This chapter describes the individual kinetics steps involved such as mass transport in slag, mass transport in metal, slag/metal interfacial chemical reaction, nucleation of bubbles, and growth of these individual bubbles in decarburizing a liquid metal droplet in oxidizing slag. The model validation is demonstrated for a wide range of conditions: varying poisoning element concentration, droplet mass, temperature, carbon concentration. This work has been published. J Biswas, K. Gu, K. Coley, *Metallurgical and Materials Transactions B*. DOI: <https://doi.org/10.1007/s11663-021-02303-6>.

Chapter 5: *'Decarburization of iron carbon droplets with oxidizing slag: An experimental study to understand the effect of ionic and electronic conductivity on decarburization kinetics'*: This chapter discusses decarburization experimental results on varying slag electronic and ionic conductivity. An oxygen transport model based on Wagner's oxidation

theory is proposed, and a demonstration of the transport model is presented based on a kinetics analysis with decarburization results at various slag conductivities.

Chapter 6: *‘Consideration of the competitive adsorption of oxygen and sulfur on droplet decarburization kinetics’*: A decarburization kinetics study on varying slag oxygen transport property at three different sulfur levels is presented. An interesting observation of the disappearance of surface poisoning at higher slag oxygen transport is reported, and competition between oxygen from slag and sulfur from metal in adsorbing the slag/metal reaction sites is proposed to be the underlying reason for it.

Chapter 7: *‘Kinetics of Simultaneous Reactions between Fe-C-Si droplets and Oxidizing slags’*: An experimental study of decarburization in the presence of different levels of silicon concentration is presented, and results from quenching experiments to understand silicon removal kinetics are also introduced in this chapter. Silicon is found to delay the decarburization and bloating behavior of droplets in oxidizing slag.

Chapter 8: Concluding Remarks: The key findings from the overall project and the future scope of this research are discussed.

## **Chapter 2**

### **2. Literature Review**

This chapter comprises three parts to demonstrate the background of my research and the critical knowledge gaps, which will be addressed in subsequent chapters of this thesis. This chapter starts with a brief overview of global steel production and the history of steelmaking, followed by a short description of the basic oxygen steelmaking process. Reaction kinetics in the Basic Oxygen Furnace (BOF) will be discussed afterward, previous studies on decarburization of iron will be reviewed. An overview of slag transport properties and conductivity will also be presented, along with an explanation of their significance in the decarburization of iron-carbon droplets in slag.

#### **2.1. History of Steelmaking**

Steel is mainly an alloy of iron which has a carbon content of  $< 2\%$ . The development of steelmaking can be traced back to the start of the iron age, when iron emerged as a much stronger and harder material than bronze. However, the quality of the iron, which was produced in that period, depended more on the quality of the iron ore and the process adopted. In the 19<sup>th</sup> century, urbanization in Europe and worldwide demanded more versatile and structurally strong high-quality steel. Fundamentals of steel production with a wide variety of iron ore were explored at that time, which was the precursor of modern iron making and steelmaking. It was not until 1856, when Henry Bessemer suggested an effective way of producing steel by introducing oxygen by blowing air into molten iron to

reduce the carbon content, large-scale steel production at a low cost was possible. This process was called the *Bessemer Process*. The major limitation of the *Bessemer process* was that it created very high oxygen and nitrogen contents in the final product, and it was unable to deal with high phosphorus ore. Later in 1879, the phosphorus problem in the *Bessemer process* was addressed by Welshman Sidney Gilchrist Thomas by adding a chemically basic flux and replacing the furnace lining with basic oxide. This process was called the *Thomas Process* or *Basic Bessemer Process*. Both these processes experienced challenges due to high nitrogen content in the final product and started to lose popularity with the *open-hearth steelmaking* process. In 1860, German engineer Karl Wilhelm Siemens and the Martin brothers developed an *open-hearth steelmaking* process which became popular for better control of final composition and dominated world steel production for about a century. The main limitation of this process was slow kinetics, and a minimum of 6-8 hours were required for each heat. In 1899, Paul Heroult invented the *Electric Arc Furnace (EAF) steelmaking* process, which could efficiently produce high-quality steel.

Around 1950, low-cost oxygen production by the Linde group triggered the replacement of air by pure oxygen in the *Basic Bessemer process*. This modification avoided the nitrogen pick-up problem and had a much-improved heat balance. This process was called the *basic oxygen steelmaking process*. The first commercial plant with such configuration was at Linz and Donawitz in Austria in 1952-1953. The process was named after these places and is now widely known as the *LD steelmaking process*. There are different blowing practices in the basic oxygen steelmaking process: top blowing, bottom blowing,

and combined blowing. Nowadays, more than 98% of world steel is produced by these two processes: *EAF and Oxygen steelmaking*.

World crude steel production has risen continuously over the years from ~189 million tonnes in 1950 to ~1869 million tonnes in 2020<sup>[4]</sup>. The production of crude steel is mainly performed in two steps: iron making and steel making. In the iron making process, the iron ore is reduced by coke or reformed natural gas in a countercurrent reactor to produce hot metal in the blast furnace or sponge iron in the Direct Reduced Iron (DRI) process. The impurities in the hot metal/ sponge iron are removed in the primary steelmaking step by oxidizing in the basic oxygen furnace (BOF) or in the electric arc furnace (EAF). The degassing and further alloying are performed in the secondary steelmaking step to produce final quality steel. The current work focuses on the reaction kinetics of droplets in Basic Oxygen Steelmaking. The remainder of this literature review will focus on the relevant background to that work.

## **2.2. Basic Oxygen Steelmaking Process**

In this process, hot metal, which is produced from blast furnace, of composition ~ Fe - 4%C - 0.5%Si - 0.3%Mn - 0.07% P, steel scrap, and lime powder are fed into the LD converter and oxygen is injected at a supersonic speed from the top of the converter. The target composition of the steel product is typically C<0.05%, Si<0.005%, Mn<0.05%, P<0.001% which is generally achieved within 16 mins from the start of oxygen blowing. The oxygen jet oxidizes a layer of metal, producing an enormous amount of slag quickly and generates a huge number of metal droplets. There are mainly three zones in which



refining happens in the basic oxygen steelmaking process: gas/metal reaction zone, slag/metal bath reaction zone and metal droplet/slag reaction zone (typically called emulsion zone). A schematic of the BOF is shown in Figure 2.1 to depict the different reaction zones. A significant number of droplets get entrapped in the oxygen jet and either oxidize completely or refine partially and fall back into the metal bath. A small fraction of the refining goes on at the interfacial area between the slag and metal bath. A considerable amount of refining happens in the slag/gas/metal emulsion, where metal droplets, generated by the oxygen jet, react with the surrounding slag. After some time, typically referred to as residence time, these droplets fall back into the metal bath. The main parameters that determine the kinetics of refining of the metal bath in the BOF are droplet generation rate & size distribution, residence time. These are discussed in the following sections.

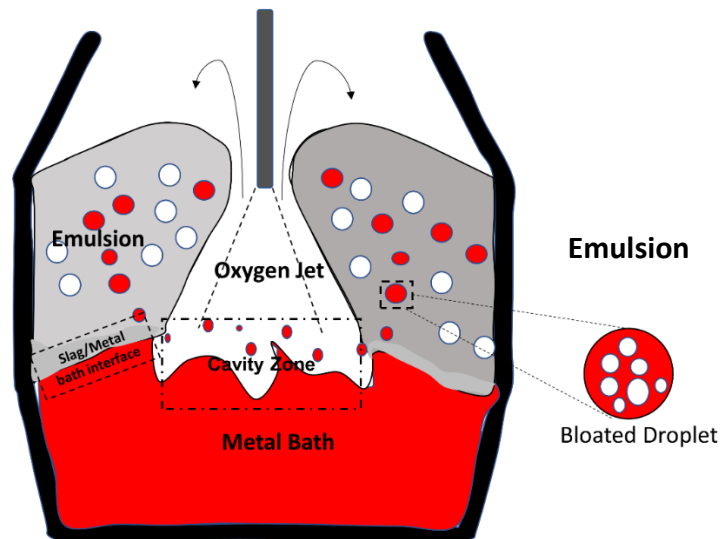


Figure 2.2: Schematic of BOF with three reaction zones

### 2.2.1. Droplet generation rate

In the BOF, when an oxygen jet at supersonic speed impinges on a liquid metal bath, a large number of liquid metal droplets of varying sizes are generated from the cavity due to transfer of momentum from the oxygen jet to the metal bath. There have been several experimental studies<sup>[5-10]</sup> to understand the droplet generation behavior. The main controlling factors are oxygen supply pressure, lance-bath separation, and liquid metal properties. Molloy<sup>[10]</sup> identified three different types of cavity modes by impinging an air jet onto a water bath. The three cavity modes are 1/ dimpling mode: shallow depression created by low jet velocity or greater lance height, 2/ splashing mode: unstable liquid surface with increasing jet velocity or decreasing lance height which creates metal droplets by tearing liquid 3/ penetrating mode: oscillating cavity in which proportion of metal ejected returns back to the metal bath being entrained by the gas. Later He and Standish<sup>[7,9]</sup> proposed two modes 1/ dropping mode, 2/ swarming mode which they stated to be different from the modes proposed by Molloy<sup>[10]</sup>. In the ‘dropping’ mode, a shallow depression forms with small ripples on the surface, and finally, single droplets are created from the crater. In the ‘swarming’ mode, large tears of liquid are generated at the edge of the crater by necking. Two modes of droplet generations are shown in the following figure (Figure 2.2). They observed that with an increase in top gas flow rate, the droplet generation rate increased, and the mode of droplet generation shifted from ‘dropping’ to ‘swarming’ mode.

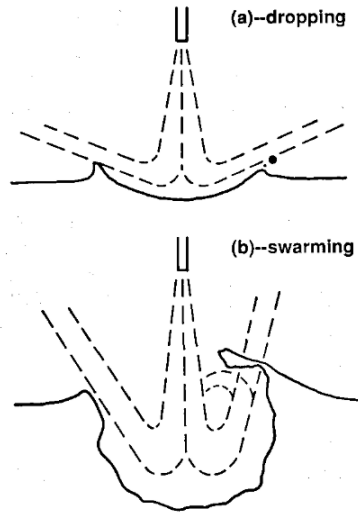


Figure 2.3: Two modes of droplet generation (a) dropping (b) swarming<sup>[9]</sup>

A maximum droplet generation rate was observed to occur at a critical lance height. When the lance height is above the critical lance height, jet momentum intensity decreases with an increase in lance height, which reduces the droplet generation rate. However, below the critical lance height, when the lance is too close to the liquid, a profound depression is formed with large bubbles underneath the nozzle and the situation becomes similar to submerged injection leading to less splashing and less droplet generation. This was explained in further detail by Sabah & Brooks<sup>[11]</sup> as the mode of cavity changed from ‘splashing mode’ to ‘penetrating mode’ when the lance height was moved very close to the metal bath and resulted in decrease of droplet generation per unit volume of blown gas almost by one order of magnitude. A significant effect of bottom blowing on droplet generation rate has also been observed by He & Standish<sup>[9]</sup>. Based on the observation of the impact of jet momentum intensity, liquid density, viscosity and surface tension on droplet generation rate, He & Standish<sup>[7]</sup> proposed a dimensionless correlation, whereas

Subagyo *et al.*<sup>[5]</sup> later modified the correlation of He & Standish<sup>[7]</sup>, suggesting a new dimensionless number, named “Blowing number”, which was based on the Kelvin Helmholtz Criterion for interface instability. Subagyo *et al.*<sup>[5]</sup> also proposed a correlation to predict the droplet generation rate per unit volume of blown gas as a function of the Blowing number. The generated droplets were observed to follow the Rosen Rammler Sperling distribution by both Koria & Lange<sup>[6]</sup> and Subagyo *et al.*<sup>[5]</sup> and these two correlations are generally used by the recent researchers to model the BOF process. The blowing number ( $N_B$ ) and the droplet generation rate ( $R_B$ ) per unit volumetric flow rate ( $F_G$ ) are expressed as<sup>[5]</sup>

$$N_B = \frac{\rho_G u_G^2}{2\sqrt{\sigma_0 g \rho_L}} \dots [2.1]$$

$$\frac{R_B}{F_G} = \frac{N_B^{3.2}}{[2.6 * 10^6 + 2.0 * 10^{-4}(N_B)^{12}]^{0.2}} \dots [2.2]$$

Where  $\rho_G$  and  $\rho_L$  are the density of blown gas and liquid metal,  $u_G$  is the critical gas velocity and  $\sigma_0$  denotes the surface tension of liquid metal. The droplet size distribution can be expressed as<sup>[6]</sup>

$$R = 100 (0.001) \left(\frac{d}{d_{limit}}\right)^{1.26} \dots [2.3]$$

Where  $R$  is the cumulative weight percentage (%) remaining on the sieve of diameter  $d$  and  $d_{limit}$  is the limiting droplet diameter corresponding to  $R=0.1\%$ . Recently, Brooks & coworkers<sup>[11]</sup> further explored the droplet generation problem as the expression of Subagyo *et al.*<sup>[5]</sup> was developed for a fixed lance height. Sabah & Brooks<sup>[11]</sup> showed that for a fixed

blowing number ( $N_B = 3$ ) the droplet generation rate ( $\frac{R_B}{F_G}$ ) was found to be in the range of 5 to 9 kg/Nm<sup>3</sup> in splashing mode and droplet generation rate decreased to approx. 0.4 kg/Nm<sup>3</sup> in penetration mode. Based on this observation, these workers concluded that a higher blowing number does not always lead to a higher droplet generation rate as is predicted in the earlier expression of Subagyo *et al.* Consideration of the type of cavity mode with the variation of lance height is crucial in predicting the droplet generation mode accurately. For the splashing mode, Sabah & Brooks<sup>[11]</sup> have proposed another correlation by considering the lance height variation for lance length to nozzle diameter ratio > 50 as

$$\frac{R_B}{F_G} = -0.8819N_B^4 + 7.4932N_B^3 - 18.567N_B^2 + 14.766N_B \dots [2.4]$$

### 2.2.2. Residence time

Due to the transfer of momentum from the supersonic jet to the metal bath, a large fraction of metal ejects from the metal bath with varying sizes of droplets which are refined in the gas/slag/metal emulsion and falls back into the metal bath. The time which is spent by a droplet in the emulsion is termed residence time. The residence time of a droplet depends upon primarily on the decarburization rate, droplet size and additionally on the ejection velocity and the ejection angle. Experimental studies<sup>[2,3,12]</sup> on decarburization of a single droplet in oxidizing slag have shown a swelling of the metal droplet due to the accumulation of internally generated CO bubbles. A mathematical model was developed by Subagyo *et al.*<sup>[13]</sup> to predict the residence time of a droplet in an emulsion based on the balance on four types of forces – 1/ gravitational force, 2/ buoyancy force, 3/ drag force

and 4/ added mass force. Brooks *et al.*<sup>[14]</sup> later incorporated the effect of decarburization rate on the droplet density and developed a model for the motion of a swelled droplet. This phenomenon was termed as ‘Bloating’<sup>[14]</sup> and this was found to influence the residence time of the droplets in the emulsion. Brooks & coworkers<sup>[14][13]</sup> demonstrated that without considering bloating it was impossible to justify a residence time that would support the refining rates observed in real BOFs. Bloating depends on the formation of CO bubbles inside the droplet. Therefore, to fully understand bloating it is essential to understand the mechanism by which internal decarburization occurs. The objective of the current work is to develop a detailed understanding of the decarburization of iron carbon droplets in oxidizing slags, the factors that allow bloating to occur, the effect of slag composition, the effect of metal composition including the presence of surface-active elements and the effect of temperature. As a foundation for this work, the remainder of this literature review will examine our existing knowledge of decarburization of iron, decarburization of droplets and other background required to develop a kinetic model of droplet decarburization and bloating in BOF slag.

### **2.2.3. Decarburization Reaction Kinetics**

Decarburization of the liquid metal in BOF steelmaking occurs at three reaction sites – the emulsion, the cavity or impact zone and the slag/metal bath interface. In the emulsion, metal droplets react with surrounding oxides, generating CO bubbles both at the slag/metal interface and within the metal droplet. As mentioned previously, these droplets in the emulsion bloat and increases the residence time and the slag/metal interfacial area. To understand bloating, it is crucial to have a good understanding of decarburization kinetics.

In the cavity, a layer of metal on the surface of the bath oxidizes, resulting in a small amount of removal of carbon. There are also metal droplets ejected into the gaseous zone from the cavity. These react with the oxygen gas in the cavity, however, despite several decades of research on droplets, till now they have not generally been considered in process models of the cavity and its contribution to overall refining. Currently, there is work ongoing in the author's lab to address the role of these droplets. While removing impurities, these droplets oxidize partially. There is also removal of carbon at the slag/metal bath interface, but the contribution to overall refining is minimal. For several decades, there have been extensive studies<sup>[15-21]</sup> for several decades to understand rate controlling steps and mechanism of the decarburization process in both oxidizing gas atmospheres and in oxidizing slags for metal baths and metal droplets. These studies are summarized here.

Philbrook & Kirkbride<sup>[22]</sup> conducted studies with a carbon saturated metal bath and a layer of slag. In their work, the rate of reduction of FeO was found to be second order with respect to FeO concentration, whereas Dancy<sup>[23]</sup> found it to be first order with respect to FeO under similar circumstances. Sarma<sup>[24]</sup> also found the rate of reduction of FeO by carbonaceous material to be limited by mass transport of FeO in the slag phase, where the rate of CO generation was  $\propto (wt\% FeO)^{1.67}$ . This was explained by the combined effect of FeO concentration on driving force and on the mass transfer coefficient; mass transfer coefficient,  $k_m \propto (wt\% FeO)^{0.67}$  due to stirring from CO gas bubbles.

Fujii<sup>[25]</sup> investigated the decarburization behavior of iron-carbon melts in an oxidizing atmosphere to study the effect of carbon content in the melt. They found the rate of decarburization was independent of carbon content  $> 0.15\%$  whereas below that

concentration decarburization rate decreased rapidly with carbon content. The decarburization rate was found to increase with an increase in oxygen concentration in the gaseous atmosphere.

Ito & Sano<sup>[26-29]</sup> performed an investigation of decarburization behavior of iron carbon melts in an oxidizing gas atmosphere. They observed the rate of decarburization to be independent of melt carbon concentration and to vary linearly with gas flow rate and gas-metal reaction surface area. At a very high gas flow rate, the decarburization rate deviated from linearity. They observed that initially carbon concentration decreased linearly till the formation of an oxide layer on top of the molten metal below a critical carbon level. Thereafter, the decarburization rate was found to be controlled by diffusion through this oxide layer. These workers noticed that the critical carbon content at which the oxide layer formed decreased upon the addition of alloying elements such as Si, Cr and Mn.

Baker *et al.*<sup>[15]</sup> performed a decarburization study of levitated iron carbon droplets in oxidizing gas. They proposed the decarburization reaction to be gas phase mass transfer controlled for high carbon melts. However, carbon diffusion in the liquid metal became rate controlling for low carbon concentration melts as shown in Figure 2.3. When the carbon concentration in the levitated droplet dropped below 1%, the rate of supply of oxygen was higher than the rate of consumption at the gas/metal interface. The remaining oxygen entered the metal droplet and reacted with the countercurrent diffusing carbon. This could develop a local CO supersaturation pressure within the metal droplet, leading to nucleation and in the absence of any second phase within droplet, homogeneous nucleation was postulated. Baker *et al.* also proposed a possible mechanism of subsurface nucleation



by surface renewal through eddy diffusion in which a small, oxygen-saturated volume of liquid metal was proposed to sweep below the surface and create a local supersaturation offering a possible source of internal nucleation. A part of the dissolved oxygen was found to oxidize the liquid metal during the slow decarburization period which was similarly observed by Fujii<sup>[25]</sup>. In another work presented by Baker<sup>[30]</sup>, evidence of subsurface nucleation of CO in the case of high carbon and low carbon droplets was presented. They proposed droplet decarburization to be under mixed control by gaseous mass transfer and carbon transfer in the metal, although gaseous transfer was considered the predominant mechanism.

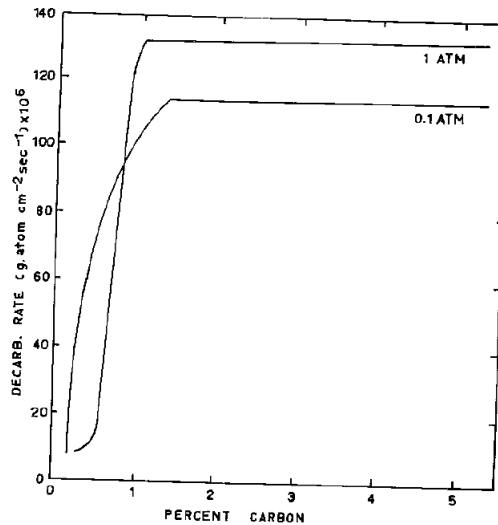


Figure 2.4: Effect of carbon content on decarburization rate of metal droplet with pure  $\text{CO}_2$ <sup>[15]</sup>

Distin, Hallett & Richardson<sup>[16]</sup> studied the decarburization behavior of levitated iron carbon droplets in oxidizing gas and the oxidation and vaporization behavior of pure iron

droplets. The decarburization of Fe-4%C droplet in pure O<sub>2</sub>, O<sub>2</sub>+CO<sub>2</sub>, O<sub>2</sub>+ Ar and O<sub>2</sub>+H<sub>2</sub>O showed the decarburization to be gas phase mass transfer controlled until a critical carbon concentration was reached and an oxide layer was formed, at that point the reaction became metal phase mass transfer controlled. These workers observed the formation of an oxide layer on the surface of the droplet followed by boiling of the droplet due to bubble bursting. They identified that the oxygen content within the droplet increased until the carbon content dropped below a certain level after which they reported the formation of an oxide layer. They proposed these oxides to be the source of subsurface nucleation of gas bubbles. A small volume element of these oxides was proposed to enter the metal droplet due to stirring, and the ensuing oxygen enrichment would increase the local CO supersaturation. Although, in theory, this reported local supersaturation was not high enough to support homogeneous nucleation, it was considered sufficiently high for the growth of bubbles on preexisting gas filled crevices on 0.1 μm or 1 μm inclusions. These workers also suggested that at the Fe/FeO interface due to the misfit of atomic arrangement, there was a chance for CO molecules to congregate and increase the probability of heterogeneous nucleation. A study with pure iron droplets in Ar/CO<sub>2</sub> mixtures showed the formation of an oxide layer when dissolved oxygen content reached 0.27 wt% at 1785<sup>0</sup>C.

See & Warner<sup>[17]</sup> also performed a decarburization study of Fe-C and Fe-C-Si liquid droplets in oxygen during free fall. They supported the phenomenon of carbon boiling after the formation of an oxide layer, as proposed by previous researchers. They observed the decarburization rate to increase with decreasing droplet size and a delay in carbon boiling in the presence of silicon. The measured rate of decarburization was explained qualitatively

by the gas diffusion-controlled decarburization mechanism but did not make sense from a quantitative perspective. They found bubble growth was controlled by oxygen diffusion in the metal. The presence of silicon in the metal was found to have a significant influence on bubble growth.

Roddis<sup>[18]</sup> investigated the decarburization behavior of levitated liquid Fe-C droplets and free falling droplets in an oxidizing atmosphere. In the levitated droplet studies, decarburization was reported to be controlled by gaseous diffusion only when the carbon content was high, whereas in the case of free-falling droplets gaseous diffusion could not fully explain the decarburization behavior. Roddis<sup>[18]</sup> proposed that stirring within the droplet determined the carbon flux to the gas metal interface and acceleration of droplets during free fall modified the gas boundary layer and both these effects contributed to control the rate as well the critical carbon concentration at which subsurface nucleation would start. In the case of levitated droplet studies, the stirring rate was much higher, so the carbon transport was much faster thereby delaying subsurface nucleation of CO. In reaction with free falling droplets, the decarburization rate was much faster due to the high rate of oxygen transport. On lowering temperature, a change in the dominant controlling step was observed from surface reaction to subsurface nucleation (Figure 2.4). These workers also reported a delay in subsurface nucleation on progressively diluting the oxidizing gas with nitrogen.

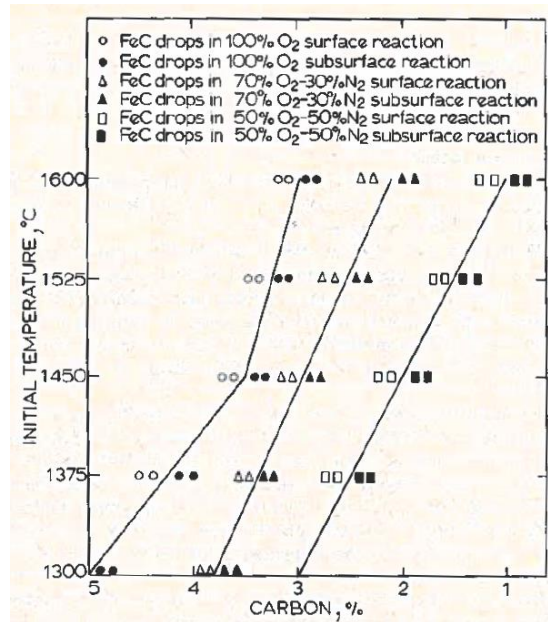


Figure 2.5: Illustration of change in reaction mechanism by varying temperature<sup>[18]</sup>

Gaye & Riboud<sup>[19]</sup> performed a detailed experimental study to understand the decarburization kinetics in oxidizing slag in the presence of other metalloids such as phosphorus and sulfur. They noticed that the rate of dephosphorization and iron loss due to oxidation was enhanced in the presence of carbon due to agitation and metal fragmentation (as shown in Figure 2.5). They recognized two-opposing effect of sulfur on decarburization reaction kinetics: 1/ decreasing decarburization rate by blocking reaction sites and 2/ increasing rate of decarburization by enhancing metal fragmentation. The initial stage of decarburization was proposed to be controlled by interfacial chemical reaction based on the observation of variation of decarburization rate in the presence of sulfur. They also investigated the effect of variation of slag oxidizing potential on the decarburization kinetics and conjectured that the end stage of decarburization was limited by oxygen transport in the slag. Although previous researchers<sup>[15,16,18]</sup> studying droplet

decarburization kinetics in oxidizing slag reported the end stage of decarburization to be controlled by carbon transfer in the droplet. These workers identified that after going through an initial peak period, decarburization reaction always stopped suddenly apparently prior to reaching equilibrium. This phenomenon took place at various oxygen potentials, but no clear explanation was provided.

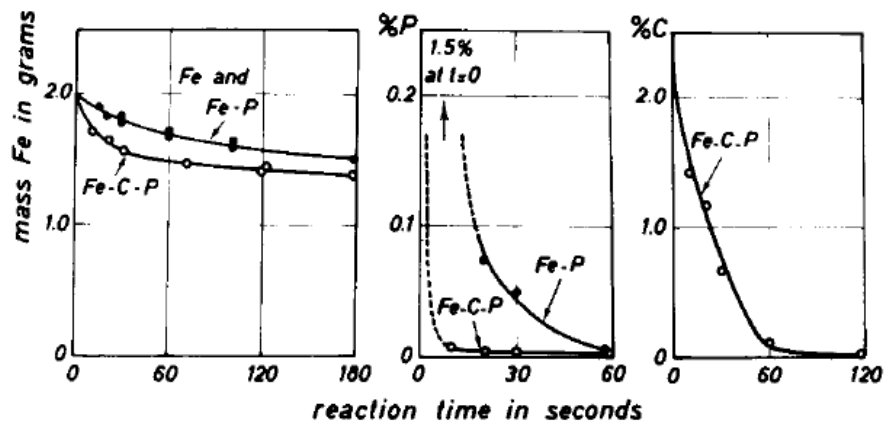


Figure 2.6: Oxidation kinetics of Fe based alloy drops with and without carbon. (a) variation of Fe, (b) variation of P and (c) variation of C with time<sup>[19]</sup>

Kaddah & Robertson<sup>[20]</sup> developed a technique to study homogeneous nucleation of dissolved gases in molten metal by allowing levitated metal drops to equilibrate with gases at high pressure and then suddenly dropping the pressure. They investigated the nucleation of N<sub>2</sub> and CO bubbles within droplets and observed a significant influence of oxygen in favoring nucleation. From their experiments at different oxygen activities as presented in Figure 2.6, homogeneous nucleation of CO bubbles was observed at as low as 10 atm supersaturation pressure. However, they could not explain these results with Classical Nucleation Theory, Dean's Theory of Nucleation by Cavitation, Levine's theory including

the electrochemical work due to adsorption of oxygen atoms, or Abraham's curvature dependence on dipole interaction. The drawbacks of classical nucleation theory and alternate theories on bubbles nucleation are discussed in section 2.2.4.

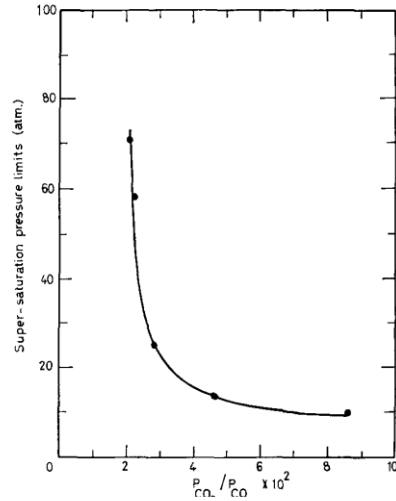


Figure 2.7: Supersaturation limits for nucleation of CO bubbles in Fe-C-O at 1600<sup>o</sup> C<sup>[20]</sup>

Acheson<sup>[31]</sup> studied the kinetics of the reaction between sodium amalgam and water-glycerin solutions in which the sodium amalgam represented the pool of metal and the water-glycerin mixture represented the slag. Hydrogen chloride-nitrogen was used to simulate the oxygen jet in LD steelmaking. Single droplet reaction kinetics were studied by placing a single droplet of amalgam in acid media. These workers proposed that in high carbon droplets, oxygen transport was controlling the kinetics and in low carbon droplets, transfer of carbon within the droplet became rate controlling. For low carbon droplets, they observed a similar behavior to that found by Hazeldean & Coworkers<sup>[21,32]</sup> that CO bubbles remained attached at the slag/metal interface supplying a buoyancy force to the droplet

inhibiting the descent through slag. In this way, the residence time of the droplets was extended favoring refining in the emulsion.

Hayer & Whiteway<sup>[33]</sup> investigated the interplay between the resistance to mass transport in the gas phase and the resistance to surface chemical reaction. They presented decarburization data showing that the rate variation with temperature changed with sulfur content in the metal droplet (Figure 2.7). This clearly showed that as the sulfur concentration was increased from 0 to 1%, the activation energy for decarburization increased and decreased upon a further increase in sulfur concentration. The total resistance may be expressed as

$$Resistance \propto \frac{\exp\left(\frac{E_1}{RT}\right)}{k_1} + \frac{\exp\left(\frac{E_2}{RT}\right)}{k_2} \dots\dots [2.5]$$

Where  $E_1$  and  $E_2$  are the activation energies and  $k_1$  and  $k_2$  are the specific rate constants from a chemical reaction and slag transport respectively, R is the gas constant. These workers also mentioned the competition between sulfur and CO<sub>2</sub> in capturing reaction sites. They have also discussed how the translational, vibrational and rotational entropy would change due to the adsorption of sulfur and CO<sub>2</sub> at the gas/metal interface.

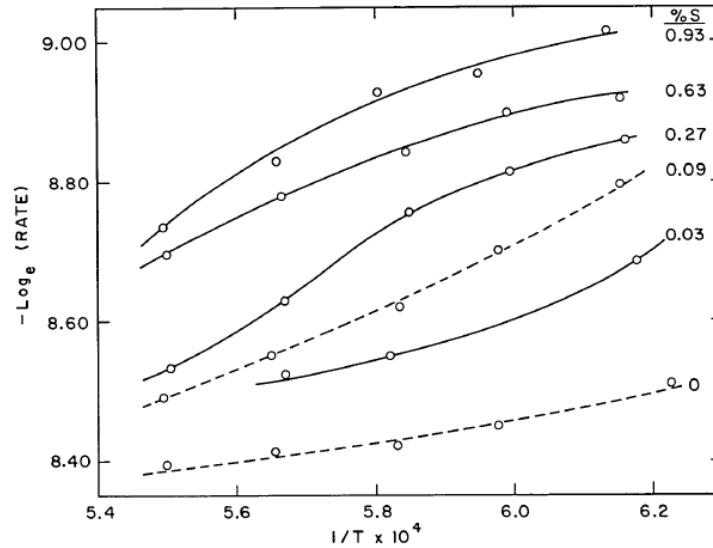
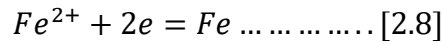
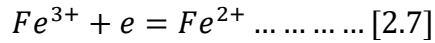
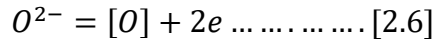


Figure 2.8: Effect of temperature and sulfur content on decarburization rate [31]

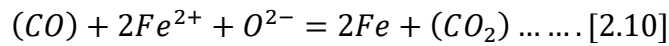
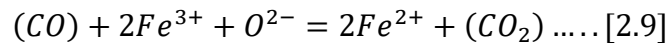
Gare & Hazeldean<sup>[21]</sup> performed a study of decarburization behavior of Fe-C-X alloy droplets in ferric and ferrous based slag. They proposed five stages of decarburization – induction period, fast external decarburization period, lull period, external internal nucleation period and internal nucleation period. These five stages were distinctly visible for ferric based slag from using X-ray fluoroscopy. In ferrous-based slag, only three stages, induction period, fast external decarburization period and slow decarburization period were observed and the rate of decarburization at the fast decarburization period was significantly slower compared to ferric based slag (5.7 times slower reaction rate for 4.2%C droplets at 1773K). During the induction period, CO nucleation at the slag/metal interface was controlling the kinetics and this period was observed to extend on lowering the initial carbon concentration of the droplet. These workers proposed that possibly a critical



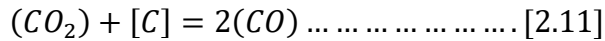
[C]\*[O] product was required to nucleate bubbles. They proposed a coupled electrochemical reaction to occur at the surface of the droplet as



This reaction possibly altered the local surface tension due to an electrocapillary effect and favored CO nucleation. In the fast-external decarburization period, a stable gas halo was observed surrounding the metal droplet and countercurrent diffusion of CO<sub>2</sub> and CO in the gas halo was proposed to be the rate limiting step. The following reactions happened at the slag/gas interface



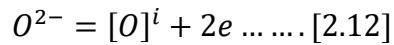
And at the metal/gas interface



With the progress of reaction, the carbon concentration decreased, and the gas halo collapsed and eventually carbon transfer within the droplet became rate controlling. A possibility of formation of iron oxide in the depleted region was also reported. A lull period was observed followed by the fast-external decarburization period due to oxygen accumulation within the droplet overcoming the CO nucleation barrier. As soon as the

oxygen reached sufficient concentration, internal and external decarburization restarted. Finally, only internal decarburization was active, and oxygen and carbon transfer within the droplet was rate controlling. The decarburization rate was observed to slow during the initial period in the presence of phosphorus due to its high affinity for oxygen whereas manganese did not alter the rate at all. In the presence of silicon, carbon was observed to oxidize first and then both silicon and carbon simultaneously. They proposed two opposing effects of silicon on decarburization kinetics – increasing the decarburization rate by increasing the activity of carbon and decreasing the decarburization rate by blocking the oxygen supply due to the formation of fayalite type slag due to oxidation of Si. They proposed sulfur to increase the carbon activity and block reaction sites at the same time. This may be regarded as similar to the observation reported previously by Hayer & Whiteway<sup>[33]</sup>. Interestingly, Gare & Hazeldean observed the decarburization ended very early in ferrous-based slag whereas in ferric based slag the decarburization continued till reaching very low carbon concentration. These workers proposed that transport limitation in slag due to less stirring was responsible for slowing of decarburization. Based on their observation of early stopping of reaction in ferrous based slags, they suggested that in the BOF, gas/metal refining at the ‘hot spot’ was possibly contributing more compared to that from slag-metal refining in the emulsion where dephosphorization was the only advantage. Murthy, Sawada & Elliot<sup>[34]</sup> studied the effect of, slag composition (varied FeO and P<sub>2</sub>O<sub>5</sub>), metal composition (sulfur) and droplet mass (1 g and 2 g) on the decarburization behavior and the end point carbon concentration. The rate of reduction of FeO was reported to increase linearly with (%FeO) in the slag and temperature. The addition of P<sub>2</sub>O<sub>5</sub> in the slag

and sulfur in the droplet helped to continue decarburization for longer times whereas the initial rates of decarburization were reported not to vary significantly. Contrary to this, Hayer and Whiteway<sup>[33]</sup> reported the decarburization rate decreased considerably with increasing sulfur content in the metal droplet. They suggested that at the slag/metal interface, the following reaction might be taking place and the extent of this reaction depended upon this electrochemical reaction.



Murthy & coworkers<sup>[34]</sup> suggested that Sulfur acts as an electron consumer and allows the reaction to continue for a longer time. They observed the rate of decarburization not to vary much with droplet size but to continue the reaction to a greater extent for smaller droplets. The decarburization reaction was always found to stop at a carbon level which was far from thermodynamic equilibrium<sup>[34]</sup>.

On the basis of the finding that decarburization stopped short of thermodynamic prediction, Murthy, Hasham & Pal<sup>[35]</sup> suggested that the reaction was not thermodynamically limited and was possibly transport limited. This would suggest a barrier that shuts down the transport of one or another reactant. Therefore, they investigated mainly three possible rate controlling steps: 1/ Transport in the metal, 2/ Transport in a gas halo, 3/ Transport in the slag. The composition mapping of the quenched droplets showed a homogeneous distribution of C leading to the conclusion that carbon transport in the metal was not the rate controlling step. To study the effect of transport through the gas halo, they estimated

the rate of decarburization with carbon concentration variation. The agreement was good at the initial stages of the reaction, but at the end the gas diffusion-controlled model could not predict the extremely slow kinetics. These workers also studied low carbon droplets, where no continuous gas film was present, and confirmed that transport through a gas film was not controlling the decarburization reaction kinetics. To investigate the effect of transport in slag, they proposed a model for the rate of CO generation per unit area of slag/metal interface considering the electronic transport in the slag as

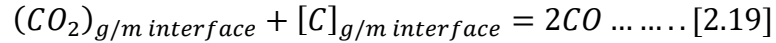
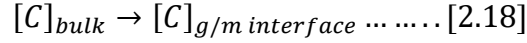
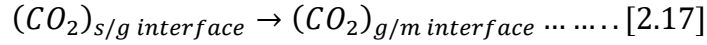
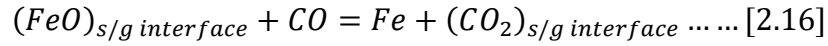
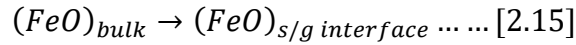
$$\frac{\dot{n}}{A} = \frac{RT}{2|Z_2|F^2\Delta x} \int_{p'_{O_2}}^{p''_{O_2}} \sigma \sum t_e d \ln p_{O_2} \dots \dots \dots [2.14]$$

Where  $p'_{O_2}$  and  $p''_{O_2}$  were partial pressure of oxygen gas ( $p_{O_2}$ ) at the slag/gas interface and at the bulk slag respectively and calculated from the equilibrium of reaction  $FeO = Fe + [O]$  and the dynamic equilibrium at the slag-gas interface in case of gas-halo present or at the slag-metal interface in case of no gas-halo present.  $Z_2$  is the valency of oxygen, R is the universal gas constant, F is the Faraday constant and T is the temperature. Here,  $\Delta x$  represents slag boundary layer thickness, and  $\sigma$  and  $t_e$  represents slag conductivity and transference number respectively. This model prediction was found to agree with the experimental results for the initial decarburization stage. At the end stage of decarburization, they proposed that the model would agree only when the transference number or the electronic conductivity of the slag decreased with the progress of the reaction. They proposed the gradual decrease in the gradient of oxygen potential ( $p_{O_2}$ ) between bulk slag and slag/metal interface was possibly lowering the driving force of

decarburization at the end stage. They also performed experiments by adding transition metal oxides,  $\text{TiO}_2$  and  $\text{Nb}_2\text{O}_5$ , to the slag to increase the electronic conductivity and observed that the extent of decarburization increased with an increase in slag conductivity. The initial rate of decarburization was observed to increase initially upon the addition of  $\text{TiO}_2$  up to 2.97% composition and decreased upon further addition of  $\text{TiO}_2$ . To further investigate the electrochemical nature of the decarburization reaction, they performed experiments putting a molybdenum foil in the crucible between the slag and crucible surface at different droplet carbon contents. The decarburization was observed to continue till the thermodynamic equilibrium was attained in the system. They explained that this molybdenum foil was acting as a sink for electrons generated at the slag/metal interface. From this observation, they postulated that the decarburization reaction was stopping due to the inability of the electrons to migrate across an electrochemical potential gradient that developed in the slag phase adjacent to the slag metal interface. Although they proposed that slag conductivity has significant effect on decarburization kinetics, there was no systematic investigation of slag electrical properties available to support their theory.

Mulholland *et al.*<sup>[36]</sup> first visualized metal droplet decarburization in slag by X-ray Fluoroscopy and observed vigorous CO bubble evolution forming a layer of foam. They confirmed the formation of CO bubbles within the droplet in the later stages of decarburization. The oxygen potential of the slag was found to be an essential rate controlling factor affecting decarburization rate but no conclusion regarding the rate controlling step was drawn.

Min & Fruehan<sup>[37]</sup> conducted an experimental study, to measure the rate of decarburization by varying slag (%FeO) and metal composition ([%C],[%S]) as well as droplet mass. They developed a mixed control kinetic model including mass transfer in slag, mass transfer in the gas halo and CO<sub>2</sub> dissociation at the gas-metal interface. They observed a gas halo of thickness varying from 0.1 to 0.4 cm in the X-ray Fluoroscopy video. The overall reduction reaction was described in five steps



Where the second and fourth steps were reported to be very fast compared to others and the rate constant of the overall reaction from the mixed control model could be determined from

$$k_o = \frac{1}{\frac{2RT}{K_1 C (A_s + A_m) m_g} + \frac{100(MW)_{FeO}}{m_s \rho A_s} + \frac{1}{k_{CO_2} A_m K_1 C}} \dots \dots [2.20]$$

Where  $A_s$  and  $A_m$  were the slag-gas and gas-metal interfacial area,  $m_g$  and  $m_s$  were the mass transfer coefficient in the slag and gas phases,  $k_{CO_2}$  was the rate constant of the CO<sub>2</sub> dissociation reaction,  $K_1$  was the equilibrium constant for  $FeO + CO = Fe + CO_2$  and C

was a constant relating the FeO percentage and activity. This model was able to predict, the rate of reaction in high sulfur droplets, the effect of FeO in the slag and the effect of droplet size. Although the model predicted no dependency with carbon on the decarburization rate, but experimental results suggested the opposite. This model could also not explain the slow rate of decarburization of droplets when carbon content in the droplet dropped below 2 to 3%. They concluded that at low sulfur concentration, transport in the gas and slag phase was rate limiting, whereas at high sulfur concentration, interfacial chemical reaction controlled the decarburization rate.

Gao *et al.*<sup>[38]</sup> studied the effect of droplet sulfur concentration and temperature on carbon boiling phenomena in Fe-C droplets reacting in an oxidizing gas. They used the *in-situ* images captured using a CCD (Charged Couple Device) camera at high temperatures during metal/gas reaction to determine the time at which carbon boiling started and the progression of the reaction. At sulfur concentrations less than 0.15%, there was no observable effect on the incubation time for boiling however at higher sulfur concentrations the incubation time decreased with increasing sulfur.

Molloseau & Fruehan<sup>[12]</sup> performed studies on decarburization for a wide range of FeO (>10%) and Fe<sub>2</sub>O<sub>3</sub> concentration in the slag, varying reaction temperature, and sulfur concentration in droplets containing 2.9% C. They observed swelling of droplets in the slag similar to observations of carbon boiling in carbon containing droplets reacting in oxidizing gases<sup>[15,16,38]</sup>. This study motivated later researchers to explore further the effect of swelling on residence time<sup>[14]</sup>. They observed the decarburization reaction to happen through a sequence of steps as shown in Figure 2.8. Initially as the droplet entered the

dense slag, within 1 sec, it expanded and simultaneously a slag foam formed on top of a dense layer of slag. The droplet came out of the dense slag and continued to react in the foamy slag. After 8 s, the decarburization slowed, and the droplet started shrinking back to its original volume by allowing the CO gases to escape. Simultaneously, the foamy slag collapsed. Finally, the droplet settled at the bottom of the slag. As Min & Fruehan's gas halo based mixed controlled model was not able to explain the high rate of decarburization in high FeO concentration slags, a new kinetic model based on slag mass transport control was proposed. It was suggested that the supply of oxygen was very high in high FeO slag, and a part of the oxygen was consumed by decarburization at the slag/metal interface, with the balance diffusing into the metal leading to nucleation and growth of CO bubbles. They observed an increase in decarburization reaction kinetics with the addition of  $\text{Fe}_2\text{O}_3$  and with increasing reaction temperature. These workers proposed that sulfur concentration in the metal droplet was found to influence decarburization rate in two ways – decreasing the rate by blocking reaction sites and increasing the rate by enhancing emulsification by lowering interfacial tension. Careful observation of droplets in the author's laboratory suggests that rather than emulsifying, the droplets disappeared from view because they swelled to such a low density that they became more transparent to x-rays than the slag<sup>[39]</sup>. So, addition of sulfur initially increased the rate of decarburization till 0.011%S, and the rate decreased upon a further increase in sulfur content in the droplet.



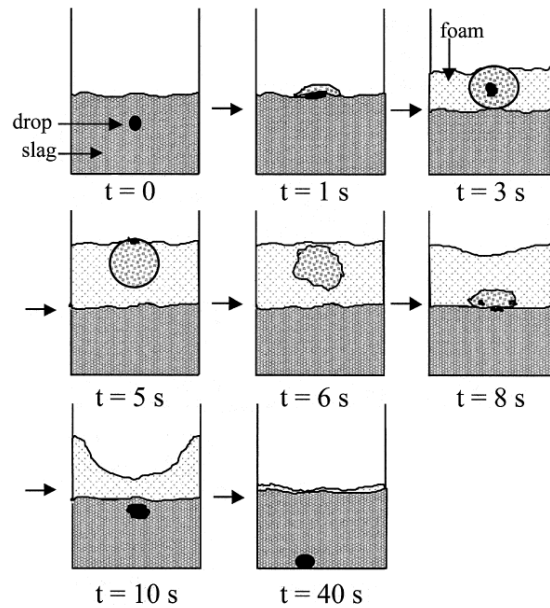


Figure 2.9: Decarburization observed of Fe-C droplet in 20% FeO containing slag<sup>[12]</sup>

In earlier work in the author's laboratory, Chen<sup>[39]</sup> studied the decarburization behavior of Fe-C droplets in CaO-SiO<sub>2</sub>-MgO-FeO slag at different temperatures and over a range of sulfur content in the metal. The carbon content was selected in the range of Molloseau in which emulsification was claimed. Chen observed a sharp rise in the rate of CO evolution above 10% FeO concentration (Figure 2.9). Faster kinetics was also observed with higher temperatures, similar to Molloseau's observation. Chen found two opposing effects of sulfur on the rate of decarburization and the highest decarburization rate was observed at 0.012%S as shown in Figure 2.9. Chen also found the swelling rate of the droplet to increase with an increase in slag FeO concentration and metal droplet sulfur concentration. She reported that, based on the metal droplet carbon concentration and slag FeO concentration, two different regimes of decarburization were possible: 1/ via gas-halo

formation around the droplet or 2/ via internal bubble nucleation. She observed the CO evolution rate to increase linearly with droplet mass and proposed the rate of CO evolution to be controlled by the kinetics of nucleation of CO bubbles in the metal. Classical nucleation theory being incapable of explaining the experimental observation, she proposed a modified nucleation theory, motivated by the mechanism proposed by Levine<sup>[40]</sup>, to calculate the rate of nucleation as

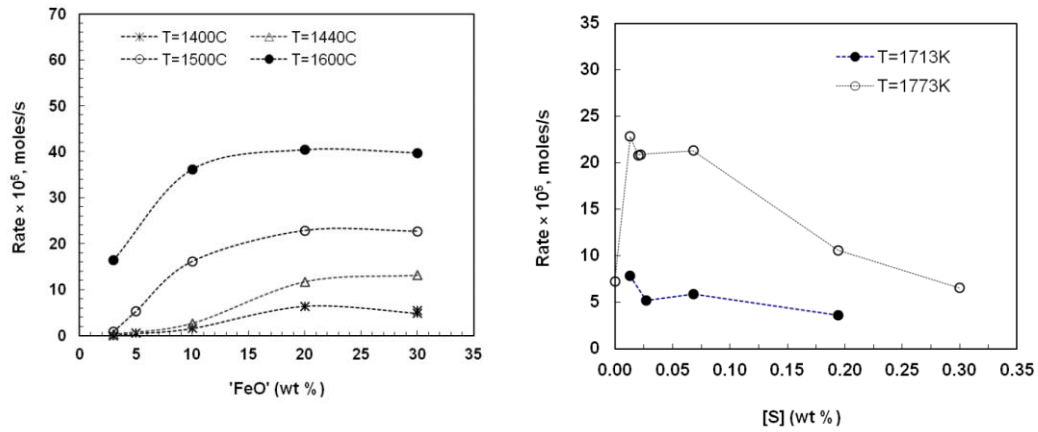


Figure 2.10: Rate of CO evolution with respect to (a) slag FeO content and (b) droplet sulfur content <sup>[39]</sup>

$$J_s = N_0 \exp\left(-\frac{\Delta H}{kT}\right) \left(\frac{3\psi\sigma_0}{\pi m}\right)^{\frac{1}{2}} \exp\left(-\frac{16\pi(\psi\sigma_0)^3}{3kT(P_{ve} - P_l)^2}\right) \dots \dots [2.21]$$

Where  $N_0$  is the number concentration of CO embryos in liquid,  $\sigma_0$  is surface tension,  $\Delta H$  is the heat of formation of CO molecule,  $m$  is the mass of single molecule,  $P_{ve}$  is the pressure in the vapor bubble equilibrium,  $P_l$  is the liquid pressure,  $k$  is the Boltzman constant,  $T$  is the temperature, and  $\psi$  is the surface tension modifying parameter which has

been introduced to fit the rate of nucleation. The details of the drawbacks of classical nucleation theory and the basis of the modified approach will be discussed in section 2.2.4.

The rate of CO generation rate can be calculated as<sup>[39]</sup>

$$R_g = J_s \left( \frac{n_e}{N_A} \right) V_0 \dots\dots [2.22]$$

Where  $R_g$  is CO generation rate(mol/s),  $J_s$  is CO nucleation rate /cm<sup>3</sup>-s,  $V_0$  is original droplet volume,  $n_e$  is no of molecules in an embryo and  $N_A$  is the Avogadro's number. According to this, the rate of CO generation should increase linearly with droplet mass, which agrees with the experimental observation (Figure 2.10).

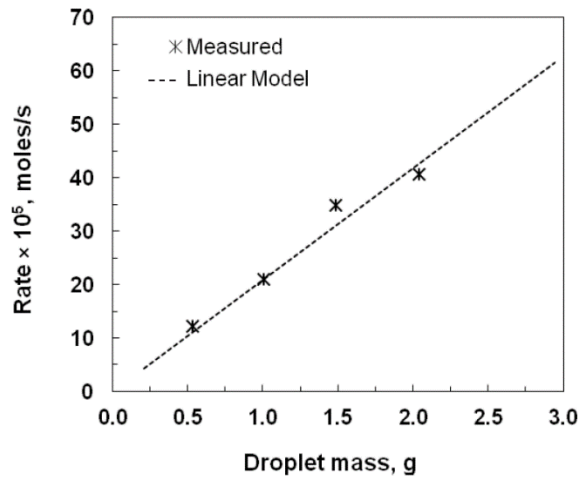


Figure 2.11: Droplet size effect on measured and predicted CO evolution <sup>[39]</sup>

Another experimental study in the author's laboratory by Gu *et al.*<sup>[41]</sup> on decarburization and dephosphorization kinetics in the presence of sulfur showed a delay in bloating due to poisoning by sulfur. They also confirmed the increasing and decreasing trend of peak rate with increasing sulfur concentration. When the droplet bloated and moved into the foamy

slag, a significant effect, of void fraction in the surrounding foamy slag was observed, on the kinetics of both decarburization and dephosphorization. These workers demonstrated that the mass transfer coefficient in the slag decreased in direct proportion to the void fraction. An enhancement in the kinetics of dephosphorization due to stirring of the metal by CO bubbles was observed. Based on Higbie's Penetration theory, they proposed a modified correlation for metal phase mass transfer coefficient as a function of CO evolution rate

$$k_m = \left[ \frac{h_C h_O K_{CO} D}{\pi \sigma} \left( \frac{R_g}{A} \right) \right]^{\frac{1}{2}} \dots \dots [2.23]$$

Where  $h_C$  and  $h_O$  are the Henrian activity coefficient of C and O,  $K_{CO}$  is the thermodynamic equilibrium constant of  $[C] + [O] = CO$  reaction, D is the diffusivity of species in the metal,  $\sigma$  is the surface tension, A is the slag-metal surface area through which gas bubbles are escaping and  $R_g$  is the rate of CO gas evolution.

As observed by the previous researchers<sup>[12,16,20,21,39]</sup> the nucleation of CO bubbles within the liquid metal droplet is evident from experimental studies of droplet decarburization both in oxidizing gas and oxidizing slags. However, attempts to explain this observation using classical nucleation theory have failed. Some researchers proposed some alternate theories to explain this, but essentially, they are flawed. In the following section classical nucleation theory and alternate theories are discussed briefly to illustrate the knowledge gap.

#### **2.2.4. Nucleation Theory**

Nucleation is a phenomenon of formation of a thermodynamically stable new phase from a metastable phase. The classical theory of nucleation was developed initially by Volmer & Weber<sup>[42]</sup> in 1927 and then was further developed over several decades by Farkas<sup>[43]</sup>(1927), Becker and Döring<sup>[44]</sup>(1935) and Zeldovich<sup>[45]</sup>(1943). The theory consists of two important factors – thermodynamic stability and kinetic feasibility. Until both are satisfied, no nucleation will be possible. The nucleation of bubbles can be categorized as either homogeneous or heterogeneous. The variation in the condition of thermodynamic stability for the two different nucleation situations will be analyzed here.

#### 2.2.4.1. Homogeneous Nucleation Theory

The formation of a bubble homogeneously in the liquid requires a negative work to be done against the positive interfacial energy barrier. The Helmholtz free energy change to form a cluster of CO molecules in the liquid metal (Fe-C) can be expressed as

$$\Delta F = -(P_g - P_l)V_g + (\mu_g - \mu_l)N_g + \sigma_0 A \dots \dots \dots [2.24]$$

Where  $P_g$  and  $P_l$  are respectively the pressure within the gas bubble and the liquid,  $\mu_g$  and  $\mu_l$  are the chemical potential of molecules in gas and liquid respectively. The volume of the newly formed gas bubble is  $V_g$  and it contains  $N_g$  gas molecules.  $A$  is the gas/metal interfacial area which is created by the formation of the bubble and  $\sigma_0$  is the interfacial tension. There are three main terms: the first accounts for the PV work done when the bubble is formed, the second term accounts for the change in chemical potential of  $N_g$  gas molecules from dissolved liquid to the gas phase and the last term in equation 2.24 accounts

for the changes in surface free energy when a new gas/metal interface is created. The pressure within the bubble is constrained by the mechanical equilibrium expressed as

$$P_g = P_l + \frac{2\sigma_0}{r} \dots \dots \dots [2.25]$$

Where  $r$  is the radius of the bubble. The difference in chemical potential from bulk liquid to gas bubble can be expressed as

$$\mu_g - \mu_l = RT \ln \frac{P_g}{P_e} = \left( P_l + \frac{2\sigma_0}{r} \right) \Omega_g \ln \frac{P_l + \frac{2\sigma_0}{r}}{P_e} \dots \dots \dots [2.26]$$

Here  $\Omega_g$  is the molar volume of the gas and  $P_e$  is the equilibrium pressure of the gas molecule in the liquid. For CO molecules, the equilibrium pressure can be calculated from the concentration of dissolved carbon and oxygen as

$$P_e = K[C][O] \dots \dots \dots [2.27]$$

Where  $K$  is the equilibrium constant of the C/CO equilibrium. The volume, gas/metal surface area and number of moles of gas in the bubble can be calculated as

$$V_g = \frac{4}{3} \pi r^3 \text{ and } N_g = \frac{\frac{4}{3} \pi r^3}{\Omega_g} \text{ and } A = 4\pi r^2 \dots \dots \dots [2.28]$$

Combining equations 2.26 to 2.28, the Helmholtz free energy would be

$$\Delta F = \frac{4}{3} \pi r^3 \left( P_l + \frac{2\sigma_0}{r} \right) \ln \left( \frac{P_l + \frac{2\sigma_0}{r}}{P_e} \right) + \frac{4}{3} \pi r^2 \sigma_0 \dots \dots \dots [2.29]$$

At the critical radius,  $\left(\frac{d\Delta F}{dr}\right)_{r=r^*} = 0$ . At this point, both chemical and mechanical equilibrium should be satisfied simultaneously as

$$\Delta\mu^* = 0 \dots \dots \dots [2.30]$$

$$P_e = P_g = P_l + \frac{2\sigma_0}{r^*}; r^* = \frac{2\sigma_0}{P_e - P_l} \dots \dots \dots [2.31]$$

$$\Delta F^* = \frac{16\pi\sigma_0^3}{3(P_e - P_l)^2} \dots \dots \dots [2.32]$$

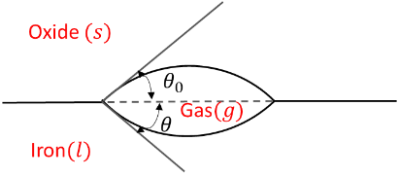
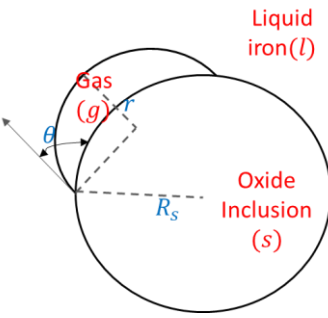
#### 2.2.4.2. *Heterogeneous Nucleation:*

When the nucleation of a bubble occurs on a secondary surface, the free energy barrier for nucleation is reduced thus favoring the nucleation process. This is called heterogeneous nucleation. When a bubble nucleates on a liquid droplet, the possible sources of heterogeneous nucleation surfaces are a/ on some liquid metal-slag interface or b/ on some foreign particles. In any of the above-mentioned cases, the critical free energy barrier decreases by a factor ( $f$ ), which is dependent upon the interfacial energies and the contact angles. The critical free energy for heterogeneous nucleation would be

$$\Delta F^*(hetero) = \Delta F^*(homo) * f \dots [2.33]$$

The variation of the  $f$  parameter with the possible variation of the secondary surfaces is summarized in the following table in details.

Table 2.1: Heterogeneous nucleation possibilities

| Types   | Factor ( $f$ )   | Parameters  |
|---|--|---|
| <p>Lens Shaped Cluster<sup>[46,47]</sup></p>   | $f = \left[ \frac{1}{4} * (2 + \cos \theta)(1 - \cos \theta)^2 + \frac{1}{4} * (2 + \cos \theta_0)(1 - \cos \theta_0)^2 \left( \frac{\sin \theta}{\sin \theta_0} \right)^3 \right]$  | $\cos \theta = \frac{\sigma_{l/s}^2 + \sigma_{l/g}^2 - \sigma_{s/g}^2}{2\sigma_{l/s}\sigma_{l/g}};$ $0^\circ < \theta < 180^\circ$<br>$\cos \theta_0 = \frac{\sigma_{l/s}^2 - \sigma_{l/g}^2 + \sigma_{s/g}^2}{2\sigma_{l/s}\sigma_{s/g}}$ $0^\circ < \theta_0 < 180^\circ$ |
| <p>On Oxide Inclusion<sup>[48,49]</sup></p>  | $f = \frac{1}{2} + \frac{1}{2} \left( \frac{1 - mx}{w} \right)^3 + \frac{1}{2} x^3 \left[ 2 - 3 \left( \frac{x - m}{w} \right) + \left( \frac{x - m}{w} \right)^3 \right] + \frac{3}{2} mx^2 \left( \frac{x - m}{w} - 1 \right)$ | $m = \cos \theta$ $x = \frac{R_s}{r}$ $w = (1 + x^2 - 2xm)^{\frac{1}{2}}$   |



### 2.2.4.3. Kinetics of Nucleation

Classical nucleation theory allows one to predict the rate of nucleation of the new phase (bubble) per unit volume of the parent phase (liquid iron) as a function of the supersaturation pressure, interfacial tension, and temperature. The rate of formation of bubbles from metastable clusters by statistical fluctuations is dependent upon four factors.

1. Equilibrium number concentration of critical size clusters ( $N$ ): The formation of the bubble of critical size from subcritical size being a thermodynamically unfavorable process, the clusters of gas molecules form by statistical fluctuations. Once a critical sized cluster has formed, then further growth of that cluster is a thermodynamically favorable process. The equilibrium concentration of a critical sized bubble in the liquid iron follows a Boltzmann distribution with the critical free energy and this can be expressed as

$$N = N_0 \exp\left(-\frac{\Delta F^*}{kT}\right) \dots \dots \dots [2.34]$$

Where  $N_0$  is the number concentration of nucleation sites per unit volume. In the case of CO bubble nucleation, the concentration of carbon is much higher than that of oxygen. So the number concentration of oxygen has been considered as same as the number concentration of nucleation sites<sup>[2]</sup>.

2. Rate of diffusive flux( $\beta$ ): The rate at which gas molecules attach to or release from the critical sized cluster allowing the growth to lower free energy. This can be expressed from the Kinetic Theory of gases as the maximum rate of vaporization

$$\beta = \frac{P}{\sqrt{2\pi mkT}} \dots \dots \dots [2.35]$$

Where P is the pressure within the gas bubble,  $m$  is the weight of the gas molecule.

3. Surface Area ( $A$ ): The surface area of the critical sized cluster would be

$$A = 4\pi r^{*2} \dots \dots [2.36]$$

4. Zeldovich Factor( $Z$ ): This non-equilibrium factor is a correction to the rate of nucleation which arises from the fact that the steady state concentration of critical sized bubbles is less than that of the equilibrium concentration. This can be expressed as

$$Z = f \left( \left[ \frac{\partial^2 \Delta F}{\partial n^2} \right]_{n=n^*} \right) = \sqrt{\frac{\Delta F^*}{3\pi kT n^{*2}}} \dots \dots \dots [2.37]$$

By incorporating these factors, the rate of nucleation of CO bubbles per unit volume (number of nuclei/m<sup>3</sup>) in liquid iron can be expressed<sup>[50]</sup> as

$$J_S = Z\beta AN = N_0 \left[ \frac{3\sigma}{\pi m} \right]^{\frac{1}{2}} \exp \left[ -\frac{\Delta F^*}{kT} \right] \dots \dots \dots [2.38]$$

#### 2.2.4.4. Application of Classical Nucleation Theory on CO bubble nucleation

Kaplan and Philbrook <sup>[46]</sup> performed experimental studies for low carbon droplets and evaluated the possibility of homogeneous nucleation of CO bubbles within the droplet and

heterogeneous nucleation on an Fe/FeO interface as proposed by Baker Warner and Jenkins<sup>[15]</sup>. The calculation showed that although heterogenous nucleation is more favorable, at those experimental temperatures the predicted rate of nucleation is effectively zero. Kaddah & Robertson<sup>[20]</sup> observed the formation of CO bubbles within a droplet at as low as 10 atm supersaturation pressure.

Levine<sup>[40]</sup> proposed a modified version for reversible work of formation of nuclei of CO including an electrostatic term related to the formation of a chemisorbed layer of oxygen ions as shown in Figure 2.11. He mentioned that the reversible work is reduced significantly due to the presence of a dipole layer. The critical free energy barrier as proposed by Levine is

$$\Delta F^* = \frac{\left(\frac{16\pi}{3}\right) \sigma^3 \psi}{(P_g^* - P_l)^2} \dots [2.39]$$

where  $\psi = \left(1 - \frac{\sigma_0}{\sigma}\right)^2 \left(1 + \frac{2\sigma_0}{\sigma}\right) = 1 - 3\left(\frac{\sigma_0}{\sigma}\right)^2 + 2\left(\frac{\sigma_0}{\sigma}\right)^3$ . Here  $\sigma$  is the surface tension,  $\sigma_0$  is the electrostatic charge density. Levine calculated the value of this parameter as a function of the activity of oxygen in the melt using the surface tension and adsorption isotherm reported by Swisher and Turkdogan<sup>[51]</sup>. The value of this parameter was found in the range of 0 to 1, and nucleation was proposed to occur for  $\psi$  value near to 0.

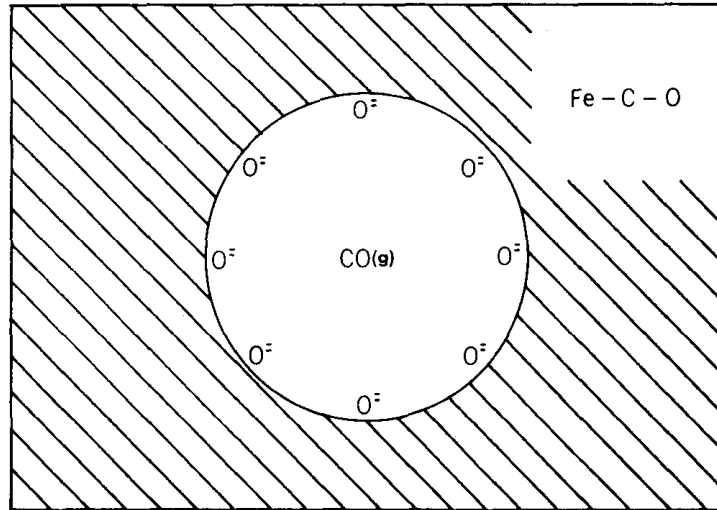


Figure 2.12: Bubble nucleation model for Fe-C-O system as suggested by Levine <sup>[40]</sup>.

Later, based on the work of Levine<sup>[40]</sup>, Chen & Coley<sup>[2]</sup> modified the classical nucleation theory using a modifying parameter to explain the experimental observation as presented in Equation 2.21. They were able to demonstrate the dependence of decarburization kinetics on nucleation rate. Although this approach was successful in explaining the experimental details, the underlying mechanism/ reason for deviation from classical nucleation theory was not clear. It has been strangely observed that mainly in those cases where dissolved gases nucleate as bubbles in the liquid, the disagreement from classical nucleation theory is large, whereas classical nucleation theory is quite successful in predicting boiling or cavitation in a single component system. The main drawbacks of classical nucleation theory are: 1/ macroscopic thermodynamic properties are applied to estimate free energy for small clusters which almost certainly vary at the microscopic and certainly the atomic level, 2/ the cluster interface, which is considered to be sharp, may be diffuse, 3/ the surface tension of a cluster is assumed to be the same as that of a planar

interface, 4/ the contribution from the variation in the entropy is not considered, 5/ due to rapid transport of reacting species through the interface, the influence on surface tension is not considered . There are some alternate theories<sup>[52,53]</sup> proposed which attempted to explain the disagreement between classical nucleation theory and the experimental observation for bubble nucleation. In the following sections, few of the alternate theories are reviewed briefly.

#### 2.2.4.5. Alternate nucleation theories

*Blob Theory of Elevated Concentration:* Bowers *et al.*<sup>[52]</sup> proposed the formation of a bubble through some lower energy pathways by forming an intermediate phase that does not have a well-defined interface and termed this phase as a ‘blob’. A ‘blob’ is a region in the liquid which has an enhanced chemical potential compared to the surrounding liquid and this region is formed by only statistical fluctuation. This ‘blob’ does not have a gas/liquid interface, so the positive barrier term due to surface energy is zero. Therefore, it is easier to nucleate a ‘blob’ compared to a bubble with a sharp gas/liquid interface. When the free energy of a ‘bubble’ is lower than the ‘blob’ containing the same number of molecules, the ‘blob’ will spontaneously transform into the ‘bubble’. The Helmholtz free energy of a ‘blob’ and a ‘bubble’ containing  $n_r$  moles of gas molecules can be calculated as

$$\Delta F_{blob} = n_r RT \ln \left( \frac{a_{elev}}{a_{liq}} \right) \dots \dots \dots [2.40]$$

$$\Delta F_{bubble} = n_r RT \ln \left( \frac{p_r}{p_{g_{liq}}} \right) + \left( \frac{4}{3} \right) * \pi * r^2 * \sigma_{0_{bubble}} \dots \dots \dots [2.41]$$

Where  $p_r$  is the pressure within the bubble and  $p_{g_{liq}}$  is the pressure of dissolved gas molecules in the liquid (same as  $P_e$  as mentioned earlier).  $r$  is the radius of the bubble.  $a_{elev}$  and  $a_{liq}$  are the activities of gas molecules in the elevated concentrated region and the bulk liquid respectively. A schematic was presented in Figure 2.12 for the free energy of the blob and bubbles.

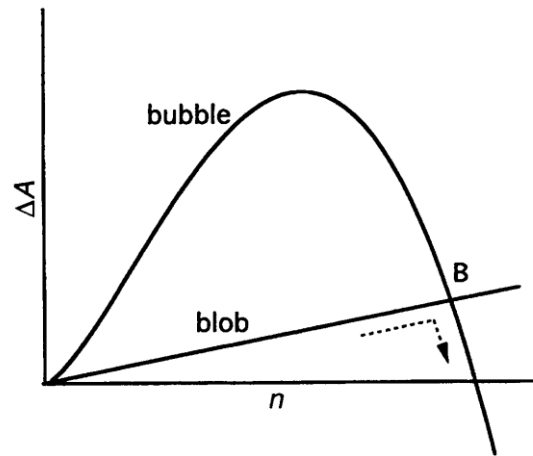


Figure 2.13: Possible pathway to bubble nucleation via a blob of dissolved gas  
(Schematic)<sup>[52]</sup>

The main drawback of this theory is that although thermodynamically this appears possible, according to kinetics, formation of such a large ‘blob’ which can transform into a supercritical bubble, seems impossible.

*Diffuse Interface Theory:* In this theory, Bowers *et al.*<sup>[52]</sup> proposed an intermediate phase that contains gas molecules, but the gas/liquid interface is diffuse i.e. a mixture of gas and liquid interface. The surface tension of this type of ‘diffuse’ interface is always lower than that of the sharp gas/liquid interface so there should be no reason for the interface to

become sharp. If this is indeed the case the diffuse interface would be the normal form of the interface and its energy would be captured in conventional measurements. These workers adopted the theory of Tolman, which incorporates the effect of curvature on surface tension. Bower proposed that the diffuse interface blob will transform into a sharp interface gas bubble when the free energy of the ‘blob’ becomes higher than that of the ‘bubble’. According to the proposed theory, the free energy of ‘diffuse interface blob’ and ‘bubble’ can be expressed as

$$\Delta F_{blob} = n_r RT \ln \left( \frac{p_{r_{blob}}}{p_{g_{liq}}} \right) + \left( \frac{4}{3} \right) * \pi * r^2 * \sigma_{0_{blob}} \dots \dots [2.42]$$

$$\Delta F_{bubble} = n_r RT \ln \left( \frac{p_{r_{bubble}}}{p_{g_{liq}}} \right) + \left( \frac{4}{3} \right) * \pi * r^2 * \sigma_{0_{bubble}} \dots \dots [2.43]$$

Where  $p_{r_{blob}}$  and  $p_{r_{bubble}}$  are the pressure within the blob and the bubble respectively and  $\sigma_{blob}$  and  $\sigma_{bubble}$  are the surface tension of blob and bubble respectively. According to the theory, the surface tension of the diffuse interface i.e.  $\sigma_{blob}$  is always lower than  $\sigma_{bubble}$ .

The surface energy of the blob, according to Tolman’s theory would be

$$\sigma_{blob} = \sigma_{bubble} * \frac{r}{\delta + r} \dots \dots [2.44]$$

Here the parameter  $\delta$  is an indication of the width of the diffuse interface of the blob. The main drawback of this proposed theory was that the surface tension of the diffuse interface blob remained lower than that of the sharp interface bubble, so thermodynamically no transformation is possible.

*Kwak & Panton's Theory:* Kwak & Oh<sup>[53]</sup> proposed a bubble nucleation model based on the model of Kwak & Panton<sup>[54]</sup> on molecular interactions, along with Levine's model of the electrical double layer. The model considers three factors to calculate the change in free energy in forming a cluster of  $n$  molecules: the change in chemical potential ( $n d\mu$ ), surface creation ( $\sigma A$ ), chemisorption ( $U^S$ ). This model does not consider the  $pV$  work in the free energy equation. From Gibbs Duhem Relation:

$$d\mu = v_m dP \text{ so, } n\Delta\mu = -nv_m(P_l - P_g) \dots \dots [2.45]$$

The surface energy term was expressed<sup>[54]</sup> in terms of the translational energy of the molecules as

$$4\pi r_n^2 \sigma = \frac{3}{2} kT n^{\frac{2}{3}} \dots \dots \dots [2.46]$$

The electrostatic energy due to dipole-dipole interaction by the adsorbed oxygen atoms have been accounted following the approach of Abraham<sup>[55]</sup> as

$$U^S = 8P_d^2 \tau^{\frac{3}{2}} \dots \dots \dots [2.47]$$

Where  $P_d$  is the dipole moment by the doubly charged oxygen atom, and  $\tau$  is the surface concentration of adsorbed oxygen atoms. The free energy involved in the clustering process including the electrostatic energy would be

$$F_n = -(P_l - P_g)nv_m + \frac{3}{2} kT n^{\frac{2}{3}} - U^S \dots \dots [2.48]$$

The condition at the critical point ( $\frac{\partial F_n}{\partial n} = 0$ ) from this equation would give



$$(P_l - P_g)n_c^{\frac{1}{3}} = \frac{kT}{v_m} \dots \dots [2.49]$$

The critical free energy of a CO cluster of  $n_c$  molecules,

$$\frac{F_{n_c}}{kT} = \frac{1}{2}n_c^{\frac{2}{3}} - \frac{U^S}{kT} \dots \dots [2.50]$$

To estimate the rate of nucleation, they introduced the effect of surface blocking in the growth of the CO cluster. They presented that the supersaturation required for CO nucleation was highly dependent upon the oxygen activity in the solution. The main drawback of this model seems that the electrostatic energy term is independent of the cluster size whereas Levine considered it to be dependent upon the surface area of the cluster. In the view of the author, the electrostatic energy term should be dependent on both the size of the cluster and the activity of oxygen due to the variation in the total number of adsorbed oxygen ions. Another drawback of this model is that the first term in the Helmholtz free energy in Equation 2.48 is a positive energy term because, from the curvature effect, we know that the bubble pressure should always be higher than the liquid pressure ( $P_g > P_l$ ). However, according to the theory of nucleation, the positive surface energy barrier (Term 3) needs to be overcome by the negative volume free energy (Term 1 + Term 2 in Equation 2.24) to allow the nucleation process to be thermodynamically feasible. In this approach of Kwak and Oh both the terms represent some positive energy barrier and won't let nucleation happen. So, in this respect, the model of Levine is more logical than that of Kwak & Oh.

This brief review on the alternate nucleation theories shows that although the idea of two step pathway is superficially appealing, there are major drawbacks. This is one of the important knowledge gaps not only in predicting CO bubble nucleation in BOF steelmaking, but also in understanding any bubble nucleation kinetics in other metallurgical reaction systems. It is interesting to mention that there is a parallel phenomenon for droplet reaction in slags where a large rate of mass transfer through the slag/metal interface, appears to cause the interfacial tension drops near to zero and the droplet breaks up into many smaller droplets. This phenomenon is called spontaneous emulsification<sup>[12,19]</sup>. It seems likely that mass transfer across the interface of a nucleating bubble would also result in the surface tension dropping close to zero.

Previous sections of this chapter cover the background of BOF steelmaking process and then the dynamic factors such as droplet generation rate and size distribution, residence time of the droplets followed by ‘bloating’ which is determined by the decarburization reaction kinetics. The variation of reaction kinetics with the variation of slag composition mainly the observations reported by Gare & Hazeldean<sup>[21]</sup> and Murthy, Sawada & Elliot<sup>[34]</sup> on the different kinetics with ferric based and ferrous based slag suggests that there is a need to understand the slag structure and the electrical properties to fully explain the decarburization kinetics. There is a scope on systematic study on varying slag electrical properties to show the decarburization variation. There are also no proper decarburization model which can predict the bloating behavior and the decarburization kinetics correctly for varying slag and metal compositions. There is also lack of understanding on CO bubble nucleation kinetics. The current research work will focus on systematically varying slag

and metal composition to control the electrical properties of slag and develop understanding on the kinetics of decarburization at each individual stages. The work will also focus on developing a decarburization model including all the kinetic steps and predict the bloating behavior for different slag metal compositions which will be useful to control the refining kinetics in BOF. The next few sections provide the background needed for the current research like slag structure and properties, electrical conductivity.

### **2.2.5. Slag structure & electrical property**

In metallurgical systems, the refining of liquid metal involves interaction with liquid slags which consist primarily of oxides (CaO, SiO<sub>2</sub>, MnO, P<sub>2</sub>O<sub>5</sub>, FeO, Al<sub>2</sub>O<sub>3</sub>, Fe<sub>2</sub>O<sub>3</sub>), sometimes with some dissolved sulfides and fluorides. Numerous studies, have been conducted to understand the slag structure and how it controls the thermodynamics and kinetics of slag/metal reactions important in the steelmaking processes; typical examples are referenced here<sup>[56-58]</sup>. Earlier metallurgists employed the molecular theory of slag, in which slag constituents are considered molecules of CaO, FeO, SiO<sub>2</sub>. The seminal paper of Ramachandran King and Grant<sup>[59]</sup> clearly demonstrated the ionic nature of slags. With the development of characterization techniques such as X-ray and neutron diffraction, Raman Spectroscopy, and nuclear magnetic resonance along with molecular dynamic simulations and physical property data, the structure of slag is now relatively well understood. In metallurgical slag, silica (SiO<sub>2</sub>) exists as 3-D tetrahedra in which four O<sup>2-</sup> ions are covalently bonded with a Si<sup>4+</sup> ion and these are connected to each other forming a polymerized structure. The addition of basic oxides such as Na<sub>2</sub>O, CaO, MgO progressively breaks the polymerized chain. Initially forming non-bridging oxygen, as O<sup>-</sup>

and after the network has been broken so that only individual tetrahedra exist along with free cations. Subsequently any further addition of basic oxide results in free  $O^{2-}$  ions. Slags with free  $O^{2-}$  ions are termed basic, slags with no free oxygen ions but only unbonded tetrahedra are termed, neutral and slags with bonded tetrahedra are termed acidic. A schematic of the silicate chain is presented in Figure 2.13, with three different types of oxygen bonds marked in different colors. The cations such as  $Al^{3+}$ ,  $Fe^{3+}$ ,  $Ti^{3+}$  can also form tetrahedra and arranges into silicate networks. The physical properties such as viscosity, conductivity are influenced by the structure of slag. It has been suggested that it is not possible for free  $O^{2-}$  to be stable<sup>[55]</sup>, however, in the absence of a better understanding of the structure, the forgoing description offers a convenient physical picture to explain the physical and chemical properties of slags.

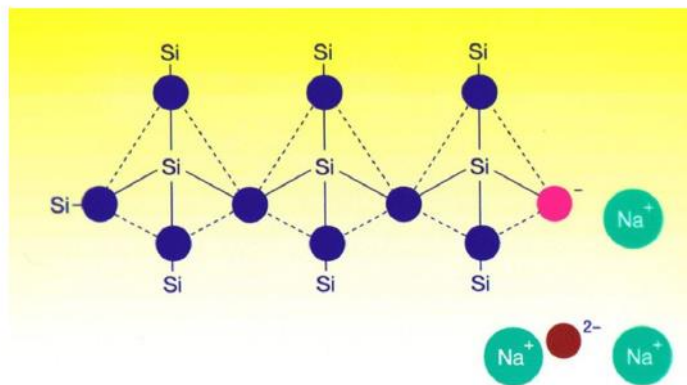


Figure 2.14: Schematic drawings and silicate chain with bridging O ( $O^0$ ) shown in blue, nonbridging O ( $O^-$ ) shown as pink and free  $O^{2-}$  shown as maroon and cations in green<sup>[57]</sup>

The viscosity of slag is dependent on the degree of polymerization of the silicate network. With the addition of basic oxides supplying cations, such as  $Na^{2+}$ ,  $Ca^{2+}$ , the slag viscosity

decreases, and this gives a measure of easiness of transport of reactant ions in the slag. To represent the viscosity variation with temperature, generally two types of dependencies are used – Arrhenius or Weymann type as shown in Equation 2.51 and 2.52, respectively

$$\eta = A_{A\eta} \exp\left(\frac{B_A}{T}\right) \dots \dots \dots [2.51]$$

$$\frac{\eta}{T} = A_{W\eta} \exp\left(\frac{B_W}{T}\right) \dots \dots \dots [2.52]$$

Where  $A_{A\eta}$  and  $A_{W\eta}$  are the pre-exponential term,  $B_A$  and  $B_W$  are the activation energy term. Riboud & Gaye<sup>[60]</sup> and Urbain<sup>[61]</sup> developed Weymann type viscosity models. Later Sridhar & Mills<sup>[62]</sup> developed a model based on Arrhenius type correlation referred to as the NPL model, where the pre-exponential term and the activation energy were correlated with the optical basicity of the slag. There is another model developed by a group of workers in KTH<sup>[63]</sup> following an approach similar to Eyring, and this is commercially available. Most of these models work for some specific slag compositions.

The diffusivity of ions varies inversely with slag viscosity according to Eyring's equation<sup>[57]</sup>. It is worth mentioning that with the addition of ions such as  $\text{Fe}^{3+}$  or  $\text{Al}^{3+}$ , the variation of viscosity may not be in one direction. Based on the concentration of other cations, the viscosity may decrease or increase affecting diffusivity in the opposite ways. For the increase in concentration of ferric fraction in slag, there are two opposite observations reported in the literature. One group<sup>[64][65]</sup> found the diffusivity to decrease with increase in ferric fraction. Contrary to that, other researchers<sup>[66,67]</sup> found diffusivity to increase with increasing ferric fraction in the slag.

The electrical properties of slag includes – ionic and electronic conductivity and these have been extensively studied by researchers<sup>[65,68–71]</sup>.

### *Ionic Conductivity*

The ionic conductivity of slag due to diffusion of ions can be calculated using the Nernst Einstein relationship<sup>[71]</sup>

$$\sigma_i = \sum \frac{C_i D_i z_i^2 F^2}{RT} \dots \dots \dots [2.53]$$

Where  $C_i$  is the concentration of mobile ion  $i$ ,  $D_i$  is the tracer diffusion coefficient of  $i$  ion,  $z_i$  is the charge on ion  $i$ ,  $F$  is Faraday constant,  $R$  is the universal gas constant,  $T$  is the temperature. Bockris *et al.*<sup>[72]</sup> reported from their electrical property studies of slags that only cations contribute to the conductance of the melt because of the much greater mobility of simple cations relative to complex, and in some cases networked, anions. For FeO-SiO<sub>2</sub>-CaO melt studies, only Ca<sup>2+</sup> and Fe<sup>2+</sup> ions have been found to be significant ionic charge carriers<sup>[68,70]</sup>.

In FeO-SiO<sub>2</sub>-CaO melts, based on the oxidizing potential of the environment ( $p_{O_2}$ ), basicity and temperature there will be a distribution of ferric and ferrous ions in the slag. A superficial assessment would suggest that both of these ions should contribute to the ionic conductivity of slag and ferric ions should have higher ionic conductivity compared to ferrous due to its higher charge. However, the mobility of the ferric ion is found to be much lower than the ferrous ion due to the formation of large complex anions such as  $FeO_4^{5-}$ ,  $Fe_2O_5^{4-}$  so it's contribution to ionic conductance can be ignored. The dominant

ionic carriers are  $\text{Ca}^{2+}$  and  $\text{Fe}^{2+}$  in  $\text{CaO-FeO-SiO}_2$  melts. In the  $\text{FeO-Fe}_2\text{O}_3\text{-SiO}_2\text{-Al}_2\text{O}_3\text{-CaO}$  slag system,  $\text{Al}^{3+}$  ions exist either in a complex anionic structure similar to silica tetrahedra or very rarely as an individual ion<sup>[57]</sup>. The mobility of these complex ions being lower, the contribution to ionic conductivity of  $\text{Al}^{3+}$  can be ignored. So for a  $\text{FeO-Fe}_2\text{O}_3\text{-SiO}_2\text{-Al}_2\text{O}_3\text{-CaO}$  type slag, the ionic conductivity ( $\sigma_{ion}$ ) can be expressed as<sup>[71]</sup>

$$\begin{aligned}\sigma_{ion} &= \frac{4F^2}{RT} (D_{\text{Ca}^{2+}}C_{\text{Ca}^{2+}} + D_{\text{Fe}^{2+}}C_{\text{Fe}^{2+}}) \\ &= \frac{4F^2}{RT} (D_{\text{Ca}^{2+}}C_{\text{Ca}^{2+}} + D_{\text{Fe}^{2+}}C_{\text{Fe}_{tot}}(1 - y)) \dots \dots [2.54]\end{aligned}$$

Where  $D_{\text{Ca}^{2+}}$ ,  $D_{\text{Fe}^{2+}}$  are the diffusivities and  $C_{\text{Ca}^{2+}}$ ,  $C_{\text{Fe}^{2+}}$  are the concentration of  $\text{Ca}^{2+}$  and  $\text{Fe}^{2+}$  ions respectively.  $C_{\text{Fe}_{tot}}$  is the total Fe concentration in the slag, in which y is the fraction of iron present as ferric ions.

### *Electronic Conductivity*

The electronic conductivity of slags containing  $\text{Fe}^{2+}$  and  $\text{Fe}^{3+}$  can be expressed as<sup>[65]</sup>

$$\sigma_{el} = cy(1 - y) \dots \dots [2.55]$$

Where c is a constant. The model used in the published literature to explain the electronic conduction process in the slag involves the hopping of electrons from a  $\text{Fe}^{2+}$  ion to an  $\text{Fe}^{3+}$  ion. In this mechanism, proposed by Mott<sup>[73]</sup>, an electronic transfer takes place by charge hopping between lower valence cations and higher valence cations in transition metal oxide containing slag's. This model is referred to as 'small polaron hopping' or 'Mott's transition' and the electronic conductivity in transition metal oxides can be expressed as

$$\sigma_e = v_{ph} \left( \frac{F^2}{RTN_a r^0} \right) \exp(-2\alpha r^0) \exp\left(-\frac{W}{RT}\right) y(1-y) \dots \dots [2.56]$$

Where  $v_{ph}$  is the phonon frequency,  $N_a$  is Avogadro's number,  $W$  is the activation energy of the hopping process and  $r^0$  is the hopping distance. The rate of wave function decay,  $\alpha$  is given as

$$\alpha = \frac{\sqrt{2mH}}{h} \dots \dots [2.57]$$

Where  $m$  is the mass of an electron,  $H$  is the difference between the energy level of electron donor and conduction band and  $h$  is the Plank's constant. Strictly speaking band theory does not apply to liquids and  $H$  represents the energy gap between the Highest Occupied Molecular Orbital and the Lowest Unoccupied Molecular Orbital (HOMO-LUMO). The separation distance of iron ions,  $r^0$  can be calculated from the concentration of FeO in the slag and the slag molar volume.

Barati and Coley<sup>[71]</sup> recognized that in dilute liquid slags ions may not be close enough together for hopping to occur and that in such a case might have to move to within a viable hopping distance. These workers proposed a two-step process in which the  $Fe^{2+}$  ion must "diffuse" to  $Fe^{3+}$  ion within a viable hopping distance of the, assumed stationary. The electronic conductivity via this diffusion assisted charge transfer process can be expressed as

$$\sigma_e = 4\pi N_a \frac{r^0 (r^*)^3}{r^0 - r_0^*} \frac{D_{Fe^{2+}} F^2}{RT} C_{Fe_{tot}}^2 y(1-y) \dots \dots [2.58]$$



Where  $r^0$  is the average spacing between  $\text{Fe}^{2+}$  and  $\text{Fe}^{3+}$ ,  $r_0^*$  is the maximum hopping distance between  $\text{Fe}^{2+}$ - $\text{Fe}^{3+}$  ions, a value that has been reported to be  $\sim 4\text{\AA}$ <sup>[71][74][75]</sup>. The agreement with the experimentally measured electronic conductivity and theoretically calculated electronic conductivity of slag using  $r_0^* = 3.87\text{\AA}$  in Equation 2.58 is presented in Figure 2.14. The approach of Barati and Coley allows Mott's model to be used for more dilute iron oxide concentrations in the slag.

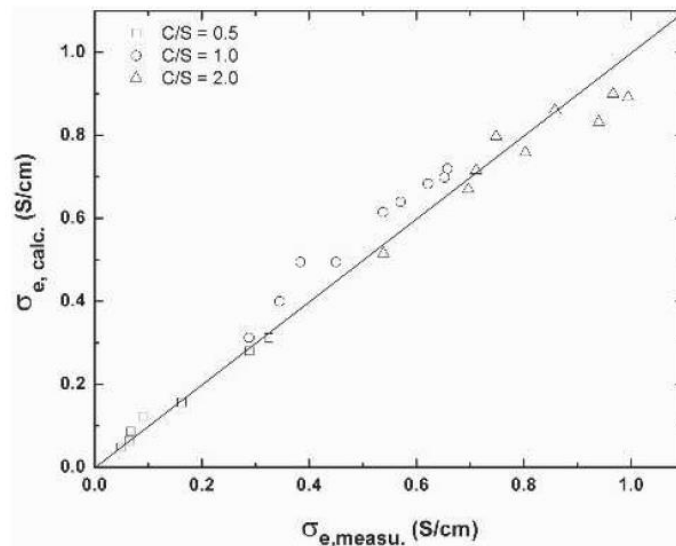


Figure 2.15: Comparison between measured and calculated electronic conductivity using

$$r_0^* = 3.87\text{\AA}^{[71]}$$

### 2.3. Summary and Knowledge Gaps

This chapter has provided the background, discussed the research on bloated droplets and identified the knowledge gaps. These gaps are summarized here in brief. Although different rate controlling mechanism have been proposed for decarburization of droplets in oxidizing slag at different stages of decarburization, there is a need to understand the kinetics of

individual stages of decarburization so that a model of bloated droplet behavior can be developed based on that clear understanding. To explain the internal CO bubble formation, Chen & Coley<sup>[2]</sup> proposed a way which works but theoretical understanding is missing. It is essential to develop a fundamental understanding of bubble formation. Based on experimental observation from Murthy & coworkers<sup>[34,35]</sup> and Gare & Hazeldean<sup>[21]</sup>, it is evident that there is a significant effect of slag composition, mainly slag conductivity, not only in the initial stages but more importantly determining the end stage of decarburization. There is no systematic study so far on varying slag electronic and ionic conductivity to understand decarburization and bloating. There is some understanding developed on addition of sulfur, how the reaction kinetics will be impacted but no study reported on the interplay between added surface-active elements sulfur and slag conductivity. There has been some development on understanding the effect of alloying elements such as phosphorus on bloating<sup>[3,76]</sup>. However, but the impact of other elements such as silicon and manganese are still unexplored. Although there has been some progress on the development of a decarburization model based on the understanding from the decade old experimental studies, most of the studies do not capture the internal bubble generation kinetics, some of the models fail when poisoning elements are present, some models force the decarburization reaction to shut down by introducing a surface blocking effect for example by SiO<sub>2</sub> or by imposing an artificially high  $\psi$  parameter. Previous experiments of decarburization without silicon also observed premature shutdown, so the assumption of the shutdown of decarburization in presence of SiO<sub>2</sub> is not valid. The assumption of high  $\psi$  parameter suggests very high free energy barrier for nucleation and using this value, it

was not possible to explain the nucleation of CO bubbles and bloating for low carbon droplets. The current work will focus on addressing some of the fundamental issues on bloating through a targeted set of decarburization experiments varying slag and metal composition and will develop a decarburization model capturing the fundamentals of each reaction step. Chapter 3 will address the gaps on understanding the decarburization kinetics by measuring decarburization rate and bloating extend over a range of slag and metal compositions and describe the complexity of the process and illustrate the need for a mixed controlled decarburization model. Chapter 4 will develop a model considering all relevant reaction steps, presenting the details of this model and validation for a wide range of slag and metal compositions. This paper will also explore the knowledge gap with regards to the end stage of decarburization and will propose a mechanism for premature cessation of the reaction which will be further investigated in Chapter 5. In chapter 5, a systematic study of decarburization over a range of slag electronic and ionic conductivity will be presented showing how conductivity affects the peak decarburization rate as well as the point at which the reaction shuts down. Chapter 6 will extent the work covered in Chapters 3 to 5 to consider the competition between adsorption of sulfur and oxygen at the slag/metal interface and the effect of this competition on decarburization. Chapter 7 will present some observations on delaying of bloating in the presence of silicon. Finally, chapter 8 will draw some general conclusions from =the combined contents of the thesis.

## **References**

- 1 Julien Hall: Historic global steel price rally sweeps iron ore to all-time high,

<https://www.spglobal.com/platts/en/market-insights/blogs/metals/042721-global-steel-price-rally-iron-ore-iindex-all-time-high-china-stimulus>.

- 2 E. Chen and K.S. Coley: *Ironmak. Steelmak.*, 2010, vol. 37, pp. 541–5.
- 3 K. Gu, N. Dogan, and K.S. Coley: *Metall. Mater. Trans. B Process Metall. Mater. Process. Sci.*, 2017, vol. 48, pp. 2984–3001.
- 4 World Steel Association: *World Steel Association Report 2020*, 2020.
- 5 Subagyo, G.A. Brooks, K.S. Coley, and G.A. Irons: *ISIJ Int.*, 2003, vol. 43, pp. 983–9.
- 6 S.C. Koria and K.W. Lange: *Met.Trans.B*, 1984, vol. 15B, pp. 109–16.
- 7 Q.L. He and N. Standish: *Isij Int.*, 1990, vol. 30, pp. 305–9.
- 8 G. Turner and S. Jahanshahi: *Trans. Iron Steel Inst. Japan*, 1987, vol. 27, pp. 734–9.
- 9 N. Standish and Q.L. He: *ISIJ Int.*, 1989, vol. 29, pp. 455–61.
- 10 N.A. Molloy: *J. iron steel Inst.*, 1970, vol. 208, p. 943.
- 11 S. Sabah and G. Brooks: *Metall. Mater. Trans. B Process Metall. Mater. Process. Sci.*, 2014, vol. 46, pp. 863–72.
- 12 C.L. Molloseau and R.J. Fruehan: *Metall. Mater. Trans. B Process Metall. Mater. Process. Sci.*, 2002, vol. 33, pp. 335–44.
- 13 Subagyo, G.A. Brooks, and K.S. Coley: *Can. Metall. Q.*, 2005, vol. 44, pp. 119–

- 30.
- 14 G. Brooks, Y. Pan, and K.S. Coley: *Metall. Mater. Trans. B*, 2005, vol. 36B, pp. 525–35.
- 15 L.A. Baker, N.A. Warner, and A.E. Jenkins: *Trans. Metall. Soc.*, 1967, vol. 239, pp. 857–64.
- 16 P.A.A. Distin, G.D.D. Hallett, and F.. D. Richardson: *J. Iron Steel Inst.*, 1968, vol. August, pp. 821–33.
- 17 J.B. SEE and N.A. Warner: *J. Iron Steel Inst.*, 1973, vol. 211, pp. 44–52.
- 18 P.G. Roddis: *J. Iron Steel Inst.*, 1973, vol. 211, pp. 53–8.
- 19 H. Gaye and P. V. Riboud: *Metall. Trans. B*, 1977, vol. 8, pp. 409–15.
- 20 N.H. El Kaddah and D.G.C. Robertson: *J. Colloid Interface Sci.*, 1977, vol. 60, pp. 349–60.
- 21 T. Gare and G.S.F. Hazeldean: *Ironmak. Steelmak.*, 1981, vol. 8, pp. 169–81.
- 22 W.O. Philbrook and L.D. Kirkbride: *J. Met.*, 1956, vol. 8, pp. 351–6.
- 23 T.E. Dancy: *J. Iron Steel Inst.*, 1951, vol. 169, pp. 17–24.
- 24 B. Sarma, A.W. Cramb, and R.J. Fruehan: *Metall. Mater. Trans. B Process Metall. Mater. Process. Sci.*, 1996, vol. 27, pp. 717–30.
- 25 T. Fujii: *Tetsu-to-Hagane*, 1959, vol. 45, pp. 1248–54.

- 26 K. ITO and K. SANO: *Tetsu-to-Hagane*, 1964, vol. 50, pp. 873–7.
- 27 K. ITO and K. SANO: *Tetsu-to-Hagane*, 1965, vol. 51, pp. 1252–9.
- 28 K. ITO, K. SANO, and S. ARINO: *Iron Steel Inst Japan-Trans*, 1969, vol. 9, pp. 465–71.
- 29 Y. NIIRI, K. ITO, and K. SANO: *Tetsu-to-Hagane*, 1969, vol. 55, pp. 437–45.
- 30 L.A. Baker and R.G. Ward: *J. Iron Steel Inst*, 1967, vol. 205, pp. 714–7.
- 31 R. Acheson: Sheffield Hallam University (United Kingdom), 1976.
- 32 M.W. Davies, G.S.F. Hazeldean, and P.N. Smith: *Inst. Min. Met, London*.
- 33 M. Hayer and S.G. Whiteway: *Can. Metall. Q.*, 1973, vol. 12, pp. 35–44.
- 34 G. Murthy, Krishna, G, Y. Sawada, and F. Elliot, J: *Ironmak. Steelmak.*, 1993, vol. 20, pp. 179–200.
- 35 G.G.K. Murthy, A. Hasham, and U.B. Pal: *Ironmak. Steelmak.*, 1993, vol. 20, pp. 191–200.
- 36 E.W. Mulholland, G.S.F. Hazeldean, and M.. Davies: *J. Iron Steel Inst.*, 1973, vol. 211, pp. 632–9.
- 37 D.J. Min and R.J. Fruehan: *Metall. Trans. B*, 1992, vol. 23, pp. 29–37.
- 38 K. Gao, V. Sahajwalla, H. Sun, C. Wheatley, and R. Dry: *ISIJ Int.*, 2000, vol. 40, pp. 301–8.

- 39 E. Chen: McMaster University, 2011.
- 40 H.S. Levine: *Met. Trans*, 1973, vol. 4, pp. 777–82.
- 41 K. Gu: McMaster University, 2017.
- 42 M. Volmer and A. Weber: *Zeitschrift für Phys. Chemie*, 1926, vol. 119U, pp. 277–301.
- 43 L. Farkas: *Zeitschrift für Phys. Chemie, Stöchiometrie und Verwandtschaftslehre*, 1927, 125, vol. 125.
- 44 R. Becker and W. Döring: *Ann. Phys.*, 1935, vol. 416, pp. 719–52.
- 45 Y.B. Zeldovich: *Acta Physicochem. USSR*, 1943, vol. 18, p. 18.
- 46 R.S. Kaplan and W.O. Philbrook: *Metall. Trans.*, 1972, vol. 3, pp. 487–91.
- 47 D. Kashchiev and A. Firoozabadi: *J. Cryst. Growth*, 2002, vol. 243, pp. 476–89.
- 48 N.H. Fletcher: *J. Chem. Phys.*, 1958, vol. 29, pp. 572–6.
- 49 X.Y. Liu: *J. Chem. Phys.*, 2000, vol. 112, pp. 9949–55.
- 50 M. Blander and J.L. Katz: *AIChE J.*, 1975, vol. 21, pp. 833–48.
- 51 J.H. Swisher and E.T. Turkdogan: *AIME Met Soc Trans*, 1967, vol. 239, pp. 426–31.
- 52 P.G. Bowers, K. Bar-Eli, and R.M. Noyes: *J. Chem. Soc. - Faraday Trans.*, 1996, vol. 92, pp. 2843–9.

- 53 H.Y. Kwak and S.D. Oh: *J. Colloid Interface Sci.*, 1998, vol. 198, pp. 113–8.
- 54 H.Y. Kwak and R.L. Panton: *J. Chem. Phys.*, 1983, vol. 78, pp. 5795–9.
- 55 F. Abraham, F: *Homogeneous Nucleation Theory*, Academic Press, INC., New York, 1974.
- 56 B.O. Mysen: *Earth-Science Rev.*, 1990, vol. 27, pp. 281–365.
- 57 K.C. Mills, M. Hayashi, L. Wang, and T. Watanabe: in *TREATISE ON PROCESS METALLURGY Process Fundamentals*, Elsevier Ltd, 2014, pp. 149–286.
- 58 F.D. Richardson: *Physical Chemistry of Melts in Metallurgy Volume 1*, 1st edn., Academic Press Inc. (London) Ltd., London, 1974.
- 59 S. Ramachandran, T.B. King, and N.J. Grant: *J. Met.*, 1956, vol. 8, pp. 1549–58.
- 60 Riboud.P.V and H. Gaye: in *4th International Conference on Molten Slags and Fluxes*, 1992, pp. 173–8.
- 61 G. Urbain: *Steel Res.*, 1987, vol. 58, pp. 111–6.
- 62 K.C. Mills and S. Sridhar: *Ironmak. Steelmak.*, 1999, vol. 26, pp. 262–8.
- 63 S. Sridhar, D. Sichen, S. Seetharaman, and K.C. Mills: *Steel Res.*, 2001, vol. 72, pp. 3–10.
- 64 K. Mori and K. Suzuki: *Trans. Iron Steel Inst. Japan*, 1969, vol. 9, pp. 409–12.
- 65 H.-J. Engell and P. Vygen: *Reports Bunsen Soc. Phys. Chem.*, 1968, vol. 72, pp. 5–11.



- 66 K.S. Goto, T. Kurahashi, and M. Sasabe: *Metall. Trans. B*, 1977, vol. 8, pp. 523–8.
- 67 D. Xie and G.R. Belton: *Metall. Mater. Trans. A Phys. Metall. Mater. Sci.*, 1999, vol. 30, pp. 465–72.
- 68 W.R. Dickson and E.B. Dismukes: *Trans. Metall. Soc. AIME*, 1962, vol. 224, pp. 505–11.
- 69 R. Hundermark: 2003.
- 70 M.T. Simnad, G. Derge, and I. George: *J. Met.*, 1954, vol. 6, pp. 1386–90.
- 71 M. Barati and K.S. Coley: *Metall. Mater. Trans. B Process Metall. Mater. Process. Sci.*, 2006, vol. 37, pp. 41–9.
- 72 J.O.M. Bockris, J.A. Kitchener, S. Ignatowicz, and J.W. Tomlinson: *Trans. Faraday Soc.*, 1952, vol. 48, pp. 75–91.
- 73 N.F. Mott: *J. Non. Cryst. Solids*, 1968, vol. 1, pp. 1–17.
- 74 H. Nasu and N. Soga: *J. Non. Cryst. Solids*, 1982, vol. 53, pp. 123–34.
- 75 K.J. Laidler: *Can. J. Chem.*, 1959, vol. 37, pp. 138–47.
- 76 K. Gu, N. Dogan, and K.S. Coley: *Metall. Mater. Trans. B Process Metall. Mater. Process. Sci.*, 2017, vol. 48, pp. 2343–53.

## **Chapter 3**

### **3. Decarburization of Bloated Droplets: An experimental study to understand the kinetics of decarburization of metallic iron droplets in FeO containing CaO-SiO<sub>2</sub> slags**

Chapter 3 presents the effects of carbon concentration from 0.5% to 4.4%, slag oxygen potential, and slag basicity on decarburization kinetics of metal droplets. Based on the experimental results, a conceptual mixed control model is presented, emphasizing the necessity of a more rigorous mathematical model. In this chapter, all the experiments were performed by me. Dr. Kezhuan Gu provided preliminary assistance in setting up the furnace and preparation of droplets. Dr. Kenneth Coley provided essential guidance in developing the kinetic model and in analyzing the data. The manuscript was prepared by me, and corrections and proofreading to the final version were done by Dr. Coley.

This manuscript is accepted for publication in Metallurgical and Materials Transactions B on 5<sup>th</sup> Oct, 2021 and in the process of publication. Doi: [10.1007/s11663-021-02344-x](https://doi.org/10.1007/s11663-021-02344-x)

#### **Abstract**

Bloating of metal droplets in the BOF is important in developing fundamental models of the process. Bloating is controlled by the decarburization behavior of individual metal droplets in oxidizing slag. In this paper, a detailed investigation has been performed to elucidate the mechanism and rate controlling steps for decarburization of droplets over a range of droplet carbon concentration, droplet mass, slag basicity and slag FeO

concentration. Four different carbon levels and three droplet masses were tested. Droplets typically exhibited three stages of decarburization: incubation period, where decarburization was mostly on the outer surface of the droplet, followed by a steady state reaction period where most decarburization was internal, and finally the end decarburization period. The rate of decarburization was found to be a mixed controlled process; the contributions of resistance from slag transport, interfacial chemical reaction, internal nucleation and growth of bubbles varied based on slag and metal chemistry. A mixed controlled kinetic model has been developed for steady state decarburization period and a partial validation of the mixed controlled kinetic model has been presented here. By varying slag FeO concentration and basicity for droplets containing 2.5 wt%C, mixed controlled kinetics of decarburization reaction were explored.

### **3.1. Introduction**

Decarburization kinetics play an important role in oxygen steelmaking. Decades of experimental research and phenomenological modeling have been conducted to understand the mechanism behind each of the stages of decarburization<sup>[1-30]</sup>. Mainly four types of experimental investigation have been performed in this field – gas-metal bath, slag over metal bath, metal droplet reacting in slag and levitated metal droplet reacting in oxidizing gas atmosphere.

Philbrook & Kirkbride<sup>[1]</sup> conducted studies with a carbon saturated metal bath and a layer of slag. In their work the rate of reduction of FeO was found to be second order with respect to FeO concentration whereas Dancy<sup>[2]</sup> found it to be first order with respect to FeO under

similar circumstances. Sarma <sup>[13]</sup> also found the rate of reduction of FeO by carbonaceous material to be limited by mass transport of FeO in the slag phase where rate of CO generation was  $\propto (wt\% FeO)^{1.67}$ . This was justified by the combined effect of FeO concentration on driving force and on the mass transfer coefficient; mass transfer coefficient,  $k_m \propto (wt\% FeO)^{0.67}$  due to stirring from CO gas bubbles. Ito & Sano performed an experimental study on the rate of decarburization of a liquid metal bath reacting with oxidizing gas such as H<sub>2</sub>O-Ar<sup>[24,25]</sup> and CO<sub>2</sub>-Ar<sup>[26,27]</sup>. These authors proposed that initially oxygen transfer through a gaseous boundary layer controlled the rate and when the oxygen content in a layer near the top of metal bath increased to the saturation value, an oxide layer formed, transport of oxygen through which controlled the rate of decarburization. In another study by the same group of researchers, oxide forming elements such as Si, Cr and Mn were found to influence the end stage of decarburization, where the rate of decarburization decayed due to oxide layer formation. There have been several studies<sup>[4,5,28,30-35]</sup> performed using levitated droplets reacting with oxidizing gas and most of the workers found gas phase mass transport controlled decarburization kinetics above some critical concentration and followed by metal phase mass transfer control. It was observed in most of these cases that the droplet exploded after reacting for certain time, and some workers<sup>[28,31,34]</sup> observed that an outer oxide layer formed on the metal droplet and this layer preceded the explosion. In metal droplet/slag type decarburization studies<sup>[7-11,19,36]</sup>, most workers found carbon containing metal droplets to swell due to internal decarburization. Mulholland *et al.*<sup>[19]</sup> first visualized the metal droplet decarburization in slag by X-ray Fluoroscopy and confirmed the formation of CO bubbles within the droplet

at the later stages of decarburization. Later Molloseau & Fruehan<sup>[10]</sup> also observed the swelling (termed “emulsification”) of droplet in oxidizing slag. The term ‘bloating’ was first introduced by Brooks *et al.*<sup>[14][37]</sup> when these workers recognized it’s importance in predicting the residence time of a droplet while decarburizing in BOF. Additionally the rate of decarburization was reported to be, under mixed control by Min & Fruehan<sup>[8]</sup>, slag mass transport control by Molloseau & Fruehan<sup>[10]</sup>, gas film diffusion & slag transport control above 2-3 wt %C and electrochemical transport controlled below that level by Murthy *et al.*<sup>[9]</sup>. Gaye & Riboud<sup>[7]</sup> proposed decarburization to be interfacial reaction controlled initially and afterwards transport controlled whereas based on the linear relationship between rate and metal volume Chen & Coley<sup>[11,38]</sup> proposed it to be controlled by internal nucleation of CO. There have been several studies conducted by the group of Pal<sup>[9,36,39-41]</sup> regarding the end stage of decarburization. They have suggested that the reaction between FeO in slag and solute C in a metal bath is electrochemical in nature and proposed a rate enhancement mechanism on applying a DC potential across the slag layer. Apart from lab scale research, there have been reports from pilot scale converter trials from IMPHOS<sup>[42]</sup> project. Metal droplets, which were collected from emulsion with diameter of the order ~ 100 μm, dropped to very low concentrations for Si, Mn, P, V whereas C concentration remained above 1 wt% due to kinetic limitation. Analysis of the slag metal samples collected by Holappa<sup>[43]</sup> and Cicutti<sup>[44]</sup> from an industrial scale converter shows that the droplets collected from the emulsion always have a carbon concentration higher than that predicted by thermodynamic equilibrium, although significantly less than that in the bath. Cicutti proposed partial decarburization to be due to short residence time of

droplets, however Cicutti's work predates the proposal of the bloated droplet concept which would lead to longer residence times for as long as internal decarburization was supported. This shows that although decarburization in the emulsion of a BOF is much higher compared to metal bath, the droplets do not reach thermodynamic equilibrium. Apart from liquid droplet decarburization studies, a recent study<sup>[45]</sup> to understand the reaction kinetics of direct reduced iron(DRI) pellets in oxidizing slag shows it to be a two stage process: initial stage controlled by heat transfer from slag to pellet and later stage controlled by FeO transport in the slag. There have been several attempts<sup>[15,18,20-22]</sup> to model the decarburization kinetics to predict the contribution of refining from emulsion in BOF and these are showing a much higher contribution (as high as above 70%) whereas Cicutti predicted the contribution to be 20-50%.

Despite the extensive research performed to-date, there is lack of clarity about the rate controlling mechanism at different stages of decarburization reaction. A sudden stop in decarburization has been observed by many researchers studying decarburization of droplets reacting in slag, but limited work has been done to understand the end stage of the decarburization process in details. In the present work, an attempt has been made to develop a mixed control kinetic model including slag transport, slag/metal interfacial reaction kinetics and internal nucleation and growth of bubbles for the steady state decarburization period when the decarburization is mostly internal. Additionally, an analysis have been performed on the end point carbon concentration on varying initial slag and metal chemistry to explore the effect of these parameters on shutting down the decarburization process.

## **3.2. Experimental Procedure**

### **3.2.1. Experimental Setup**

A resistance heated vertical tube furnace with 80 mm inner diameter alumina tube was used for all experiments. An X-ray imaging system was installed with the furnace to observe the bloating and other changes of droplets throughout the progress of the reaction. The X-ray video was recorded in the computer via One Touch Grabber Software. A differential pressure transducer with a maximum pressure limit of 13.8 kPa (FLW Southeast, Inc, 157C-W050NR, Very Low Pressure Transducer) with sensitivity of  $3 \times 10^{-5}$  atm was connected with the sealed reaction chamber to measure the change in pressure due to gas evolution from the decarburization reaction. The data was recorded by a computer software (RS232 Interface) at a selected frequency i.e. 10 Hz in this study. The pressure transducer data was converted to the number of moles of CO produced assuming all the pressure change is due to CO gas. The pressure change was calibrated after each experiment by injecting a fixed volume of air into the sealed furnace.

### **3.2.2. Sample Preparation**

Metal droplets were prepared by mixing electrolytic iron of 99.99% purity, graphite and Fe-S alloy and heating to 1550°C in a vertical tube furnace under an inert Argon atmosphere and kept for 1 hour for homogenizing and then sampling was done by pipetting through quartz tube and quenching in water. The resulting cylindrical metal rods were then polished and cut into sections of nominal mass 1.0, 1.5 and 2.0 g sections. For use in calculations, the actual mass of each section was measured to within  $\pm 0.0005$  g. The carbon and sulfur

concentration of these sections from each batch was measured with LECO carbon sulfur analyzer to make sure the desired composition was achieved. These individual cylindrical sections from each batch were remelted in an Electric Arc Melter to further homogenize and produce droplets. The composition of the droplets were further confirmed by testing samples from each batch with LECO analysers. The oxygen concentration of the samples was measured to be around  $50 \pm 30$ ppm. To prepare the slag, a proportionate mixture of calcium oxide, silica and alumina powders were premelted in a platinum crucible at  $1550^{\circ}\text{C}$  and homogenized for 1 hour and then quenched on top of a steel slab in air. The premelted slag was then crushed and mixed with FeO powder to prepare a batch of slag weighing  $25.0 \pm 0.5$  g for each experiment. The composition of post reacted slag was analyzed using Inductively Coupled Plasma Optical Emission Spectroscopy (ICP-OES). The metal and slag chemistry employed in this study are listed in Table 3.1 and Table 3.2. The first set of experiments were carried out with four different carbon levels and three different sizes of droplets. Then other set of experiments were performed by varying the slag FeO concentration, slag basicity.

Table 3.1: Metal composition used in experiments

| <b>Sample</b> | <b>Wt % C</b>   | <b>Wt % S</b>     |
|---------------|-----------------|-------------------|
| 1             | $0.50 \pm 0.02$ | $0.010 \pm 0.002$ |
| 2             | $1.50 \pm 0.01$ | $0.010 \pm 0.002$ |
| 3             | $2.50 \pm 0.01$ | $0.010 \pm 0.001$ |
| 4             | $4.40 \pm 0.03$ | $0.010 \pm 0.002$ |



Table 3.2: Slag composition used in set of experiments

| <b>Set of Experiments</b>  | <b>CaO/SiO<sub>2</sub></b> | <b>FeO (wt%)</b> | <b>Temperature (°C)</b> |
|----------------------------|----------------------------|------------------|-------------------------|
| Carbon & Mass Variation    | 0.91                       | 16               | 1580                    |
| Wt% FeO Variation in slag  | 0.91                       | 2.5, 5, 10, 16   | 1580                    |
| Basicity Variation in slag | 0.91, 1.5, 2.0             | 16               | 1580                    |

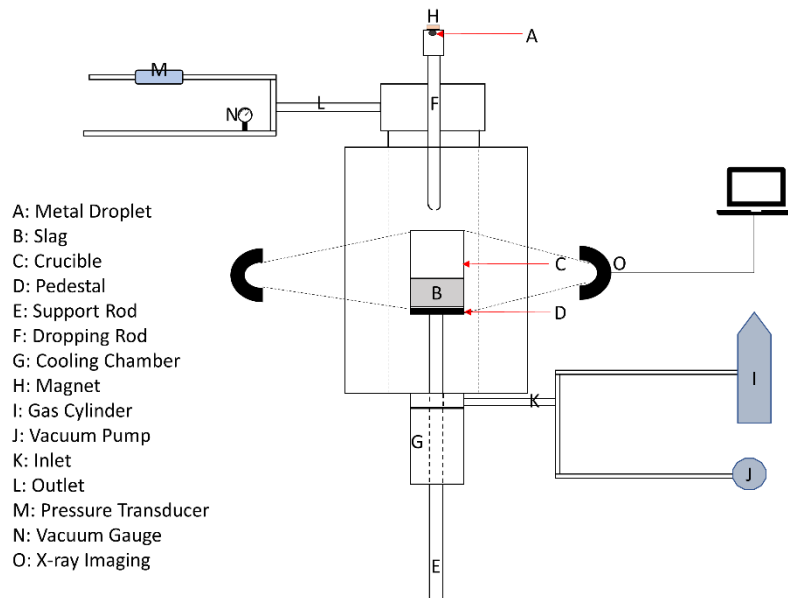


Figure 3.1: Schematic of experimental set up

### 3.2.3. Experimental Procedure

A schematic of the experimental set up is shown in Figure 3.1. A metal droplet (A) of specific size was held at the end of an alumina tube using a magnet (H). A 99.99% pure alumina crucible (C) with outer diameter of 40mm, containing 25 g of slag (B) was inserted from the bottom of the furnace and placed in the hot zone of the furnace using a support rod (E). The furnace was sealed and evacuated to 700 millitorr (i.e. 93.33 Pa). The furnace was then backfilled with high purity argon. After backfilling the outlet valve on the furnace was opened to allow argon to flow continuously. The argon was passed through a gas purifying system to absorb moisture and oxygen. The argon flow continued till the target temperature was attained. At the target temperature, the flow was interrupted, and the valves connected to furnace were closed to make a sealed chamber. The droplet was then

allowed to fall by removing the magnet. The droplet could not pass through the hole at the bottom of the delivery tube until it melted, at which point it dropped into the slag and the progress of the decarburization reaction was recorded by capturing the pressure change from a pressure transducer(M). X-ray video was recorded of the droplet from the time where the magnet was removed until the end of the experiment. The melting time of the droplet before releasing the magnet was determined from X-ray Video and is presented in Table 3.3 for the cases of varying carbon cases and for varying droplet mass.

Table 3.3: Droplet melting time(s) before dropping into the slag

| <b>Wt% C</b> | <b>2 g</b> | <b>1.5 g</b> | <b>1 g</b> |
|--------------|------------|--------------|------------|
| 4.4          | 34 s       | 27 s         | 26 s       |
| 2.5          | 44 s       | 27 s         | 28 s       |
| 1.5          |            | 36 s         | 27 s       |
| 0.5          | 80 s       | 63 s         | 48 - 55 s  |

The melting time varied with the size of the droplet as well as with droplet carbon concentration. For droplets with the same carbon concentration smaller droplets needed less time to melt, whilst lower carbon concentration droplets needed a longer melting time due to their higher melting point. The time at which the melted droplet fell into the slag was defined as time zero for kinetic analysis. For initial experiments two calibration methods were used to determine the volume of gas generated during the experiment. In one method the pressure data was calibrated by comparing the difference between the final and

initial carbon content of the droplet with the constant volume pressure increase. In another technique, 10ml, 20ml and 30ml of air were injected into the sealed furnace and the pressure change recorded. This data was used to calibrate the pressure change against the known gas addition. The calibration was then used to calculate the volume of CO generated during the decarburization reaction. There was no significant ( $\pm 10\%$ ) difference between these two methods in calculating the number of moles of CO generated during the reaction. Therefore, the method of calibration using the carbon concentration measurement, before and after was employed for all datasets. The total CO generation data which was calculated from the pressure data was then filtered in MATLAB to reduce the noise introduced during data collection and presented in the following sections.

### **3.3. Experimental Results**

#### **3.3.1. The Effect of Carbon Concentration and Mass on Decarburization of Droplets**

The kinetics of the decarburization reaction was investigated by varying the droplet initial carbon concentration and the droplet mass. Droplets containing 0.01 wt% S and carbon concentrations between 0.5 and 4.4 wt% were reacted with slag having 16 wt% FeO and basicity ( $V_{ratio} = \frac{CaO}{SiO_2}$ ) of 0.91 at a temperature of 1580°C.

The cumulative CO generation profiles for 1, 1.5 and 2 g droplets with 4.4 wt%, 2.5 wt%, 1.5 wt% and 0.5 wt% C are presented respectively in Figure 3.2(a), (b), (c) and (d). The bloating behavior of droplets having different masses is also reported here in Figure 3.2(e), (f), (g) and (h) which show as a function of time, the volume of CO retained in the droplets normalized with respect to original droplet volume. These data have been extracted at one

second intervals from the recorded X-ray videos. The measure droplet area from the 2-D image was converted to volume by calibrating the measured area at reaction time zero with the initial liquid droplet volume<sup>[46]</sup>. Finally, the normalized retained CO gas volume was calculated according to Equation 3.1.

$$\text{Normalized Retained Volume}(t) = \frac{V(t)-V(0)}{V(0)} = \frac{\text{Retained CO Volume}}{\text{Original Droplet Volume}} \quad [3.1]$$

Where  $V(t)$  is the volume of the bloated droplet at time  $t$ , and  $V(0)$  is the original volume of the droplet. All curves of CO gas generation exhibit a similar decarburization behavior. Some droplets showed an initial slow decarburization rate which increased to a relatively constant rate, referred to as peak decarburization rate, which eventually decayed and finally stopped altogether. In most of the cases, the initial slow period, termed the incubation period, was absent but the data showed an approximately steady-state rate followed by a characteristic slowing and stopping. It can be observed from the CO generation profile at 4.4 wt%C that the peak rate of decarburization increased with increasing droplet size from 1 g to 2 g. Here, the peak decarburization rate was determined from the slope of each curve in the period of faster, relatively constant rate. Based on the curves drawn in Figure 3.2 the 1.5 g droplet showed a higher peak rate compared to 1 and 2 g droplets, however this depends very much on exactly where the incubation time ends. Given the uncertainty over this choice, and the observation of other workers that CO generation rate scales with droplet mass, it is probably fair to say that the current results are not sufficiently precise to dispute that finding. The normalized retained volume also demonstrated that with increasing droplet size the maximum volume of gas retained within the droplet increased from 2, to

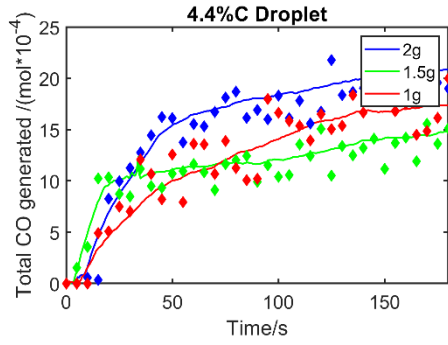
3.5 to 4 times of the original volume respectively for 1 g, 1.5 g and 2 g droplet. It is to be noted that 1 and 2 g droplets showed ~ 6 s of incubation period whereas the incubation period was shorter, ~2 s, for 1.5 g droplet. As found in previous research in the authors' laboratory, during the reaction the slag separated into two layers; a foamy layer lying over a dense layer. The droplets were observed in the X-ray image to bloat and rise up into the foamy slag, shrink then sink back into the dense slag. The entire sequence of behavior is indicated by individual peaks in the normalized retained volume plot and was found to occur 7 times in the case of 1g droplet and 2 to 3 times for 1.5 g and 2 g droplets respectively. The droplets in some cases were observed to remain bloated and sit between the dense and foamy slag.

Figure 3.2(b) presents the decarburization behavior of droplets containing 2.5 wt%C. It shows that the peak rate of decarburization increased significantly with increase in droplet size from 1.5 to 2 g but the increase in peak rate was not significant with an increase in droplet size from 1 to 1.5 g. The extent and rate of bloating was found to be similar for droplets of different sizes based on Figure 3.2(f). The re bloating phenomena usually did not occur in the case of droplets with 2.5 wt% carbon, for all three droplet sizes presented here. Furthermore, the decarburization behavior did not show an incubation period according to Figure 3.2(b) and (f).

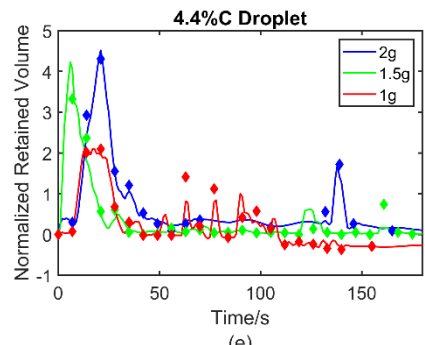
For the case of droplets with 1.5 wt%C of 1.5 and 1 g, Figure 3.2(c) and (g) show that the peak decarburization rate increased with increasing droplet size and the maximum amount of retained gas within droplet increased from 1.5 to 2 times the original volume as the droplet mass increased from 1 g to 1.5 g. Compared to the case of the 1.0 g droplet, the

1.5 g droplet remained bloated for a longer time period as shown in Figure 3.2(g). No rebloating was observed for droplets containing 1.5 wt%C.

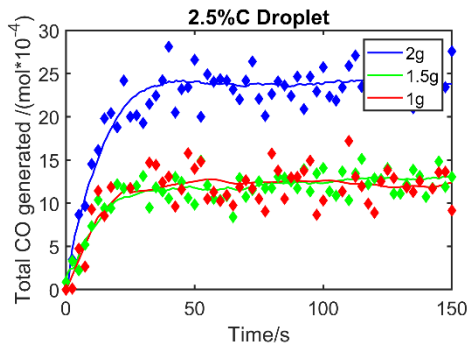
The decarburization behavior for droplets with 0.5 wt%C at three different masses is presented in Figure 3.2(d) and (h). The peak decarburization rate was found to increase with increasing droplet size and the droplets also showed bloating at this low level of carbon concentration. The extent of bloating was found to be smallest in the case of the 1g droplet and increased with increasing droplet mass, which is consistent with all other droplets studied here regardless of carbon concentration.



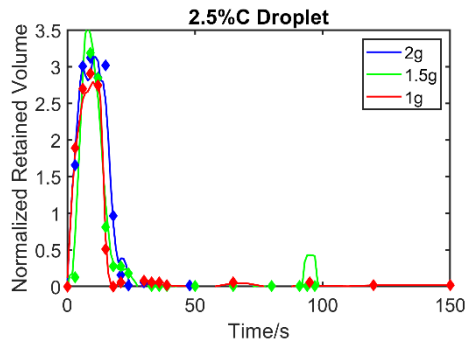
(a)



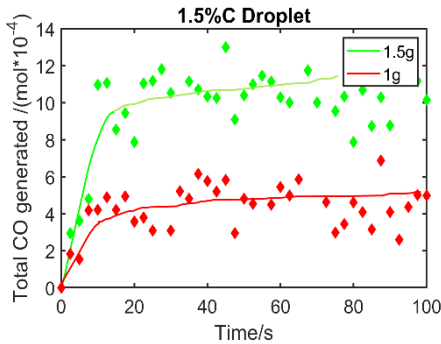
(e)



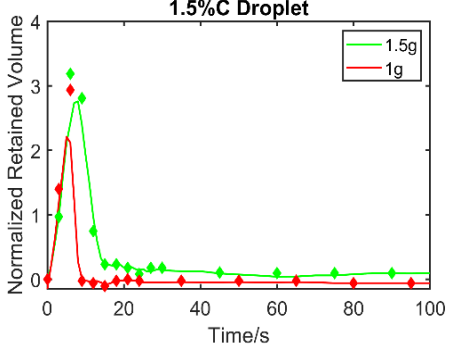
(b)



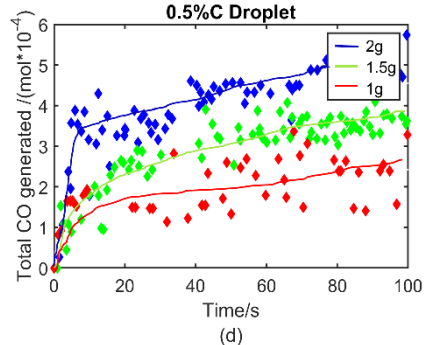
(f)



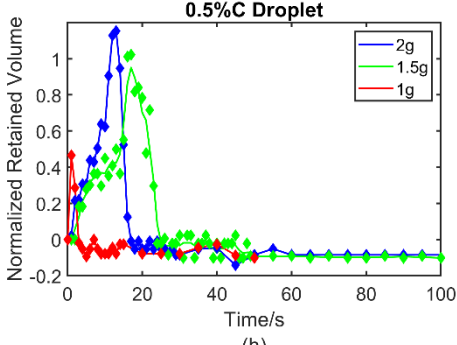
(c)



(g)



(d)



(h)



Figure 3.2: Total CO generation with time (a), (b), (c), (d) and normalized retained volume variation with time (e), (f), (g), (h) at different carbon concentration and at different droplet masses

### 3.3.2. The effect of Slag FeO Concentration on Decarburization of Droplets

Another set of experiments were performed at 1580<sup>0</sup>C, to observe the decarburization behavior of 2 g droplets with 2.5 wt%C and 0.01wt%S over a range of oxygen potential of the slag as defined by the wt%FeO in the slag. Experiments were conducted with 2.5 wt%, 5 wt%, 10 wt% and 16 wt% FeO in the slag, while keeping the *V-ratio* constant at 0.91. The CO generation and the bloating behavior under these conditions are presented in Figure 3.3(a) and (b). These figures show that the peak rate of decarburization increased with increasing FeO concentration in the slag which is consistent with findings in the literature<sup>[10]</sup>. The droplets were found to bloat in all cases except that with 2.5 wt% FeO. The maximum gas volume within bloated droplets increased from 5 wt%FeO (3 times) to 10 wt%FeO (4.8 times) followed by a decrease to 3.5 times at 16 wt% FeO. The CO generation rate for droplets reacting with slag containing 2.5 wt% FeO was found to be linear with respect to time, which along with the observation that those droplets did not bloat indicates that they are most likely experiencing external decarburization and that the rate is most likely controlled by mass transport of oxygen in the slag or by chemical reaction at the slag metal interface. The transport of carbon towards slag/metal interface seems to be fast enough compared to the transport of oxygen towards the slag/metal interface from bulk slag in 2.5 wt% FeO slag, otherwise there would have been oxygen transport into the bulk metal leading to bloating. Decarburization for droplets ceased, in

order of increasing FeO concentration, at 1.79 wt%C, 1.67 wt%C, 1.43 wt%C and 1.1 wt%C, whereas the thermodynamic estimation from FactSage suggests that carbon concentration can be reduced to 0.08 wt%, 0.03 wt%, 0.01 wt% and 0.005 wt% with increasing order of FeO concentration. Calculation of the lower limit of carbon concentration from the supersaturation limit suggests that the end point carbon should have been 1.25 wt%, 0.67 wt%, 0.4 wt% and 0.3 wt% with increasing order of FeO concentration. In calculating the limiting supersaturation pressure, the authors considered the barrier to nucleation rather than thermodynamic equilibrium. Many practical studies indicate that this barrier for CO nucleation will be overestimated if one employs classical nucleation theory. For this reason, the authors employed the methodology used by Chen & Coley<sup>[11]</sup> to address this issue. In any case, this offers a conservative calculation of the endpoint carbon and still shows that the decarburization terminated prior to reaching the limiting carbon concentration (thermodynamic equilibrium limit as well as nucleation barrier limit) for range of slag FeO concentrations.

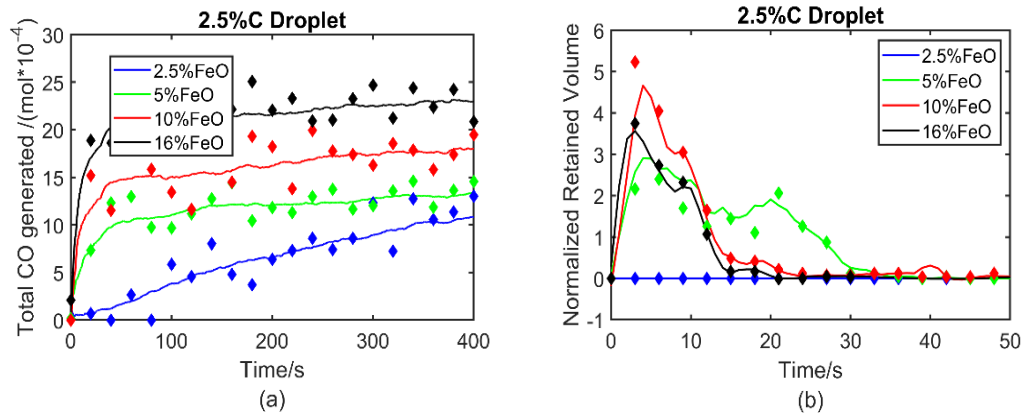


Figure 3.3: Total CO generation with time (a) and normalized retained volume profile with time (b) on varying FeO wt%

### 3.3.3. The Effect of Slag Basicity on Decarburization

The decarburization behavior for 2.5 wt%C-0.01 wt%S 2g droplets reacting with different basicity slags, *V-ratio* varied from 0.9 to 2, was investigated at 1580<sup>0</sup>C and the results are presented in Figure 3.4. The gas volume within the droplet increased up to 7 times its original volume for reaction with slag  $V = 2.0$ , compared to 6 times in the case of  $V = 1.5$  and 3 times in the case of  $V = 0.9$ . The CO generation for  $V = 2.0$  has highest peak rate of decarburization compared to the cases of  $V = 1.5$  and  $V = 0.9$ . The extent of decarburization is much greater, and the end point carbon goes down to 0.33 wt% for  $V = 2.0$  compared to 0.96 wt% for the case of  $V = 1.5$  and 1.1 wt% for  $V = 0.9$ . In the case of the higher basicity slag, the decarburization proceeded to a carbon concentration close to that predicted by considering the barrier to nucleation in the supersaturation limit ( $\sim 0.3$  wt%). This value is higher than that predicted for thermodynamic equilibrium but is consistent with the idea that the nucleation barrier would set the supersaturation limit beyond which carbon could

not decrease. At that point, the droplet sank back into the dense slag as observed by X-ray fluoroscopy. Gaye & Riboud<sup>[7]</sup> studied the decarburization and dephosphorization with much higher basicity slag ( $V$ -ratio of 9.6) than used in the current work at 1550°C. The end point carbon concentration was reported to be between 0.3 to 0.5 wt% over a range of oxidizing slag ( $N_O/N_{Fe}$  from 1.43 to 1.17) whereas Min & Fruehan<sup>[8]</sup> and Molloseau & Fruehan<sup>[10]</sup> reported a much higher end point carbon concentration. In Min & Fruehan's studies, the end point carbon concentration varied between 3.5wt% to 2 wt% as the slag FeO concentration was changed from from 3.2 wt% to 15.2 wt% with  $V$ -ratio of 1 at 1400°C. Molloseau & Fruehan conducted studies with slag of  $V$ -ratio 1.2, and reported end point carbon concentration was 2.65 wt% to 1.65 wt% for slag FeO concentration from 3 to 30 wt% at 1440°C. It appears that for higher basicity slags in the current work and in the published literature decarburization stops at a point consistent with the calculated supersaturation limit for nucleation of CO bubbles. Whereas for lower basicity slags the reaction stops at much higher carbon concentrations.

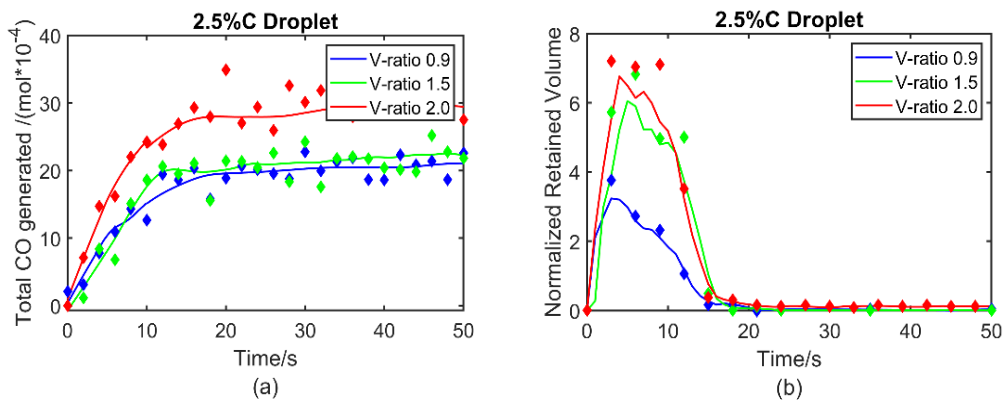


Figure 3.4: Total CO generation with time (a) and normalized retained volume profile with time (b) on varying Slag V-ratio

### 3.4. Discussion

#### 3.4.1. Decarburization of Droplets; Effect of Carbon Concentrations and Droplet Mass

Decarburization data for droplets with different carbon concentrations, presented in Fig 3.2, show that the rate of decarburization goes through a short incubation period followed by a peak, steady-state decarburization period and a subsequent slow decarburization period i.e the end stage of decarburization. In this section a qualitative discussion is conducted of the underlying mechanism during the incubation period along with a quantitative discussion of the peak decarburization period. Additionally, few interesting observations will be discussed for the final stage. To assist in discussion of the mechanism a theoretical framework is proposed in the following section.

*Theoretical Framework:*

A mixed controlled kinetic model is developed in this section to describe the steady state period during which the rate is fastest. At steady state, the rate of generation of CO would likely be controlled by oxygen transport in the slag, interfacial chemical reaction, internal nucleation of CO, internal growth of CO bubbles or a combination of the four. If the rate of CO generation is controlled by oxygen transport in the slag, then the rate of CO generation(mol/s) is represented by Equation 3.2 where oxygen transport is considered phenomenologically as the transport of FeO.

$$\frac{dn_{CO}}{dt} \propto A_{s-m}(t)k_s(\Delta C_{FeO}) \dots \dots [3.2]$$

$k_s$  is the mass transfer coefficient,  $A_{s-m}(t)$  instantaneous slag-metal surface area, and  $(\Delta C_{FeO})$  is the difference between interface and bulk concentration of FeO in the slag. In this work, the maximum change in FeO concentration in the slag was ~ 2%, so the changes in slag mass transfer coefficient due to variation in composition was ignored. If the rate of CO generation(mol/s) at steady state is controlled by transfer of oxygen by interfacial chemical reaction, then

$$\frac{dn_{CO}}{dt} \propto A_{s-m}(t) * (1 - \theta_s) * \vec{k} \left( a_{FeO}^i - \frac{a_O^i}{K_{FeO_{eq}}} \right) \dots \dots [3.3]$$

Where  $\vec{k}$  is the forward reaction rate constant,  $\theta_s$  is the fraction of site blocked by surface active species sulfur,  $a_{FeO}^i$  and  $a_O^i$  are the activities of reactant, FeO, and product, dissolved oxygen, respectively.

When the rate of CO generation(mol/s) is controlled by internal nucleation<sup>[11][47]</sup> of CO bubbles within droplet, then

$$\begin{aligned}
 \left(\frac{dn_{CO}}{dt}\right)_{nuc} &\propto J * \left(\frac{n_e}{N_A}\right) * V_m \approx N_0 \left(\frac{3\sigma}{\pi m}\right)^{\frac{1}{2}} \exp\left(-\frac{\Delta G_{crit}}{k_B T}\right) * \left(\frac{n_e}{N_A}\right) * V_m \\
 &\approx \frac{W_m[\%O]}{100M_o V_m} N_A \left(\frac{3\sigma}{\pi m}\right)^{\frac{1}{2}} \exp\left(-\frac{\Delta G_{crit}}{k_B T}\right) * \left(\frac{n_e}{N_A}\right) * V_m \\
 &\approx \frac{[\%O]}{100M_o} \left(\frac{3\sigma}{\pi m}\right)^{\frac{1}{2}} \exp\left(-\frac{\Delta G_{crit}}{k_B T}\right) * n_e * W_m \\
 &\approx \frac{[\%O]}{100M_o} \frac{\rho_m}{\rho_o} \left(\frac{3\sigma}{\pi m}\right)^{\frac{1}{2}} \exp\left(-\frac{\Delta G_{crit}}{k_B T}\right) * n_e * V_m \dots \dots [3.4]
 \end{aligned}$$

Where  $J$  is the rate of nucleation per unit volume,  $n_e$  is the no of molecules in an embryo,  $N_A$  is the Avogadro's number and  $V_m$  is the volume of the metal droplet.  $N_0$  is the number concentration of CO embryos in the liquid,  $\Delta G_{crit}$  critical free energy barrier for CO nucleation,  $\Delta H$  is the heat of formation of CO molecule,  $m$  is the mass of one molecule of CO,  $\sigma$  is the surface tension of liquid metal,  $W_m$  is the mass of the metal droplet,  $V_m$  is the volume of metal,  $[\%O]$  is the bulk oxygen concentration in metal,  $M_o$  is the molar mass of [O],  $k_B$  is the Boltzman constant and  $T$  is the temperature of the system. The CO bubbles are observed to form inside the metal droplet, this introduces intensive stirring, hence, carbon and oxygen transport within the liquid metal droplet are not likely rate determining steps during bloating. Growth of bubbles may also contribute to CO generation in which case Equation 3.5 for chemical reaction at the gas/metal interface may describe the CO

generation rate(mol/s) or more likely a combination of Equations 3.4 and 3.5 will describe the rate.

$$\left(\frac{dn_{CO}}{dt}\right)_{growth} = k_{gr}A_{g-m}(t)a_C a_O = k_{gr}A_{g-m}(t)f_C f_O [\%C][\%O] \dots [3.5]$$

Where  $k_{gr}$  is the growth rate constant,  $A_{g-m}(t)$  is the total gas/metal surface area within the metal droplet at time instant  $t$ ,  $f_C$  and  $f_O$  are the Henrian activity coefficient of carbon and oxygen with respect to 1 wt% Henrian standard state,  $[\%C]$  is the wt% of bulk carbon concentration. The total gas/metal surface area ( $A_{g-m}(t)$ ) at any time instant within the metal droplet is a function of rate of nucleation and rate of escape of gas bubbles.

The rate of change of carbon concentration in metal droplets can be calculated from the rate of CO generation as

$$\frac{d[\%C]}{dt} = -\frac{100 M_C}{\rho_m V_m} \frac{dn_{CO}}{dt} \dots \dots [3.6]$$

The carbon concentration at any time can be evaluated as

$$[\%C] = [\%C]^0 - n_{CO}(t) * \frac{100M_C}{W_m} \dots \dots [3.7]$$

Where  $[\%C]^0$  is the starting carbon concentration,  $n_{CO}(t)$  is the total of CO generated in moles after  $t$  s. In this analysis, the total CO generation profiles will be investigated with respect to  $A(t)$  and  $V_m$  to qualitatively understand the combination of reaction steps responsible for rate control in the decarburization process. To represent the overall system, a circuit analogy is presented in Figure 3.5 in terms of several resistances.



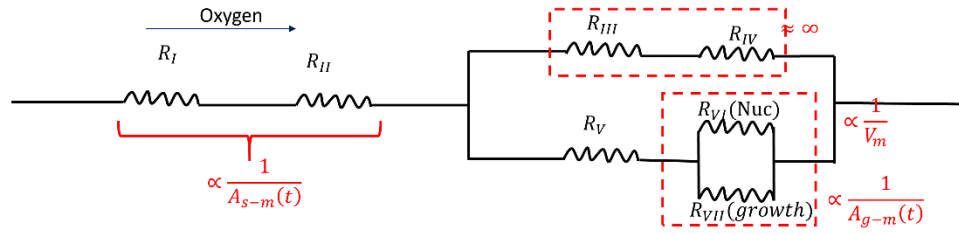


Figure 3.5: Circuit analogy of the decarburization system

$R_I$  is the resistance to transport of oxygen in the slag from the bulk to slag/metal interface,  $R_{II}$  is the resistance to dissociation at the slag/metal interface,  $R_{III}$  and  $R_{IV}$  combine to give the resistance to CO generation at the slag metal interface i.e. external decarburization.  $R_{III}$  represents the resistance to CO formation and  $R_{IV}$  is the resistance to transport of carbon in the metal phase.  $R_V$  is resistance to transport oxygen in metal phase,  $R_{VI}$  is the resistance to nucleation of CO bubbles within the metal droplet and  $R_{VII}$  is the resistance to growth of these bubbles. The overall resistance can be expressed as

$$R_{Ov} = R_I + R_{II} + \frac{1}{\left(\frac{1}{R_{III} + R_{IV}}\right) + \left(\frac{1}{R_V + \left(\frac{1}{R_{VI}} + \frac{1}{R_{VII}}\right)^{-1}}\right)} \dots [3.8]$$

The decarburization results presented earlier show that the decarburization is mostly internal during the peak decarburization period. The resistance from external decarburization can be ignored at this period of decarburization. It is also to be noted that due to stirring introduced by CO bubbles within droplet, there is negligible resistance of transport in the metal during this period. With an assumption that at steady state, decarburization will only be by internal decarburization, the analogous circuit simplifies to

that presented in (Figure 3.6) and the overall resistance can be expressed as in Equation

(3.9)

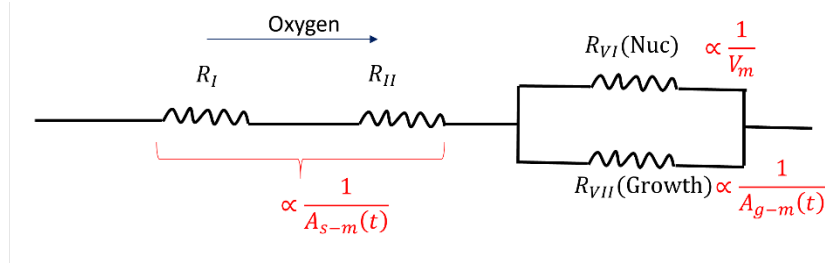


Figure 3.6: Simplified circuit of decarburizing droplets

$$R_{ov} = R_I + R_{II} + \left( \frac{1}{R_{VI}} + \frac{1}{R_{VII}} \right)^{-1} \dots [3.9]$$

These resistances are  $R_I \propto \frac{1}{k_s A(t)}$ ,  $R_{II} \propto \frac{1}{\vec{k}(1-\theta_s)A(t)}$ ,  $R_{VI} \propto \frac{1}{V_m}$  and  $R_{VII} \propto \frac{1}{A_{g-m}(t)}$ . After few rearrangements, combining the Equations 3.2,3.3, 3.4, and 3.5, the overall rate constant(mol/s) for liquid metal droplet reacting in oxidizing slag can be expressed as

$$\begin{aligned} & \frac{1}{k_o} \\ &= \frac{100M_{FeO}}{k_s \rho_s A_{s-m}(t)} + \frac{100M_{FeO}}{M_s \gamma_{FeO} \vec{k}(1-\theta_i) A_{s-m}(t)} \\ &+ \frac{1}{\left( \frac{\rho_m M_s \gamma_{FeO} K_{FeO}}{10^4 M_O M_{FeO} f_o} * \left( \frac{3\sigma}{\pi m} \right)^{\frac{1}{2}} * n_e \exp\left(-\frac{\Delta G_{crit}}{k_B T}\right) * V_m + \frac{M_s \gamma_{FeO} K_{FeO}}{100 M_{FeO}} k_{gr} f_C [\%C]^b * A_{g-m}(t) \right)} \dots [3.10] \end{aligned}$$

$$\frac{1}{k_o} = \frac{1}{K_a A_{s-m}(t)} + \frac{1}{K_b^{nuc} V_m + K_b^{gr} A_{g-m}(t)} \dots [3.11]$$

The rate constants  $K_a$ ,  $K_b^{nuc}$  and  $K_b^{gr}$ , for a specific slag and metal chemistry are

$$K_a = \frac{1}{100M_{FeO}} \left( \frac{1}{k_s \rho_s} + \frac{1}{M_S \gamma_{FeO} \vec{k} (1 - \theta_i)} \right)^{-1} \approx 0.14 * \left( \frac{3.45 * 10^4}{k_s} + \frac{4.63}{\vec{k}} \right)^{-1} .. [3.12]$$

$$K_b^{nuc} = \frac{\gamma_{FeO} K_{FeO} M_S \rho_m}{10^4 M_O M_{FeO} f_O} \left( \frac{3\sigma}{\pi m} \right)^{\frac{1}{2}} n_e \exp \left( -\frac{\Delta G^{crit}}{k_B T} \right)$$

$$\approx 71.27 * 10^{11} * n_e \exp \left( -\frac{\Delta G^{crit}}{k_B T} \right) .. [3.13]$$

$$K_b^{gr} = \frac{M_S \gamma_{FeO} K_{FeO}}{100 M_{FeO}} k_{gr} f_C [\%C]^b \approx 0.013 * k_{gr} [\%C]^b .. [3.14]$$

Here the activity coefficient of FeO ( $\gamma_{FeO}$ ) in the slag was calculated for this specific slag composition using the correlation proposed by Basu *et al.*<sup>[48]</sup>, the density of metal ( $\rho_m$ ) was calculated from Jimbo & Cramb's correlation and the surface tension ( $\sigma$ ) was evaluated using Chung & Cramb<sup>[49]</sup> correlation.

At steady state under mixed controlled kinetic conditions, the overall rate equation can be stated as

$$\frac{dn_{CO}}{dt} = k_o (\%FeO)^{bulk}$$

$$= \frac{K_a A_{s-m}(t) \left( K_b^{nuc} V_m + K_b^{gr} A_{g-m}(t) \right)}{K_a A_{s-m}(t) + \left( K_b^{nuc} V_m + K_b^{gr} A_{g-m}(t) \right)} (\%FeO)^{bulk} \dots [3.15]$$

If one assumes that there is no contribution from growth (growth rate constant,  $K_b^{gr} = 0$ ) to simplify the analysis further, the overall rate constant and the rate equation simplifies as

$$\frac{1}{k_o} = \frac{1}{K_a A_{s-m}(t)} + \frac{1}{K_b^{nuc} V_m} \dots [3.16]$$

$$\frac{dn_{CO}}{dt} = k_o (\%FeO)^{bulk} = \frac{K_a A_{s-m}(t) * K_b^{nuc} V_m}{K_a A_{s-m}(t) + K_b^{nuc} V_m} (\%FeO)^{bulk} \dots [3.17]$$

It can be observed from this correlation, that under mixed controlled kinetic conditions, the rate would show a linear behavior with  $A_{s-m}(t)$  and nearly linear with  $V_m$  except at very small droplet sizes region and non-linear variation with area/volume ratio if the droplet mass is varied linearly. If the droplet size is varied in very small droplet size region, the variation of volume of metal would show a parabolic increase of FeO flux. The overall rate constant is analyzed qualitatively to understand the rate controlling steps in decarburization kinetics at different level of carbon concentration reacting in oxidizing slag.

The decarburization reaction kinetics of the three different stages are discussed in detail in the following section.

*I. Incubation Period:* The bloating profile along with the CO generation profile shows an elongated incubation period for droplets with 4.4 wt% C concentration whereas the incubation period is very short for droplets with lower carbon concentrations (2.5 wt%, 1.5 wt% and 0.5 wt%). During this period, mostly external decarburization occurs with very limited amount of internal decarburization where droplets retain their original size and shape. In a decarburizing droplet, there is a competition between two processes: 1/ transport of oxygen from the bulk slag to the slag/metal interface crossing that interface and transporting into the bulk metal, and 2/ the transport of carbon from bulk metal to the slag-metal interface. If the former is faster the oxygen will build up in the metal until the supersaturation pressure for CO nucleation is reached at which point carbon and oxygen will react to form CO bubbles. If the latter process is faster CO will nucleate at the

slag/metal interface. It is also possible under many conditions for both processes to proceed simultaneously. In that case where transport of oxygen to the slag/metal interface is slightly faster than transport of carbon in the metal, CO may form on the surface and excess oxygen may diffuse into the melt and eventually exceed the supersaturation pressure for internal CO nucleation. As the carbon at the surface becomes depleted CO nucleation at the slag metal interface may stop further increasing oxygen supply into the melt. The interplay between these effects has a strong influence on the incubation time for bloating. With increase in droplet initial carbon concentration, the transport of carbon towards slag metal interface becomes faster, whereas the oxygen transport rate in the slag remains the same. For high carbon droplets, there would be sufficient carbon supply to the slag-metal interface to support external decarburization for a longer period, thereby delaying the onset of bloating, by consuming oxygen which would have otherwise been transported into the bulk droplet. For lower carbon droplets, lower oxygen consumption at the slag-metal interface would enable higher oxygen flux into the droplet and thus a very short incubation period for bloating is observed.

II. *Steady State Decarburization Period:* To investigate the rate controlling step/s for decarburization of droplets with different carbon concentrations at steady state, the total CO generation profiles were divided by the time averaged slag/metal area ( $A_{avg}(t)$ ) and the volume of the metal ( $V_{metal}$ ) and presented in Fig 3.8 to 3.11 in order to understand the underlying mechanism for different droplet sizes. The importance of using time averaged area with this type of data was demonstrated by Rhamdhani *et al.* <sup>[50]</sup>. The time averaged area is calculated as

$$A_{avg}(t) = \frac{1}{t} \int_0^t A_{s-m}(t) dt \dots \dots [3.18]$$

Based on Equations 3.2 and 3.3 we can see that if the steady state rate of decarburization changes linearly with  $A_{s-m}(t)$ , then the reaction rate is likely to be controlled by either slag-metal interfacial reaction or transport in the slag whereas, if the rate is proportional to  $V_{metal}$  then internal nucleation of bubbles within the metal droplet is the most likely rate determining step as illustrated by Equation 3.4. As shown in Figures 3.7-3.10 the data does not offer a perfect fit when normalized with respect to either area or volume. This is consistent with the reaction being under mixed controlled kinetics.

It is not within the scope of the current work to develop and validate the type of numerical model required to describe the full complexity of the reaction mechanism. However, by developing a conceptual model capturing the essential details of the system, the following section will estimate the contribution of the rate control of each reaction step involved. This will be done by employing parameters from the literature obtained under reasonably comparable conditions to those used in the present work.

Considering mixed controlled kinetics, in the overall rate constant expression, the first two terms in Equation 3.10 mainly determine oxygen transport from bulk slag into the metal droplet whereas the third term corresponds to the rate of internal nucleation and growth of bubbles. The overall rate constant (simplified in Equation 3.16) increases with increase in slag-metal interfacial area ( $A_{s-m}(t)$ ) and metal droplet volume ( $V_m$ ). Due to bloating at steady state, there is a rise in instantaneous slag/metal area by between 50% and 200% in

the range of carbon concentration 0.5 wt% to 4.4 wt%. The volume of the metal is fixed for a given droplet.

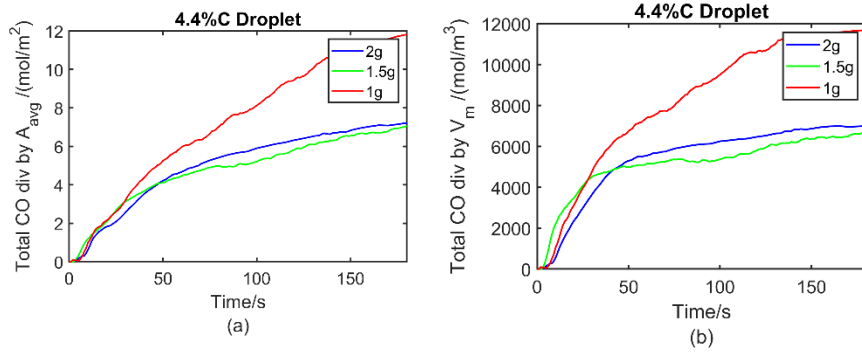


Figure 3.7:  $Total\ CO(t)/A_{avg}(t)$ ,  $Total\ CO(t)/V_{metal}$  variation with time for droplets with 4.4 wt% carbon in (a), (b) respectively

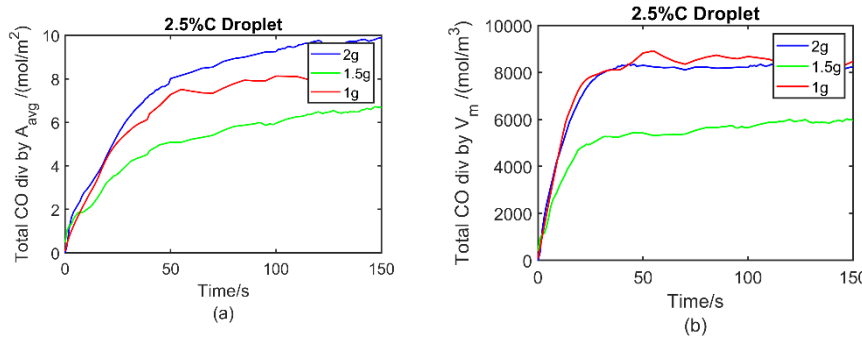


Figure 3.8:  $Total\ CO(t)/A_{avg}(t)$ ,  $Total\ CO(t)/V_{metal}$  variation with time for droplets with 2.5 wt% carbon in (a), (b) respectively

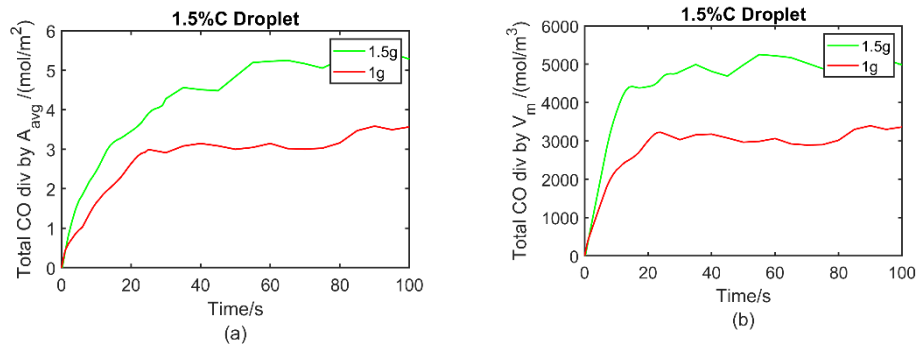


Figure 3.9: Total CO(t)/A<sub>avg</sub>(t), Total CO (t) /V<sub>metal</sub> variation with time at 1.5 wt% carbon level in (a), (b) respectively

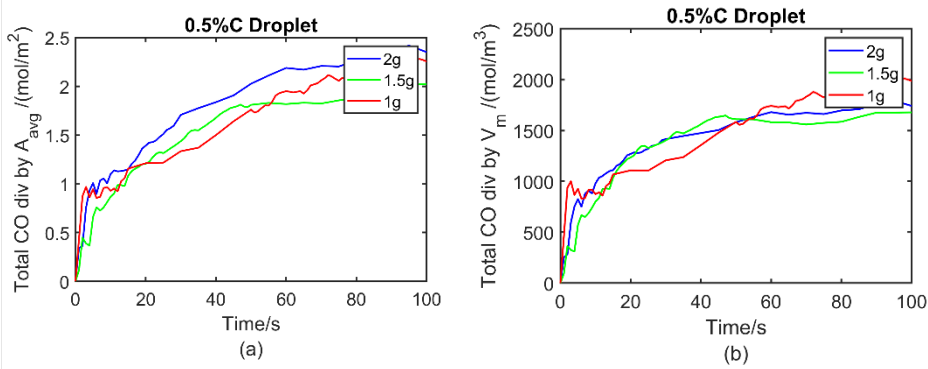


Figure 3.10: Total CO (t)/A<sub>avg</sub>(t), Total CO(t) /V<sub>metal</sub> variation with time at 0.5 wt% carbon level in (a), (b) respectively

An attempt has been made to validate the mechanism of decarburization during the steady state stage, based on the mixed controlled model described in Equation 3.16. The parameter  $K_a$  (mol  $\cdot$  m<sup>-2</sup>  $\cdot$  s<sup>-1</sup>) is constant for a fixed slag mass transfer coefficient and interfacial chemical reaction condition and should vary with temperature, slag composition and stirring conditions in the slag. It has been approximated as 0.02 mol  $\cdot$  m<sup>-2</sup>  $\cdot$  s<sup>-1</sup> using values for mass transfer coefficient in the slag ( $k_s$ ), the chemical reaction rate constant of



dissociation of FeO at the s/m interface ( $\vec{k}$ ) and the fraction of the surface poisoned by sulfur ( $\theta$ ). A literature value obtained under similar conditions to the present work, was used for mass transfer coefficient [8]. It is worth noting that previous work in authors' laboratory shows that there is a significant effect of void fraction on the slag mass transfer coefficient in foamy slag. However, the mass transfer coefficient determined experimentally under similar conditions already includes this effect. In selecting this value, the authors compared values from several workers studying decarburization of droplets in FeO based slag. The range of value was  $10^{-5}$  to  $10^{-4}$  m/s and the average value  $5 \cdot 10^{-5}$  was selected for this calculation.  $\theta$  was calculated using the Langmuir isotherm based on a well established value for the adsorption coefficient for sulfur<sup>[49]</sup> and the chemical reaction rate constant( $\vec{k}$ ) was taken from parallel work by the authors<sup>[51]</sup>.

$K_b^{nuc}$  (mol  $\cdot$  m<sup>-3</sup>  $\cdot$  s<sup>-1</sup>) may be calculated using Equation 3.13 and requires knowledge of the parameters  $\Delta G^{crit}$  and  $n_e$ . The variation of  $\Delta G^{crit}$  and  $n_e$  with the variation of carbon concentration has been estimated based on the approach suggested by Chen & Coley<sup>[11]</sup> employing a surface tension modifying parameter ( $\psi$ ) determined from the authors parallel work<sup>[51]</sup>. The calculated values of  $K_b^{nuc}$  are given in column 2 of Table 3.4.

The parameter  $K_b^{nuc}$  can also be determined from experimental data using Equation 3.16. The volume( $V_m$ ) is known from droplet mass and density<sup>[46]</sup>. The surface area  $A_{s-m}(t)$  of the droplet was determined using X-ray video images.  $k_o$  was determined from the peak reaction rate and the other parameters ( $K_a$ ) for equation 3.16 were determined as described

above. The values for  $K_b^{nuc}$  determined by this method are presented in column 3 of Table 3.4.

The values presented in Table 3.4, for the two different calculation methods follow a similar trend with the exception of the value for 4.4% C. The rate constant,  $K_b^{nuc}$  decreases with decreasing carbon concentration in the metal droplet for the range of 2.5 wt% to 0.5 wt% C and this is due to lowering of supersaturation pressure with decreasing carbon concentration, whereas for the case of 4.4 wt%, there may be significant contribution from external decarburization which wouldn't validate this calculation method. It should also be noted that the values calculated using the current experimental data are quite a bit higher than the predicted values. It seems likely that both discrepancies arise from the same source that the prediction is theoretically based whereas the calculation based on experimental data assumes that all CO production comes from nucleation. The latter assumption is clearly untrue but the authors were not able to distinguish between nucleation and growth.

Table 3.4: Comparison of  $K_b^{nuc}$  value calculated and found experimentally

| Wt% C | $K_b^{nuc}$ From Equation 3.13<br>(Calculated using nucleation parameters <sup>[51][11]</sup> ) | $K_b^{nuc}$<br>Experimental (Equation 3.16)<br>(Experimentally Determined peak rate) |
|-------|---|--|
| 4.4   | 96.22   | 43.36  |
| 2.5   | 71.28   | 101.14   |

|     |       |       |
|-----|-------|-------|
| 1.5 | 21.38 | 54.90 |
| 0.5 | 0.07  | 2.86  |

There are complex interrelations among the parameters and to fully explore the complex interacting effects in the mixed controlled decarburization of droplets, a detailed numerical modeling is required. The authors are currently working to develop this type of model.

At steady state, the metal droplet bloats due to a difference between gas generation and gas escape rate. The gas escape behavior depends on the interfacial tension, viscosity, average size of escaping bubbles, pressure within the bubbles [52,53] and the available surface area through which it escapes. The rate of bloating is observed to increase with increase in droplet initial carbon concentration due to increase in rate of generation of CO gas whereas no specific trend is observed with the variation of droplet mass.

III. *End Decarburization Period:* With the progress of reaction, decarburization slows down irrespective of end point carbon concentration eventually leading the droplet to sink into the dense slag due to lack of buoyancy. A comparison of the carbon concentration, before and after reaction, is presented in Table 3.5. It can be observed that decarburization for the case of 2 g droplet containing 4.4 wt%C ended when the remaining carbon concentration was 3.04 wt%. When experiments were conducted with 2.5 wt% C 2 g droplets, i.e. lower than 3.04 wt%, bloating occurred due to decarburization and suddenly shut down the reaction when the carbon reached 1.1 wt%. When this ‘decarburized’ droplet with 1.1 wt% C were reacted again in fresh slag of same composition as earlier (16 wt%

FeO and *V-ratio* 0.9), the decarburization started again and went through a peak decarburization period with bloating followed by cessation of the reaction at ~ 0.5 wt% carbon. Another experiment with a ‘fresh’ 2 g droplet with 0.5 wt% C also showed decarburization with bloating and finally the reaction stopped at 0.11 wt% carbon. However, for decarburizing droplets with fixed slag oxygen potential, the end point carbon concentration should be a fixed value (i.e. 0.3 wt%C from supersaturation limit and 0.05 wt%C from thermodynamic limit) which should not vary with droplet mass or droplet initial carbon concentration. It has been mentioned earlier that for low basicity slag, the decarburization stopped at much higher carbon concentration than that predicted from supersaturation limit or thermodynamic limit, and this was consistently observed for all initial carbon concentrations. One can conclude from this observation that the shutdown of decarburization is not due to lack of carbon or to insufficient FeO remaining in the slag. This leaves the authors to conclude that some mechanism is in play which prevents sufficient oxygen from coming into contact with sufficient carbon. The authors are currently not able to offer an explanation for this observation.

Table 3.5: Initial and final carbon content in droplet before and after the decarburization reaction with 16wt% FeO slag (*V-ratio* 0.9)

| <b>Droplet initial Mass</b> | <b>Initial wt% C</b> | <b>Final wt% C</b> |
|-----------------------------|----------------------|--------------------|
| 2                           | 4.4                  | 3.04               |
|                             | 2.5                  | 1.10               |
|                             | 0.5                  | 0.11               |

|   |     |       |
|---|-----|-------|
| 1 | 4.4 | 1.94  |
|   | 2.5 | 0.96  |
|   | 1.5 | 0.78  |
|   | 0.5 | 0.063 |

### 3.4.2. Decarburization of Droplets Reacting with Slag at Different FeO Concentrations

The decarburization along with the normalized volume profile for droplets with 2.5 wt% C of 2 g with a range of FeO (5 to 16 wt%) concentration does not show any incubation period before bloating whereas for 2.5 wt% FeO case, the droplet did not bloat at all. The transport of oxygen from bulk slag to slag/metal interface and then into the bulk metal droplet is fast enough compared to the transport of carbon from the bulk metal to the slag/metal interface, resulting early bloating for cases with 5, 10 and 16 wt% FeO concentration in the slag and for 2.5 wt% FeO case, the carbon transport towards slag/metal interface being faster consumes all the oxygen at the slag/metal interface.

The rate at the peak decarburization period is observed to increase due to increase in bulk slag oxygen potential with increase in slag FeO concentration. The bulk slag oxygen potential determines both the rate of transport of oxygen from bulk slag to slag/metal interface and the rate of oxygen dissolution at the slag/metal interface as illustrated in Equation 3.2 and 3.3. Under mixed controlled kinetics the rate of decarburization by internal or external nucleation or by both are in balance with the rate of transport of oxygen

in slag and the rate of the interfacial FeO dissociation reaction. In all of the cases, rate of decarburization is influenced by bulk slag oxygen potential. With decreasing slag oxygen potential, a threshold point is reached where all the oxygen is consumed at the slag/metal interface. In the current work the threshold is in the range 2.5 to 5 wt% FeO. This threshold will vary based on the temperature, slag basicity and conductivity as well as carbon concentration.

The decarburization has been observed to shut down at a much higher carbon concentration than that predicted by supersaturation limit or by thermodynamic limit presented in Figure 3.11(a), for over a range of slag FeO concentrations. The path of reaction either via internal decarburization or external decarburization or both doesn't improve the shutting down condition.

With increasing slag FeO concentration, the rate of bloating is found to increase, and this may be attributed to the higher rate of CO generation with higher oxygen potential slag. Between 10-16 wt% FeO in the slag, the rate of bloating does not increase appreciably.

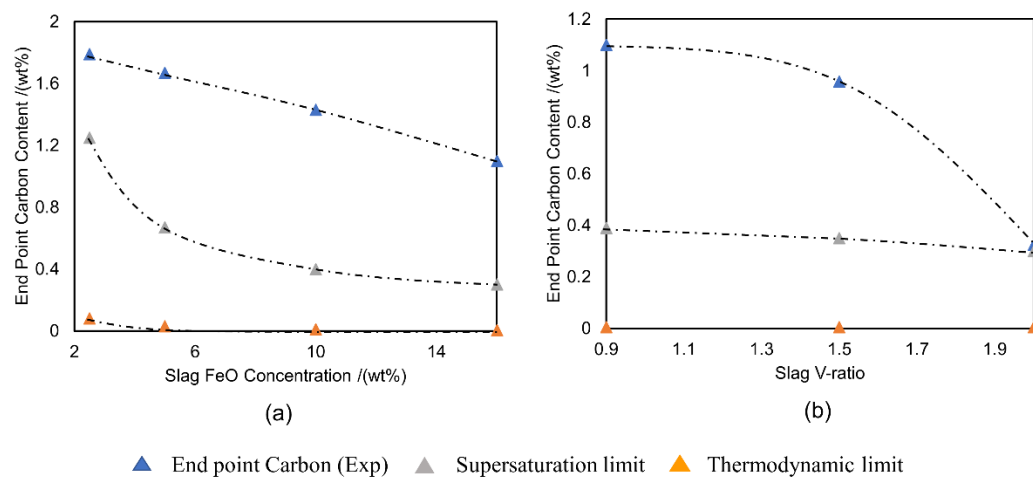


Figure 3.11: End point carbon concentration variation on varying slag FeO wt% and slag basicity ( $V\text{-ratio} = \text{CaO}/\text{SiO}_2$ ) in (a) and (b) respectively

### 3.4.3. Decarburization of Droplets Reacting with Slags of Different Basicity

The absence of an incubation period in the decarburization profile for 2 g droplets with 2.5 wt% C, over a range of slag  $V\text{-ratio}$ , can be attributed to faster transport of oxygen from the bulk slag into bulk the metal compared to carbon transport within the metal towards slag/metal interface.

The peak rate of decarburization has been observed to increase with increasing slag basicity (Figure 3.4). The increase in slag  $V\text{-ratio}$  lowers the slag viscosity leading to higher rates of transport of oxygen in the slag for the same total Fe. The overall rate constant in Equation 3.10 increases with increase in slag mass transfer coefficient ( $k_s$ ) with slag  $V\text{-ratio}$ , resulting in higher rate of CO generation.

The comparison of end-point carbon concentration in Figure 3.11(b) shows that with increasing slag basicity, the decarburization reaches close to the limiting carbon concentration as predicted from supersaturation limit, although this is far beyond the thermodynamic limit. The authors do not have a definitive explanation for this observation, but it appears that increasing the slag basicity, prevents the decarburization from shutting prematurely by facilitating sustained the oxygen transport. Ongoing work in the authors' laboratory seeks to provide a detailed explanation.

The rate of bloating was found to increase with increasing slag basicity which can be attributed to the higher rate of gas generation along with negligible variation in gas escape.

This analysis suggests that there are multiple factors working simultaneously to control the decarburization kinetics at different stages. Qualitative agreement with a mixed control kinetic model, which includes slag mass transport, interfacial chemical reaction and internal nucleation, is found at the steady state period.

Another important finding of this analysis is that the cessation of decarburization does not occur due to lack of carbon in metal or lack of FeO in the slag, but seems to be most likely caused by an interruption of oxygen supply to the metal droplet. In all the studied cases, decarburization stops earlier than can possibly be justified by either the thermodynamic equilibrium or by the nucleation barrier despite having sufficient reactants. In case of higher basicity, the decarburization gets close to the supersaturation limit suggesting that the cessation of decarburization cannot be related to conventional transport breaking down, because transport circumstances do not change significantly. It may be that the oxygen in



the slag is facing a barrier to transport at the slag/metal interface due to charge accumulation<sup>[9,36]</sup>. In this work, the authors are not able to present a definitive mechanism due to insufficient evidence. Currently, the authors are pursuing an experimental program to elucidate the mechanism by which decarburization of droplets is inhibited.

### **3.5. Conclusions**

1. The overall decarburization kinetics are under mixed control at steady state: including mass transport in slag, interfacial chemical reaction and either internal nucleation and growth of bubbles or external decarburization or both internal and external decarburization. The dominant rate determining step changes with slag and metal chemistry and reaction progress.
2. The transition from non-bloating to bloating is driven by increasing driving force for oxygen transfer into the bulk of the droplet. FeO concentration in the slag and at 10 wt% FeO concentration, highest rate of bloating has been observed.
3. The end point carbon concentration of decarburizing droplets occurs long before reaching equilibrium or the supersaturation limit of CO. This fact and the observed dependency on the slag FeO concentration and basicity suggests that the mechanism is related to oxygen transport. The authors have suggested that decarburization is inhibited by the build up of charge at the droplet/slag interface, blocking oxygen transfer to the droplet. Although there is no definitive proof for this mechanism it is supported by the fact that factors which mitigate this effect generally increase electrical conductivity of the slag.

## Acknowledgements

The authors wish to thank McMaster Steel Research Center and Natural Science and Engineering Research Council of Canada for funding this project.

## Conflict of Interest

On behalf of all authors, the corresponding author states that there is no conflict of interest.

## References

- 1 W.O. Philbrook and L.D. Kirkbride: *J. Met.*, 1956, vol. 8, pp. 351–6.
- 2 T.E. Dancy: *J. Iron Steel Inst.*, 1951, vol. 169, pp. 17–24.
- 3 R.S. Kaplan and W.O. Philbrook: *Metall. Trans.*, 1972, vol. 3, pp. 487–91.
- 4 P.G. Roddis: *J. Iron Steel Inst.*, 1973, vol. 211, pp. 53–8.
- 5 N.H. El Kaddah and D.G.C. Robertson: *J. Colloid Interface Sci.*, 1977, vol. 60, pp. 349–60.
- 6 N.H. El Kaddah and D.G.C. Robertson: *Metall. Mater. Trans. B*, 1988, vol. 19, pp. 831–7.
- 7 H. Gaye and Riboud.P.V: *Metall. Trans. B*, 1977, vol. 8, pp. 409–15.
- 8 D.J. Min and R.J. Fruehan: *Metall. Trans. B*, 1992, vol. 23, pp. 29–37.
- 9 G.G.K. Murthy, A. Hasham, and U.B. Pal: *Ironmak. Steelmak.*, 1993, vol. 20, pp.

- 191–200.
- 10 C.L. Molloseau and R.J. Fruehan: *Metall. Mater. Trans. B Process Metall. Mater. Process. Sci.*, 2002, vol. 33, pp. 335–44.
  - 11 E. Chen and K.S. Coley: *Ironmak. Steelmak.*, 2010, vol. 37, pp. 541–5.
  - 12 K. Gu, N. Dogan, and K.S. Coley: *Metall. Mater. Trans. B Process Metall. Mater. Process. Sci.*, 2017, vol. 48, pp. 2984–3001.
  - 13 B. Sarma, A.W. Cramb, and R.J. Fruehan: *Metall. Mater. Trans. B Process Metall. Mater. Process. Sci.*, 1996, vol. 27, pp. 717–30.
  - 14 Subagyo, G.A. Brooks, and K.S. Coley: *Can. Metall. Q.*, 2005, vol. 44, pp. 119–30.
  - 15 N. Dogan, G.A. Brooks, and M.A. Rhamdhani: *ISIJ Int.*, 2011, vol. 51, pp. 1093–101.
  - 16 R. Sarkar, P. Gupta, S. Basu, and B. Ballal, N: *Metall. Mater. Trans. B*, 2015, vol. 46B, pp. 961–76.
  - 17 D. Dering, C. Swartz, and N. Dogan: *Processes*, 2020, vol. 8, pp. 1–23.
  - 18 A. Kadrolkar and N. Dogan: *Metall. Mater. Trans. B Process Metall. Mater. Process. Sci.*, 2019, vol. 50, pp. 2912–29.
  - 19 E.W. Mulholland, G.S.F. Hazeldean, and M.. Davies: *J. Iron Steel Inst.*, 1973, vol. 211, pp. 632–9.

- 20 B.K. Rout, G. Brooks, M.A. Rhamdhani, Z. Li, F.N.H. Schrama, and A. Overbosch: *Metall. Mater. Trans. B*, 2018, vol. 49B, pp. 1022–33.
- 21 B. Deo, P. Ranjan, and A. Kumar: *Steel Res.*, 1987, vol. 58, pp. 427–31.
- 22 H. Sun: *ISIJ Int.*, 2006, vol. 46, pp. 1560–9.
- 23 H. Sun, K. Gao, V. Sahajwalla, K. Mori, and R.D. Pehlke: *ISIJ Int.*, 1999, vol. 39, pp. 1125–33.
- 24 K. ITO and K. SANO: *Tetsu-to-Hagane*, 1964, vol. 50, pp. 873–7.
- 25 K. ITO and K. SANO: *Tetsu-to-Hagane*, 1965, vol. 51, pp. 1252–9.
- 26 Y. NIIRI, K. ITO, and K. SANO: *Tetsu-to-Hagane*, 1969, vol. 55, pp. 437–45.
- 27 K. ITO, K. SANO, and S. ARINO: *Iron Steel Inst Japan-Trans*, 1969, vol. 9, pp. 465–71.
- 28 P.A.A. Distin, G.D.D. Hallett, and F.. D. Richardson: *J. Iron Steel Inst.*, 1968, vol. August, pp. 821–33.
- 29 L.A. Baker and R.G. Ward: *J. Iron Steel Inst*, 1967, vol. 205, pp. 714–7.
- 30 L.A. Baker, N.A. Warner, and A.E. Jenkins: *Trans. Metall. Soc.*, 1967, vol. 239, pp. 857–64.
- 31 M. Hayer and S.G. Whiteway: *Can. Metall. Q.*, 1973, vol. 12, pp. 35–44.
- 32 M. Sano, H.-Y. Tao, and M. Katoh: *Sixth Int. Iron Steel Congr.*, 1990, vol. 1, pp. 370–7.

- 33 D. Widlund, D.S. Sarma, and P.G. Jönsson: *ISIJ Int.*, 2006, vol. 46, pp. 1149–57.
- 34 J.B. SEE and N.A. Warner: *J. Iron Steel Inst.*, 1973, vol. 211, pp. 44–52.
- 35 S. Jahanshahi: Imperial College of Science and Technology, London, 1980.
- 36 G. Murthy, Krishna, G, Y. Sawada, and F. Elliot, J: *Ironmak. Steelmak.*, 1993, vol. 20, pp. 179–200.
- 37 G. Brooks, Y. Pan, and K.S. Coley: *Metall. Mater. Trans. B*, 2005, vol. 36B, pp. 525–35.
- 38 E. Chen and K.S. Coley: McMaster University, 2010.
- 39 D.E. Woolley and U.B. Pal: *Ironmak. Steelmak.*, 2002, vol. 29, pp. 125–32.
- 40 U.B. Pal, S.A. Macdonald, D.W. Woolley, and A.C. Powell: *Metall. Mater. Trans. B*, 2005, vol. 36B, pp. 209–18.
- 41 D.E. Woolley and U.B. Pal: *ISIJ Int.*, 1999, vol. 39, pp. 103–12.
- 42 M. Millman, A. Kapilashrami, M. Bramming, and D. Malmberg: *Impfos: Improving Phosphorus Refining*, 2011.
- 43 L. Holappa: *Scand. J. Metall.*, 2005, vol. 34, pp. 66–78.
- 44 C. Cicutti, M. Valdez, T. Perez, J. Petroni, A. Gomez, R. Donayo, and L. Ferro: in *6th International Conference on Molten Slags, Fluxes and Salts*, vol. 367, 2000.
- 45 J. Li and M. Barati: *Metall. Mater. Trans. B Process Metall. Mater. Process. Sci.*, 2009, vol. 40, pp. 17–24.

- 46 I. Jimbo and A.W. Cramb: *Metall. Trans. B*, 1993, vol. 24B, pp. 5–10.
- 47 M. Blander and J.L. Katz: *AIChE J.*, 1975, vol. 21, pp. 833–48.
- 48 S. Basu, A.K. Lahiri, and S. Seetharaman: *Metall. Mater. Trans. B Process Metall. Mater. Process. Sci.*, 2008, vol. 39, pp. 447–56.
- 49 Y. Chung and A.W. Cramb: *Metall. Mater. Trans. B*, 2000, vol. 31B, pp. 957–71.
- 50 M.A. Rhamdhani, K.S. Coley, and G.A. Brooks: *Metall. Mater. Trans. B*, 2005, vol. 36, pp. 219–27.
- 51 J. Biswas and K.S. Coley: *A Decarburisation Model for a Fe-C Droplet Reacting in Oxidizing Slag*, McMaster University, Unpublished Research, 2021.
- 52 A. Rozario, N.N. Viswanathan, and S. Basu: *Metall. Mater. Trans. B Process Metall. Mater. Process. Sci.*, 2019, vol. 50, pp. 10–5.
- 53 T.X. Zhu: *Bubble Escape Model*, Private Communication, Hamilton, 2018.

## **Chapter 4**

### **4. A Decarburization Model for a Fe-C Droplet Reacting in Oxidizing Slag**

Chapter 4 is a prepublication version of a manuscript published online on 25th August 2021 in Metallurgical and Materials Transaction B, DOI <https://doi.org/10.1007/s11663-021-02303-6>.

This chapter describes the development of a mathematical model for bloating of droplets in slag, demonstrating applicability for a wide range of conditions. The model offers an excellent prediction of experimental results; however, it breaks down in the later stages of decarburization. Factors contributing to this observation are discussed, establishing the need for further experimental study relating to the effect of slag conductivity on decarburization and premature shutdown.

The development of the model, coding, validation, and preliminary analysis against experimental data were performed by me. Part of the experimental data for validation was provided by Dr. Kezhuan Gu and had already been published. The manuscript was originally prepared by me. An extensive discussion was conducted with Dr. Kenneth Coley during the development of the model and analysis of the results. Proofreading was done by Dr. Coley.

### **Abstract**

A decarburization model has been developed for a Fe-C-S liquid droplet reacting in an oxidizing slag at high temperature (1580 to 1640°C). The model incorporates the partitioning of oxygen at the slag/metal interface between decarburization at the slag/metal interface and transport into the droplet. The kinetics of nucleation and growth of CO bubbles within the liquid metal droplet have also been introduced to describe internal decarburization. The model parameters were determined using one set of experimental conditions and then used to predict behavior over a wide range of conditions. The prediction was validated for variation of, sulfur concentration, droplet mass, temperature, and droplet carbon concentration. Decarburization was found to proceed in three stages. The model was found to show good agreement for the initial two stages of decarburization: the incubation period and peak decarburization period. This observation suggested that the oxygen partitioning and nucleation kinetics had been incorporated properly. The model failed to predict the sudden shutdown of decarburization at the end stage of decarburization.

#### **4.1. Introduction**

Throughout the last several decades, there has been a substantial body of research performed by several groups of researchers to understand the underlying phenomena behind the decarburization of metal droplets under steelmaking conditions. These phenomena in the Basic Oxygen Furnace (BOF) control four important factors of droplet refining reactions in the slag/metal/gas emulsion<sup>[1-18]</sup>

1. Residence time of droplets in emulsion



2. Area for refining reactions
3. Dynamic oxygen potential at the slag/droplet interface
4. Mass transfer in the droplets due to stirring by bubbles

Many experiments have been performed on the decarburization of droplets<sup>[1,14,15,19]</sup>. Some authors have observed a gas halo forming around the droplet<sup>[15]</sup> whereas others have found the droplet to swell because of CO nucleation inside the droplet<sup>[1,14,19]</sup>. This latter effect is the basis of the ‘bloated droplet’ concept<sup>[20]</sup> which is finding much use in models of BOF refining<sup>[21–23]</sup>. For this reason, it is important to understand the mechanism of internal nucleation of CO. The current work is focused on developing a mechanistically based model for decarburization of bloated droplets. Figure 4.1 presents the presence of a liquid metal droplet in emulsion which is bloated while refining and the authors are aiming to developing a decarburization model which can predict this bloating trajectory of metal droplet in oxidizing slag.

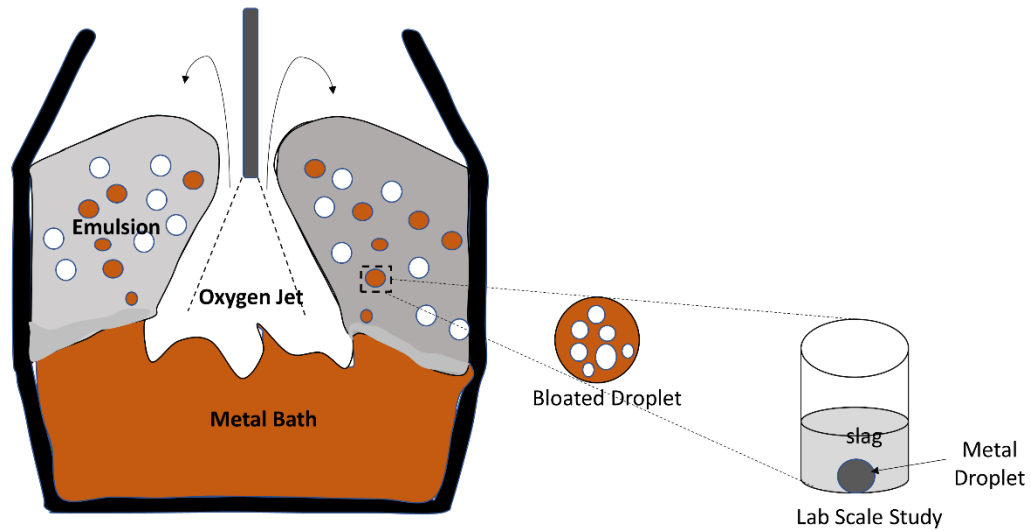


Figure 4.1: A 'Bloated Droplet' reacting in the emulsion in Basic Oxygen Furnace

To understand the nucleation mechanism of CO bubbles within liquid metal during decarburization, levitated droplet experiments<sup>[2,12,17]</sup>, have been performed at different starting carbon compositions and different temperatures. Baker & Ward<sup>[12]</sup> proposed that the rate of decarburization in oxidizing gas for metal droplets with high carbon concentration is controlled by gas film diffusion and for droplets with low carbon concentration, diffusion of carbon within the metal phase controls the reaction kinetics. These workers proposed that the explosion of droplets during decarburization was due to homogeneous nucleation of CO bubbles beneath the surface of the metal. Kaplan and Philbrook<sup>[17]</sup> proposed nucleation of CO bubbles at the iron-iron oxide interface as the cause of boiling. Although theoretical calculation showed that this mechanism is favorable compared to homogeneous nucleation, it does not result in internal CO bubble nucleation. Levine<sup>[24]</sup> proposed an idea of chemisorption of oxygen ions which he deemed was required

to reduce the reversible work for bubble nucleation. The main drawback of this hypothesis is that the effect of oxide ions should already be accounted for in the measured surface tension, so in this way the effect is being double counted. Min and Fruehan<sup>[15]</sup> performed experimental studies to understand the process by observing droplets using X-ray fluoroscopy. Based on their investigation of decarburization behavior by varying the carbon and sulfur concentration of the droplets, they proposed a mixed controlled kinetic model for decarburization including mass transport in the slag, mass transport through a gas halo and chemical reaction at the slag/gas and gas/metal interface. Later, Molloseau and Fruehan<sup>[19]</sup> conducted a study of decarburization for a wide range of FeO concentration in the slag and they proposed the phenomena of swelling and emulsification for metal droplet reacting in slag with more than 10% FeO. They proposed the transport of FeO in the slag to be controlling the rate of decarburization of an emulsified droplet. They noticed the effect of sulfur concentration on the decarburization rate and observed the rate of decarburization to go through a maximum at about 0.011% S.

There have been several<sup>[21-23,25-29]</sup> approaches to model the decarburization process in the emulsion phase in the steelmaking process. Knoop *et al.*<sup>[29]</sup> developed a slag droplet model based on multicomponent mixed transport assuming equilibrium at the slag/droplet interface and that all the decarburization reactions occur at the slag/metal interface. Sun<sup>[25]</sup> developed a model of decarburization of a single droplet in FeO bearing slag, employing thermodynamics as well as kinetics. Sun's model considered diffusion in metal and slag as well as interfacial reactions but assumed no barrier to nucleation of bubbles within the droplet. Dogan *et al.*<sup>[21]</sup> developed a decarburization model based on the first order reaction

kinetics as proposed by Brooks *et al.*<sup>[20]</sup> to predict the refining kinetics in the emulsion zone. Later, Rout *et al.*<sup>[23]</sup> further developed the model of Dogan *et al.* incorporating the effect of blocking of reaction sites by SiO<sub>2</sub> and P<sub>2</sub>O<sub>5</sub> which are generated during refining in the emulsion. Pomeroy<sup>[27]</sup> developed a CO nucleation model by including the partitioning of oxygen between external and internal decarburization and also incorporated the poisoning of the surface by sulfur to predict the elongated incubation period with higher sulfur concentration droplets. Recently, Kadrolkar & Dogan<sup>[22]</sup> adopted the approach of Pomeroy and implemented a single droplet decarburization model as part of a “global” BOF model to predict the refining kinetics in the emulsion. Although Pomeroy’s model was able to predict the delay in nucleation due to the presence of poisoning elements, Kadrolkar’s model did not fully capture the poisoning effect. In earlier studies in the authors’ laboratory, the droplet swelling behavior<sup>[1]</sup> due to internal nucleation of CO bubbles and the effect of sulfur on the peak rate of decarburization<sup>[18]</sup> were investigated. The steady state rate of decarburization has been found to follow an increasing and decreasing trend with increasing sulfur concentration in the metal. To predict the bloating behavior of a single droplet accurately, it is important to capture the partitioning of oxygen at the slag/metal interface along with the external and internal decarburization kinetics. It also may be important to consider the contribution of both nucleation and growth to internal CO formation.

In the current work, a decarburization model will be developed building on previous work<sup>[1,22,27,30]</sup>, focusing on external and internal decarburization and the competition between these two mechanisms. The kinetics of internal formation of CO will include

nucleation combined with chemical reaction-controlled growth of bubbles. This last contribution is absent from previous models. The model will also incorporate FeO depletion in the foamy slag based on previous experimental studies in authors' laboratory. This particular step is less important in industrial scale modelling but allows the authors to eliminate artifacts of small-scale laboratory experiments which would otherwise complicate the interpretation of results. The model will attempt to capture the poisoning effect of sulfur in decarburization kinetics not only to predict the delay in internal nucleation, but also to predict the variation in the rate of decarburization during the incubation period, peak (or steady state) period and the end point of reaction. The present work will develop the model parameters used in the modelling based on a single data set and seek to validate the model with 10 additional sets of experimental data. A sensitivity analysis will be conducted to determine the relative precision to which each parameter must be known and the relative importance of each reaction step in controlling the rate of the decarburization process.

## **4.2. Model Formulation**

The decarburization behavior of a liquid Fe-C droplet in an oxidizing slag has been discussed earlier by several groups of researchers<sup>[1,11,15,18,19]</sup>. The present model has been formulated based on these following sequences of events.

1. Transport of FeO from slag to the slag-metal interface
2. Dissociation of FeO into Fe and  $\underline{O}$  at the slag-metal interface
3. External decarburization via formation of CO bubbles at the slag-metal interface

4. Transport of some fraction of the oxygen into the metal from slag-metal interface
5. Internal nucleation of CO bubbles based on level of supersaturation
6. Growth of these individual bubbles within the droplet
7. Escape of bubbles from the droplet based on build up volume of CO
8. Slag foam formation above a dense slag layer in the crucible
9. Floating of droplets within the foamy slag
10. Decrease in decarburization rate
11. Sinking of droplet into the dense slag
12. Collapse of foam
13. And prediction of reactivation, of the decarburization process when the droplet contacts the high FeO dense slag

A schematic of the sequence of events as mentioned previously is presented in Figure 4.2 along with the model workflow in Figure 4.3. A detailed description of each of the modules has been presented later.

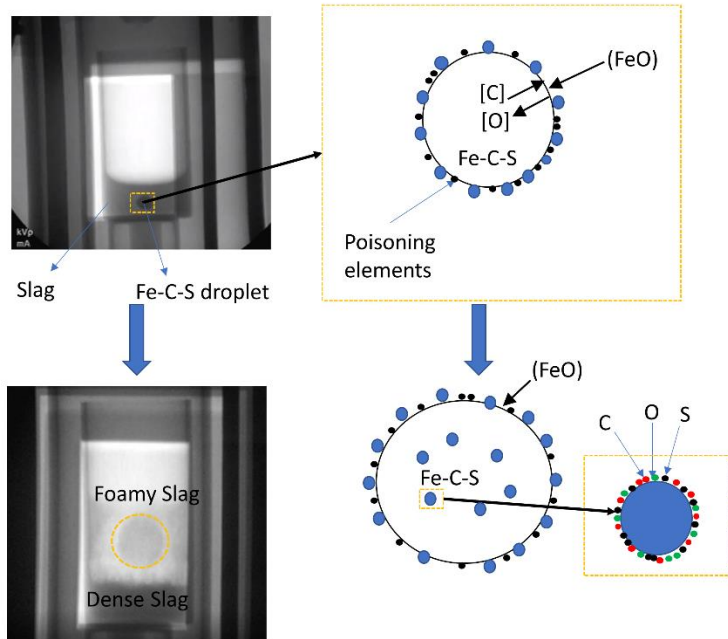


Figure 4.2: Schematic of sequence of events happening when a droplet enters into oxidising slag.

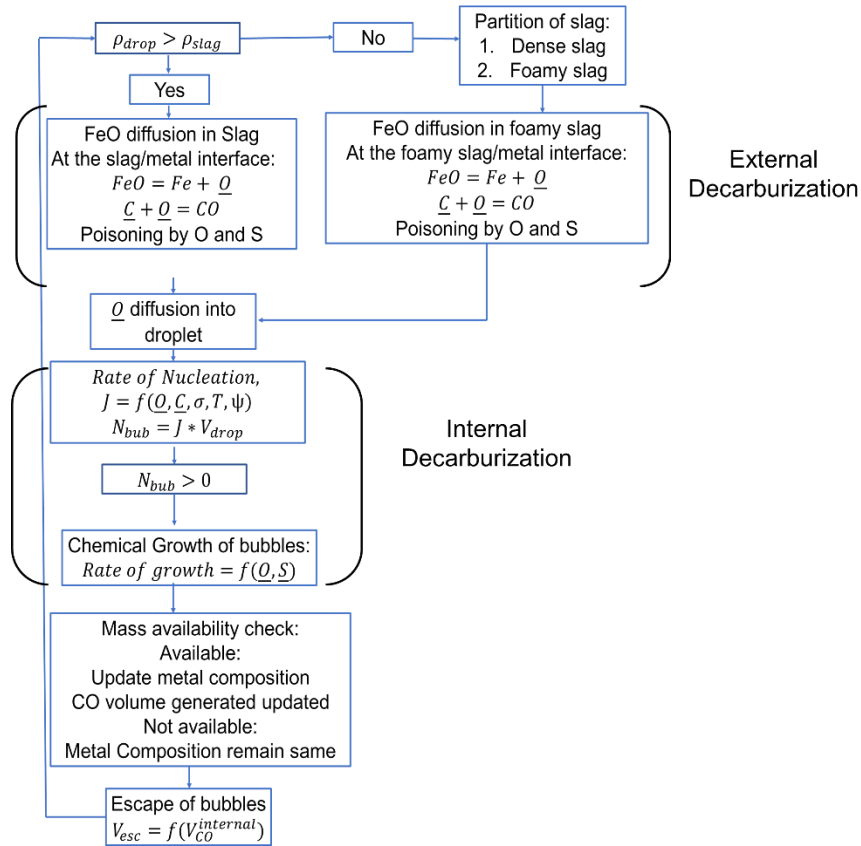
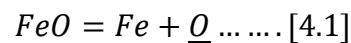


Figure 4.3: Schematic of the workflow of decarburisation model

#### 4.2.1. External decarburization

The slag, containing FeO, acts as a source of oxygen for decarburization of droplets in the steelmaking process. The FeO in the slag is transported from the bulk to the slag/metal interface and then dissociates into Fe and dissolved oxygen([O]) at the interface. Please note FeO does not transport in slag as molecules of FeO but many authors have found a phenomenological treatment assuming transport as FeO works very well. It would be fair to argue that this practice is the norm when defining oxygen transport in iron bearing slags.





A fraction of the oxygen transported to the interface is consumed at the interface, by reaction with available carbon. The remaining fraction is transported into the bulk metal phase and, when it reaches sufficient concentration, it will react with carbon to form CO bubbles inside the droplet. The approach of Pomeroy<sup>[27]</sup> in modeling the external decarburization has been adapted here. The model considers poisoning of the reaction at the slag/metal interface by sulfur. The rate of FeO dissociation and the external decarburization reaction are both influenced by this poisoning effect. The FeO dissociation reaction at the slag metal interface which may control the supply of oxygen to the steel is described by Equation 4.2.

$$R_{FeO} = \vec{k}A_{s/m}(1 - \theta_j) \left( a_{FeO}^i - \frac{a_O^i}{K_{FeO_{eq}}} \right) \dots \dots \dots [4.2]$$

where  $\theta_j$  is the fraction of surface area blocked due to sulfur poisoning,  $\vec{k}$  is the forward rate constant of the dissociation reaction,  $a_{FeO}^i$  is the activity of FeO at the interface,  $a_O^i$  is the activity of the oxygen at the interface and  $A_{s/m}$  is the surface area of the slag metal interface. The  $\theta_j$  parameter is governed by the Langmuir isotherm<sup>[31]</sup> described in Equation 4.3

$$\theta_j = \frac{\sum K_j a_j}{1 + \sum K_j a_j} \dots \dots \dots [4.3]$$

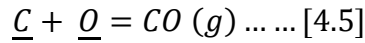
where  $K_j$  is the adsorption coefficient for species  $j$  and  $a_j$  is the activity of species  $j$  in this case the only surface active species considered is sulfur ([S]).

The rate equation for transport of FeO to the slag/metal interface from the bulk of the slag can be expressed as

$$J_{FeO} = \frac{A_{s/m} * k_s * \rho_s}{100 * M_{FeO}} ((\%FeO)^i - (\%FeO)^b) \dots \dots [4.4]$$

where  $k_s$  is the mass transfer coefficient in the slag phase,  $\rho_s$  is the density of slag,  $M_{FeO}$  is the molecular weight of FeO,  $(\%FeO)^i$  is the slag-metal interface FeO concentration and  $(\%FeO)^b$  is the bulk slag FeO concentration in weight percentage.

At the slag metal interface, the decarburisation reaction can occur as



The rate of this reaction is determined by the following rate equation

$$R_{CO} = (1 - \theta_j) * \frac{A_s}{m} * \frac{k_r}{100 * M_C} \left( a_O^i a_C^i - \frac{P_{CO}^i}{K_{CO}} \right) \dots \dots \dots [4.6]$$

where  $k_r$  is the forward reaction rate constant for the decarburisation reaction,  $a_O^i$  and  $a_C^i$  are the activities of oxygen and carbon at the interface,  $P_{CO}^i$  is the CO pressure at the interface and  $K_{CO}$  is the equilibrium constant for the above-mentioned decarburization reaction. The interface CO pressure has been assumed to be same as that of the atmospheric pressure in this model calculation.

Transport of carbon and oxygen within the bulk droplet can be calculated<sup>[25]</sup> from

$$J_C = \frac{A_{s/m} * \rho_m}{100 * M_C} * k_m * ([\%C]^b - [\%C]^i) \dots \dots \dots [4.7]$$

$$J_O = \frac{A_{s/m} * \rho_m}{100 * M_O} * k_m * ([\%O]^b - [\%O]^i) \dots \dots \dots [4.8]$$

With the exception of a thin boundary layer at the surface, the model assumes that there would be no compositional gradient within the metal droplet due to vigorous stirring caused

by the internally nucleated bubbles. The overall molar balance for oxygen and carbon at the slag/metal interface would be

$$J_{FeO} = R_{FeO} \dots [4.9]$$

$$J_C = R_{CO} \dots [4.10]$$

$$J_{FeO} = J_O - J_C \dots [4.11]$$

No assumption is made about equilibrium at the slag metal interface. Where rate of reaction as defined in Equations 4.6 is very fast relative to the transport rates defined by Equations 4.4, 4.7 and 4.8, this rate equation collapses to represent the condition of local equilibrium at the interface. Therefore, these equations are used to determine the fluxes and concentration on either side of the slag metal interface. The rate of external decarburization will be determined by the balance between the rate of transport of FeO in the slag, the rate of chemical reaction at the slag/metal interface and the rate of supply of carbon from the bulk to the slag/metal interface. The remaining oxygen from the interfacial chemical reactions will be transported from the slag metal interface into the bulk metal.

The interfacial concentration of CaO, SiO<sub>2</sub> and Al<sub>2</sub>O<sub>3</sub> have been assumed to be same as that of the bulk slag composition. The activity of FeO can be estimated as

$$a_{FeO}^i = \gamma_{FeO}^b * X_{FeO}^i \dots [4.12]$$

where  $\gamma_{FeO}^b$  is the activity coefficient of FeO of the bulk slag concentration using the correlation developed by Basu *et al.* [32].

$$\log(\gamma_{FeO}^b) = \frac{1262}{T} - 1.1302 * X_{FeO}^b + 0.96 * X_{SiO_2}^b + 0.123 * X_{CaO}^b - 0.4198 \dots [4.13]$$

and  $X_{FeO}^i$  is the mole fraction of FeO for the interface slag concentration. This interface mole fraction of FeO has been calculated as

$$X_{FeO}^i = \frac{\frac{(\%FeO)^i}{M_{FeO}}}{\frac{(\%FeO)^i}{M_{FeO}} + \frac{(\%CaO)^b}{M_{CaO}} + \frac{(\%SiO_2)^b}{M_{SiO_2}} + \frac{(\%Al_2O_3)^b}{M_{Al_2O_3}}} \dots \dots [4.14]$$

For the activity of metal components

$$a_C^i = f_C^i * [\%C]^i \dots \dots [4.15]$$

$$a_O^i = f_O^i * [\%O]^i \dots \dots [4.16]$$

where  $f_C^i$  and  $f_O^i$  are the Henrian activity coefficients of carbon and oxygen at the interface which have been determined using interaction parameter model using first order interaction<sup>[33]</sup>. These above mentioned non-linear equations have been solved simultaneously using a function (lsqnonlin) in MATLAB to evaluate the instantaneous equilibrium interfacial concentration of the slag and metal components ( $(\%FeO)^i, [\%C]^i, [\%O]^i$ ) and then from these interfacial concentrations, the extent of external decarburisation reaction at the slag/metal interface and the amount of oxygen transfer from slag/metal interface to bulk metal has been estimated from Equation 4.6 and 4.8 respectively at each time step.

## 4.2.2. Internal Decarburization

**4.2.2.1. Nucleation of bubbles:** As the metal droplet enters the slag, external decarburization starts immediately at the slag-metal interface and in parallel to that the metal droplet enriches in oxygen. When the oxygen content is sufficiently high, CO

bubbles will start to form within the droplet. The rate of nucleation (Number of nuclei/m<sup>3</sup>-s) of CO has been calculated using the rate equation proposed by Blander & Katz<sup>[34]</sup> with the addition of the surface tension modifying parameter proposed by Chen & Coley<sup>[6]</sup>.

$$J = N_0 \left[ \frac{3(\psi\sigma_0)}{\pi m} \right]^{\frac{1}{2}} \exp \left[ -\frac{16\pi(\psi\sigma_0)^3}{3kT(P_{ve} - P_L)^2} \right] \dots \dots [4.17]$$

$N_0$  is the no of nucleation sites per unit volume,  $k$  is the Boltzmann constant,  $T$  is the temperature,  $\sigma_0$  is the surface tension of the metal,  $\psi$  is the surface tension modifying parameter,  $m$  is the mass of one CO molecule,  $P_{ve}$  is the pressure of bubble at equilibrium with C and O in the bulk metal and  $P_L$  is the liquid pressure. This surface tension modifying parameter was introduced by Chen & Coley<sup>[6]</sup> based on the theory of Levine<sup>[24]</sup> for reduction of the work barrier at the gas bubble interface during bubble formation. It is important to mention that there is a significant body of work<sup>[35]</sup> where classical nucleation theory(CNT) has failed to explain gas bubble nucleation kinetics. Researchers have come up with several theories such as “Harvei nuclei”<sup>[36]</sup>, “Blob theory with a diffuse interface”<sup>[37]</sup>, “Tolman’s theory incorporating the curvature effect on surface tension”<sup>[38]</sup>, “Multistep nucleation<sup>[37]</sup>” but none of these are widely accepted. The primary drawback of classical nucleation theory is its failure to predict the nucleation of gas bubbles under circumstances where bubbles are known to nucleate. However, the theory can show the correct dependence with the supersaturation pressure, temperature and surface tension<sup>[34]</sup>. Employing a modified version of this theory is a convenient way to capture the dependence of supersaturation pressure, on temperature, chemical activities and surface tension.

The surface tension of liquid iron has been evaluated as a function of temperature, C, O and S concentration. The correlation developed by Chung & Cramb [39] based on Szyszkowskie-Langmuir equation<sup>[40,41]</sup> has been used here to calculate surface tension(N/m) of liquid metal.

$$\sigma_0 = [1913 + 0.43 * (1823 - T) + 67.75 * [wt\%C] - 0.107 * T * \ln(1 + K_S a_S) - 0.153 * T * \ln(1 + K_O a_O)] * 10^{-3} \dots \dots \dots [4.18]$$

Bubbles will nucleate within the liquid metal droplet at a critical radius based on the surface tension of metal and the supersaturation pressure of CO within the metal as

$$r^{crit} = \frac{2 * \sigma_0 * \psi}{P_{ve} - P_L} \dots \dots \dots [4.19]$$

The homogeneous nucleation of bubbles will create fresh gas/metal interfacial area within the liquid metal droplet and these gas/metal interfacial areas will act as sites for growth of bubbles during the subsequent reaction time. At any time step ( $\Delta t$ ), the generated gas/metal interfacial area from nucleation can be calculated as

$$A_{g/m}^{nuc}(t) = J * V_m(t) * 4\pi(r^{crit})^2 * \Delta t \dots \dots \dots [4.20]$$

Where  $V_m(t)$  is the volume of liquid metal at time  $t$ , and  $J$  is the rate of nucleation according to Equation 4.17 and  $r^{crit}$  is the critical radius of bubbles from Equation 4.19.

**4.2.2.2. Growth of bubbles:** In the current model, the contribution to CO gas formation from bubble growth inside a bloated droplet has been considered for the first time. As mentioned in section 4.2.1, a high level of stirring within the droplet means that the transport of C and O within the droplet can be assumed to be very fast so not rate-

controlling for bubble growth. Whereas the presence of sulfur in the metal will poison reaction sites at the bubble/metal interface. Therefore, bubble growth will be controlled by interfacial chemical reaction at the bubble/metal interface. Thus, the rate of generation of CO (mol/s) due to growth of a bubble of specific radius  $r_{(t-\Delta t)}$  would be

$$\frac{dn_{CO}}{dt} = A_{g/m} k_o \left( \frac{1}{1 + K_S * a_S} \right) \left[ a_C a_O - \frac{p_{CO}}{K_{CO}} \right] \dots [4.21. (a)]$$

$$= 4\pi r_{t-\Delta t}^2 k_o \left( \frac{1}{1 + K_S * a_S} \right) \left[ a_C a_O - \frac{p_{CO}}{K_{CO}} \right] \dots \dots [4.21. (b)]$$

$k_o$  is the rate constant for growth,  $A_{g/m}$  is the gas/metal surface area of previously existed bubble of radius  $r_{(t-\Delta t)}$ , and the parameter, (note  $k_o$  was determined by fitting to match one set of experimental results and then used for all other cases). So, at any time the number of moles of CO in the bubble after growth can be expressed as

$$n_{CO_t} = n_{CO_{(t-\Delta t)}} + \frac{dn_{CO}}{dt} * \Delta t \dots \dots [4.22]$$

It has been assumed that at the end of each time step, mechanical equilibrium is maintained at the gas/metal interface due to curvature and that the ideal gas law is followed. So, the radius,  $r_t$  of a bubble after growth at time step( $t$ ) is updated by using Equation 4.23

$$\frac{\left( P_L + \frac{2\sigma_0}{r_t} \right) * \frac{4}{3} \pi r_t^3}{RT} = n_{CO_t} \dots \dots [4.23]$$

Where  $R$  is the universal gas constant,  $T$  is the temperature. This similar procedure is followed for all the bubbles of different sizes which are present at the end of earlier time step ( $t - \Delta t$ ) and the size distribution of these bubbles are tracked at each time step. If

there are N no of bubbles of different sizes which take part in the growth process, then the total gas/metal surface area generated from the growth process at time  $t$  would be

$$A_{g/m}^{gr}(t) = \sum_N 4\pi r_t^2 \dots \dots [4.24]$$

Because of the relative ease of bubble growth compared with nucleation, it is important to consider this aspect of CO formation in the decarburization model, although experimental evidence distinguishing growth from nucleation of bubbles is difficult to obtain due to the rapid nature of the processes.

The extent of internal decarburization are estimated at each time step by tracking the total generation of CO from nucleation and growth within the bulk metal and the concentration of carbon and oxygen are updated accordingly.

### **4.2.3. Escape of bubbles**

The bubbles generated within the droplet, due to internal nucleation and growth, escape after a certain time period. The combination of rate of generation and rate of escape of CO bubbles controls the expansion of the volume of the droplet with time. From the experimental results of Gu *et al.* <sup>[18]</sup>, it has been shown that the expansion of droplets with time differs with varying sulfur concentrations. It is important to include an escape module which destroys generated bubbles in the decarburization model. Otherwise, the bubbles would grow for infinite time resulting in over prediction of the decarburization rate. Currently research is on-going in the authors' laboratory<sup>[42]</sup> to model the escape rate of bubbles as a function of CO generation rate, and droplet and slag physical properties. For



the time being, to facilitate the development of the current model, a polynomial curve was empirically fitted to the experimental data for each droplet (Note: This is only data that was fitted separately for each individual droplet). The spline function in MATLAB has been used to perform this. The fitted polynomial was used to calculate bubble escape rate within the model. Thus, during bloating, the volume of the CO bubbles remaining in the droplet at the end of each time step can be calculated as

$$V_{CO}(t) = V_{CO}(t)^{nuc} + V_{CO}(t)^{gr} - V^{esc}(t) \dots \dots [4.25]$$

Where  $V_{CO}(t)^{nuc}$  and  $V_{CO}(t)^{gr}$  are the volume of CO bubbles which are generated from nucleation and growth respectively and  $V^{esc}(t)$  is the volume of bubbles which are escaping from the bloated droplet at that time step. The above equation can be further expanded according to the contribution from nucleation and growth as

$$V_{CO}(t) = \frac{4}{3}\pi(r^{crit})^3 * J * V_m(t) * \Delta t + \sum_N \frac{4}{3}\pi r_t^3 - V^{esc}(t) \dots \dots [4.26]$$

In this way, the total volume of CO bubbles within the liquid metal droplets are tracked at each time step to estimate the extent of swelling and the overall density of the droplet. The overall density of the metal droplet has been calculated at each time step as

$$\rho_d(t) = \frac{\rho_m * V_m(t)}{V_m(t) + V_{CO}(t)} \dots [4.27]$$

Where  $\rho_m$  and  $\rho_{CO}$  are the density of liquid metal and CO gas respectively.  $V_m(t)$  is the volume of the liquid metal and  $V_{CO}(t)$  is the volume of the CO gas remaining within the metal droplet based on the balance between the rate of generation and escape of bubbles as mentioned in Equation 4.26.

#### 4.2.4. Foaming

Foaming of the slag must be considered in modeling the current experimental data, because droplets move between a dense slag and a foamy slag. Certain model parameters changed depending on the type of the slag. Therefore, it is important that the model track whether the droplet is in foamy slag or dense slag. This is only necessary because of specific characteristics of the current experiments and would not be relevant to a real BOF.

In the experiments used to validate the current model, a layer of foamy slag forms on top of a dense slag layer. With the progress of reaction, the density of the bloated droplet decreases to a point where it moves into the foamy slag. Subsequently, as the reaction subsides, the droplet falls back into the dense slag. This behavior is illustrated schematically in Figure 4.4. While this process is probably not relevant to a real BOF, it is important that we consider it as a real effect in modeling laboratory experiment because a high void fraction in the foamy slag impedes mass transport<sup>[43]</sup>.

Based on the variation of the density of the droplet ( $\rho_d(t)$ ), there are two cases possible at any time; the droplet density is higher than that of the dense slag in which case it will remain in the dense slag (Figure 4.4(a) and (c)) or the droplet is sufficiently bloated that it will float into the foamy slag (Figure 4.4(b)). For the purposes of the current work, when the droplet is in the dense slag it is assumed that it only reacts with the slag mass in the dense slag and when it is in the foamy slag, it can only react with the mass that is in the foamy slag. This distinction is important for the mass balance between slag and metal. At each time step, the model calculates the density of the droplet according to Equation 4.27 and decides whether the droplet is in the foamy slag or in the dense slag and thereby,

employs the appropriate kinetic parameters and mass balance. The partitioning of the total mass of the slag into foamy slag and the dense slag for the two different cases has been incorporated into the model as described here.

Case 1: Droplet in dense slag - Droplet density ( $\rho_d(t)$ ) > Dense slag density ( $\rho_s$ )

$$W_{slag}^{dense} = W_{slag}^{tot} \dots 4.28. (a)$$

$$W_{slag}^{foamy} = 0 \dots 4.28. (b)$$

$$k_{eff} = k_s \dots 4.28. (c)$$

Case 2: Droplet in foamy slag - Droplet density ( $\rho_d(t)$ ) < Dense slag density ( $\rho_s$ )

$$W_{slag}^{dense} = (1 - f) * W_{slag}^{tot} \dots 4.29. (a)$$

$$W_{slag}^{foamy} = f * W_{slag}^{tot} \dots 4.29. (b)$$

$$k_{eff} = (1 - \epsilon) * k_s \dots 4.29. (c)$$

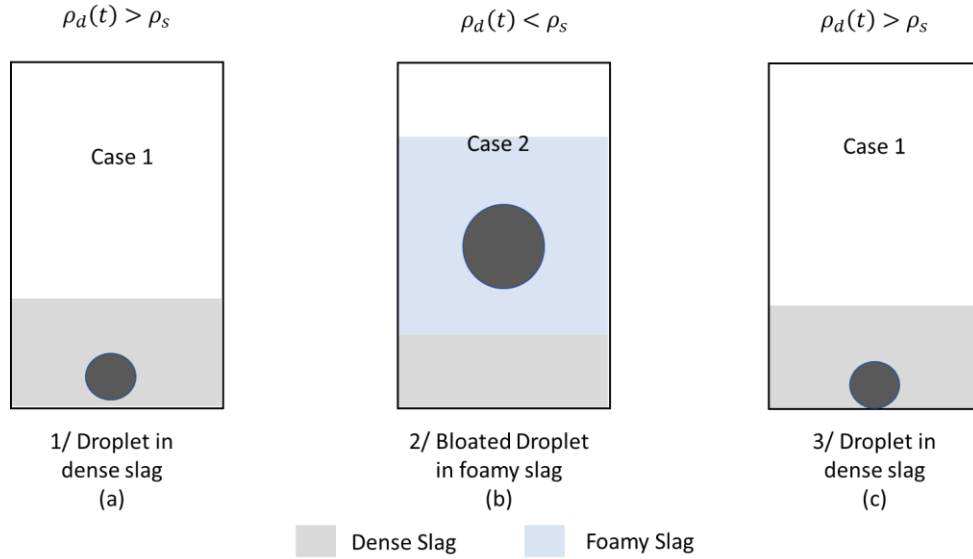


Figure 4.4: Schematic of the transition from dense slag state to foamy slag state (a) droplet in dense slag (b) bloated droplet in foamy slag (c) droplet coming back in the dense slag at the end

$W_{slag}^{tot}$ ,  $W_{slag}^{dense}$ ,  $W_{slag}^{foamy}$  are the mass of total slag, dense slag and foamy slag respectively.

$k_{eff}$  is the effective mass transfer coefficient. Based on videos of individual experiments, the fraction of slag in the foamy state ( $f$ ) and the void fraction ( $\epsilon$ ) of that slag remain constant during the period from foam formation until the point when the decarburisation shuts down. Therefore, for the model calculation, it has been assumed that 75% of the total slag is foamy and the void fraction is 0.8. These assumptions are representative of all the experimental conditions used to validate the model in this paper.

To model the process, where available parameters were taken from the published literature.

These parameters specific to the current model i.e. forward reaction rate constant ( $\vec{k}$ ), surface tension modifying parameter( $\psi$ ) and apparent growth rate constant ( $k_o$ ) were fitted

to match the experimental data for droplet with 2.62 %C - 0.014 %S - 0.088% P reacting in oxidizing slag, having 16% FeO and  $\text{CaO/SiO}_2 = 0.9$ . This data was selected because all three characteristic stages were clearly represented in the CO generation profile. To validate the model, the fitted parameters were then used to model a number of other cases. For higher temperature predictions, the parameters fitted at 1580°C were modified according to appropriate theoretical relations.

### **4.3. Results & Discussion**

#### **4.3.1. Effect of Sulfur on Decarburisation**

The decarburisation model has been tested against the experimental data reported by Gu *et al.*<sup>[18]</sup> at different sulfur concentrations at 1580°C. The results are reported in this section. Metal droplets of 1 g and of composition Fe - 2.62% C - 0.007% S - 0.088% P, Fe - 2.62% C - 0.014% S - 0.088% P, Fe - 2.62% C - 0.021% S - 0.088% P are reacted with 25 g of CaO-SiO<sub>2</sub>-Al<sub>2</sub>O<sub>3</sub>-FeO type slag in which  $\text{CaO/SiO}_2 = 0.9$ , 16% FeO, 17% Al<sub>2</sub>O<sub>3</sub> and the decarburisation profile are predicted from the current model. It is important to mention that in this work, the model performance is validated with decarburization data for low basicity slag only because of availability of data from the authors laboratory. The low basicity slag was chosen primarily because it is easier to work with and less expensive alumina crucibles can be used. The model performance has been evaluated based on the accurate prediction of incubation time, the rate of decarburisation during the incubation period, the peak rate of decarburisation and the end of decarburisation. In the work of Pomeroy<sup>[27]</sup> and Sun<sup>[25]</sup> the incubation period was defined as the time to achieve sufficient supersaturation for nucleation of CO bubbles. Experimentally it is not possible to detect the formation of the

first bubble. Therefore, Pomeroy interpreted this as the time at which bloating was first observed. Rather than continue with the contradiction between the model and experiment, in the current work, the incubation period has been calculated as the time required to initiate bloating based on the time at which the density of the droplet becomes less than that of the dense slag.

Decarburisation profiles predicted by the model are presented in Figure 4.5, Figure 4.6, and Figure 4.7 along with experimental data for 0.007% S, 0.014% S and 0.021% S respectively. It can be observed that the incubation period was almost nonexistent for 0.007% sulfur and increased with increasing sulfur to 0.021% S. The most important factor controlling the incubation period is the partitioning of oxygen at the slag/metal interface between internal and external decarburisation reactions. With increasing sulfur concentration, the surface poisoning slows the external decarburisation reaction rate at the slag/metal interface and the oxygen supply into the droplet for internal decarburisation, thereby increasing the length of the incubation period and decreasing the rate of CO formation at the surface. It is worthwhile to mention that there might be some adsorption of oxygen replacing sulfur creating pathways through the adsorbed layer. But only consideration of sulfur as adsorbed species using Langmuir isotherm is justified by the fact that the model is able to capture very well, the variation of the incubation period and oxygen partitioning with changes in sulfur concentration from 0.007% to 0.021%. Further analysis of the decarburisation profiles shows that the peak rate of decarburisation increases from 0.007% S to 0.014% S then decreases with further increase in sulfur concentration. Gu *et al.*<sup>[18]</sup> attributed this observation to two opposing factors, and these

are well captured in the current model; with increasing sulfur concentration, the surface tension of the metal decreases, reducing the free energy barrier for nucleation, while surface poisoning inhibits reaction at both the slag/metal interface and the bubble/metal interface. The contributions to decarburisation expressed as a fraction, from external decarburisation, internal nucleation and internal growth of bubbles are presented in Figure 4.5(b), Figure 4.6(b), and Figure 4.7(b) for droplets with 0.007% S, 0.014% S and 0.021% S respectively. Comparing these contributions at different sulfur concentrations, shows that the model has captured the contributions from both surface poisoning and the changes in surface tension caused by sulfur. These effects combine resulting in a peak decarburization rate which is at its highest with 0.014% S. The model has captured this phenomenon very well. The model also predicts that there is large contribution from external decarburisation in the early stages of reaction however as soon as CO bubbles nucleate within the droplet, internal decarburisation becomes the prime contributor. The earlier model presented by Kadrolker & Dogan<sup>[22]</sup> predicted the decarburization behaviour well for 0.007% S but failed to capture the variation of incubation period and peak decarburisation rate with sulfur concentration. The modifications introduced in the current model capture these stages accurately. It is worth noting that this supersaturation level required for nucleation of bubbles occurs after one or two seconds in Figures 4.5 and 4.6 but the incubation times, determined from the decarburisation profile are approximately six and ten seconds, respectively. This apparent discrepancy results from the difference between the first nucleated bubble and the time for bloating to start; the model agrees well with the experimental time for bloating.

It can be observed that the model overpredicts the decarburisation extent for droplets with 0.007 and 0.014% S but the overprediction is less for droplets with 0.021% S. The experimental data show that there is a sudden shutdown of decarburisation whereas the model predicts continuation of decarburization. In the case of the droplet with 0.021% S there is better agreement between the model and the experimental data as the endpoint is approached than there is for experiments at lower sulfur level. It is also acknowledged that the data shown in Figure 4.7 does not actually reach shutdown. It is worth noting that the shutdown observed in Figures 4.5 and 4.6 occurs despite sufficient carbon present in the droplet and FeO in the slag to continue reaction. This is true whether the criterion used to define sufficiency of reactants is supersaturation relative to 1 atmosphere of CO or includes the supersaturation required to overcome the nucleation barrier <sup>[44]</sup>. Figure 4.8 shows the variation of carbon concentration based on CO evolution of the droplet for three different sulfur concentration along with predicted equilibrium carbon content as well as supersaturation limit. This confirms that the reaction shutdown is not due to depletion of carbon. This would suggest that there is some mechanism which inhibits decarburisation but is not captured in the model. The authors are not able to develop a definitive explanation which could be incorporated into the model without adversely affecting the ability of the model to describe the early stages of the reaction. To address this problem, Rout *et al.*<sup>[23]</sup> modified the surface reaction by introducing blockage effects by SiO<sub>2</sub> and P<sub>2</sub>O<sub>5</sub>, whereas in this work, there is no SiO<sub>2</sub> and P<sub>2</sub>O<sub>5</sub> present. Kadrolker & Dogan<sup>[22]</sup> stopped the reaction at the end stage in their model by constraining the maximum allowable oxygen



concentration to 0.07% [O]. However, their approach is not consistent with the significantly higher oxygen activity in equilibrium with the slag.

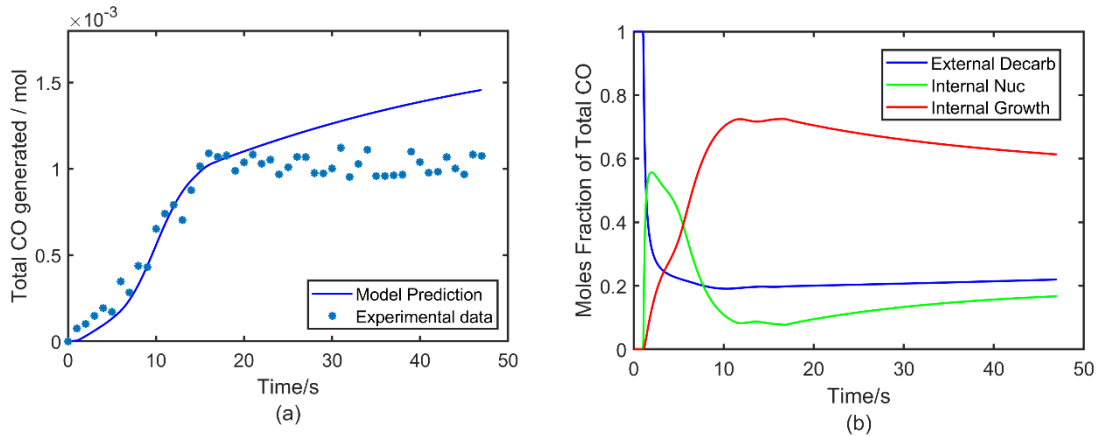


Figure 4.5: (a) Total CO gas generation in moles with time from model and experiment<sup>[18]</sup> and (b) fraction of moles from external and internal decarburisation with time for 1g droplet with 2.62% C 0.007% S at 1580°C

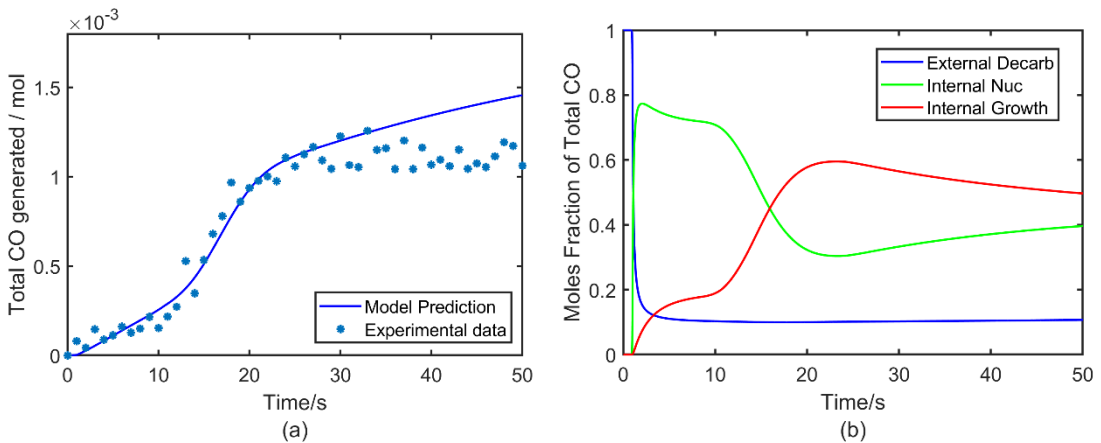


Figure 4.6: (a) Total CO gas generation in moles with time from model and experiment<sup>[18]</sup> and (b) fraction of moles from external and internal decarburisation with time for 1g droplet with 2.62% C-0.014% S at 1580°C

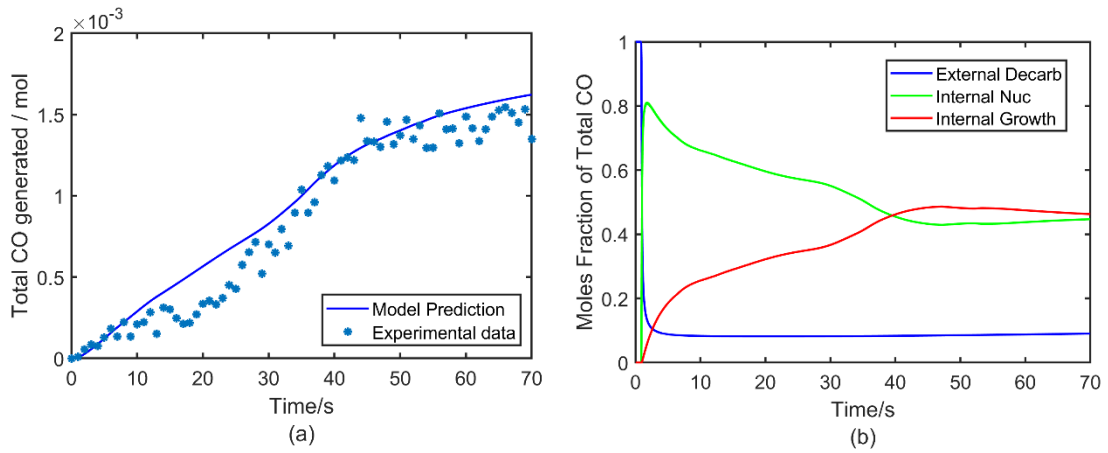


Figure 4.7: (a) Total CO gas generation in moles with time from model and experiment<sup>[18]</sup> and (b) fraction of moles from external and internal decarburisation with time for 1g droplet with 2.62% C-0.021% S at 1580°C

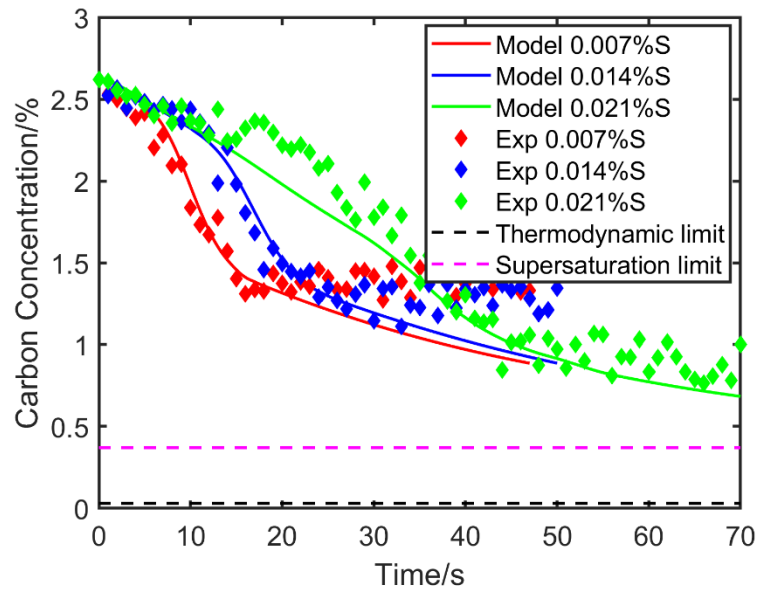


Figure 4.8: Variation of carbon concentration of droplet with reaction time for different sulfur and with thermodynamic and supersaturation limit

Several researchers [45–48] have reported the formation of a liquid FeO layer at the end of decarburization in levitated droplet decarburization experiments when the outer most layer is depleted of carbon and rather than forming CO bubbles, oxygen has been observed to react with Fe. However, no literature has been found by the authors which suggests the formation of an oxide layer on a droplet reacting with slag. Several researchers [5,11,48–51] have talked about the sudden shut down of decarburization independent of the carbon content. The model predicts that the slag/metal interfacial oxygen potential is always higher than the bulk metal droplet oxygen potential but much lower (nearly 10 times lower) than that required to form any iron oxide. Therefore, the possibility of formation of an oxide layer to shut down the decarburization process can be ignored. The authors have chosen not to include an artificial ‘switch’ to shutdown the reaction and to address the mechanism of shutdown in a subsequent publication. The authors are currently investigating the premature shutdown of decarburization.

#### **4.3.2. Effect of Temperature**

To study the performance of the model on varying temperature, the prediction of the model for droplet of 2.62% C -0.007% S at two different temperatures 1580<sup>0</sup>C and 1640<sup>0</sup>C with CaO-SiO<sub>2</sub>-Al<sub>2</sub>O<sub>3</sub>-FeO slag having 16% FeO and 0.9 basicity have been compared with experimental data<sup>[30]</sup>. The model prediction of total CO generation at 1580<sup>0</sup>C and 1640<sup>0</sup>C is presented in this Figure 4.9 (a) and (b) respectively. To account the effect of increase in temperature in the model, the effect of slag viscosity and temperature on the slag mass transfer coefficient has been incorporated as follows. From the Stokes Einstein and the Eyring’s relations, it may be seen that diffusivity in liquids is proportional to temperature

and inversely proportional to the viscosity ( $D \propto \frac{T}{\eta}$ ). Based on a range of mass transfer models  $k_s \propto D^n$  where n is in the range 0.5 – 1.3. Therefore,

$$k_s \propto \left(\frac{T}{\eta}\right)^n \dots \dots \dots [4.30]$$

The model prediction in Figure 4.9 (b) is based on the conversion of the mass transfer coefficient determined at 1580°C converted to 1640°C using equation 4.30 for n = 1 and n = 0.5. The difference in prediction based on the choice of n is seen to be negligible. The viscosity variation with increase in temperature has been calculated from Factsage 6.4™ for this current slag composition to incorporate the effect of temperature variation. At both temperatures, the model prediction shows good agreement in the first two stages of decarburisation and in common with most data presented in this paper, it did not predict correctly at the end point of decarburisation. When one considers the model prediction at 1640°C was based entirely on data obtained at 1580°C modified using appropriate theoretical functions, the agreement can be considered remarkable. The relative contributions to CO formation from external decarburisation, internal nucleation, and growth, are compared in Figure 4.9 (c) and (d). With increase in temperature, the rate of nucleation and growth became faster during the peak decarburisation period.

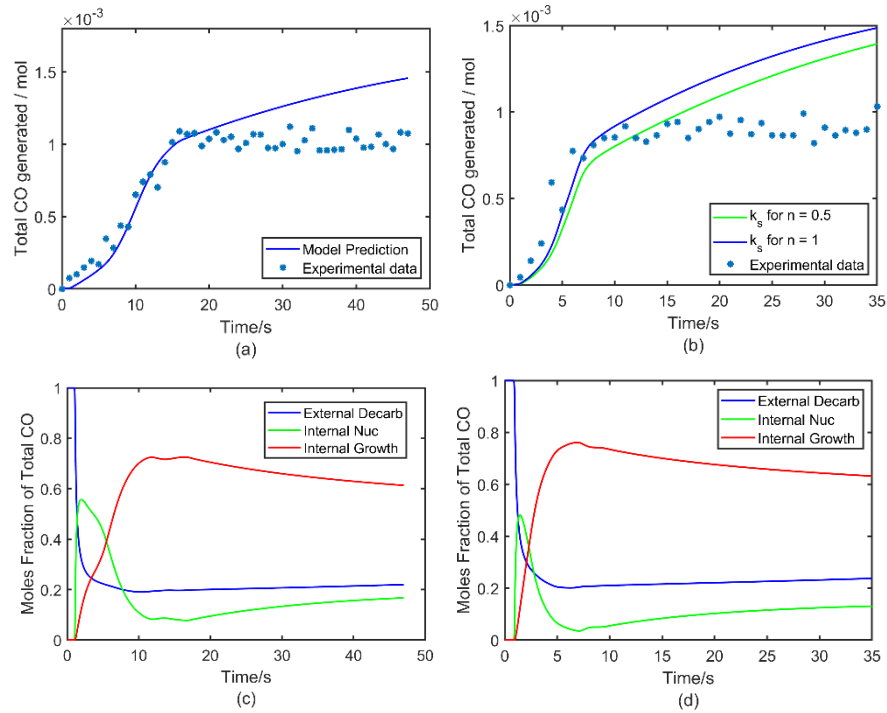


Figure 4.9: Total CO generation with time from model and experiment<sup>[30]</sup> for 1 g droplet with 0.007% S at 1580°C (a) and 1640°C (b). The fraction of external and internal decarburisation for droplet at 1580°C (c) and 1640°C(d) respectively

### 4.3.3. Effect of Droplet Size

To validate the model performance for droplets of different size, the predicted decarburisation profile for 0.5 g, 1 g and 1.5 g droplets with 2.62% C and 0.007% S have been compared in Figure 4.10 against experimental data<sup>[52]</sup> from authors' laboratory. The droplets were reacted with 25 g of CaO-SiO<sub>2</sub>-Al<sub>2</sub>O<sub>3</sub>-FeO slag having CaO/SiO<sub>2</sub> ratio 0.9 and 16% FeO at 1640°C temperature. For 0.5 g and 1.0 g, there is no observable incubation period in the decarburisation profiles. However, for a 1.5 g, there is an approximately 10s incubation time for the droplet to become bloated<sup>[52]</sup>. This incubation time is well predicted

by the model based on the procedures described above without the use of additional fitting. It can be observed for all droplet masses that the model performs well for the first two stages of reaction. This agreement could be considered remarkable particularly recognizing that only one set of constants has been used to describe all experimental conditions.

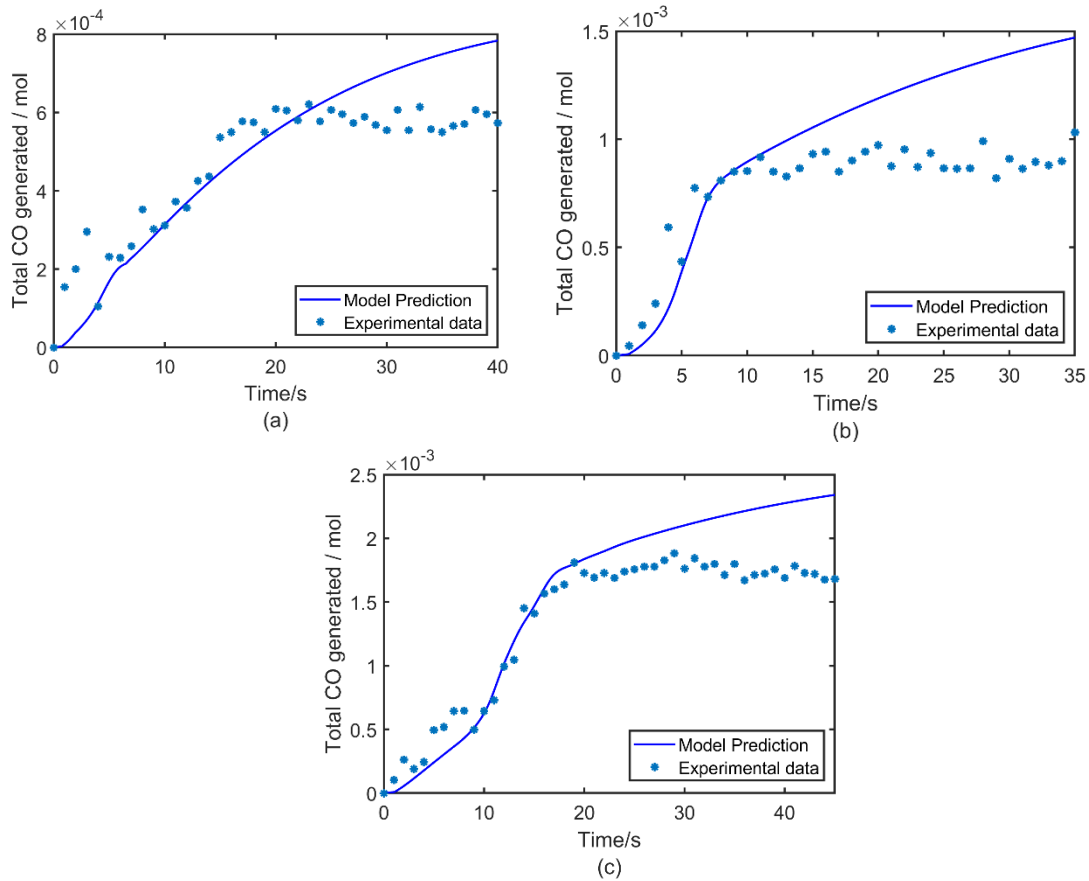


Figure 4.10: Total CO gas generation profile with time from model and experiment<sup>[52]</sup> for droplets with 2.62% C on varying droplet mass (a) 0.5 g (b) 1.0 g (c) 1.5 g respectively

#### 4.3.4. Effect of Droplet Carbon Content

In order to further validate the model performance, the ability of the model to predict decarburisation was tested for a range of initial carbon concentrations, and compared

against experimental data<sup>[44]</sup> for 1.0 g metal droplets with 1.5% C, 2.5% C and 4.5% C in CaO-SiO<sub>2</sub>-Al<sub>2</sub>O<sub>3</sub>-FeO slag having 16% FeO and CaO/SiO<sub>2</sub> ratio 0.9 at 1580°C. Results are shown in Figure 4.11 (a), (b) and (c). The model prediction shows a fairly good agreement with the experimental data in the initial stages of reaction – a negligible or short incubation period and a faster decarburisation period. It is worth noting that the faster decarburisation period for these cases does not show a steady state “peak” period as seen in previous data sets, however, the data are still quite well represented by the model. As with other data sets examined in this paper, the decarburisation ceases prematurely which is not captured by the model. It is worth noting that deviation of the model from the real data becomes more pronounced with increasing initial carbon concentration. The fractional contribution from external decarburisation, internal nucleation and growth are compared in Figure 4.11 (d), (e), and (f). The model prediction shows that the contribution from internal nucleation increases compared to growth with increasing carbon concentration. According to equation 4.17, the rate of nucleation of CO bubbles within the droplet is dependent on the supersaturation pressure of CO, which is dependent on the products of dissolved carbon and oxygen activities. At higher carbon activity, the droplet can achieve the critical supersaturation pressure at lower dissolved oxygen activity compared to that for lower carbon activities. This effect will hasten the onset of internal nucleation. However, in a counter current competition between oxygen and carbon, at higher carbon concentrations, more oxygen will be consumed at the slag metal interface by external decarburisation. This will leave less oxygen to enter the bulk metal, thereby delaying internal nucleation. Thus, these two factors compete to determine the incubation time.





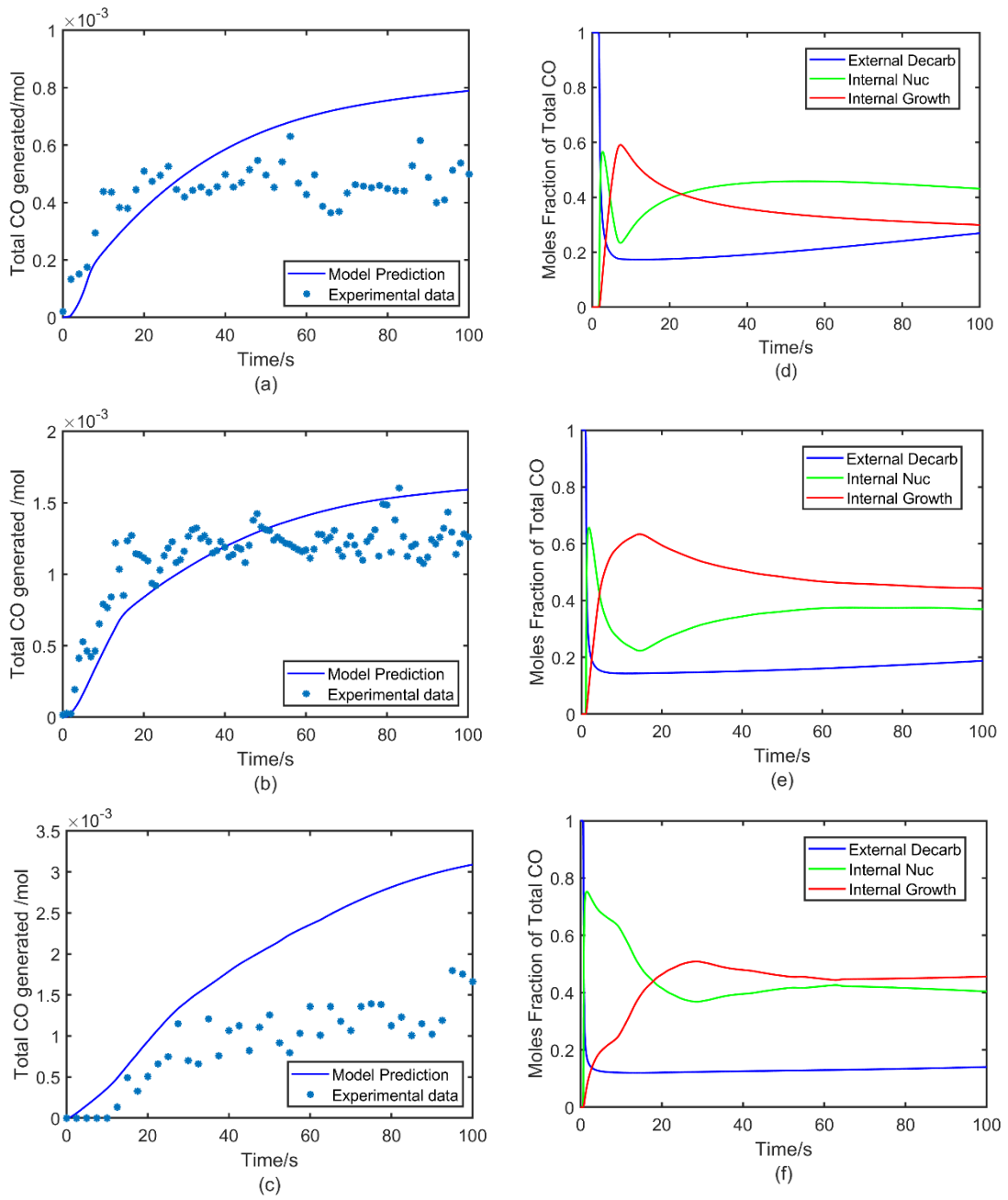


Figure 4.11: Total CO generation with time from model and experiment<sup>[44]</sup> on varying carbon concentration in (a), (b) and (c) for 1.5% C, 2.5% C and 4.5% C respectively. The

contribution in mole fraction from external decarburisation internal nucleation and growth with time for (d) 1.5% C (e) 2.5% C and (f) 4.5% C respectively.

#### 4.4. Sensitivity analysis

Sensitivity analysis on the model parameters has been performed to understand the effect of these parameters individually on the decarburization reaction kinetics. The parameters selected for this analysis are, mass transfer coefficient of FeO in slag ( $k_s$ ), forward rate constant of FeO dissociation ( $\vec{k}$ ), the surface tension modifying parameter ( $\psi$ ), growth rate constant ( $k_o$ ). The effect of these parameters is presented in Figure 4.12 (a), (b), (c) and (d) respectively. This analysis has been performed for a decarburizing droplet of 1 g with composition Fe- 2.62% C – 0.014% S and 0.088% P which is reacting in CaO-SiO<sub>2</sub>-Al<sub>2</sub>O<sub>3</sub>-16% FeO slag at 1580<sup>o</sup>C<sup>[18]</sup>. From the CO generation profile in Figure 4.12 (a) and (b), the effect of varying  $k_s$  and  $\vec{k}$ , can be observed. Both affect the length of the incubation period, the rate during the incubation period, and the peak rate of decarburization. However, the effect of mass transfer coefficient is significantly greater.

The role of surface tension modifying parameter ( $\psi$ ) in the model is that it lowers the critical free energy barrier to very low value (1% of theoretical value) favoring the internal nucleation of CO bubbles. It can be observed in Figure 4.12 (c) that with increase in  $\psi$  value, the rate of decarburization decreases both in the incubation period and peak decarburization period. However, any decrease beyond the experimentally determined value makes no difference to the rates or the length of the incubation period. Figure 4.12(d) shows that within a reasonable range of variation, the growth rate constant has no

discernible influence on the decarburization profile. This observation, combined with the previous observation regarding the surface tension modifying parameter, is further strong evidence that the overall decarburization rate is controlled almost entirely by supply of oxygen to the droplet. Notwithstanding the previous statement, inspection of Figure 4.13 shows that the surface tension modifying parameter and the growth rate constant combine to strongly influence the relative contributions from nucleation and growth to a relatively constant overall reaction rate.

If instead of sensitivity analysis, the steps based on the concept of resistance<sup>[44]</sup> to the reaction are compared, the relative resistances can be evaluated. The overall resistance would be

$$R_{Ov} = R_{transport} + R_{chem\ Rxn} + \frac{1}{\frac{1}{R_{nuc}} + \frac{1}{R_{growth}}} \dots \dots [4.31]$$

The resistances for transport in the slag, dissociation of FeO at the interface, and internal nucleation and growth are compared in Figure 4.14 for droplet of Fe - 2.62%C – (0.007%, 0.014%, 0.021%S) compositions reacting with slag of 16% FeO and CaO/SiO<sub>2</sub> = 0.9. It can be observed that, there is an order of magnitude difference between the resistance due to transport in the slag and chemical reaction at the interface for 0.007%S droplet. However, for the higher sulfur experiments this ratio drops to a factor of 3. Please note the minimum in the two resistance curve arises because of the increase in surface area during bloating. Because of the way the model was developed, the definition of resistance for nucleation and growth of bubbles does not lend itself to direct comparison. Here the

combined resistance including nucleation and growth within the metal is presented in Figure 4.14 for the comparison with the other resistances. It is known that until the supersaturation limit is exceeded there can be no nucleation of bubbles within the liquid metal droplet, so the resistance is infinite and after the supersaturation limit is achieved the resistance is of a similar order of magnitude to the others. Also, for the growth of bubbles there is no gas/metal surface area to grow until the supersaturation limit is exceeded meaning that the growth resistance will also be infinite. The combined resistance profile shows infinite resistance initially and then sudden decrease as soon as the supersaturation limit exceeds. It is also worth noting that the resistance due to bubble nucleation and growth is lower than the others once supersaturation is achieved, then after sometime it starts to increase as carbon is depleted from the droplet.

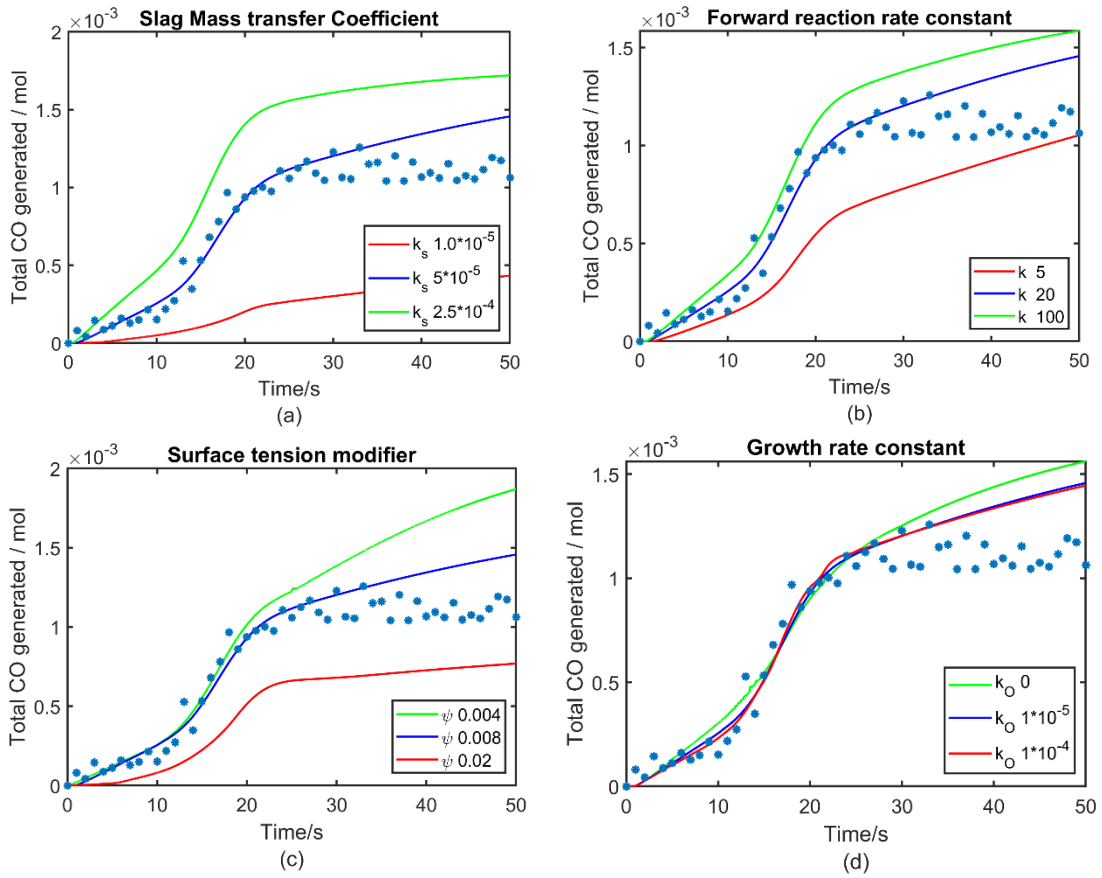


Figure 4.12: Total CO generation with time on varying model parameters as (a) slag mass transfer coefficient, (b) forward reaction rate constant of FeO dissociation, (c) surface tension modifier, (d) growth rate constant

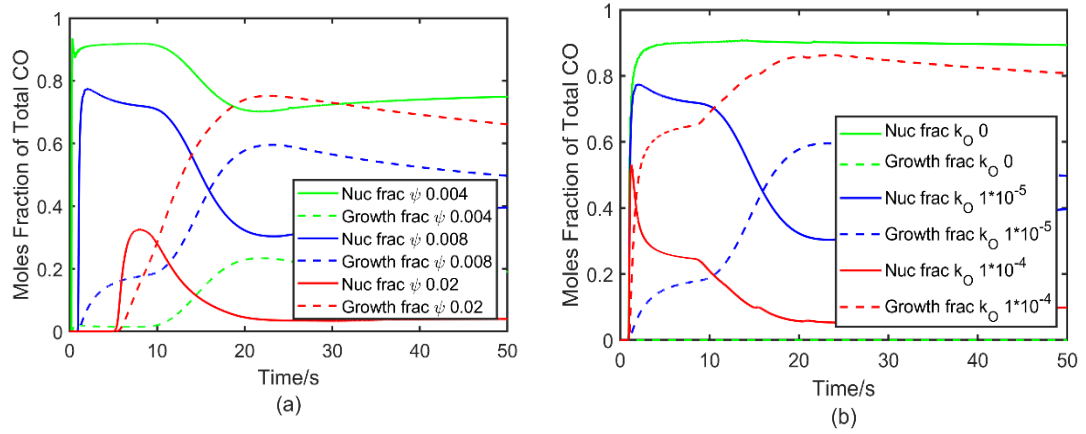


Figure 4.13: Variation of fraction of contribution from internal nucleation and growth in total CO generation by varying  $\psi$  parameter,  $k_O$  in (a) and (b) respectively

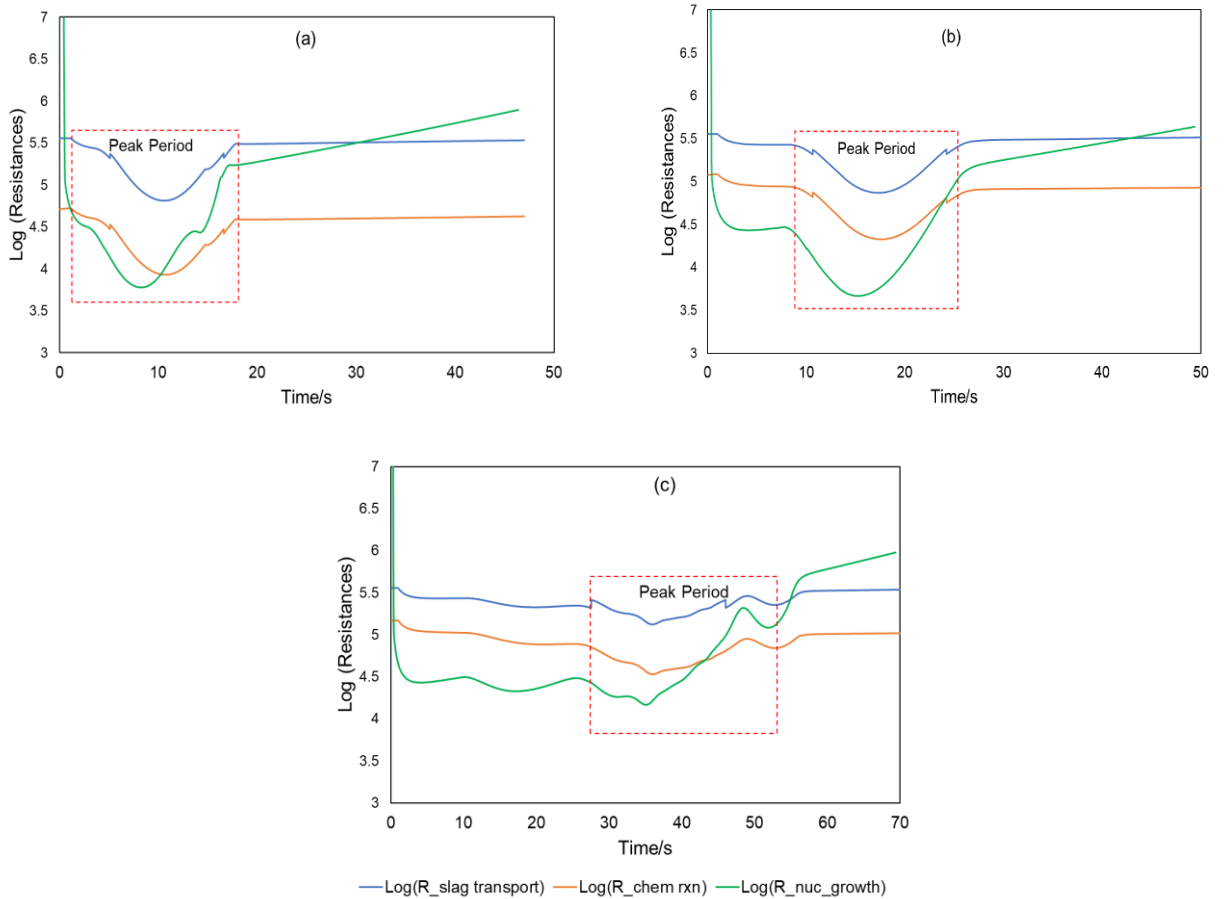


Figure 4.14: Variation of resistances due to slag transport, chemical reaction and internal nucleation-growth of bubbles with time for 0.007%S(a), 0.014%S(b) and 0.021%S(c) droplets

#### 4.5. Error Analysis

To build confidence on the model performance it is important to perform error analysis on the model prediction results with the experimental results. This analysis has been performed for all different cases as mentioned earlier.

RMSE is an extensively used error metric to compare the model performance of a variable.

This is calculated as

$$RMSE = \sqrt{\frac{\sum(y_t^{Model} - y_t^{exp})^2}{N'}} \dots [4.32]$$

Where  $y_t^{Model}$  is the model predicted value and  $y_t^{exp}$  is the experimental data points at time step  $t$  and  $N'$  is the no of data points. This metric cannot be used to compare the prediction of two different variables due to its scale-dependent nature. The RMSE errors has been estimated for three stages of the decarburization process: incubation period, peak decarburization period and end stage on varying droplet sulfur concentration, droplet mass and droplet carbon concentration and presented in Table 4.1, Table 4.2, Table 4.3 respectively. The average RMSE error of the model prediction at the incubation period is  $1.57 * 10^{-4}$ , at the peak decarburization period  $1.71 * 10^{-4}$  and at the end stage  $3.75 * 10^{-4}$ . The error analysis quantitatively shows that there is a large deviation in the prediction at the end stage of decarburization, and this deviation increases with increase in carbon concentration and reaches of the order of  $10^{-3}$  at 4.5 % C concentration droplet. The model is missing the mechanism of decarburization reaction shut down at the end stage and the author is currently working on it.

Table 4.1: RMSE error of model prediction on varying wt% S of 1 g droplet at 1580°C

|  | Wt% S | Stage 1 | Stage 2          | Stage 3          |
|--|-------|---------|------------------|------------------|
|  | 0.007 | NA      | $8.42 * 10^{-5}$ | $2.88 * 10^{-4}$ |



|           |       |                       |                       |                       |
|-----------|-------|-----------------------|-----------------------|-----------------------|
| Droplet   | 0.014 | $5.38 \times 10^{-5}$ | $8.93 \times 10^{-5}$ | $2.18 \times 10^{-4}$ |
| Sulfur    | 0.021 | $1.74 \times 10^{-4}$ | $1.27 \times 10^{-4}$ | $1.22 \times 10^{-4}$ |
| Variation |       |                       |                       |                       |

Table 4.2: RMSE error of model prediction on varying droplet mass with 2.62% C –  
0.007% S at 1640°C

| Droplet   | Droplet Mass(g) | Stage 1               | Stage 2               | Stage 3               |
|-----------|-----------------|-----------------------|-----------------------|-----------------------|
| Mass      | 0.5             | NA                    | $8.76 \times 10^{-5}$ | $1.23 \times 10^{-4}$ |
| Variation | 1               | NA                    | $1.45 \times 10^{-4}$ | $3.67 \times 10^{-4}$ |
|           | 1.5             | $1.72 \times 10^{-4}$ | $9.20 \times 10^{-5}$ | $4.09 \times 10^{-4}$ |

Table 4.3: RMSE error of model prediction on varying carbon concentration of 1.0 g  
droplet at 1580°C

| Droplet   | Wt% C | Stage 1               | Stage 2               | Stage 3               |
|-----------|-------|-----------------------|-----------------------|-----------------------|
| Carbon    | 1.5   | NA                    | $1.55 \times 10^{-4}$ | $2.49 \times 10^{-4}$ |
| Variation | 2.5   | NA                    | $3.39 \times 10^{-4}$ | $2.81 \times 10^{-4}$ |
|           | 4.5   | $2.27 \times 10^{-4}$ | $4.22 \times 10^{-4}$ | $1.32 \times 10^{-3}$ |

## 4.6. Conclusion

In the present work, a decarburization model has been developed with few assumptions. The model parameters, determined for one dataset, have been validated over a wide range of experimental conditions. A sensitivity analysis has also been performed on the key parameters of the model. The model agrees well with the experimental data. Based on the model predictions and subsequent sensitivity analysis, the following conclusions can be drawn.

1/ The overall rate of decarburization of bloated droplets is controlled by oxygen supply to the droplet, the rate of supply being mostly controlled by mass transport of FeO in the slag.

2/ The length of the incubation period is controlled by a combination of, the rate of oxygen supply to the droplet and the partitioning of oxygen between the surface and the bulk. The latter is controlled by the rate of oxygen consumption by decarburization at the surface, and the carbon and sulfur content in the bulk.

3/ During the peak decarburization period, nucleation and growth of bubbles both contribute to CO generation. The ratio of the contributions depends on the relative values of the surface tension modifying parameter and the rate constant for bubble growth.

4/ The model fails to predict a sudden cessation of decarburization observed in almost all cases. This event occurs despite ample availability of both oxygen and carbon to continue the reaction. This issue requires further research to establish a mechanism.

## **Acknowledgements**

The authors wish to thank McMaster Steel Research Center and Natural Science and Engineering Research Council of Canada for funding this project.

## List of Symbols

[%  $C$ ] Concentration of dissolved carbon in liquid metal (wt pct)

[%  $O$ ] Concentration of dissolved Oxygen in liquid metal (wt pct)

(% $Al_2O_3$ ) Slag  $Al_2O_3$  concentration (wt pct)

(% $CaO$ ) Slag  $CaO$  concentration (wt pct)

(% $FeO$ ) Slag  $FeO$  concentration (wt pct)

(% $SiO_2$ ) Slag  $SiO_2$  concentration (wt pct)

$A$  Interfacial area ( $m^2$ )

$A_{g/m}^{gr}(t)$  Total gas/metal surface area generated from the growth at time  $t$  ( $m^2$ )

$A_{g/m}^{nuc}(t)$  Total gas/metal interfacial area generated due to nucleation at time step  $t$  ( $m^2$ )

$J_C$  Flux of  $C$  in the metal (mol/s)

$J_{FeO}$  Flux of  $FeO$  in the slag (mol/s)

$J_O$  Flux of  $O$  in the metal (mol/s)

$K_{CO}$  Equilibrium constant of  $CO$  formation reaction (-)

$K_{FeO_{eq}}$  Equilibrium constant of  $FeO$  dissociation reaction (-)

$K_j$  Adsorption coefficient of species  $j$ , where  $j$  are [S] and [O] (-)

$M_C, M_O$  Molecular weight of C and O (kg/mol)

$M_{FeO}, M_{CaO}, M_{SiO_2}, M_{Al_2O_3}$  Molecular weight of FeO, CaO, SiO<sub>2</sub> and Al<sub>2</sub>O<sub>3</sub> respectively (kg/mol)

$N_0$  No of nucleation sites per unit volume (/m<sup>3</sup>)

$P_L$  Liquid Pressure (Pa)

$P_{ve}$  Pressure of CO bubble at equilibrium (Pa)

$P_{CO}$  Pressure of CO at the interface (Pa)

$R_{CO}$  Rate of CO formation at the slag/metal interface (mol/s)

$R_{FeO}$  Rate of FeO dissociation reaction at the slag/metal interface (mol/s)

$V_{CO}(t)^{nuc}, V_{CO}(t)^{gr}$  Volume of CO bubbles which are generated from nucleation and growth respectively at time  $t$  (m<sup>3</sup>)

$V_{CO}(t)$  Volume of the CO bubbles remaining in the droplet at time  $t$  (m<sup>3</sup>)

$V^{esc}(t)$  Volume of bubbles which are escaping from the bloated droplet at time  $t$  (m<sup>3</sup>)

$V_m$  Volume of liquid metal (m<sup>3</sup>)

$W_{slag}^{dense}$  Mass of dense slag (kg)

$W_{slag}^{foamy}$  Mass of foamy slag (kg)

$W_{slag}^{tot}$  Total slag mass (kg)

$X_{FeO}$ ,  $X_{SiO_2}$ ,  $X_{CaO}$  Mole fraction of FeO, SiO<sub>2</sub> and CaO (-)

$a_j$  Activity of species  $j$ , where  $j$  can be [O], [C], [S] in metal or (FeO) in slag (-)

$f_C$  Henrian activity coefficient of carbon (-)

$f_O$  Henrian activity coefficient of oxygen (-)

$\vec{k}$  Forward reaction rate constant of FeO dissociation (mol/m<sup>2</sup>-s)

$k_O$  Overall growth rate constant (mol/m<sup>2</sup>-s)

$k_{eff}$  Effective slag mass transfer coefficient (m/s)

$k_m$  Mass transfer coefficient of species in metal (m/s)

$k_r$  Forward reaction rate constant of CO formation (kg/m<sup>2</sup>-s)

$k_s$  Slag Mass transfer coefficient (m/s)

$n_{CO}$  No of moles of CO in a bubble of radius  $r$  (mol)

$r^{crit}$  Critical radius of CO bubble in liquid metal (m)

$r_t$  Radius of a bubble at  $t$  times step (m)

$y_t^{Model}$  Model predicted data point at time  $t$  (mol)

$y_t^{exp}$  Experimentally found data point at time  $t$  (mol)

$\gamma_{FeO}$  Activity coefficient of FeO of the bulk slag concentration (-)

$\theta_j$  Fraction of surface area blocked due to poisoning (-)

$\rho_d(t)$  Density of droplet at time  $t$  ( $\text{kg}/\text{m}^3$ )

$\rho_m$  Density of metal ( $\text{kg}/\text{m}^3$ )

$\rho_s$  Density of slag ( $\text{kg}/\text{m}^3$ )

$\sigma_0$  Surface tension of the metal (N/m)

$\Delta t$  Time step

$R$  Universal gas constant (J/mol-K)

$J$  Rate of Nucleation ( $1/\text{m}^3\text{-s}$ )

$N$  No of bubble at any time  $t$  (-)

$N'$  No of data points (-)

$T$  Temperature (K)

$k$  Boltzmann constant ( $\text{m}^2 \text{kg s}^{-2} \text{K}^{-1}$ )

$m$  Mass of one CO molecule (kg)

$n$  Coefficient of Mass transfer model

$\eta$  Slag Viscosity (Pa-s)

$\psi$  Surface tension modifying parameter (-)

## **Superscripts & Subscripts**

*i* At the slag/metal interface

*b* Within the bulk

*s/m* Slag/metal interface

*g/m* Gas/metal interface

### **Conflict of Interest**

On behalf of all authors, the corresponding author states that there is no conflict of interest.

### **References**

- 1 E. Chen and K.S. Coley: *Ironmak. Steelmak.*, 2010, vol. 37, pp. 541–5.
- 2 L.A. Baker, N.A. Warner, and A.E. Jenkins: *Trans. Metall. Soc.*, 1967, vol. 239, pp. 857–64.
- 3 N.H. El Kaddah and D.G.C. Robertson: *Metall. Mater. Trans. B*, 1988, vol. 19, pp. 831–7.
- 4 D. Widlund, D.S. Sarma, and P.G. Jönsson: *ISIJ Int.*, 2006, vol. 46, pp. 1149–57.
- 5 G. Murthy, Krishna, G, Y. Sawada, and F. Elliot, J: *Ironmak. Steelmak.*, 1993, vol. 20, pp. 179–200.
- 6 E. Chen and K.S. Coley: McMaster University, 2010.
- 7 SUBAGYO, G.A. Brooks, and K.S. Coley: *Can. Metall. Q.*, 2005, vol. 44, pp.

- 119–30.
- 8 N.H. El Kaddah and D.G.C. Robertson: *J. Colloid Interface Sci.*, 1977, vol. 60, pp. 349–60.
- 9 J.H. Zong and J.K. Yoon: *Metall. Trans. B*, 1990, vol. 21, pp. 49–57.
- 10 N. Simento, H. LEE, and P. Hayes: *ISIJ Int.*, 1999, vol. 39, pp. 1217–23.
- 11 T. Gare and G.S.F. Hazeldean: *Ironmak. Steelmak.*, 1981, vol. 8, pp. 169–81.
- 12 L.A. Baker and R.G. Ward: *J. Iron Steel Inst.*, 1967, vol. 205, pp. 714–7.
- 13 G.G.K. Murthy, A. Hasham, and U.B. Pal: *Ironmak. Steelmak.*, 1993, vol. 20, pp. 191–200.
- 14 E.W. Mulholland, G.S.F. Hazeldean, and M.. Davies: *J. Iron Steel Inst.*, 1973, vol. 211, pp. 632–9.
- 15 D.J. Min and R.J. Fruehan: *Metall. Trans. B*, 1992, vol. 23, pp. 29–37.
- 16 K. Gao, V. Sahajwalla, H. Sun, C. Wheatley, and R. Dry: *ISIJ Int.*, 2000, vol. 40, pp. 301–8.
- 17 R.S. Kaplan and W.O. Philbrook: *Metall. Trans.*, 1972, vol. 3, pp. 487–91.
- 18 K. Gu, N. Dogan, and K.S. Coley: *Metall. Mater. Trans. B Process Metall. Mater. Process. Sci.*, 2017, vol. 48, pp. 2343–53.
- 19 C.L. Molloseau and R.J. Fruehan: *Metall. Mater. Trans. B Process Metall. Mater. Process. Sci.*, 2002, vol. 33, pp. 335–44.



- 20 G. Brooks, Y. Pan, and K.S. Coley: *Metall. Mater. Trans. B*, 2005, vol. 36B, pp. 525–35.
- 21 N. Dogan, G.A. Brooks, and M.A. Rhamdhani: *ISIJ Int.*, 2011, vol. 51, pp. 1093–101.
- 22 A. Kadrolkar and N. Dogan: *Metall. Mater. Trans. B Process Metall. Mater. Process. Sci.*, 2019, vol. 50, pp. 2912–29.
- 23 B.K. Rout, G. Brooks, M.A. Rhamdhani, Z. Li, F.N.H. Schrama, and A. Overbosch: *Metall. Mater. Trans. B*, 2018, vol. 49B, pp. 1022–33.
- 24 H.S. Levine: *Met. Trans*, 1973, vol. 4, pp. 777–82.
- 25 H. Sun: *ISIJ Int.*, 2006, vol. 46, pp. 1560–9.
- 26 C. Kattenbelt and B. Roffel: *Metall. Mater. Trans. B*, 2008, vol. 39B, pp. 764–9.
- 27 M.D. Pomeroy: McMaster University, 2011.
- 28 R. Sarkar, P. Gupta, S. Basu, and N.B. Ballal: *Metall. Mater. Trans. B*, 2015, vol. 46, pp. 961–76.
- 29 W. van der Knoop, B. Deo, A.B. Snoeijer, G. van Unen, and R. Boom: *4th Int. Conf. Molten Slags Fluxes*, 1992, pp. 302–7.
- 30 K. Gu, N. Dogan, and K.S. Coley: *Metall. Mater. Trans. B Process Metall. Mater. Process. Sci.*, 2017, vol. 48, pp. 2984–3001.
- 31 I. Langmuir: *J. Am. Chem. Soc.*, 1918, vol. 40, pp. 1361–403.

- 32 S. Basu, A.K. Lahiri, and S. Seetharaman: *Metall. Mater. Trans. B Process Metall. Mater. Process. Sci.*, 2010, vol. 41, pp. 414–9.
- 33 M. Hino and K. Ito: *Thermodynamic Data for Steelmaking*, 2010th edn., KONNO Printing Co. Ltd, Japan, 2010.
- 34 M. Blander and J.L. Katz: *AIChE J.*, 1975, vol. 21, pp. 833–48.
- 35 S.D. Lubetkin: *Langmuir, Am. Chem. Soc.*, 2003, vol. 19, pp. 2575–87.
- 36 E.N. Harvey, A. Whiteley, W. McElroy, D. Pease, and D. Barnes: *J. Cell. Comp. Physiol.*, 1944, vol. 24, pp. 23–34.
- 37 P.G. Bowers, K. Bar-Eli, and R.M. Noyes: *J. Chem. Soc. - Faraday Trans.*, 1996, vol. 92, pp. 2843–9.
- 38 R.C. Tolman: *J. Chem. Phys.*, 1949, vol. 17, pp. 333–7.
- 39 Y. Chung and A.W. Cramb: *Metall. Mater. Trans. B*, 2000, vol. 31B, pp. 957–71.
- 40 B. von Szyszkowski: *Zeitschrift für Phys. Chemie*, 1908, vol. 64, pp. 385--414.
- 41 G.R. Belton: *Metall. Trans. B*, 1976, vol. 7, pp. 35–42.
- 42 T.X. Zhu: *Bubble Escape Model*, Private Communication, Hamilton, 2018.
- 43 K. Gu, N. Dogan, and K.S. Coley: *Metall. Mater. Trans. B Process Metall. Mater. Process. Sci.*, 2017, vol. 48, pp. 2595–606.
- 44 J. Biswas, K. Gu, and K.S. Coley: *Decarburization of Bloated Droplets: An Experimental Study to Understand the Kinetics of Decarburization of Metallic Iron*

*Droplets in FeO Containing CaO-SiO<sub>2</sub> Slags.*, McMaster University, Unpublished Research, 2020.

- 45 P.A.A. Distin, G.D.D. Hallett, and F. D. Richardson: *J. Iron Steel Inst.*, 1968, vol. August, pp. 821–33.
- 46 J.B. SEE and N.A. Warner: *J. Iron Steel Inst.*, 1973, vol. 211, pp. 44–52.
- 47 K. ITO and K. SANO: *Tetsu-to-Hagane*, 1965, vol. 51, pp. 1252–9.
- 48 H. Sun, K. Gao, V. Sahajwalla, K. Mori, and R.D. Pehlke: *ISIJ Int.*, 1999, vol. 39, pp. 1125–33.
- 49 H. Gaye and P. V. Riboud: *Metall. Trans. B*, 1977, vol. 8, pp. 409–15.
- 50 D.E. Woolley and U.B. Pal: *Ironmak. Steelmak.*, 2002, vol. 29, pp. 125–32.
- 51 U.B. Pal, S.A. Macdonald, D.W. Woolley, and A.C. Powell: *Metall. Mater. Trans. B*, 2005, vol. 36B, pp. 209–18.
- 52 K. Gu, N. Dogan, and K.S. Coley: *Metall. Mater. Trans. B*, 2018, vol. 49, pp. 1119–35.

## **Chapter 5**

### **5. Decarburization of iron carbon droplets with oxidizing slag: An experimental study to understand the effect of ionic and electronic conductivity on decarburization kinetics.**

As highlighted in previous chapters, most of the occasions when droplet decarburization was observed to shut down prematurely involved low conductivity slag. It is also noted that there is an enhancement of kinetics with ferric based slag and mixed ferric/ferrous slag. Chapter 5 presents a systematic experimental study to observe the effect of slag ionic and electronic conductivity on droplet decarburization and bloating.

In chapter 5, all the experiments and an initial analysis of the data was performed by me. The data analysis and the related kinetic model were derived jointly through extensive discussion with Dr. Coley. The manuscript was originally prepared by me and proofreading was done by Dr. Coley.

This manuscript was submitted to Metallurgical and Materials Transaction B on 7<sup>th</sup> Sept 2021 and currently under review.

#### **Abstract**

An experimental study has been performed to investigate the effect of ionic and electronic conductivity of oxidizing slags on the kinetics of decarburization of liquid metal droplets. An approach based on Wagner's Oxidation theory was developed to analyze the reaction kinetics with the variation of the slag conductivity. Despite the sufficiency of reactants, a

sudden shut down of decarburization reaction was observed for lower conductivity slag, whereas the reaction reached near to thermodynamic equilibrium where the conductivity was higher. Based on this observation, a mechanism of accumulation of charge at the slag/metal interface has been proposed as the cause of premature shutdown of the reaction. Whilst increasing basicity was also found to accelerate reaction kinetics and to eliminate or mitigate against premature shutdown of the reaction, it made no difference for slags of high electronic conductivity. This observation suggests that the desired rate of decarburization can be attained at lower basicity if the electronic conductivity of the slag is high.

## **5.1. Introduction**

The rate of decarburization of liquid metal droplets in the slag/gas/metal emulsion plays a crucial role in oxygen steel making. The kinetics of this reaction determines the bloating behavior of individual metal droplets, which in turn will decide the overall rate of refining by increasing the slag/metal interfacial area and the residence time of the droplets in the emulsion<sup>[1,2]</sup>. There have been several studies performed to understand droplet decarburization kinetics in oxidizing gases<sup>[3-9]</sup> and in oxidizing slag<sup>[10-12]</sup>. In case of decarburization of droplets in oxidizing gases, mass transport in gas phase is reported to be rate controlling until the carbon concentration drops below a critical value when the rate of reaction is controlled by the mass transfer in metal phase. For droplets in oxidizing slag, Min & Fruehan<sup>[12]</sup> reported the decarburization to be a mixed control reaction involving mass transport in slag, mass transfer in a gas halo and interfacial reaction kinetics. Whereas Molloseau & Fruehan<sup>[11]</sup> reported that in the case of an emulsified or bloated droplet (note

these workers employed the term emulsified, bloated was introduced by Brooks et al<sup>[11]</sup> reaction kinetics were controlled by mass transfer of FeO in slag. Gaye & Riboud<sup>[10]</sup> reported the reaction kinetics to be controlled by mass transport in slag, interfacial reaction and nucleation of CO bubbles. Based on the relationship between peak rate and droplet volume, Chen and Coley<sup>[13]</sup> proposed control by nucleation. Despite having decades of research to understand decarburization reaction kinetics, there have been very few systematic studies to understand the conduction behavior of slag in controlling the decarburization reaction kinetics. There have been some studies on the effect of electronic conduction on oxygen transport in the slag (Pal et al and others <sup>[14-16]</sup>).

Several decades ago, Ramachandran *et al.*<sup>[17]</sup> studied desulfurization kinetics between carbon-saturated iron and slags and proposed an electrochemical mechanism for sulfur transfer. Gare & Hazeldean<sup>[18]</sup> conducted a study to understand the reaction kinetics in ferric and ferrous based slags and proposed the possibility of electrochemical reaction at the slag/metal interface in the context of a local electrocapillary effect caused by charge separation and accumulation of oxygen near the anode which was acting as a CO nucleation site. They also found that the decarburization progressed to very low carbon concentration by reaction with ferric based slag whereas decarburization ended at quite high carbon concentrations for reaction with ferrous based slag. In the latter case the decarburization reaction stopped without coming close to equilibrium. Murthy *et al.*<sup>[15]</sup> investigated the reduction behavior of FeO in CaO-SiO<sub>2</sub>-Al<sub>2</sub>O<sub>3</sub>-X slags by iron-carbon droplets and reported that when droplet carbon concentration is greater than 2-3% in the droplet, gas film diffusion was the rate controlling step and below that carbon level, an electrochemical

transport barrier was controlling the rate. They also studied the effect on decarburization, of altering the electronic conductivity of the slag by addition of transition metal oxides –  $\text{TiO}_2$  (0 to 5.2%) and  $\text{Nb}_2\text{O}_5$  (1.79%). They observed an increase in rate with addition of transition metal oxides. On increasing  $\text{TiO}_2$  from 0 to 5.2%, they observed the kinetics to be fastest at 2.97%  $\text{TiO}_2$ . Despite the enhancement of kinetics by adding transition metal oxides, the decarburization reaction was found to cease below 2% carbon concentration; again, this was long before reaching equilibrium. In another article, Murthy *et al.*<sup>[19]</sup> presented the effect of varying slag FeO concentration and temperature on the rate of FeO reduction. Woolley & Pal<sup>[14,20,21]</sup> performed experimental studies to understand the electrochemical nature of reaction between carbon in the metal and FeO in slag and reported  $\text{Fe}^{2+}$  transport in slag to be the rate determining step. These workers proposed an enhancement of reaction kinetics by applying a DC voltage. Recently, Judge *et al.*<sup>[22,23]</sup> performed an electrochemical study to demonstrate the possibility of electrorefining of liquid iron and assessed the potential of calcium-aluminate and calcium-silicate slags to support electrolysis. These workers<sup>[24]</sup> identified the presence of an electrochemical double layer at the molten iron(carbon free) in slag and estimated the Nernst diffusion layer thickness, potentials zero charge, excess charge density and electrocapillary curves. Several groups of workers<sup>[25–29]</sup> studied the effect, on oxygen permeability of slag, by varying ionic and electronic conductivity. Speelman *et al.*<sup>[28]</sup> proposed that the oxygen transport in the slag was limited by conduction of electrons in the slag. Guo *et al.*<sup>[27]</sup> and Pal *et al.*<sup>[25]</sup> observed an increase in permeability of oxygen with addition of  $\text{Fe}_2\text{O}_3$  to the slag(Pure PbO or PbO-SiO<sub>2</sub> melt). To develop a deeper understanding of the effect of

electronic properties on oxygen transport in slag, systematic collection of experimental data is required. The current work is focused on a detailed kinetic study to understand the way in which decarburization kinetics are affected by slag conductivity. This work is part of a larger project to develop a kinetic model for the decarburization to predict bloating of iron-carbon droplets<sup>[30][31]</sup> and is specifically intended to address observations regarding the effect of slag conductivity from earlier work by the authors<sup>[32]</sup>.

In the current work a systematic investigation was performed to understand the effect of varying the ionic and electronic conductivity of the slag on the decarburization kinetics. A detailed study has been performed by varying the total Fe content and basicity of the slag at different ferric ratios. A kinetic model based on Wagner's Oxidation theory has been applied to explain the variation in reaction kinetics with the variation of slag conductivity. A mechanism has been proposed to explain the premature cessation of the decarburization reaction for low conductivity slags.

## **5.2. Experimental Technique**

The experimental technique used in the current work was identical to that reported elsewhere<sup>[31,33]</sup>. The details are reproduced below for the convenience of the reader.

### **5.2.1. Sample Preparation**

To prepare the metal droplets, an alloy mixture of high purity electrolytic iron, graphite and Fe-S alloy were melted in a vertical tube furnace at 1550°C and homogenized for 1 hour under constant flow of Argon. Cylindrical sections of  $2 \pm 0.01$  g were prepared by pipetting the alloy melt with quartz tubes, quenching in water, cutting. These cylindrical



sections were remelted in Electric Arc Melter to produce droplets. The composition of these droplets was confirmed to be  $2.5 \pm 0.01$  % C and  $0.011 \pm 0.001$  %S by LECO C & S Analyzer.

To prepare the slag samples, CaO, SiO<sub>2</sub> and Al<sub>2</sub>O<sub>3</sub> powders were premelted in specific proportions in a box furnace at 1550°C in platinum crucible, homogenized for 1.5 hours, quenched and then crushed. During the experiment, these premelted slag mixture were mixed with FeO and Fe<sub>2</sub>O<sub>3</sub> slag powders as per the requirement of total Fe content and ferric fraction in the slag and placed  $25 \pm 0.5$  g of the slag in an alumina crucible in the furnace for individual experiments. The total Fe<sub>t</sub>O content in the slag were varied for 2.5%, 5%, 10% and 16% for three different ferric ratios (0, 0.5 and 1). For 16% Fe<sub>t</sub>O concentration, experiments were performed for additional two ferric ratios 0.25 and 0.75. The V-ratio of the slag were varied between 0.9 to 2 for three different ferric ratios 0, 0.5 and 1. To validate the slag composition uniformity, the composition of the slag after premelting one time and two times were compared with Inductively Coupled Plasma Optical Emission Spectroscopy (ICP-OES) and confirmed that one-time premelting and homogenization for 1.5 hours was sufficient to achieve desired composition and homogeneity. The initial ferric fraction of the slags was confirmed by collecting slag samples from blank experiments. In these experiments, three of the slag compositions used in the kinetic experiments, were heated under the same conditions as for kinetic experiments. These slags were sampled by pipetting into silica sampling tubes and quenching. The samples were dissolved in acid under flowing argon and subsequently titrated to determine the ferric fraction. The measured ferric fraction as presented in Table

1 shows a close match with the values calculated from mass ratio of FeO to Fe<sub>2</sub>O<sub>3</sub>. The authors did not conduct blank experiments for other cases, so have assumed as the charged values. The ferric fraction in the pure iron oxide powder were calculated from the lattice parameter<sup>[34]</sup> determined from X-ray diffraction. The ferric fraction was estimated of 0.15 in the iron oxide powder which is consistent with the ferric fraction value measured from titration in slag.

Table 5.1: Expected ferric fraction based on FeO, Fe<sub>2</sub>O<sub>3</sub> mass ratio vs measured value

| <b>Slag Mixture</b>  | <b>Expected Fe<sup>3+</sup>/Fe from mass ratio</b> | <b>Fe<sup>3+</sup>/Fe from Blank Experiments</b> |
|--|--|--|
| CaO-SiO <sub>2</sub> -Al <sub>2</sub> O <sub>3</sub> -FeO                                    | 0.0  | 0.1  |
| CaO-SiO <sub>2</sub> -Al <sub>2</sub> O <sub>3</sub> -FeO-<br>Fe <sub>2</sub> O <sub>3</sub> | 0.5  | 0.5  |
| CaO-SiO <sub>2</sub> -Al <sub>2</sub> O <sub>3</sub> -Fe <sub>2</sub> O <sub>3</sub>         | 1.0  | 0.8  |

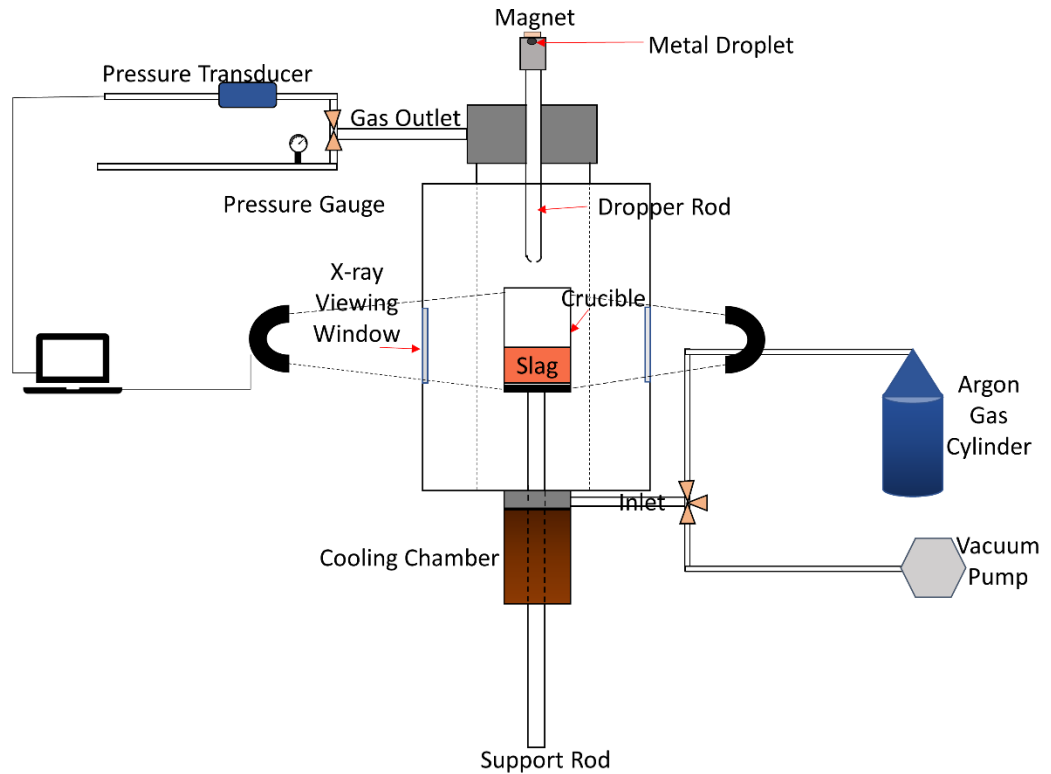


Figure 5.1: Schematic of experimental set up

### 5.2.2. Apparatus

A resistance heated vertical furnace with 80 mm inner diameter alumina tube was equipped with an X-ray fluoroscopy imaging unit, a pressure transducer, and a computer to record the pressure data. A schematic of this set up is presented in Figure 5.1. The length of the hot zone of the tube furnace was measured to exist across 3 cm height at higher temperatures (1500°C, 1550°C and 1600°C) with  $\pm 1^\circ\text{C}$  temperature difference. The furnace had a viewing window aligning with the hot zone and the X-ray device was set up

in the same alignment so that the dynamic behavior in the crucible during reactions can be captured. To record the pressure variation due to CO generation during decarburization, a differential pressure transducer having maximum pressure limit of 13.8 kPa (FLW Southeast, Inc, 157C-W050NR, Very Low-Pressure Transducer) with sensitivity of  $3 \times 10^{-5}$  atm was connected with the sealed reaction chamber. The pressure variation data recorded in pounds per square inch was converted into CO moles using constant volume pressure increase (CVPI) technique assuming no other gas was possible at that temperature based on thermodynamic assessment.

### **5.2.3. Procedure**

To begin experiment, a 99.99% pure alumina crucible with outer diameter of 40mm, loaded with 25 g of slag was placed from the bottom of the furnace to the hot zone of the furnace using a support rod. A metal droplet was placed at the top of the furnace with a magnet. The sealed furnace is then evacuated and backfilled with argon. The argon was flowed through a refining channel consisting of Titanium turnings and drierite column to remove moisture and oxygen. The furnace was heated under constant flow of argon (at 112 ml/min flow rate) at a heating rate of 2.5°C/min till 100°C, 5°C/min till 200°C and 10°C/min till desired temperature. At the desired temperature the slag was homogenized for 30 minutes and the argon flow was stopped followed by sealing of the furnace chamber. As soon as the magnet was removed to drop the droplet through the dropper tube, recording of pressure data and X-ray video was started and continued till the reaction nearly stops. After the desired period of reaction, the recordings were stopped, and the crucible loaded with reacted slag and droplet were quenched. The pressure data were converted to moles of CO

based on the final carbon concentration of the droplet which were measured in LECO carbon sulfur analyzer. The total CO gas generation data in moles were averaged for each second (10 data points in 1 s) without altering the features and presented here.

## 5.3. Results

### 5.3.1. Ferric Fraction Variation

A set of decarburization experiments were performed to analyze the effect of electronic conductivity on the peak rate of decarburization and bloating of iron carbon droplets. The variation in electronic conductivity was achieved by varying the ferric to ferrous ratio in the slag. In each experiment, a 2 g liquid metal droplet of composition Fe - 2.5%C-0.01%S, was reacted with a slag of basicity ( $V_{ratio} = \frac{CaO}{SiO_2}$ ) 0.9 and 16% Fe<sub>2</sub>O (total iron oxide concentration normalized to FeO) at 1505<sup>0</sup>C. The ferric fraction (Fe<sup>3+</sup>/Fe) in the slag was in the range 0.1 to 0.8.

The cumulative CO generation profiles with time for different ferric fractions ( $\frac{Fe^{3+}}{Fe^{2+}+Fe^{3+}}$ ) are presented in Figure 5.2(a). All the CO generation curves in Figure 5.2(a) show<sup>[35]</sup> a relatively constant decarburization rate(i.e. peak decarburization period / steady state) sharply transitioning to a very slow rate or even complete cessation. The peak rate of decarburization has been plotted against  $\frac{Fe^{3+}}{Fe^{2+}+Fe^{3+}}$  in Figure 5.2 (b). This figure shows that the rate goes through a maximum at  $\frac{Fe^{3+}}{Fe^{2+}+Fe^{3+}} = 0.5$  which also coincides with the highest electronic conductivity<sup>[32]</sup>. It can be observed that the peak rates with Fe<sup>3+</sup> rich slag are higher than for Fe<sup>2+</sup> rich slag. This is likely due to the higher oxygen potential in Fe<sup>3+</sup>

rich slag which will at least partially compensate for a low electronic conductivity. The extent of decarburization is also highest at  $\frac{Fe^{3+}}{Fe^{2+}+Fe^{3+}}=0.5$  and comparatively higher for  $Fe^{3+}$  rich slag than  $Fe^{2+}$  rich slag. The carbon concentration of the reacted droplet with  $\frac{Fe^{3+}}{Fe^{2+}+Fe^{3+}}=0.5$  slag was close to thermodynamic equilibrium whereas in other all other cases the reaction ceased at carbon concentrations quite far from equilibrium.

The normalized volume of CO retained in the droplet for different slag ferric fractions is presented with respect to time in Figure 5.3. The normalized retained gas volume was calculated by dividing the increase in droplet volume, obtained from the 2-D X-ray video, by the original volume of the droplet. The volume calibration was performed based on the 0<sup>th</sup> second droplet volume, using ImageJ software. This procedure can be expressed as

$$\text{Normalized Retained Volume} = \frac{V(t)-V(0)}{V(0)} = \frac{\text{Retained CO Volume}}{\text{Original Volume}} \quad [5.1]$$

Bloating of a reacting metal droplet depends on the balance between rate of gas generation and rate of escape. The rate of escape of gas bubbles from the metal droplet is dependent on the metal droplet surface tension, viscosity and average bubble size, and most importantly the force applied by on-going gas generation inside the droplet. The bloating behavior (Figure 5.3) of droplets, shows that internal decarburization continued for the longest time for slag having ferric fraction 0.5. This may be interpreted as the slag continuing to transport oxygen to the metal droplet for longer so that internal decarburization can continue, whereas the oxygen supply stopped within approximately 20 seconds of the reaction period in the other cases presented in Figure 5.3.

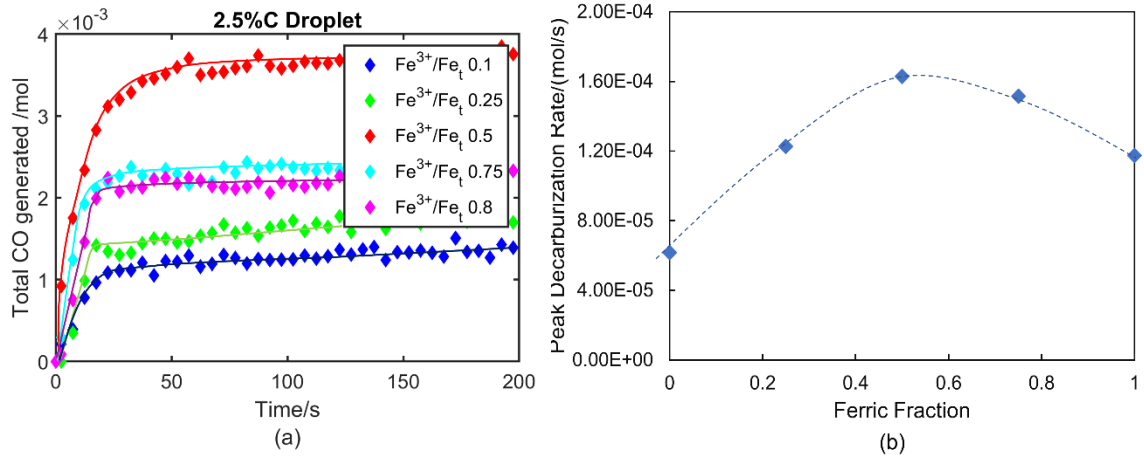


Figure 5.2: (a) Total CO gas generation with time and (b) Peak rate variation on varying ferric fraction in the slag

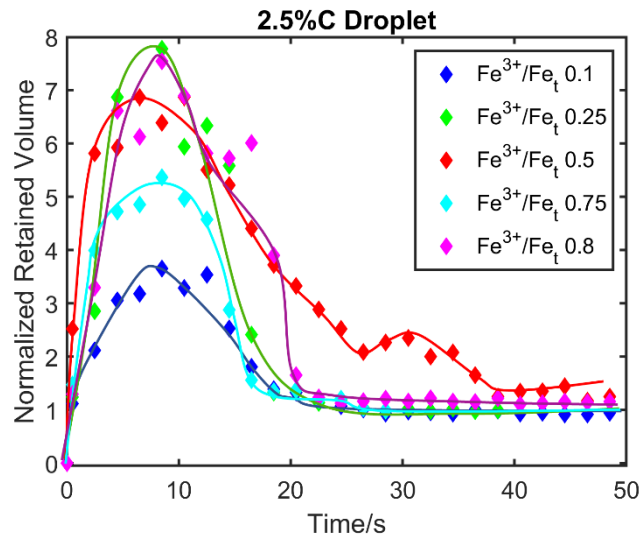


Figure 5.3: Normalized retained volume profile variation with time on varying ferric fraction in the slag

### 5.3.2. Slag Fe<sub>t</sub>O Variation at different Ferric Ratios

Decarburization experiments were conducted for a range of Fe<sub>t</sub>O concentration (2.5%, 5%, 10% and 16%) at three different ferric ratios to understand the interdependence between oxygen transport, ionic conductivity and electronic conductivity. Metal droplets of composition Fe - 2.5% C- 0.01% S were reacted at 1505°C with each of the slag compositions in this set. The peak decarburization rate is plotted in Figure 5.4, against the slag Fe<sub>t</sub>O concentration for three different ferric fractions,  $\frac{Fe^{3+}}{Fe^{2+}+Fe^{3+}} = 0.1, 0.5, 0.8$ . This figure shows that the rate of increase of the peak rate of decarburization with increasing Fe<sub>t</sub>O concentration in the slag was highest for ferric ratio,  $\frac{Fe^{3+}}{Fe^{2+}+Fe^{3+}} = 0.5$ , followed by ferric ratio = 1 and then ferric ratio = 0. The peak rate of decarburization was higher for ferric ratio = 0.5 for 10% and 16% Fe<sub>t</sub>O concentration compared to the cases with ferric ratio 0.1 and 0.8, whereas the peak rates were very close for different ferric ratios for lower Fe<sub>t</sub>O concentration slag.

It is to be noted that reaction reached near to completion for 16% Fe<sub>t</sub>O and 0.5 ferric ratio, whereas in the lower oxidizing potential cases till the time (8 min) the droplets were quenched the reaction was observed to continue for ferric ratio 0.5 in contrast to the observation for other ferric ratios.



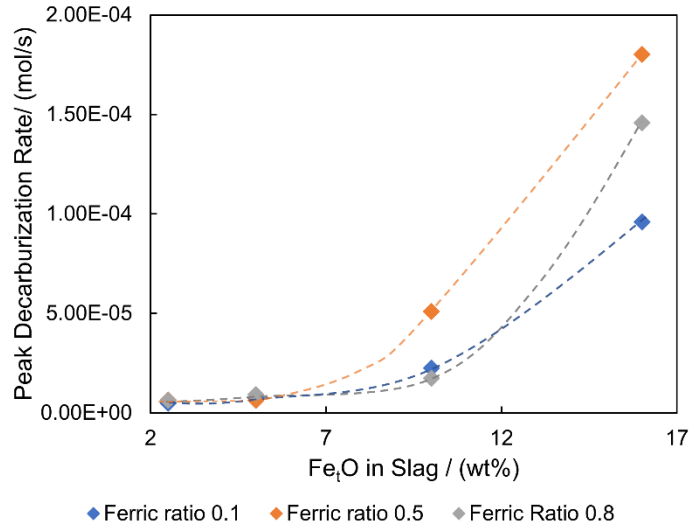


Figure 5.4: Variation in the peak decarburization rate on varying slag Fe<sub>2</sub>O<sub>3</sub> concentration at three ferric ratios

### 5.3.3. Slag Basicity Variation at different Ferric Ratios

A series of decarburization experiments were performed for 2 g droplets with 2.5% C and 0.01% S reacting with slags with CaO/SiO<sub>2</sub> 0.9, 1.5 and 2) at three different ferric ratios ( $\frac{Fe^{3+}}{Fe^{2+}+Fe^{3+}} = 0.1, 0.5 \text{ and } 0.8$ ) at 1505°C. The total CO generation with time for these experiments is plotted in Figure 5.5. The peak rate of decarburization increased with increasing basicity for ferric ratio 0.1 and 0.8, whereas for ferric ratio 0.5, there was a negligible change in the peak rate with basicity. The decarburization profiles for basicity 1.5 and 2 almost overlap (within the range of error limit) for ferric fraction 0.8.

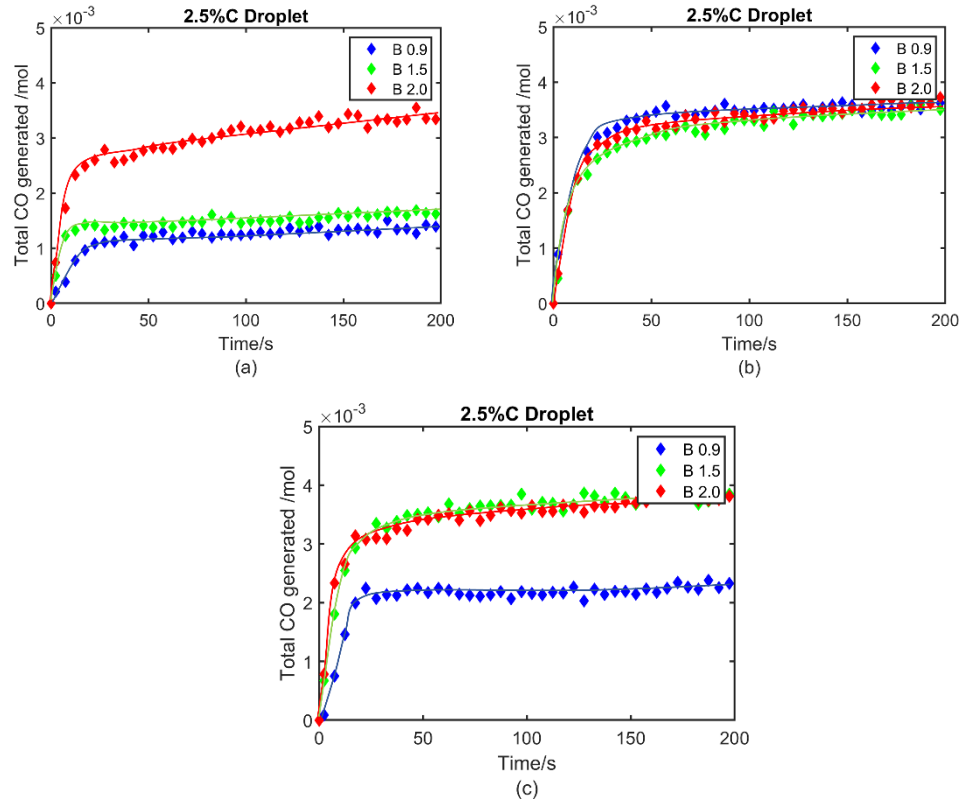


Figure 5.5: Variation in the decarburization profile on varying slag basicity concentration at three ferric ratio 0.1, 0.5 and 0.8 in (a), (b), (c) respectively

## 5.4. Discussion

The decarburization profiles presented in Figure 5.2 for different ferric fractions at 16 % Fe<sub>2</sub>O suggest that there is a significant effect of the electrical conductivity of the slag on the reaction kinetics. The occurrence of the maximum rate at a ferric fraction of 0.5, which also represents a maximum in electronic conductivity<sup>[32]</sup>, suggests a strong role of electronic conduction in the reaction mechanism. The influence of basicity also suggests a role for ionic conduction. To analyze these effects, the ionic and electronic conductivity of each of the slags has been calculated for the relevant conditions. The ionic conductivity

has been evaluated from the Nernst Einstein relationship, assuming the  $\text{Ca}^{2+}$  and  $\text{Fe}^{2+}$  to be the only significant ionic charge carriers<sup>[36-38]</sup>. The electronic conductivity of the slag was calculated using the diffusion assisted charge transfer model of Barati and Coley<sup>[32]</sup>. When the electronic conductivity was very high, the droplet initially containing 2.5% C reacted until coming very close to thermodynamic equilibrium (~ 0.06%) whereas with low electronic conductivity slag the reaction for a droplet of identical starting composition, stopped at 1.49% C. The results presented in Figures 5.2(a) and (b) also show that, with increasing slag electronic conductivity, the peak rate of decarburization increased. The observed premature shutdown of reaction for low conductivity slags is consistent with the results obtained in a previous study by the current authors<sup>[31]</sup> for a range of carbon concentration (0.5% C to 4.4% C). Based on the current observations and those from the authors' previous study<sup>[31]</sup>, a kinetic analysis has been performed to explain the rate controlling step in section 5.4.1, in section 5.4.2 a kinetic model involving ionic and electronic conductivity is proposed along with kinetic analysis and in section 5.4.3, a mechanism is proposed to explain the premature shutdown of decarburization.

#### **5.4.1. Rate Controlling step Analysis**

Decarburization of a droplet with oxidizing slag involves multiples kinetic steps – mass transport in slag, interfacial chemical reaction, nucleation and growth of bubbles within the metal. A mixed controlled kinetic model was developed by the current authors involving all the above-mentioned kinetic steps. To analyze the effect of individual kinetic steps involved in the decarburization reaction of a droplet in oxidizing slag, previously developed model by the current authors<sup>[30]</sup> is employed for different ferric fraction slags.

To consider the effect of variation of slag conductivity, the only kinetic parameter i.e. the slag mass transfer coefficient was varied within a range of  $3 \times 10^{-5}$  m/s to  $1.4 \times 10^{-5}$  m/s to predict the CO generation rate. The model prediction agrees very well with the experimental results considering that only the slag mass transfer coefficient was adjusted to match the results. This is entirely in keeping with the fact that the changes made to slag composition were designed to a specifically target slag transport properties. The model predictions and the experimental data are compared in Figure 5.6. It is to be noted that model prediction is very good for the initial period of the reaction for all different cases, but as presented in the previous work<sup>[30]</sup>, the model fails to predict premature shutdown for lower conductivity slags. For the highest conductivity slag, the model fits the data very well over the entire reaction period. A tentative explanation based on charge accumulation is proposed in the section 5.4.3 to explain the disagreement at the end stage of decarburization for low conductivity slag. It would be fair in some cases to consider what the authors have termed premature shut down, as a dramatic slowing of the reaction because of a change in mechanism. Regardless of the terminology employed, the physics responsible for the shutdown are clearly not captured in the model which would suggest a change in mechanism. It is important to note that although the reaction is under mixed control the dominant step is mass transport in the slag. Some workers<sup>[12,39]</sup> have included a combination of gas/slag and gas/metal chemical reaction to explain the kinetics. These workers were typically operating at lower  $\text{Fe}_t\text{O}$  concentrations. On the other hand, Molloseau and Fruehan<sup>[11]</sup> who were working under similar conditions to the current work did not invoke a slag/gas, gas/metal reaction scheme and suggested that the reaction control

was dominated by slag mass transport. Notwithstanding the foregoing argument, the possibility of slag/gas reaction control is analyzed below.

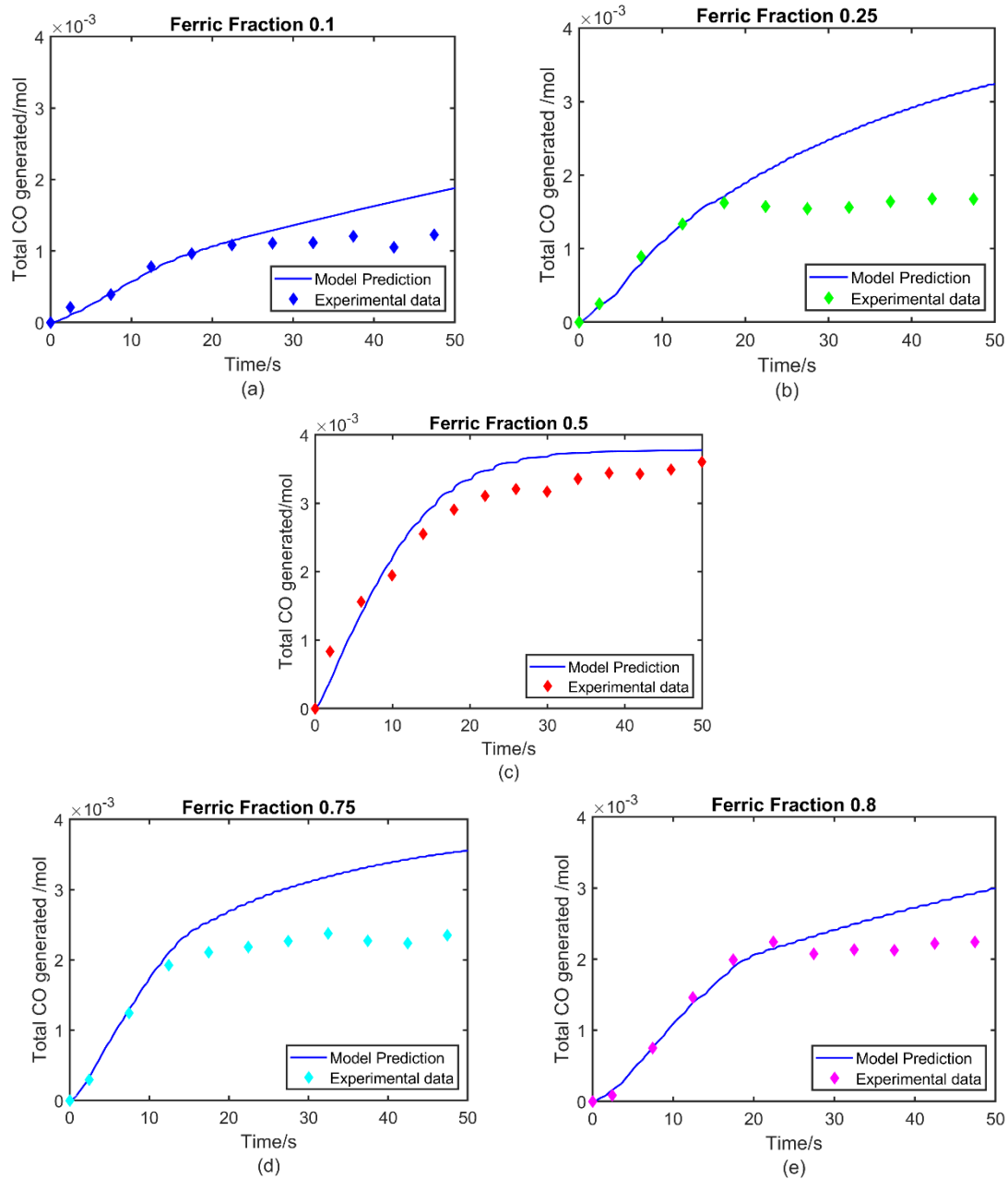


Figure 5.6: Prediction of total CO generation profiles for (a) ferric fraction 0.1 and (b) ferric fraction 0.25 (c) ferric fraction 0.5 (d) ferric fraction 0.75 and (b) ferric fraction 0.8 cases

As mentioned above, the authors have assumed that the slag/metal chemical reaction occurs by direct contact of slag and metal. This assumption is based on numerous experiments on this reaction system conducted in the authors laboratory<sup>[13,31,35,40]</sup>. Furthermore, this assumption is supported by predictions of the expected rate from the work of Sasaki et al.<sup>[41]</sup> and similar work<sup>[42]</sup> from the authors' own laboratory. The table below shows that in almost all cases, the decarburization rate measured is close to an order of magnitude greater than that predicted from the work of Sasaki et al.<sup>[41]</sup> and from Barati & Coley<sup>[42]</sup>. The authors submit that the overall rate can only be faster, than that for slag reaction with CO if the reaction actually proceeds by slag/metal contact rather than a gaseous intermediary. This is supported by visual observation by X-ray video although the resolution is such that these observations could not be deemed conclusive. In addition, the work of Molloseau and Fruehan<sup>[11]</sup> shows similar rates to those presented in the current work.

Table 5.2: Comparison of peak decarburization rate with possible gas/slag reaction rate

| Ferric Fraction | Peak Rate from experiments (mol/m <sup>2</sup> -s) | Rate of possible gas/slag reaction              |  |
|-----------------|--|---|--|
|                 |  | Correlation From Barati & Coley <sup>[42]</sup> | Correlation from Sasaki et al. <sup>[41]</sup> |
| 0.1             | 3.19E-01   | 3.21E-02  | 1.55E-01                                       |
| 0.25            | 6.33E-01   | 3.41E-03  | 1.64E-01                                       |
| 0.5             | 8.40E-01   | 9.60E-03  | 2.36E-02                                       |
| 0.75            | 7.81E-01   | 2.46E-05  | 1.67E-01                                       |
| 0.8             | 6.05E-01   | 9.44E-06  | 1.68E-01                                       |

### 5.4.2. Kinetic Model

In this section, a theoretical framework is developed to address electrochemical mass transport of oxygen in the slag and a steady state kinetic model is developed based on Wagner's oxidation theory<sup>[43]</sup> to introduce the effect of electronic and ionic conductivity on the transport of ions in the slag. This approach has been used by a number of other authors to describe oxygen transport in slag<sup>[15,25,27,43]</sup>.

Based on a qualitative assessment of the data presented in section 5.3, it is clear that an appropriate model of oxygen transport in the slag should consider the transport of ions in the presence of not only a chemical potential gradient but also due to the presence of an electrical field. It is important to consider both the effect of chemical and electrical potential gradient because the slag is an ionic melt and involves electron transfer while reacting with metal. In this regard we may take a similar approach to that taken by Wagner in the development of his model for oxidation of metals<sup>[15,25,27,43]</sup>. The flux ( $J_i$ ) of a charged species ( $i$ ) in an electrochemical potential gradient would be

$$J_i(\text{mol. m}^{-2} \cdot \text{s}^{-1}) = J_{chem} + J_{elec} = -\frac{\sigma_{tot} t_i}{(z_i F)^2} \left[ \frac{d\mu_i}{dx} + z_i F \frac{d\phi}{dx} \right] \dots \dots [5.2]$$

Where  $\sigma_{tot}$  is the total conductivity of slag,  $t_i$  is the transference no of species  $i$ ,  $z_i$  is the charge number of species  $i$ ,  $\frac{d\mu_i}{dx}$  is the chemical potential gradient of species  $i$ , and  $\frac{d\phi}{dx}$  is the electrical field. For high temperature systems, Wagner developed a theoretical equation to predict the rate of oxidation of metal assuming that mobilities of ions and electrons limit the kinetics. Based on Wagner's theory, an expression may be developed for the rate of



transport of oxygen in the slag, however, it is established convention in process metallurgy to express oxygen transport in the slag as the transport of FeO. Whilst the authors acknowledge that the latter approach is entirely phenomenological and does not represent the mechanism of transport, its widespread use confers some value in probing the relationship between the two approaches. Combining these approaches, yields Equation 5.3.

$$\frac{dn_{FeO}}{dt} = A_0 * \frac{\sigma_{ion} * \sigma_{el}}{(\sigma_{ion} + \sigma_{el})} * \frac{RT}{8F^2} * \left(\frac{1}{\Delta x}\right) d \ln p_{O_2} \dots \dots \dots [5.3]$$

For metal oxidation systems, the driving force for the transport of oxygen ions in the oxide layer is the difference in  $p_{O_2}$  between the gas/oxide and metal/oxide interface. For the current system, the driving force for transport of oxygen in slag is the difference in oxygen potential between the bulk slag and the slag/metal interface. With the variation of oxygen potential from slag/metal interface to bulk, there will also be a variation in ionic and electronic conductivity. The ionic and electronic conductivity<sup>[32,44,45]</sup> and the  $p_{O_2}$ <sup>[46-48]</sup> can be expressed as a function of ferric fraction ( $y = \frac{Fe^{3+}}{Fe^{2+} + Fe^{3+}}$ ) and introducing the relevant relations for each, Equation 5.3 can be integrated from the slag/metal interface to the bulk slag and the flux of FeO (mol/m<sup>2</sup>-s) can be expressed as

$$\frac{dn_{FeO}}{dt} = \frac{RT}{16F^2} * \left(\frac{A_1 a}{\Delta x}\right) \left[ \ln(\sigma_0 - ay + by(1 - y)) - \frac{a(a-b) + 2b\sigma_0}{a\sqrt{(a-b)^2 + 4b\sigma_0}} \ln \frac{2by + (a-b) - \sqrt{(a-b)^2 + 4b\sigma_0}}{2by + (a-b) + \sqrt{(a-b)^2 + 4b\sigma_0}} \right]_{s/m int}^{bulk} \dots [5.4]$$

Where  $A_1$ , is a function of slag composition and is typically in the range of 0.2 to 0.25,  $\sigma_0$ ,  $a$  and  $b$  are functions of slag composition but are independent of ferric fraction. The details of this integration and a comprehensive list of the parameters used in this paper are given

in Appendix A. To avoid having to repeat this long and cumbersome Equation, we will define the terms as follows

$$D^* = \frac{a}{2} \left[ \ln(\sigma_0 - ay + by(1 - y)) - \frac{a(a-b)+2b\sigma_0}{a\sqrt{(a-b)^2+4b\sigma_0}} \ln \frac{2by+(a-b)-\sqrt{(a-b)^2+4b\sigma_0}}{2by+(a-b)+\sqrt{(a-b)^2+4b\sigma_0}} \right]_{s/m int}^{bulk} \dots [5.5]$$

$$S = \frac{RT}{8F^2} * \left( \frac{A_1}{\Delta x} \right) \dots [5.6]$$

If one wants to think about the physical meaning of these terms,  $D^*$  combines the diffusivities with the electronic and ionic conductivities. Because it is not possible to separate the diffusivities and the conductivities from the driving force, this term also includes the chemical driving force for oxygen transport.  $S$  combines a number of known constants with the boundary layer thickness  $\Delta x$ . These constants are explained in more details in Appendix A. Equation 5.4 now can be written as

$$\frac{dn_{FeO}}{dt} = S * D^* \dots [5.7]$$

In this section, an analysis has been performed based on the kinetic model represented by Equation 5.7 to study the effect of slag conductivity during the initial decarburization period for cases where mass transfer of oxygen in the slag seems to control<sup>[30]</sup> the decarburization kinetics. During the initial decarburization period, the rate of CO generation is at a maximum i.e., ‘peak rate’. Based on previous work in the authors laboratory, the model employed in the current work showed that mass transport in the slag dominated the rate control during this period. In addition, during the initial period of reaction there is more certainty over slag composition and slag conductivity. For these reasons, the authors have chosen this period of the reaction to compare the rate with electrical properties of the slag according to Equation 5.4 and 5.7. From experimental

decarburization data, the  $\left(\frac{dn_{CO}}{dt}\right)_{max}$  can be determined and the term 'D\*' can also be calculated as presented in Equation 5.5, where  $\sigma_0$ ,  $a$  and  $b$  all vary as known functions of concentration of total Fe and  $Ca^{2+}$  ions in the slag. For the analysis,  $\left(\frac{dn_{CO}}{dt}\right)_{max}$  is plotted against D\*. To calculate D\*, the ferric fraction(y) must be known for both bulk slag and slag/metal interface. At the slag/metal interface, it has been assumed that the local ferric fraction(y) is controlled by the C/CO equilibrium and in the case of the bulk slag, the measured ferric fraction values were used as mentioned in Table 5.1 and for rest cases, the ratio of  $Fe_2O_3$  to FeO in the original mixture was used to determine this fraction.

*Case 1:* Figure 5.7 shows the variation of the 'Peak decarburization rate' with 'D\*' for a range of ferric ratio (between 0.1 to 0.8) at 16%  $Fe_2O$  slag. Figure 5.7 shows excellent agreement between theoretical calculation and experimentally measured decarburization rate for a range of ferric fraction. The electronic conductivity is maximum at  $Fe^{3+}/Fe$  of 0.5<sup>[32]</sup>. So, for slag with ferric fraction 0.5, the peak rate of decarburization was highest, and the decarburization also continued until close to the thermodynamic equilibrium. This latter observation is believed to be due to fast rate of charge dissipation in high electronic conductive slag as shown in Figure 5.2. In this case, the ionic conductivity of the slag being comparatively higher compared to the electronic conductivity (Nearly 10 times), the kinetics are possibly limited by the electronic transport of the slag.

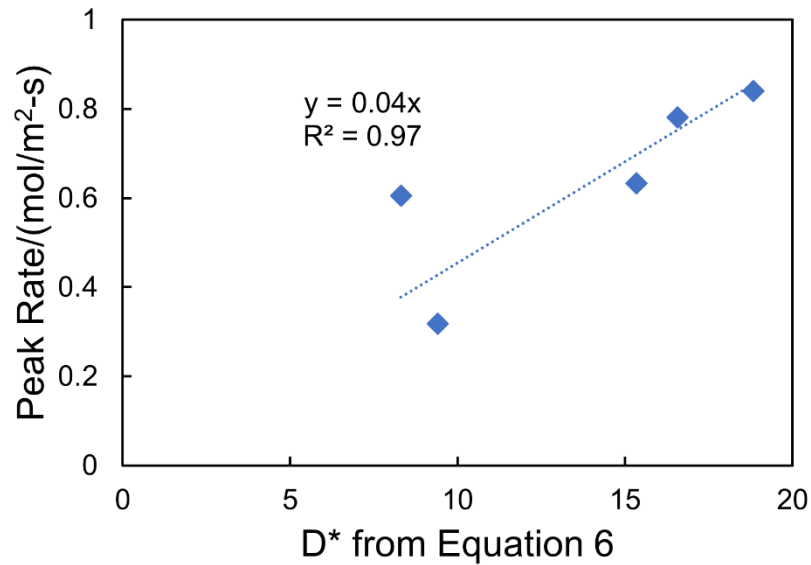


Figure 5.7: ‘Peak decarburization rate’ plotted against the calculated ‘D\*’ for a range of Ferric fractions at 16% Fe<sub>t</sub>O concentration in slag

Case 2: The ‘Peak decarburization rate’ vs ‘D\*’ plot is presented for variation of Fe<sub>t</sub>O concentration in the slag from 2.5% to 16% at a ferric ratio 0.1, 0.5 and 0.8 in Figure 5.8 (a), (b) and (c) respectively. It is to be observed that the decarburization rate follows the trends expected for electrochemical transport of oxygen in the slag including the effect of ionic and electronic conductivity. It may be further observed that the slope of the line(S) is higher for ferric fraction 0.1 whereas it is smaller for higher ferric fraction slags. The slope is  $\left(\frac{A_1}{\Delta x}\right) * constant$ . A<sub>1</sub> is typically in the range 0.2 to 0.25<sup>[32,48]</sup>. The slope includes (1/Δx) and Δx may vary with slag viscosity. But again the slag viscosity changes between ferric fraction of 0.1 to 0.5 is less than 10 percent<sup>[49]</sup> making it difficult to justify the almost three fold change in slope.

From Figure 5.4, the maximum decarburization rate increases sharply with increasing  $\text{Fe}_t\text{O}$  concentration in the slag. Barati & Coley<sup>[50]</sup> showed that the electronic conductivity of slag increases with  $\text{Fe}_t\text{O}$  concentration to the power 2. At low  $\text{Fe}_t\text{O}$  concentration in the slag, the electronic conductivity is very low due to a low concentration of ferric and ferrous ions. So, the effect of variation of ferric fraction ( $\frac{\text{Fe}^{3+}}{\text{Fe}^{2+} + \text{Fe}^{3+}}$ ) on the decarburization rate is not significant. However, as the  $\text{Fe}_t\text{O}$  concentration in the slag increases, the influence of ferric fraction ( $\frac{\text{Fe}^{3+}}{\text{Fe}^{2+} + \text{Fe}^{3+}}$ ) on electronic conductivity becomes significant. Therefore, its effect on decarburization kinetics is also prominent.

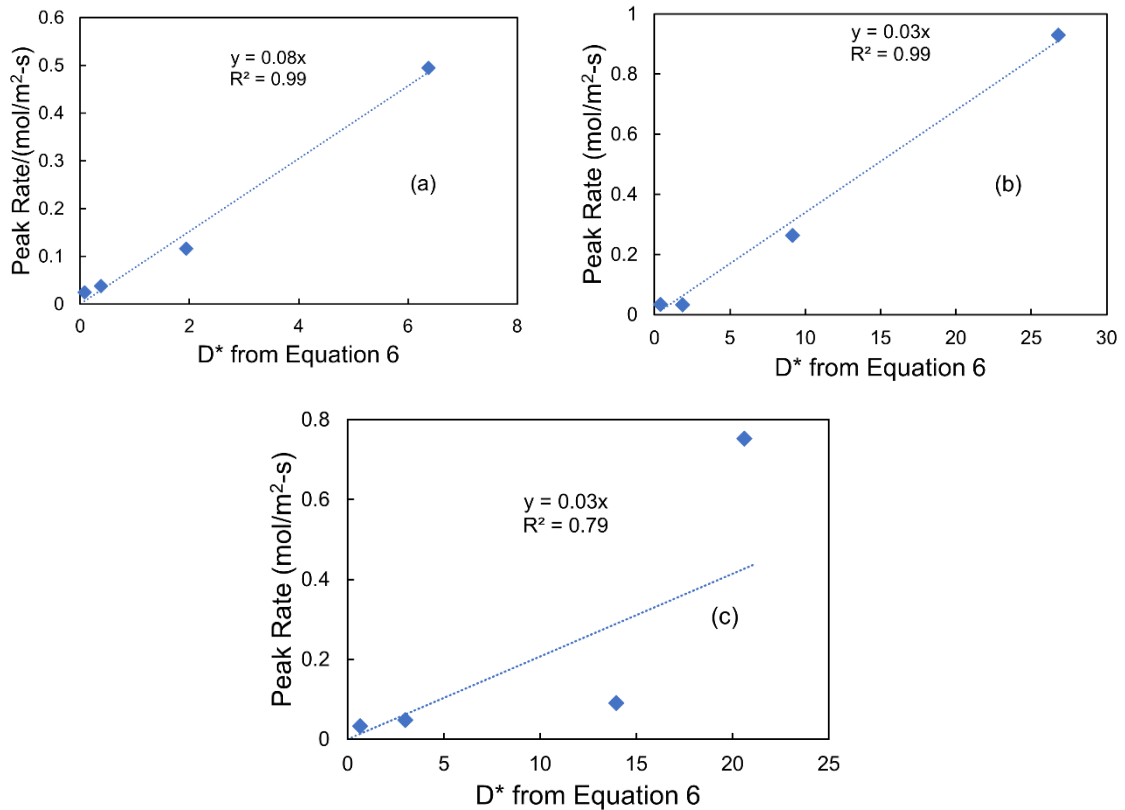


Figure 5.8: ‘Peak decarburization rate’ plotted against the calculated ‘D\*’ for a range of Fe<sub>2</sub>O concentration in the slag at Ferric fraction 0.1, 0.5 and 0.8 in (a), (b), (c) respectively

*Case 3:* The study of decarburization with increasing basicity shows that there is a significant effect at ferric ratio 0.1 and 0.8, whereas from Figure 5.5, it appears that for ferric ratio 0.5, slag transport is sufficiently fast that either does not control the decarburization kinetics or that further increases in basicity do not significantly alter the rate of oxygen transport. With increasing basicity, a significant increase in slag transport properties is expected due to depolymerization of silica network. This results in higher ionic conductivity in slags with higher basicity<sup>[32,37]</sup>. However, for a ferric ratio 0.5, the

electronic conductivity being very high regardless of the basicity, the influence of the increase in ionic transport due to high basicity is insignificant. Whereas in lower electronic conductivity systems ( $\frac{Fe^{3+}}{Fe^{2+}+Fe^{3+}}$  0.1 and 0.8), the ionic conductivity has a significant effect on the kinetics of decarburization as presented in Figure 5.5. So, the kinetic model as presented in Equation 5.7 is applied only for the ferric fractions 0.1 and 0.8 in Figure 5.9, showing a fairly good agreement. As previously discussed, similar observation of smaller slope with higher ferric fraction slag is found in Figure 5.9.

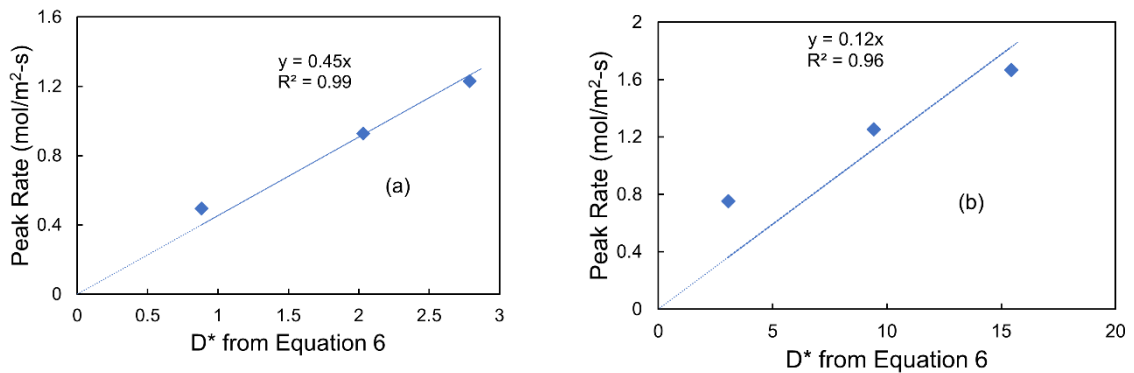


Figure 5.9: ‘Peak decarburization rate’ plotted against the calculated ‘D\*’ for a range of basicity in the slag at ferric fraction 0.1 and 0.8 in (a), (b) respectively

This analysis suggests that it is important to include the effect of ionic and electronic conductivity on oxygen transport in slag. However, Equation 5.4 used for the foregoing analysis is rather cumbersome but is required to fully take account of the dependence of  $\sigma_{ion}$  and  $\sigma_{el}$  on the ferric fraction. If it is possible to assume that the bulk values of  $\sigma_{ion}$  and  $\sigma_{el}$ , are relatively constant across the boundary layer, then the integration of Equation 5.3 becomes much simpler resulting in Equation 5.8.

$$\frac{dn_{FeO}}{dt} = \frac{\sigma_{ion} * \sigma_{el}}{(\sigma_{ion} + \sigma_{el})} * \frac{RT}{8F^2} * \left(\frac{1}{\Delta x}\right) (\ln p_{O_2}^{bulk} - \ln p_{O_2}^{int}) \dots [5.8]$$

This equation can be expressed in a similar way to Equation 5.4 as a function of  $y$ ,  $A_1$ ,  $\sigma_0$ ,  $a$  and  $b$

$$\frac{dn_{FeO}}{dt} = \frac{(\sigma_0 - ay) * by(1 - y)}{(\sigma_0 - ay + by(1 - y))} * \frac{RT}{8F^2} * \left(\frac{1}{\Delta x}\right) A_1 \left[ \ln \frac{y}{1 - y} \right]_{s/m int}^{bulk} \dots [5.9]$$

Following the practice employed for Equation 5.7, this equation can be further divided into two terms  $D_1^*$  and  $S$  where

$$D_1^* = \frac{(\sigma_0 - ay) * by(1 - y)}{(\sigma_0 - ay + by(1 - y))} \left[ \ln \frac{y}{1 - y} \right]_{s/m int}^{bulk} \text{ and } S = \frac{RT}{8F^2} * \left(\frac{A_1}{\Delta x}\right) \dots [5.10]$$

The first term includes the driving force and the slag conductivity, and the second term is the slope which consists of a number of known constants (as previously shown in Equation 5.7). Equation 5.8 may be expressed as

$$\frac{dn_{FeO}}{dt} = S * D_1^* \dots [5.11]$$

To verify the validity of this approach, the peak rate is plotted against  $D_1^*$  in Figure 5.10 using the experimental data originally presented in Figure 5.7. This plot demonstrates a very poor correlation further suggesting the importance of including the ionic and electronic conductivity effect.



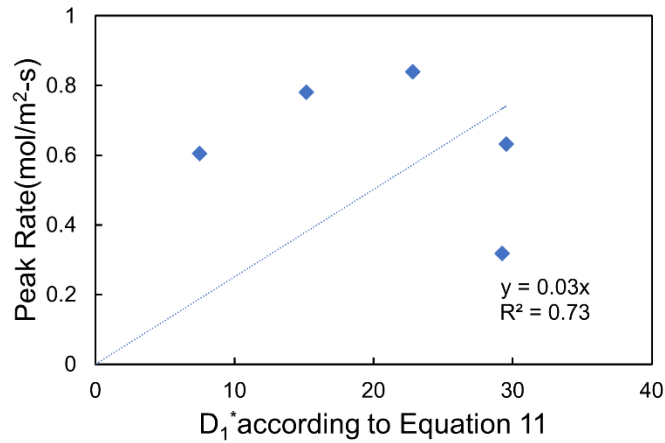


Figure 5.10: ‘Peak decarburization rate’ plotted against the calculated ‘ $D_1^*$ ’ for a range of ferric fractions at 16% Fe<sub>2</sub>O concentration in slag

It is common to employ Equation 5.12 in calculating oxygen transport in slag and in particular Fruehan & Co-workers<sup>[11,12]</sup> have successfully employed this method in a similar situation to the current work.

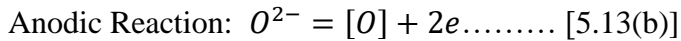
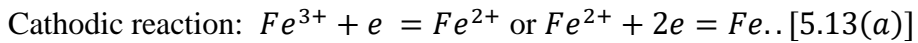
$$\frac{dn_{FeO}}{dt} = k_s \Delta C_{FeO} \dots \dots [5.12]$$

Where  $k_s$  is the mass transfer coefficient in slag. The reason for considerable success of Equation 5.12 could be that metallurgical industries deals with mostly highly conducting slag systems such as in BOF the slag is highly basic and highly electronic conducting.

### 5.4.3. Proposed Mechanism for Premature Shutdown:

When a liquid iron carbon droplet reacts with oxidizing slag, the reaction happens through several steps some of which involve transfer of electrons. Typically, slags may conduct through ionic conduction or, if multivalent ions are present, they can conduct electronically

through charge hopping<sup>[37,45]</sup>. At the slag metal interface, possible electron transfer reactions may occur:



Depending on the difference in the rate of transport of different charged species and the relative rates of the reactions which produce and consume electrons, there is a possibility of accumulation of charge at the slag/metal interface. This accumulation may create a barrier to transport, and to further reaction. This barrier will be dissipated if the slag is sufficiently conductive. Whereas in case of lower conductivity slag, a local charge build up may cause a local electric field at the surface of the metal droplet, thereby inhibiting the reaction. Depending upon the variation in electronic and ionic conductivity of the slag, the rate of charge build up will vary and will determine the point at which the reaction stops. At this point, it is worth considering the various factors effecting conductivity. Electronic conductivity in iron oxide containing slags is typically controlled by the total iron content and the ferric fraction<sup>[32]</sup>. The ionic conductivity is typically controlled by the concentration of  $Ca^{2+}$  and  $Fe^{2+}$  cations<sup>[36-38]</sup> and their mobilities. The latter being strongly influenced by the viscosity of the slag. The interplay between these different factors and the way in which they are influenced by changing oxygen potential and slag composition leads to a complex picture of changing conductivity. For example, increasing the oxygen potential will initially increase the electronic conductivity as the ferric ratio increases, decreases again once the ferric ratio reaches 0.5. The same increase in oxygen potential will decrease the

ionic conductivity as  $\text{Fe}^{2+}$  is converted to  $\text{Fe}^{3+}$  and the viscosity is increased. Increasing the basicity will increase the ionic conductivity because of the increased concentration of  $\text{Ca}^{2+}$  as well as the decreased viscosity. The former effect is expected to be less important in the current case, because as a non-reducible ion  $\text{Ca}^{2+}$  will make no contribution to DC conductivity after initial polarization. Increasing total iron oxide concentration will increase both ionic and electronic conductivity of the slag.

If we examine each of these factors in the context of the results shown in Figures 5.2 and 5.5, we may develop some understanding of the premature shutdown of the reaction. The data presented in Figure 5.2 shows that premature shutdown occurs for low conductivity slags; those with ferric ratios close to 0.1 and those approaching 0.8. Whereas, in the case of high conductivity slag with ferric fraction 0.5, the reaction approaches thermodynamic equilibrium. These observations are consistent with the idea that charge accumulation at slag metal interface is responsible for the premature shutdown of the reaction. If we now consider the data presented in Figure 5.5, we see that in the case of higher basicity slags the reaction approaches equilibrium regardless of ferric fraction. This observation suggests that ionic conduction may also contribute to charge dissipation. In which case the contribution of basicity must be to the mobility of the  $\text{Fe}^{2+}$  ions. It is worth noting that for ferric ratio of 0.5 the basicity has no effect on the extent or rate of decarburization. This would suggest that highly conducting slags both the dissipation of charge and the facilitation of oxygen transport are more than adequate to support the reaction.

Previous research by Drain *et al.*<sup>[51]</sup> on decarburization kinetics for droplets of 2.51% C - 0.07% P - 0.008%S composition with higher basicity slag ( $\text{CaO}/\text{SiO}_2 = 2.56$ ) containing

16% FeO at 1650°C showed that the reaction shut down when the droplet carbon reached approximately 0.8%C which was considerably higher than the equilibrium value. Based on the calculation method employed here, the electronic conductivity of the slag employed by these workers was very low. Relating the observations of Drain *et al.* to the current work it appears to be consistent with the aforementioned idea that although ionic conductivity may offer ability to dissipate charge in the case of irreducible  $\text{Ca}^{2+}$  ions, this ability is limited, and polarization eventually leads to cessation of the reaction.

It is to be noted that the premature shutdown of decarburization is only observed when metal droplets are reacted in slag but not in oxidizing gases. There are several studies<sup>[9,52,53]</sup> of decarburization kinetics of levitated droplets reacting in oxidizing gases ( $\text{O}_2$  or  $\text{O}_2 + \text{Ar}$ ), and in all of these cases, the reaction has been observed to approach thermodynamic equilibrium.

To further investigate the conductivity effect, a measurement of ferric fraction was conducted of slag samples which were collected after completion of decarburization for experiments with an initial slag ferric fraction of 0.5. The analysis showed that at the end of reaction, the ferric fraction was 0.1. A charge balance calculation suggests that decarburization mainly occurred reduction of ferric ions which is in agreement with the study of Woolley and Pal<sup>[14]</sup>. This result presents some problem in interpretation of current work. From the foregoing discussion, it seems clear that mass transport in the slag is highly dependent on the electrical conductivity of the slag. In addition, analysis of the current data employing Equation 5.4 and 5.7 offers quantitative agreement with this assertion. On the other hand, a strong dependence on electrical conductivity and therefore ferric fraction

would suggest that the mass transfer coefficient should have changed significantly with time, as ferric ions were reduced to ferrous ions. This was clearly not the case, as very good agreement was obtained between the experimental data and the mixed control model, based on a single mass transfer coefficient over the entire time of reaction. The authors have shown in their previous work that for a given slag composition a mixed control model, which considers the transport of oxygen in the slag as transport of FeO, works very well. The utility of considering transport of oxygen as transport of FeO is also supported by numerous practitioners over many years<sup>[11,12,54,55]</sup>. The authors are left to conclude that while mass transport of oxygen in slag is strongly dependent on electrical conductivity and the concepts developed here shows some promise, the way in which this is incorporated into kinetic models requires further development.

In summary, for cases where the slag exhibits low electronic conductivity, the foregoing experiments show that the decarburization of iron carbon droplets stop prematurely, despite the existence of ample thermodynamic driving force. When the low conductivity slag is replaced with a slag of higher conductivity the reaction proceeds to very close to equilibrium. These observations suggest that the cessation mechanism is related to charge accumulation at the interface, however, the authors are currently not able to offer a definitive explanation, or to develop a sufficiently detailed mechanism to predict the shutdown of the reaction. It is worth noting that, despite the absence of such an explanation, recognition of these facts allow researcher engaged in developing kinetic models for BOF steelmaking, to ignore the possibility of premature shutdown because the conditions will always involve highly conducting slags.

## 5.5. Conclusion

This article investigates the effect on decarburization kinetics of varying the slag ionic and electronic conductivity. The investigation shows that both electronic and ionic conductivity are important in determining the decarburization rate. A few key outcomes of this analysis are

- 1/ The variation of  $\frac{Fe^{3+}}{Fe^{2+}+Fe^{3+}}$  at constant total iron oxide concentration in the slag shows clearly that peak rate of decarburization increases with electronic and ionic conductivity, and that electronic conduction is more significant in controlling oxygen transport.
- 2/ The observed shutdown of the decarburization reaction under conditions of ample thermodynamic driving force is most likely to be due to charge accumulation at the slag metal interface. When the electronic conductivity of the slag is sufficiently high this charge can be dissipated, and the reaction may proceed to equilibrium.
- 3/ The electrochemical approach to oxygen transport explains very well the effect of basicity, ferric ratio and  $Fe_tO$  concentration on the decarburization kinetics.

## Acknowledgement

The authors are grateful to McMaster Steel Research Center and the Natural Sciences and Engineering Research Council for financial support. The authors wish to thank Dr. Kezhuan Gu for his valuable suggestions.

## Conflict of Interest

On behalf of all authors, the corresponding author states that there is no conflict of interest.

## Appendix A

The slag oxygen potential is a function of  $Fe^{3+}/Fe^{2+}$  ratio and can be expressed as following

$$\ln p_{O_2} = A_1 * \ln \frac{Fe^{3+}}{Fe^{2+}} \quad \text{where } A_1 \text{ is a constant}$$

$$d \ln p_{O_2} = A_1 * d \ln \frac{Fe^{3+}}{Fe^{2+}} = A_1 * d \ln \frac{\frac{Fe^{3+}}{Fe_t}}{\frac{Fe^{2+}}{Fe_t}} = A_1 * d \ln \frac{y}{1-y}$$

The slag conductivities can be expressed as a function of ferric fraction(y)

### 1. Ionic Conductivity

$$\sigma_{ion} = \sigma_0 - ay$$

### 2. Electronic Conductivity

$$\sigma_{el} = b[Fe^{2+}][Fe^{3+}] = by(1-y)$$

Where the constants  $\sigma_0$ ,  $a$  and  $b$  are function of slag composition. From Nernst Einstein equation for ionic conductivity,

$$\sigma_0 = \frac{4F^2}{RT} * (C_{Ca^{2+}}D_{Ca^{2+}} + C_{Fe}D_{Fe^{2+}})$$

$$a = \frac{4F^2}{RT} C_{Fe}D_{Fe^{2+}}$$

From diffusion assisted charge hopping model for electronic conductivity,

$$b = 4\pi N_a * \frac{r^0 r^*}{r^0 - r^*} * \frac{D_{Fe^{2+}} F^2}{RT} * C_{Fe}^2$$

Applying these on equation 4 and integrating from slag/metal interface to bulk

$$\begin{aligned}
\frac{dn_{FeO}}{dt} &= \frac{RT}{8F^2} * \left(\frac{A_1}{\Delta x}\right) \int_{int}^{bulk} \frac{(\sigma_0 - ay)by(1-y)}{\sigma_0 - ay + by(1-y)} d \ln \frac{y}{1-y} \\
&= \frac{RT}{8F^2} * \left(\frac{A_1}{\Delta x}\right) \int_i^b \left[ \frac{b(\sigma_0 - ay)(1-y)}{\sigma_0 - ay + by(1-y)} dy + \frac{(\sigma_0 - ay)by}{\sigma_0 - ay + by(1-y)} dy \right] \\
&= \frac{RT}{8F^2} * \left(\frac{A_1}{\Delta x}\right) \int_i^b \left[ \frac{b(\sigma_0 - ay)}{\sigma_0 - ay + by(1-y)} dy \right] \\
&= \frac{RT}{16F^2} * \left(\frac{A_1 a}{\Delta x}\right) \int_{int}^{bulk} \left[ \frac{-2by + (b-a)}{\sigma_0 - ay + by(1-y)} dy + \frac{\frac{2b\sigma_0}{a} - (b-a)}{\sigma_0 - ay + by(1-y)} dy \right] \\
&= \frac{RT}{16F^2} * \left(\frac{A_1 a}{\Delta x}\right) \left[ \ln(\sigma_{tot}) + \int_{int}^{bulk} \left\{ \frac{2b\sigma_0 - a(b-a)}{-ab} \right\} \frac{dy}{\left(y + \frac{a-b}{2b}\right)^2 - \left\{ \left(\frac{a-b}{2b}\right)^2 + \frac{\sigma_0}{b} \right\}} \right]
\end{aligned}$$

We know from integration,  $\int \frac{dx}{x^2-a^2} = \frac{1}{2a} \ln \frac{x-a}{x+a} + constant$

$$\begin{aligned}
&= \frac{RT}{16F^2} * \left(\frac{A_1 a}{\Delta x}\right) \left[ \ln(\sigma_{tot}) + \frac{2b\sigma_0 - a(b-a)}{-ab} * \frac{1}{2\sqrt{\left(\frac{a-b}{2b}\right)^2 + \frac{\sigma_0}{b}}} \ln \frac{y + \frac{a-b}{2b} - \sqrt{\left(\frac{a-b}{2b}\right)^2 + \frac{\sigma_0}{b}}}{y + \frac{a-b}{2b} + \sqrt{\left(\frac{a-b}{2b}\right)^2 + \frac{\sigma_0}{b}}} \right]_{int}^{bulk} \\
\frac{dn_{FeO}}{dt} \left(\frac{mol}{m^2-s}\right) &= \frac{RT}{16F^2} * \left(\frac{A_1 a}{\Delta x}\right) \left[ \ln(\sigma_{tot}) - \frac{a(a-b) + 2b\sigma_0}{a\sqrt{(a-b)^2 + 4b\sigma_0}} \ln \frac{2by + (a-b) - \sqrt{(a-b)^2 + 4b\sigma_0}}{2by + (a-b) + \sqrt{(a-b)^2 + 4b\sigma_0}} \right]_{int}^{bulk}
\end{aligned}$$

### List of Symbols

$\left(\frac{dn_{CO}}{dt}\right)_{peak}$  decarburization rate at the peak period (mol/m<sup>2</sup>-s)

$C_{FeO}$  concentration of FeO (mol/m<sup>3</sup>)

$E^{crit}$  Electric Field at the critical point of reaction shut down (V/m)



$J_i$  Flux of charged species  $i$  (mol/m<sup>2</sup>-s)

$a_{FeO}$  activity of FeO in the slag (-)

$a_i^{bulk}$  and  $a_i^{int}$  activity of charged species  $i$  at the bulk slag and s/m interface respectively

(-)

$\frac{dn_{FeO}}{dt}$  Flux of FeO in the Slag (mol/m<sup>2</sup>-s)

$\frac{d\mu_i}{dx}$  Chemical Potential Gradient of species  $i$  (J/mol-m)

$\frac{d\phi}{dx}$  Electrical Potential Gradient (V/m)

$k_s$  Mass Transfer Coefficient(m/s)

$k_s^{elec}$  Electrochemical Mass Transfer Coefficient (m/s)

$p_{O_2}$  oxygen potential in the slag (Pa)

$t_i$  Transference number of charged species  $i$  (-)

$z_i$  Charge no of species  $i$  (-)

$\mu_i$  Chemical Potential of species  $i$  in slag

$\sigma_{el}$  Electronic Conductivity of slag (S/m)

$\sigma_{ion}$  Ionic Conductivity of slag (S/m)

$\sigma_{tot}$  Total conductivity of slag (S/m)

$\Delta x$  Boundary Layer thickness in the slag (m)

$F$  Faraday Constant (C/mol)

$R$  Universal Gas Constant (J/mol-K)

$T$  Temperature (K)

$V(t)$  Volume of droplet at time  $t$  ( $\text{m}^3$ )

$y$  Ferric Fraction ( $\frac{Fe^{3+}}{Fe^{2+}+Fe^{3+}}$ ) in the slag (-)

## References

- 1 G. Brooks, Y. Pan, and K.S. Coley: *Metall. Mater. Trans. B*, 2005, vol. 36B, pp. 525–35.
- 2 Subagyo, G.A. Brooks, and K.S. Coley: *Can. Metall. Q.*, 2005, vol. 44, pp. 119–30.
- 3 H. Sun, K. Gao, V. Sahajwalla, K. Mori, and R.D. Pehlke: *ISIJ Int.*, 1999, vol. 39, pp. 1125–33.
- 4 K. Gao, V. Sahajwalla, H. Sun, C. Wheatley, and R. Dry: *ISIJ Int.*, 2000, vol. 40, pp. 301–8.
- 5 M. Hayer and S.G. Whiteway: *Can. Metall. Q.*, 1973, vol. 12, pp. 35–44.
- 6 P.G. Roddis: *J. Iron Steel Inst.*, 1973, vol. 211, pp. 53–8.
- 7 J.B. SEE and N.A. Warner: *J. Iron Steel Inst.*, 1973, vol. 211, pp. 44–52.
- 8 D.. Sain and G.R. Belton: *Metall. Trans. B*, 1976, vol. 7B, pp. 235–44.
- 9 P.A.A. Distin, G.D.D. Hallett, and F.. D. Richardson: *J. Iron Steel Inst.*, 1968, vol.

- August, pp. 821–33.
- 10 H. Gaye and P. V. Riboud: *Metall. Trans. B*, 1977, vol. 8, pp. 409–15.
  - 11 C.L. Molloseau and R.J. Fruehan: *Metall. Mater. Trans. B Process Metall. Mater. Process. Sci.*, 2002, vol. 33, pp. 335–44.
  - 12 D.J. Min and R.J. Fruehan: *Metall. Trans. B*, 1992, vol. 23, pp. 29–37.
  - 13 E. Chen and K.S. Coley: *Ironmak. Steelmak.*, 2010, vol. 37, pp. 541–5.
  - 14 D.E. Woolley and U.B. Pal: *ISIJ Int.*, 1999, vol. 39, pp. 103–12.
  - 15 G.G.K. Murthy, A. Hasham, and U.B. Pal: *Ironmak. Steelmak.*, 1993, vol. 20, pp. 191–200.
  - 16 G.G.K. Murthy, A. Hasham, and U.B. Pal: *ISIJ Int.*, 1994, vol. 34, pp. 408–13.
  - 17 S. Ramachandran, T.B. King, and N.J. Grant: *J. Met.*, 1956, vol. 8, pp. 1549–58.
  - 18 T. Gare and G.S.F. Hazeldean: *Ironmak. Steelmak.*, 1981, vol. 8, pp. 169–81.
  - 19 G. Murthy, Krishna, G, Y. Sawada, and F. Elliot, J: *Ironmak. Steelmak.*, 1993, vol. 20, pp. 179–200.
  - 20 D.E. Woolley and U.B. Pal: *Ironmak. Steelmak.*, 2002, vol. 29, pp. 125–32.
  - 21 D.E. Woolley and U.B. Pal: *Metall. Mater. Trans. B Process Metall. Mater. Process. Sci.*, 1999, vol. 30, pp. 877–89.
  - 22 W.D. Judge, J. Paeng, and G. Azimi: *Nat. Mater.*, DOI:10.1038/s41563-021-01106-

z.

- 23 W.D. Judge and G. Azimi: *ECS Trans.*, 2018, vol. 85, pp. 91–102.
- 24 W.D. Judge, J. Paeng, and G. Azimi: *Electrochim. Acta*, 2021, vol. 389, p. 138755.
- 25 U. Pal, T. Debroy, and G. Simkovich: *Metall. Trans. B*, 1985, vol. 16, pp. 77–82.
- 26 F.E. Metallurgy and C. South: pp. 839–44.
- 27 X.J. Guo, R. Li, and R. Harris: *Can. Metall. Q.*, 1999, vol. 38, pp. 33–41.
- 28 J.L. Speelman, W.F. Caley, and K.G. Leewis: *Metall. Trans. B*, 1989, vol. 20, pp. 31–7.
- 29 Y. Sayadyaghoubi, S. Sun, and S. Jahanshahi: *Metall. Mater. Trans. B*, 1995, vol. 26, pp. 795–802.
- 30 J. Biswas, K. Gu, and K.S. Coley: *Metall. Trans. B*, 2021, vol. 52, pp. 3888–3906.
- 31 J. Biswas, K. Gu, and K.S. Coley: *Metall. Mater. Trans. B Process Metall. Mater. Process. Sci.*, 2021, vol. 52, pp. 4215–4229.
- 32 M. Barati and K.S. Coley: *Metall. Mater. Trans. B Process Metall. Mater. Process. Sci.*, 2006, vol. 37, pp. 41–9.
- 33 K. Gu, N. Dogan, and K.S. Coley: *Metall. Mater. Trans. B Process Metall. Mater. Process. Sci.*, 2017, vol. 48, pp. 2984–3001.
- 34 J. Berthon, A. Revcolevschi, and H. Morikawa: *J. Cr.*, 1979, vol. 47, pp. 736–8.

- 35 K. Gu, N. Dogan, and K.S. Coley: *Metall. Mater. Trans. B Process Metall. Mater. Process. Sci.*, 2017, vol. 48, pp. 2343–53.
- 36 W.R. Dickson and E.B. Dismukes: *Trans. Metall. Soc. AIME*, 1962, vol. 224, pp. 505–11.
- 37 M.T. Simnad, G. Derge, and I. George: *J. Met.*, 1954, vol. 6, pp. 1386–90.
- 38 J.O.M. Bockris, J.A. Kitchener, S. Ignatowicz, and J.W. Tomlinson: *Trans. Faraday Soc.*, 1952, vol. 48, pp. 75–91.
- 39 E.W. Mulholland, G.S.F. Hazeldean, and M. Davies: *J. Iron Steel Inst.*, 1973, vol. 211, pp. 632–9.
- 40 M.D. Pomeroy: McMaster University, 2011.
- 41 Y. Sasaki, S. Hara, D.R. Gaskell, and G.R. Belton: *Metall. Trans. B*, 1984, vol. 15, pp. 563–71.
- 42 M. Barati and K.S. Coley: *Metall. Mater. Trans. B Process Metall. Mater. Process. Sci.*, 2006, vol. 37, pp. 61–9.
- 43 C. Wagner: *Z Phys. Chem.*, 1933, vol. B21, p. 25.
- 44 E.A. Pastukhov, O.A. Esin, and S.K. Chuchmarev: *Sov. Electrochem.*, 1966, vol. 2, pp. 193–8.
- 45 H.-J. Engell and P. Vygen: *Reports Bunsen Soc. Phys. Chem.*, 1968, vol. 72, pp. 5–11.

- 46 Y. Takeda, S. Nakazawa, and A. Yazawa: *Can. Metall. Q.*, 1980, vol. 19, pp. 297–305.
- 47 K.S. Goto, T. Kurahashi, and M. Sasabe: *Metall. Trans. B*, 1977, vol. 8, pp. 523–8.
- 48 H. Larson and J. Chipman: *J. Met.*, 1953, vol. 5, pp. 089–1096.
- 49 S. Wright and L. Zhang: in *VII Int. Conf. on Molten Slags Fluxes and Salts*, 2004, pp. 231–6.
- 50 M. Barati and K.S. Coley: *Metall. Mater. Trans. B*, 2005, vol. 36B, pp. 169–78.
- 51 P.B. Drain, K. Gu, N. Dogan, R.J. Longbottom, M.W. Chapman, B.J. Monaghan, and K.S. Coley: *ISIJ Int.*, 2021, vol. 61, pp. 734–44.
- 52 S. Jahanshahi: Imperial College of Science and Technology, London, 1980.
- 53 N. Simento, H. LEE, and P. Hayes: *ISIJ Int.*, 1999, vol. 39, pp. 1217–23.
- 54 B. Sarma, A.W. Cramb, and R.J. Fruehan: *Metall. Mater. Trans. B Process Metall. Mater. Process. Sci.*, 1996, vol. 27, pp. 717–30.
- 55 S. Ohguchi, D.G.C. Robertson, B. Deo, P. Grieveson, and J.H.E. Jeffes: *Ironmak. Steelmak.*, 1984, vol. 11, pp. 202–13.

## **Chapter 6**

### **6. Consideration of the competitive adsorption of oxygen and sulfur on droplet decarburization and bloating kinetics**

In Chapter 5, a major influence on the droplet decarburization kinetics on the peak decarburization period and at the end stage is reported. In particular it is noted that the normal effect of sulfur in retarding the reaction is diminished in the presence of high conductivity slags. In Chapter 6, an experimental study for droplets with a varying sulfur concentration in high conductivity slags is presented. An explanation of these results is offered based on the concept of competitive adsorption of oxygen and sulfur, suggesting that for slags offering high oxygen transport rates the higher oxygen potential results in a greater fraction of the droplet surface being occupied by oxygen, creating pathways through the otherwise resistant adsorbed sulfur layer.

This chapter will be submitted as a manuscript shortly.

All the experiments were done by me along with assistance from Dr. Kezhuan Gu. The preliminary draft preparation along with theoretical analysis was done by me. Dr. Kezhuan Gu helped editing the initial draft. Dr. Kenneth Coley guided me to understand the theoretical background and to analyze the data.

### **Abstract**

An experimental study was performed to understand the effect of competitive adsorption between oxygen and sulfur on the kinetics of decarburization of droplets in oxidizing slag. Experiments were conducted by varying droplet sulfur concentration and slag electrical conductivity. The results show that for a fixed slag composition, with increasing sulfur concentration in the droplet, the kinetics of decarburization were impeded by surface poisoning. On the other hand, for a fixed sulfur concentration in the droplet, increasing the slag conductivity at constant  $\text{Fe}_t\text{O}$  concentration accelerated the transport of oxygen in the slag and leading to increased oxygen adsorption on the droplet surface. The interplay between oxygen and sulfur adsorption appeared to control the oxygen flux into the metal. When sulfur adsorption was dominant, transport of oxygen into the droplet and subsequent decarburization were inhibited, whereas by displacing adsorbed sulfur, enhanced oxygen adsorption appeared to create pathways for oxygen into the droplet.

## **6.1. Introduction**

In pyrometallurgical refining industries, slag/metal interfacial reaction kinetics is very crucial in controlling the process especially when surface active elements such as sulfur is present in the system. This surface-active element reduces the interfacial tension which in turn favors the nucleation kinetics of new phases. Another major role of this surface-active elements is blocking the reaction sites on the surface thereby slowing down the interfacial reaction kinetics. When a surface-active element is a reactant involved in the refining reactions, then its influence on reaction kinetics is different. Most importantly when two types of surface-active elements are present, for example oxygen and sulfur in this study,



one of these, in this case oxygen, is a participant in the reaction and the other one is not, the reaction kinetics become even more complicated.

The influence of sulfur in the metal on refining reactions has been investigated extensively. Several researchers<sup>[1-5]</sup> found that sulfur has a profound and reproducible retarding effect on the decarburization of iron carbon melts in oxidizing gas atmosphere. In terms of droplet decarburization, few studies have been carried out to understand the poisoning effect of sulfur on the decarburization kinetics of droplets in oxidizing slag. Gaye *et al.*<sup>[6]</sup> and Min *et al.*<sup>[7]</sup> observed that the decarburization rate slowed down with increasing sulfur concentration in droplet. However, Gare and Hazeldean<sup>[8]</sup> observed an opposite trend that the decarburization kinetics were enhanced with the presence of sulfur. Molloseau and Fruehan<sup>[9]</sup> observed the droplet decarburization rate first increased till 0.011 wt% thereafter decreased with increasing sulfur concentration in the droplet having sulfur ranges from 0.003 to 0.42 wt%. They further proposed two opposing factors regarding the sulfur effect, *i.e.*, first sulfur lowers the surface tension of droplet, which enhances the tendency of metal fragmentation leading to a larger slag/metal reaction area; second sulfur blocks reaction sites on the surface therefore slowing the decarburization kinetics. Later, studies in the authors laboratory<sup>[10-13]</sup> on the effect of sulfur on droplet decarburization kinetics confirmed the work of Molloseau and Fruehan proposing the following mechanisms: first sulfur reduces the metal surface tension which enhances the nucleation kinetics, second sulfur blocks both slag/metal and gas/metal reaction sites thereby slowing down the oxygen supply and bubble growth rate. Several researchers<sup>[14-17]</sup> have claimed that the presence of a surface active element or transfer of a surface active element through an interface created

turbulence at the slag/metal interface due to variation of local interfacial tension enhancing the reaction kinetics significantly. On the other hand, there are very scarce studies on the kinetics of oxygen adsorption in iron melts. There have been few studies<sup>[1,17,18]</sup> showing the effect of oxygen as a surface-active element on surface tension variation. Reports related to the influence of oxygen as surface active element on interfacial reaction kinetics are limited in the literature. Most relevant works are confined to understand the effect of oxygen on nitrogen desorption into liquid iron<sup>[19–23]</sup>. The common agreement from those works is that oxygen is surface active in liquid iron and blocks reaction sites for the formation or dissociation of the nitrogen molecule.

For droplet decarburization in oxidizing slag, there two surface active elements involved, *i.e.*, oxygen and sulfur. The adsorption of oxygen is part of the decarburization mechanism; whereas the adsorption of sulfur impedes the interfacial reaction kinetics and at the same time favors the kinetics by lowering surface tension. To date, no studies have been reported to investigate the interplay between the adsorption of these two surface active elements in relation to decarburization kinetics. It is the purpose of the present investigation to understand the influence of competitive absorption of oxygen and sulfur on droplet decarburization kinetics for droplets reacting with oxidizing slag. By varying the metal sulfur concentration and the oxygen transport properties of the slag, this competitive adsorption effect is discussed in detail in the current study.

## **6.2. Experimental Procedure**

### **6.2.1. Material Preparation**

Metal droplets were prepared from high purity electrolytic iron, graphite rods and ferro sulfur alloys. Three materials were weighted according to the desired composition, mixed and melted in an alumina crucible in resistance heated furnace at 1550°C temperature. After homogenizing for 1.5 hours, cylindrical samples were pipetted out, cut into sections of specific mass and remelted in electric arc melter to prepared droplets. The composition of this droplets were confirmed using LECO C & S analyzer. To prepare the slag, CaO, Al<sub>2</sub>O<sub>3</sub> and SiO<sub>2</sub> powders were premelted at 1550°C, quenched, crushed and mixed together with FeO, Fe<sub>2</sub>O<sub>3</sub> powders for experiments. The ferric fraction of the slags was varied by varying the mass percentage of FeO, Fe<sub>2</sub>O<sub>3</sub> powders, while kept the total iron oxide (FetO) as constant (16 wt%). For this study, 2 gram droplets of three sets were prepared by varying the metal droplet carbon and sulfur concentration and three different slag compositions were prepared. The Al<sub>2</sub>O<sub>3</sub> concentration (17 wt%) was same for all three slags. The composition of droplet and slag employed in this study are listed in Table 6.1. Here the basicity of slag (B) refers to the ratio of CaO to SiO<sub>2</sub> in wt%.

Table 6.1. Droplet and slag composition(wt%)

|          | Type 1   | Type 2   | Type 3   |
|----------|--|--|--|
| Droplets | Fe-2.5%C-0.011%S   | Fe-2.5%C-0.016%S   | Fe-3.9%C -0.129%S  |
| Slags    | B = CaO/SiO <sub>2</sub> = 0.9<br>Fe <sup>3+</sup> /Fe = 0 | B = CaO/SiO <sub>2</sub> = 0.9<br>Fe <sup>3+</sup> /Fe = 0.5 | B = CaO/SiO <sub>2</sub> = 2<br>Fe <sup>3+</sup> /Fe = 0 |

### 6.2.2. Experimental setup

The experimental technique is the same as that used in recent work by the authors<sup>[24,25]</sup>. For convenience the description from a recent publication is reintroduced here. A resistance heated vertical tube furnace connected to a pressure transducer along with an X-ray imaging device were used for the experiments. The furnace consisted of molybdenum disilicide heating elements, an alumina tube of 80 mm inner diameter, water cooling jackets at the top and the bottom ends of the alumina tube, dropper rod from the top along with a metal cap to hold the metal droplet, a support rod from the bottom to hold the crucible and a cooling column surrounding water cooled copper coils. The furnace was connected to a cylinder of argon, which had a column of drierite and titania turnings to absorb moisture and oxygen before entering the furnace. The X-ray video were recorded during experiments in a computer using One touch grabber software. A schematic of the setup is shown in Figure 6.1.

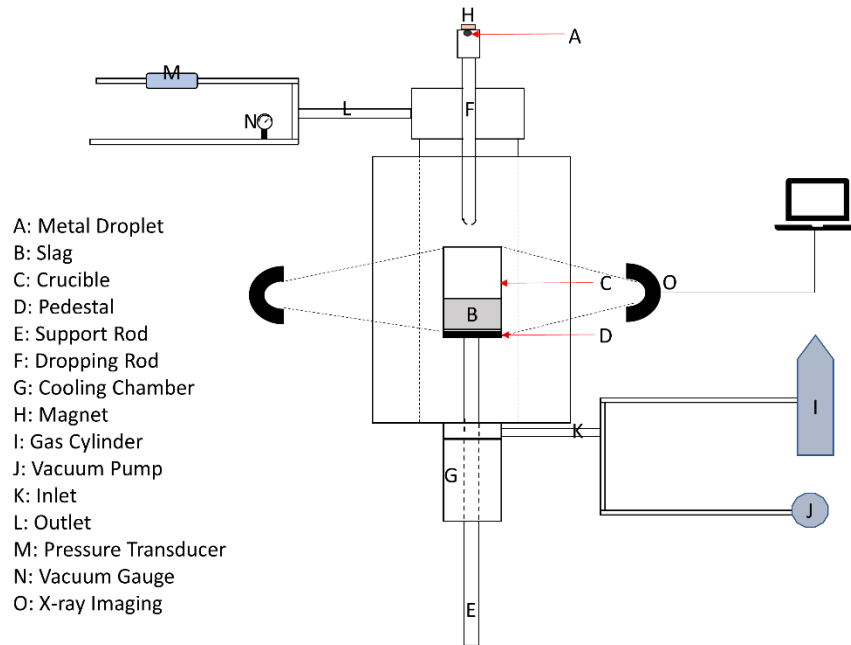


Figure 6.1: Schematic of experimental setup [24]

### 6.2.3. Procedure

To do the experiment, first the crucible with  $25 \pm 0.5$  gram slag was placed in the hot zone of the furnace and the metal droplet at the top was hold using magnet. The furnace valves for inlet and outlet were closed and evacuated to 800 millitorr. Then the furnace was backfilled with argon and the flow was continued during the heating. At the desired temperature, the argon flow was stopped, all the inlet and outlet valves were closed except the one connected with the pressure transducer. The X-ray device were placed aligning with the hot zone to record the video of the crucible. The metal droplet was dropped by removing the magnet and the reaction time were started counting from the point when liquid metal droplet enters the slag, and this can be exactly pointed from continuous X-ray video. Once the experiment was done, the support rod with the crucible (having slag and

the reacted droplet) was lowered to the cooling chamber to quench and the furnace was cooled down slowly. The reacted droplets were collected and performed LECO C & S analysis to measure the final carbon concentration of the droplets. The recorded pressure transducer data were calibrated based on the final carbon concentration of the droplets. The data were smoothed in MATLAB and presented. The recorded X-ray video was splitted into image frames for each second, and the area of the droplets from the 2-D image frames were measured using ImageJ software and then the area were converted to volumes by calibrating with the known droplet volume for time zero. All experiments in this study were carried out at the temperature of 1505°C.

### **6.3. Results**

A set of decarburization experiments were performed to understand the effect of competitive adsorption between S and O at the slag/metal interface on droplet decarburization. The droplet sulfur concentration was varied at three different levels and the oxygen transport kinetics in the slag were controlled by varying the slag composition. The results are presented for three different sulfur levels in the following separated sections. For each of the sulfur levels, droplet decarburization kinetics were investigated under three different slag compositions listed in Table 6.1.

#### **6.3.1. Decarburization for droplets with 0.011 wt% sulfur**

Metal droplets with composition of Fe-2.5 wt% C-0.011 wt% S of 2 g were reacted with oxidizing slag (16% Fe<sub>2</sub>O<sub>3</sub>) of three different compositions at 1505°C. The total CO generation and the bloated droplet volume profiles are presented in Figures 6.2 (a) and (b).

For the case of  $B=0.9$ , with increasing slag ferric fraction from 0 to 0.5, the reaction rate increased by almost three times during the initial period and the CO formation was observed to continue for longer time. The rate of bloating also increased by approximately two times in the case of higher ferric fraction slag. For a constant ferric fraction, when the basicity ( $B$ ) was increased from 0.9 to 2, the peak rate of decarburization and the rate of bloating were found to increase by approximately a factor of two. The droplet sulfur concentration being low, no poisoning was observed in any of these cases.

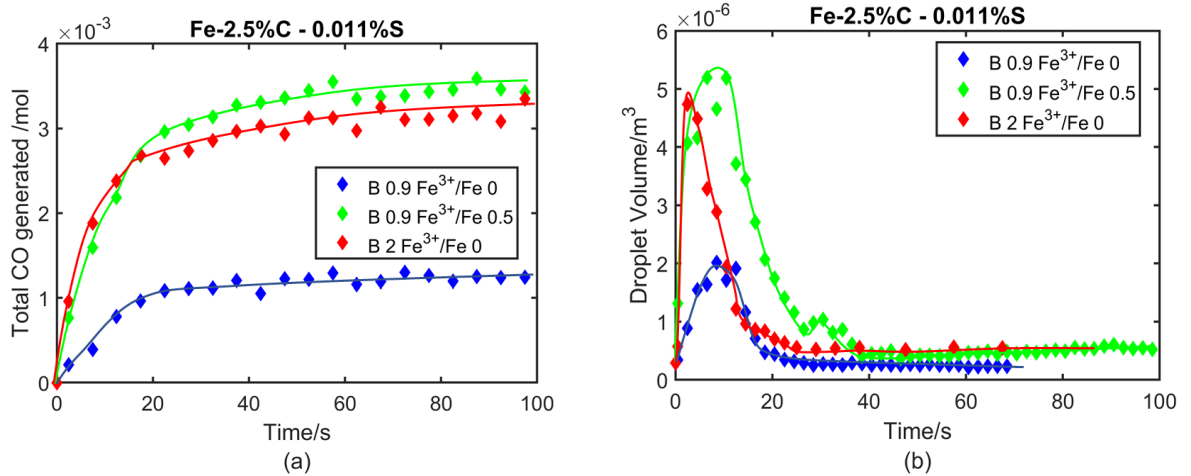


Figure 6.2: Total CO generation with time (a) and the droplet volume variation with time (b) for 2.5 wt% C - 0.011 wt% S droplets

### 6.3.2. Decarburization for droplets with 0.016 wt% sulfur

Three experiments with three different compositions of slag were performed for 2 g droplets with the composition 2.5 wt% C-0.016 wt% S at 1505°C temperature. The CO generation and bloating profiles are presented in Figures 6.3 (a) and (b) respectively. Figure 6.3 (a) shows that the decarburization for droplets with 0.016 wt% sulfur experiences a

very large effect of poisoning during the initial 10 seconds in the case of  $B=0.9$  and  $\text{Fe}^{3+}/\text{Fe} = 0$  slag. The corresponding droplet volume profile presented in Figure 6.3(b) shows the same trend. However, when the slag ferric fraction was increased from 0 to 0.5, the sulfur poisoning effect disappeared. Similarly, for slag with  $B=2$ , poisoning was not observed. The droplet volume profile shows that although the bloating was delayed for the case of  $B=0.9$  and  $\text{Fe}^{3+}/\text{Fe} = 0$  slag, the extent of bloating was highest compared to the volume profiles for other two slags despite the fact that less CO was generated than for the other conditions.

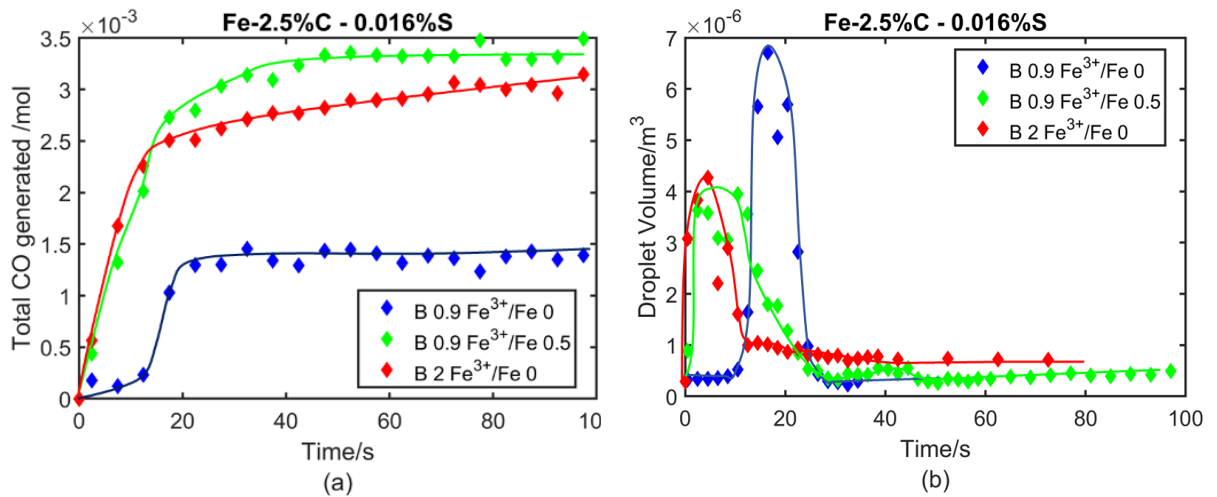


Figure 6.3: Total CO generation with time (a) and the droplet volume variation with time (b) for 2.5 wt%C - 0.016 wt%S droplets

### 6.3.3. Decarburization for droplets with 0.129 wt% sulfur

Decarburization experiments were carried out for Fe-3.9 wt%C-0.129 wt%S with three different slags at 1505°C. The CO generation profile and the bloating behavior are presented in Figures 6.4 (a) and (b). Figure 6.4 (a) shows that decarburization kinetics



slowly increased with increasing ferric fraction from 0 to 0.5 as well as with increasing slag basicity. In this case, the increase in peak decarburization rate was not as great as presented in the previous two cases where the sulfur content was an order of magnitude less. However, the bloated droplet volume profiles presented in Figure 6.4(b) show a significant delay in bloating for all three cases. In the case of B = 0.9 slag with  $\text{Fe}^{3+}/\text{Fe} = 0$ , there was hardly any bloating observed. With increasing ferric fraction ( $\text{Fe}^{3+}/\text{Fe} = 0.5$ ) for the B=0.9 slag, the droplet partially bloated from the beginning of reaction and then became fully bloated after roughly 380 seconds. Whereas in the case of B=2.0 and  $\text{Fe}^{3+}/\text{Fe} = 0$ , the droplet bloated to almost 5 times its original volume after 100 seconds of reaction. Another important result in Figures 6.4(a) and (b) is that droplet decarburization in the cases of B = 0.9 slag with  $\text{Fe}^{3+}/\text{Fe} = 0.5$  and B=2.0 experienced two distinct stages, *i.e.*, a relatively slower external decarburization rate before 100 seconds followed by a faster internal decarburization. This was not observed in the previous two different sulfur cases. Whilst the decarburization mainly occurs externally in the case of B = 0.9 and  $\text{Fe}^{3+}/\text{Fe} = 0$  slag. This two-stage reaction mechanism was mainly due to the poisoning effect of sulfur and has been explained in detailed in the authors' previous studies<sup>[10-12,24,25]</sup>. Moreover, the external decarburization for all three cases, occurring before 100s of reaction, presented in Figure 6.5 suggest it is independent of slag properties.

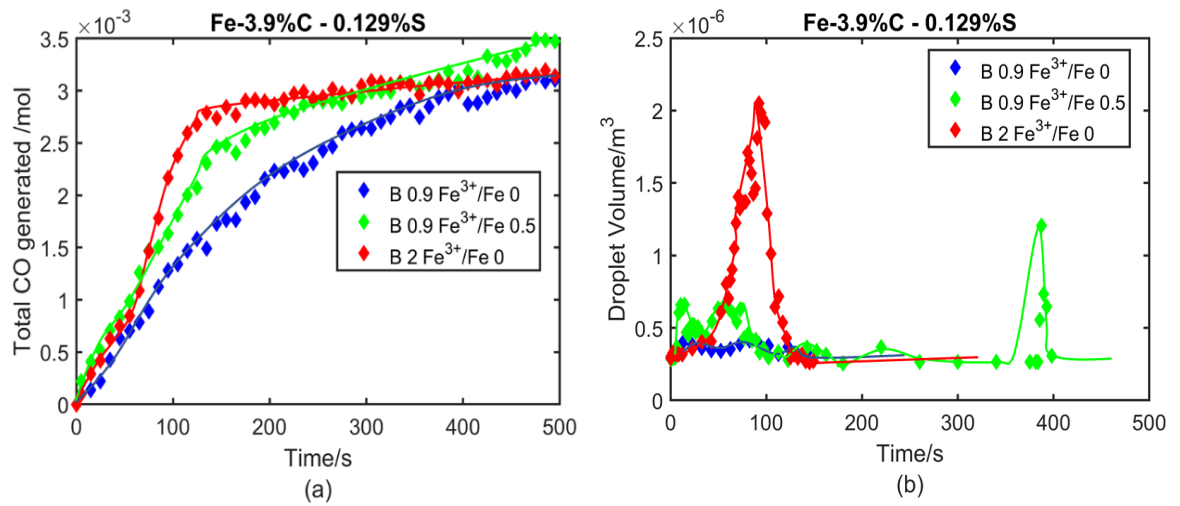


Figure 6.4: Total CO generation with time (a) and the droplet volume variation with time (b) for 3.9 wt% C - 0.129 wt% S droplets

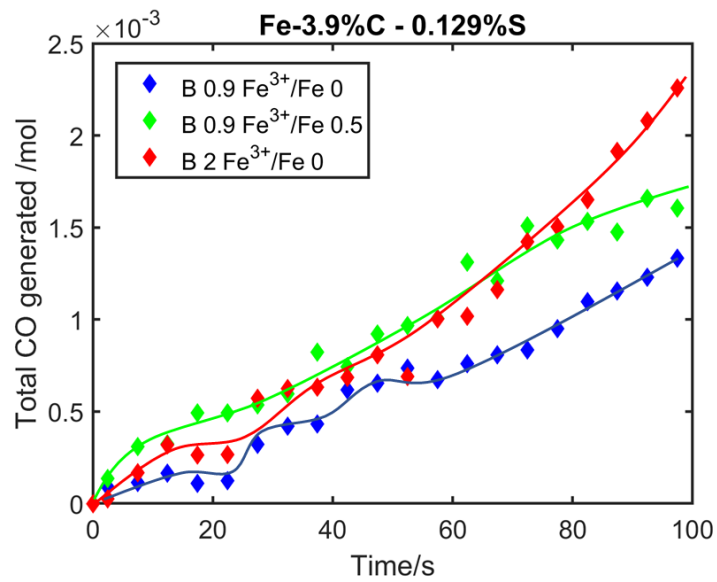


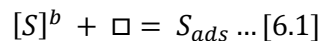
Figure 6.5: Total CO generation profile for 3.9 wt% C - 0.129 wt% S for initial 100 seconds

## 6.4. Discussion

In this work, an experimental study to investigate the effect of competitive adsorption of oxygen and sulfur on decarburization kinetics was performed by varying the droplet sulfur concentration and slag composition. At the slag/metal interface, sulfur is known to inhibit the decarburization reaction kinetics by blocking available reaction sites<sup>[9][10][17]</sup>, whereas oxygen being a reactant in the decarburization reaction, its adsorption is a step in the reaction process. By increasing the concentration of sulfur in the droplet, the occupancy of surface sites by sulfur is increased. On the other hand, increasing the oxygen transport in the slag by increasing slag basicity and ferric fraction, the supply of oxygen for adsorption at the slag metal interface increases. The competition between sulfur and oxygen determines the fraction of slag/metal interface to be occupied by each of these elements. In this section, a brief theoretical framework is presented to facilitate discussion of the experimental results. Based on a decarburization model previously developed<sup>[26]</sup> by the current authors<sup>[26]</sup>, the prediction of decarburization kinetics is shown which incorporates the partitioning of oxygen at the slag/metal interface in the presence of the surface active element, sulfur.

#### 6.4.1. Theoretical Framework

When a droplet containing sulfur reacts with oxidizing slag, the adsorption of sulfur at the slag/metal interface occurs in following way



Where  $[S]^b$  is the bulk metal sulfur concentration,  $S_{ads}$  is the adsorbed sulfur concentration,  $\square$  is the vacant reaction site.

The rate of adsorption of sulfur at the interface can be expressed as

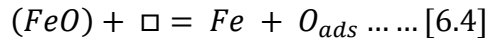
$$R_1 = \overrightarrow{k_1} \left( a_s^b (1 - \theta_s - \theta_o) - \frac{\theta_s}{K_s} \right) \dots [6.2]$$

Where  $\overrightarrow{k_1}$  is the forward rate constant of sulfur adsorption reaction with unit of mol/cm<sup>2</sup>-s,  $a_s^i$  is the activity of sulfur at the interface,  $K_s$  is the adsorption constant.  $\theta_s$  and  $\theta_o$  are the fraction of reaction sites occupied by the adsorbed sulfur and oxygen respectively.

On the other side of the slag/metal interface, oxygen transports from the bulk slag to the slag/metal interface, adsorbs and then dissolves into the liquid metal and reacts with dissolved carbon. Assuming the transport of oxygen in the slag in the conventional molecular way, the rate of transport of oxygen (mol/cm<sup>2</sup>-s) from the bulk slag to the slag/metal interface can be expressed as

$$J_{FeO} = \frac{k_s * \rho_s}{100 * M_{FeO}} \left( (\%FeO)^b - (\%FeO)^i \right) \dots [6.3]$$

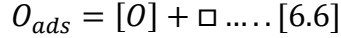
Where  $k_s$  is the mass transfer coefficient in the slag (cm/s), which is dependent on slag electronic and ionic conductivity.  $\rho_s$  is the slag density (g/cm<sup>3</sup>),  $M_{FeO}$  is the molecular mass of FeO,  $(\%FeO)^i$  and  $(\%FeO)^b$  are the bulk and interfacial concentration of FeO in wt%. At the slag/metal interface, this molecular FeO dissociates, and oxygen gets adsorbed as



The rate of adsorption of oxygen according of the reaction can be written as

$$R_2 = \overrightarrow{k_2} a_{FeO}^i (1 - \theta_s - \theta_o) - \overleftarrow{k_2} \theta_o a_{Fe}^i = \overrightarrow{k_2} (a_{FeO}^i (1 - \theta_s - \theta_o) - \frac{\theta_o a_{Fe}^i}{K_{eq}}) \dots [6.5]$$

Where  $a_{FeO}^i$  and  $a_{Fe}^i$  are the activity of FeO and Fe at the interface,  $\overrightarrow{k_2}$  and  $\overleftarrow{k_2}$  is the forward and backward reaction rate constant and  $K_{eq}$  is the equilibrium constant for  $(FeO) + \square = Fe + O_{ads}$  reaction. In the third step, this adsorbed oxygen dissolves into liquid metal as



The rate of dissolution of oxygen can be expressed as

$$R_3 = \overrightarrow{k_3} \theta_o - \overleftarrow{k_3} a_o^i * (1 - \theta_s - \theta_o) = \overrightarrow{k_3} (\theta_o - K_o * a_o^i * (1 - \theta_s - \theta_o)) \dots \dots [6.7]$$

Where  $\overrightarrow{k_3}$  and  $\overleftarrow{k_3}$  are the forward and backward rate constants of oxygen dissolution reaction and  $a_o^i$  is the activity of oxygen at the interface.

By rearranging and combining equations 6.3, 6.5 and 6.7, the rate of dissolution of oxygen can be expressed as

$$R_3 = \frac{(\%FeO)^b - \frac{100M_{FeO}a_{Fe}}{\gamma_{FeO}M_S K_{eq}} * K_o * a_o^i}{\frac{100M_{FeO}}{k_s * \rho_s} + \frac{100M_{FeO}}{\gamma_{FeO}M_S} * \frac{1}{\overrightarrow{k_2}(1 - \theta_s - \theta_o)} + \frac{100M_{FeO}a_{Fe}}{\gamma_{FeO}M_S K_{eq}} * \frac{1}{\overrightarrow{k_3}(1 - \theta_s - \theta_o)}} \dots \dots [6.8]$$

The overall rate constant for oxygen dissolution can be written as

$$\frac{1}{k_{ov}} = \frac{100M_{FeO}}{k_s * \rho_s} + \frac{100M_{FeO}}{\gamma_{FeO}M_S} * \frac{1}{\overrightarrow{k_2}(1 - \theta_s - \theta_o)} + \frac{100M_{FeO}a_{Fe}}{\gamma_{FeO}M_S K_{eq}} * \frac{1}{\overrightarrow{k_3}(1 - \theta_s - \theta_o)} \dots \dots [6.9]$$

Both the external and internal decarburization rate depend upon the availability of dissolved oxygen in the metal. Oxygen dissolved into the metal partitions at the interface – if sufficient carbon is available a part reacts at the interface only; the remainder enters into the metal droplet and causes internal bubble generation. The countercurrent

competition between carbon and oxygen determines what fraction of oxygen will be consumed at the slag/metal interface and what fraction will enter into the metal droplet to cause internal decarburization. During internal decarburization, due to the difference between the rate of generation and rate of escape of bubbles, a swelling or ‘bloating’ is observed.

If one assumes that both oxygen and sulfur adsorption reactions are very fast, then the equation 6.2 and 6.5 collapses to the equilibrium condition described by equations 6.10 and 6.11.

$$\theta_S^e = \frac{K_S a_S^b}{1 + K_S a_S^b + K_{eq} a_{FeO}^i} \dots [6.10]$$

$$\theta_O^e = \frac{K_{eq} a_{FeO}^i}{1 + K_S a_S^b + K_{eq} a_{FeO}^i} \dots [6.11]$$

It is interesting to mention that in the case of the adsorption at the bubble/metal interface during bubble growth, the oxygen for adsorption comes from the dissolved oxygen in the liquid metal. So, in that case the equilibrium fraction of sulfur and oxygen could be expressed according to the Langmuir adsorption isotherm as

$$\theta_S^e = \frac{K_S a_S^i}{1 + K_S a_S^i + K_O a_O^i} \dots [6.12]$$

$$\theta_O^e = \frac{K_O a_O^i}{1 + K_S a_S^i + K_O a_O^i} \dots [6.13]$$

In previous work by the current authors, a decarburization model was developed for an iron carbon droplet reacting with oxidizing slag. The model considered, the transport of oxygen

in the slag, interfacial chemical reaction and nucleation and growth of bubbles in metal droplet. The model only considered the poisoning effect of sulfur both at the slag/metal interface and at the bubble/metal interface. It did not consider the effect of competition for surface sites between oxygen and sulfur. In this work, the previous model has been improved incorporating the dynamic variation of fraction of sulfur and oxygen adsorption as a function of bulk sulfur concentration and interfacial FeO activity. The model has been applied for three different sulfur cases (0.011, 0.016 and 0.129 wt%) sulfur droplets reacting with different slag compositions. The effect of ionic and electronic conductivities on the transport kinetics of oxygen in slag and the consequent effect on decarburization kinetics is presented in previous work by the current authors <sup>[25]</sup>. It has been shown that by increasing ferric fraction in the slag and/or slag basicity(B) for a fixed oxygen potential or fixed total Fe<sub>t</sub>O concentration, the conductivity of the slag increases which increases the rate of transport of oxygen. In the current model, for simplification the mass transfer coefficient has been adjusted to reflect the effect of variation of ionic and electronic conductivity in the transport kinetics, *i.e.* the oxygen flux was modulated by varying the mass transfer coefficient. But the same mass transfer coefficient was used for different sulfur concentration droplets reacting with a single type of slag. The model results are presented in the following sections.

#### **6.4.2. Case for 0.011 wt% Sulfur**

As shown above in Figure 6.2 when a droplet with Fe-2.5wt% C-0.011wt% S reacted with oxidizing slag, the decarburization mainly occurred within the droplet *i.e.*, internal decarburization. In this particular case the lower sulphur concentration, resulted in low

levels of surface poisoning. As the CO generation profile and the droplet volume profile presented in Figure 6.2 for  $B=0.9$  and  $Fe^{3+}/Fe = 0$  slag, shows droplet started internal decarburization immediately after falling into the slag and no delay in bloating was observed. Increasing the slag ferric fraction from 0 to 0.5, the electronic conductivity of the slag reached a maximum for that total  $Fe_2O$  concentration due to the presence of highest number of  $Fe^{3+}-Fe^{2+}$  couple<sup>[25]</sup>. In the previous work of current authors<sup>[25]</sup>, the flux of oxygen in the slag was presented as a function of ferric fraction and the effect of variation of electronic and ionic conductivity on oxygen transport was shown. Based on that analysis, it is known that both by increasing slag ferric fraction and the slag basicity, the oxygen transport rate can be increased. According to equation 6.5, the rate of oxygen adsorption at the slag/metal interface is expected to increase with increasing activity of FeO which in turn would be dictated by the slag mass transfer coefficient. As the mass transfer coefficient of the slag was increased with increasing slag conductivity, the interfacial iron oxide concentration would have risen close to that of the bulk composition. This would have increased the rate of adsorbed oxygen thus facilitating a higher rate of dissolution of oxygen in the metal creating higher driving force for decarburization. The sulfur concentration being low in this case, a large fraction of reaction sites would have been available for oxygen in comparison to other high sulfur cases which will be discussed below. The countercurrent competition between C and O within the droplet allows most of the dissolved oxygen to enter into the metal droplets. So nearly 100% internal decarburization is observed in this range of carbon concentration droplets.



The equilibrium fraction of adsorbed sites by sulfur and oxygen according to Equation 6.10 and 6.11 with the variation of iron oxide activity is presented in Figure 6.6. In the same plot, the estimated interfacial iron oxide activity during very initial decarburization period (initial few seconds) for three different slag concentrations from the model is presented. It is important to mention that iron oxide activity at the interface increases with the progress of reaction, but for comparison purpose, selection of values for very early period is reasonable. This shows that with increasing iron oxide activity the oxygen adsorption increases, whereas sulfur adsorption decreases resulting in a faster decarburization kinetics.

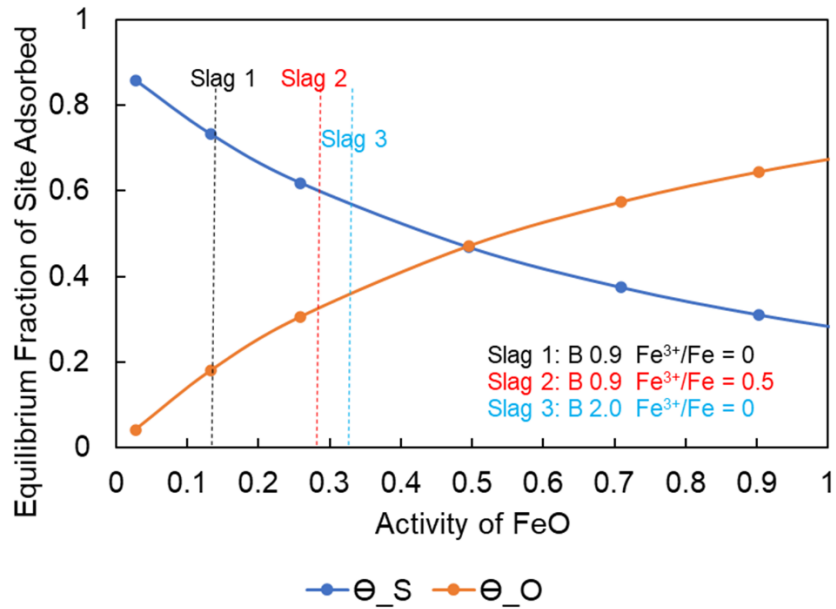


Figure 6.6: Equilibrium fraction of adsorption sites variation with activity of oxygen for 2.5 wt%C - 0.011 wt%S

The predictions of droplet decarburization from the model with three different slag composition are compared with experimental data in Figure 6.7. The figure shows that the

model is able to capture the effect of variations in oxygen transport properties on the decarburization kinetics. However, the model overpredicts the decarburization at the end stage for the case of  $B=0.9$  and  $Fe^{3+}/Fe = 0$  slag. A mechanism of charge accumulation to inhibit the ion transport was proposed in previous work by the authors<sup>[25]</sup>. Whilst the authors believe that mechanism to be correct, it is not incorporated in the current model. It is important to mention that as the ferric fraction and basicity increases, the slag electronic and ionic conductivity increases, and the mechanism that causes premature shutdown of the reaction no longer operates so the model is able to capture the decarburization kinetics in all reaction stages very well. In reality, the condition of slag in BOF process is highly

basic, and the electronic conductivity is also comparatively high, so the model would be expected to perform well in the industrial case.

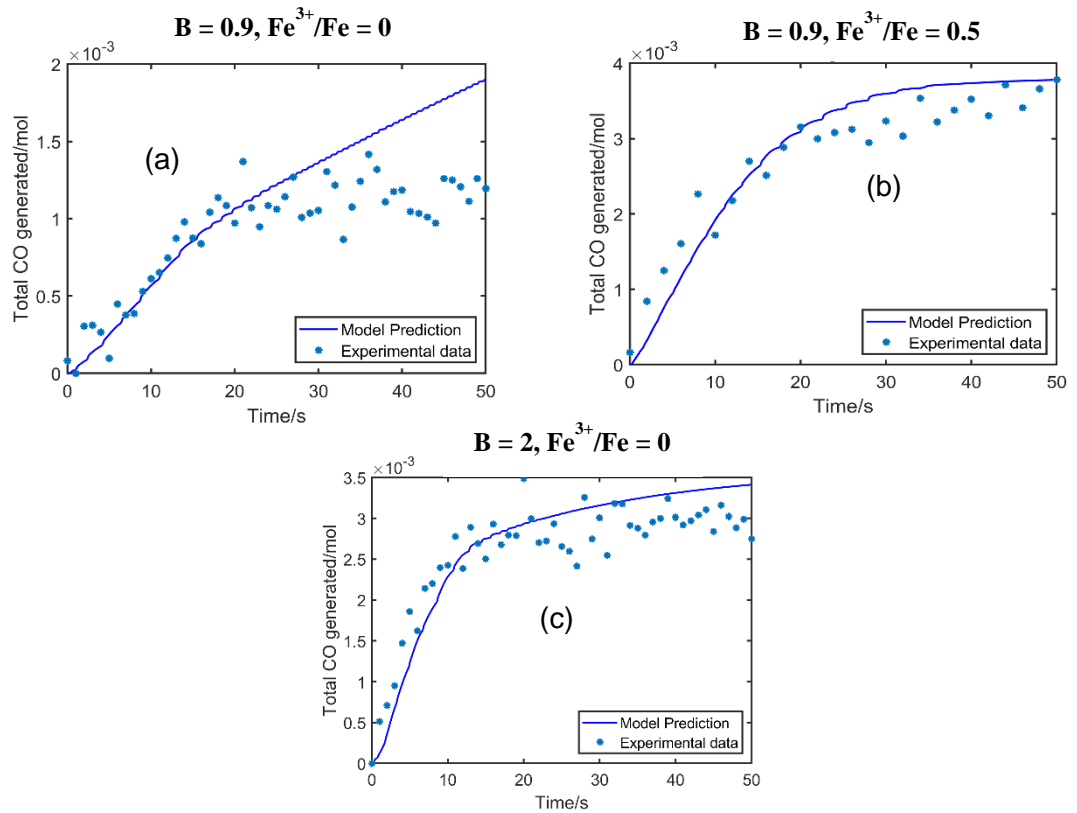


Figure 6.7: Model predicted total CO generation profile for 2.5% C - 0.011% S droplets in

(a)  $B=0.9$  with  $Fe^{3+}/Fe = 0$ , (b)  $B=0.9$  with  $Fe^{3+}/Fe = 0.5$ , (c)  $B=2.0$  with  $Fe^{3+}/Fe = 0$

As per the model calculations, the dynamic variation of the fraction of slag/metal interfacial area covered by sulfur and oxygen for three different slag compositions are presented in Figure 6.8. The figure shows that for all the cases, initially the fraction of reaction sites covered by oxygen compared to sulfur is smaller rising with the progress of reaction. Comparison of Figure 6.8 (a) and (b) shows that the fraction of reaction sites occupied by

oxygen increases more sharper than that for sulfur in the cases of high conductivity slag. If one compares the surface fraction blocked by sulfur among three different slags, it decreases from  $\sim 0.7$  to  $\sim 0.5$  as slag mass transfer coefficient increases. It is to be noted that with this sulfur concentration, the poisoning effect is not dominant therefore no significant delay on oxygen supply and subsequently the bloating of droplet is observed.

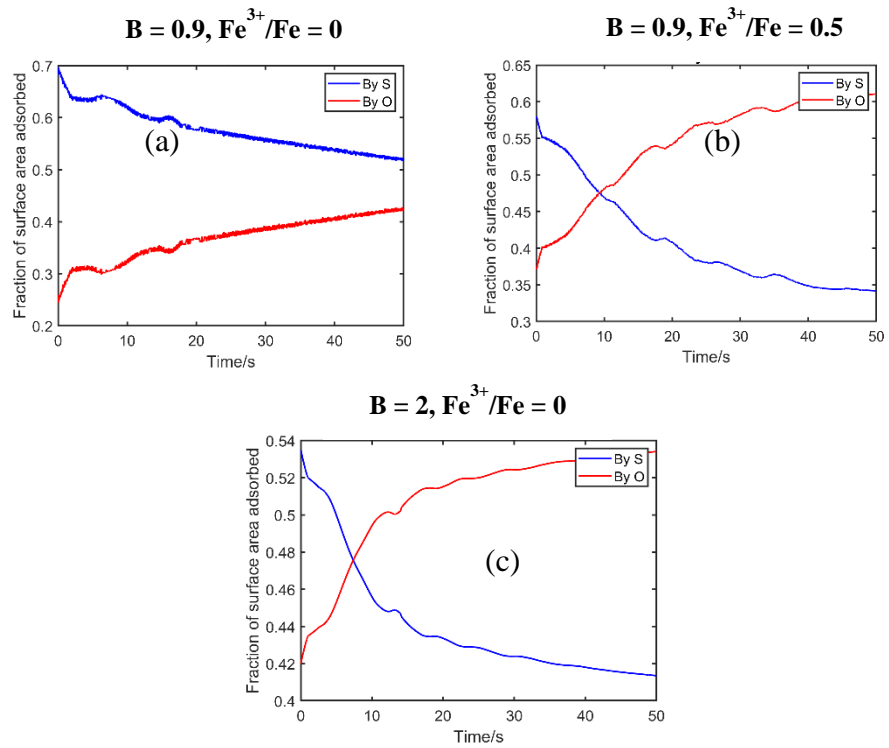


Figure 6.8: Variation of fraction of surface area covered by oxygen and sulfur with three different slags: (a)  $B=0.9$  with  $Fe^{3+}/Fe = 0$ , (b)  $B=0.9$  with  $Fe^{3+}/Fe = 0.5$ , (c)  $B=2.0$  with  $Fe^{3+}/Fe = 0$

### 6.4.3. Case for 0.016 wt% Sulfur

The decarburization results in Figure 6.3 for droplets with 0.016 wt%S and of 2.5 wt%C concentration in oxidizing slag show that for a slag with  $B=0.9$  and  $Fe^{3+}/Fe=0$ , there is a

significant delay in bloating. In that case, at a sulfur concentration of 0.016 wt% sulfur, the occupancy of surface sites by sulfur may be expected to be higher ( $\theta_s^e$  in Equation 6.10). This will have impeded oxygen dissolution taking longer time for the dissolved oxygen to build up to the critical concentration required for homogeneous bubble nucleation. For this reason, this case, showed a significant time of delay for internal decarburization and droplet bloating to commence. Similarly, for the case of 0.016 wt% sulfur concentration droplet, with increasing slag electronic and ionic conductivity, the oxygen flux ( $J_{\text{FeO}}$  in Equation 6.3) would have increased, and accordingly the interfacial FeO activity increased. Higher interfacial activity of FeO would have promoted adsorption of oxygen and in comparison, to sulfur adsorption, the oxygen adsorption would have become dominant as reaction proceeded. These phenomena would have resulted in a greater fraction of reaction sites at the slag/metal interface being occupied by oxygen. Consequently, more oxygen would have dissolved into the liquid metal resulting in early bloating. A schematic for the adsorption situations at the slag metal interface is presented in Figure 6.9 which shows how the fractional coverage of sulfur and oxygen varies from low to high conductivity slag.

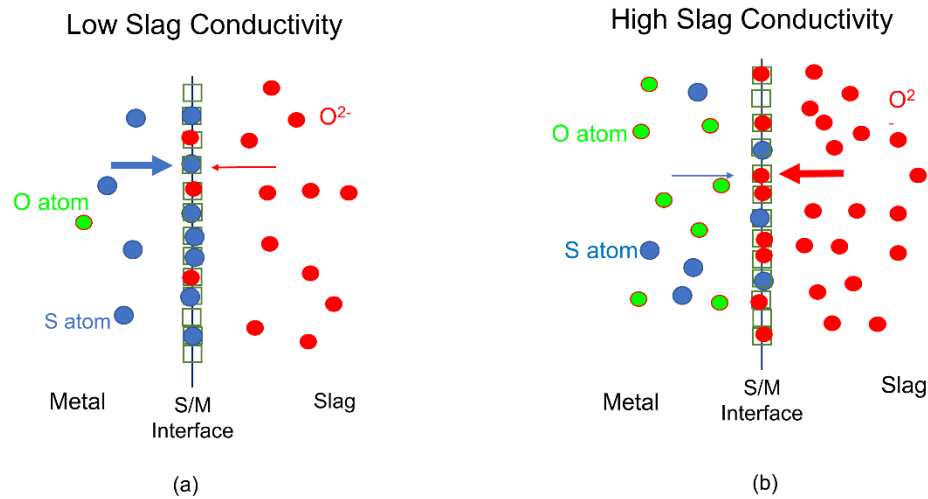


Figure 6.9: Competition in adsorption between sulfur and oxygen at the slag/metal interface with  
 (a) low conductivity slag (b) high conductivity slag for Fe - 2.5% C - 0.016% S droplets

For a better understanding, the equilibrium fraction of reaction sites occupied by sulfur and oxygen as a function of interfacial iron oxide activity for 0.016 wt% sulfur droplets is presented in Figure 6.10 along with estimated interfacial iron oxide concentration for three different slag concentrations. Similar like in Figure 6.6, the interfacial iron oxide activity value during early time period is selected for comparison for three different slags. Here it has been assumed that transport of sulfur within the metal droplet is fast enough, so that the concentration of sulfur at the interface is same as that in bulk phase. It can be seen that the fraction of sites adsorbed by sulfur decreases with increasing activity of iron oxide at the interface. It is to be noticed that the point at which fraction oxygen adsorbed site becomes more than 50% has shifted from iron oxide activity of 0.5 to 0.65 by increasing sulfur concentration from 0.011% to 0.016%.

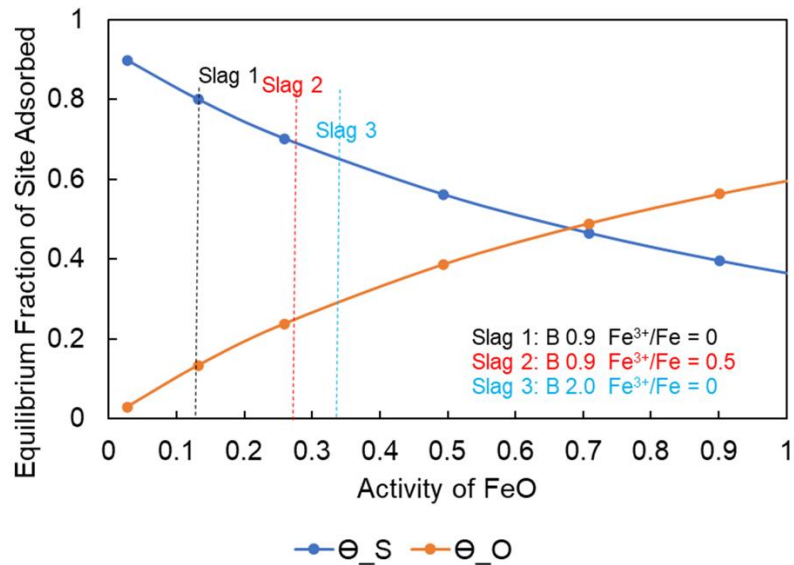


Figure 6.10: Equilibrium fraction of adsorption sites variation with activity of oxygen for 2.5 wt% C - 0.016 wt% S

The prediction of total CO generation from the model is shown in Figure 6.11 for the three different slag conditions discussed in this section. Figure 6.11 shows that the model is able to capture the behavior of poisoning by sulfur in competition with oxygen and the way in which it is affected by the transport properties of the slag. It should be noted that the slag transport properties are fitted for each slag case using one data set for each. They are not adjusted to accommodate different sulphur conditions. Similarly, the effect of competitive adsorption is included entirely based on theoretical considerations and adsorption coefficient data from the published literature. For the case of B=0.9 and Fe<sup>3+</sup>/Fe=0 slag, the significant incubation period shown in the data is predicted well by the model. This feature was a result of the combination of sulfur poisoning and the low slag electronic conductivity slag. The incubation period does not appear in the data for higher slag basicity

or ferric fraction. The elimination of the incubation period is also predicted by the model the only change being the increased slag mass transfer coefficient.

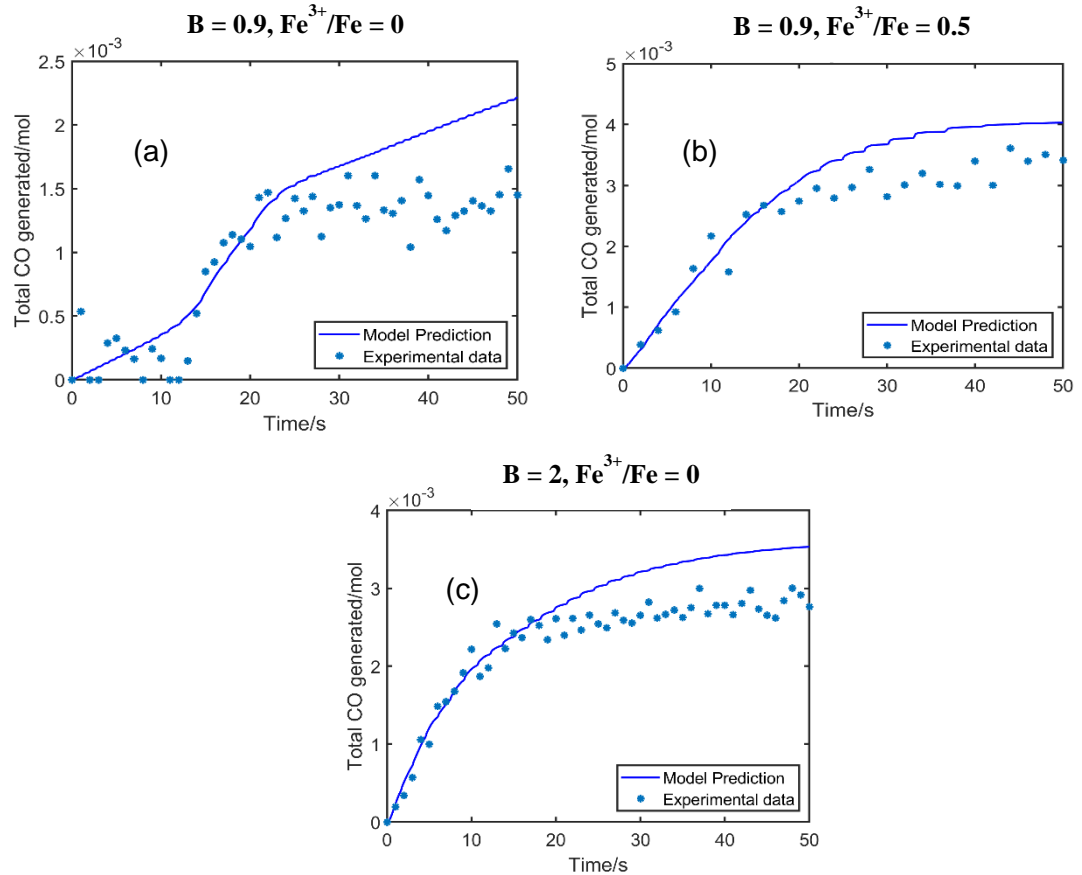


Figure 6.11: Model predicted total CO generation profile for 2.5 wt%C - 0.016 wt%S droplets in

(a)  $B=0.9$  and  $Fe^{3+}/Fe = 0$ , (a)  $B=0.9$  and  $Fe^{3+}/Fe = 0.5$ , (c)  $B=2.0$  and  $Fe^{3+}/Fe = 0$

A comparison for the fraction of surface area occupied by sulfur and oxygen is presented in Figure 6.12 for the case of 0.016 wt% sulfur droplets. It can be observed that with increasing the ferric fraction from 0 to 0.5, the corresponding increase in slag mass transfer coefficient results in increasing the surface coverage of oxygen. For higher basicity slags ( $B = 2$ ), the oxygen fractional coverage is comparatively higher from the start itself



compared to other two cases, but with the progress of reaction, the oxygen potential at the interface is not high enough to facilitate the oxygen adsorption reach more than 50% of surface coverage. Although the mass transfer coefficient in the slag with both low basicity  $\text{Fe}^{3+}/\text{Fe} = 0.5$  and higher basicity  $\text{Fe}^{3+}/\text{Fe} = 0.0$  slag has higher transport of FeO due to higher conductivity, but smaller activity coefficient with higher basicity slag is possibly keeping the interfacial iron oxide activity low compared to lower basicity  $\text{Fe}^{3+}/\text{Fe} = 0.5$  slag. Similar to the case of 0.011 wt% sulfur, this dynamic variation in adsorption fractions shows why the effect of poisoning diminished for droplets with 0.016 wt% sulfur as the conductivity of the slag was increased.

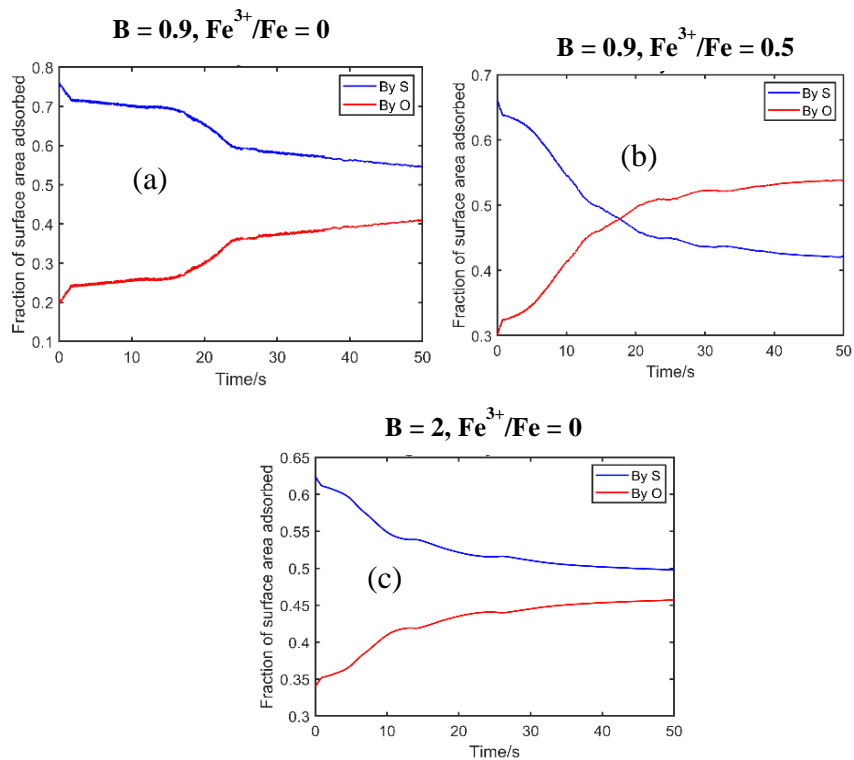


Figure 6.12: Variation of fraction of surface area covered by oxygen and sulfur with three different slags (a) B=0.9 with Fe<sup>3+</sup>/Fe = 0, (b) B=0.9 with Fe<sup>3+</sup>/Fe = 0.5, (c) B=2.0 with Fe<sup>3+</sup>/Fe = 0

#### 6.4.4. Case for 0.129 wt% Sulfur

The CO generation profile along with the droplet volume profile for droplets with 3.9 wt%C- 0.129 wt%S presented in Figures 6.4 and 6.5 show that there was a significant effect of sulfur in inhibiting the reaction kinetics. For the case of B=0.9 and Fe<sup>3+</sup>/Fe=0 slag, for 20 seconds, a negligible amount of CO generation is observed. This is because sulfur occupied almost all of the surface reaction sites, so that there was almost no possibility of either external or internal decarburisation.. Then slowly decarburization started but only

externally at the slag/metal interface and no bloating was observed for this case even at the end of reaction. It is worth mentioning that in all related work of the authors<sup>[24]</sup> for high carbon droplets, in the countercurrent competition between C and O, carbon has always won reaching the the slag/metal interface before reacting. Along with this, the presence of high sulfur allows even less oxygen to enter the droplet. Therefore, no bloating was observed for this case. When the slag electronic conductivity was increased by increasing the ferric fraction, the oxygen transfer rate increased. Based on the model prediction, subsequently the rate of oxygen adsorption ( $R_2$ ) also increased. and the consequent increase in adsorbed oxygen increased oxygen transport into the droplet to initiate internal decarburization. In addition to the fraction of the oxygen entering the droplet, a large fraction of decarburization was seen to occur at the slag/metal interface. Therefore, the droplet volume profile shows a partial bloating of the droplet from the very early period later fully bloating after a long time of reaction (approximately 380 seconds). When the slag basicity was increased to  $B=2.0$ , after 40 seconds of reaction the droplet bloated very rapidly to almost 5 times of its original volume. This fast rate of bloating would not have been possible at sulfur poisoning levels expected predicted from theory, even for the case of higher conductivity slags.. There was a significant desulfurization during droplet decarburization which decreased the level of surface poisoning allowing faster oxygen transfer across the slag metal interface subsequently enabling a faster rate of internal decarburization and bloating The sulfur concentration dropped almost by an order of magnitude with  $B= 2.0$  slag whereas in the case of other two slags, there was no desulfurization during decarburization. So sulfur poisoning continued till the end for the

cases of B=0.9 slags. The equilibrium fraction of reaction sites covered by sulfur and oxygen as the function of iron oxide activity is presented in Figure 6.13. It shows that when the iron oxide activity is low, the reaction sites are almost completely blocked by sulfur, so decarburization would be very slow and external (at the slag/metal interface) as shown in both the prediction and the data in Figure 6.14 and 6.15.

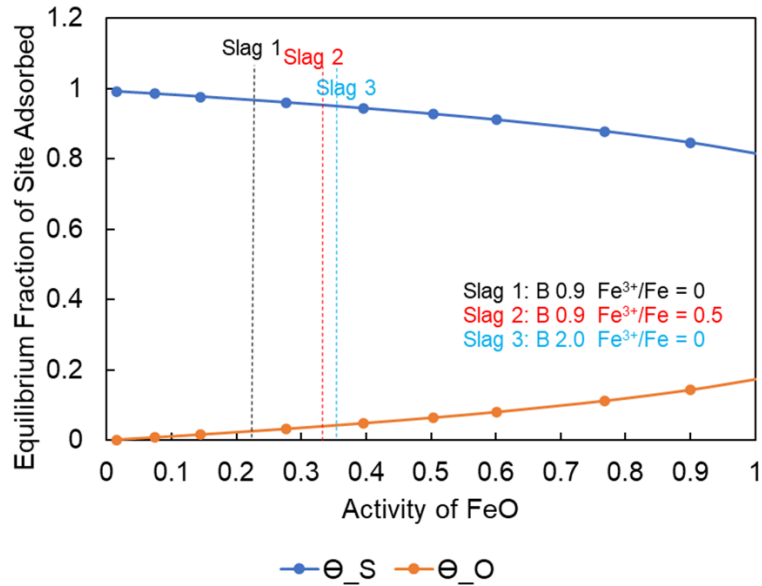


Figure 6.13: Equilibrium fraction of adsorption sites variation with activity of oxygen for 3.9 wt%C - 0.129 wt%S

The model prediction of total CO generation profile with time for three different conductivity slags for Fe - 3.9%C – 0.129%S droplet is presented in Figure 6.14. It is important to mention that for this high carbon droplets, the model required a high  $\psi$  parameter for calculating the CO nucleation rate from modified classical nucleation theory as discussed in the previous paper<sup>[26]</sup>, otherwise the model overpredicted. The model results

agree well for the  $B = 0.9$   $Fe^{3+}/Fe = 0$  which is a low conductivity slag, but overpredicts for the low basicity  $Fe^{3+}/Fe = 0.5$  slag and underpredicts for  $B = 2$ ,  $Fe^{3+}/Fe = 0$  slag.

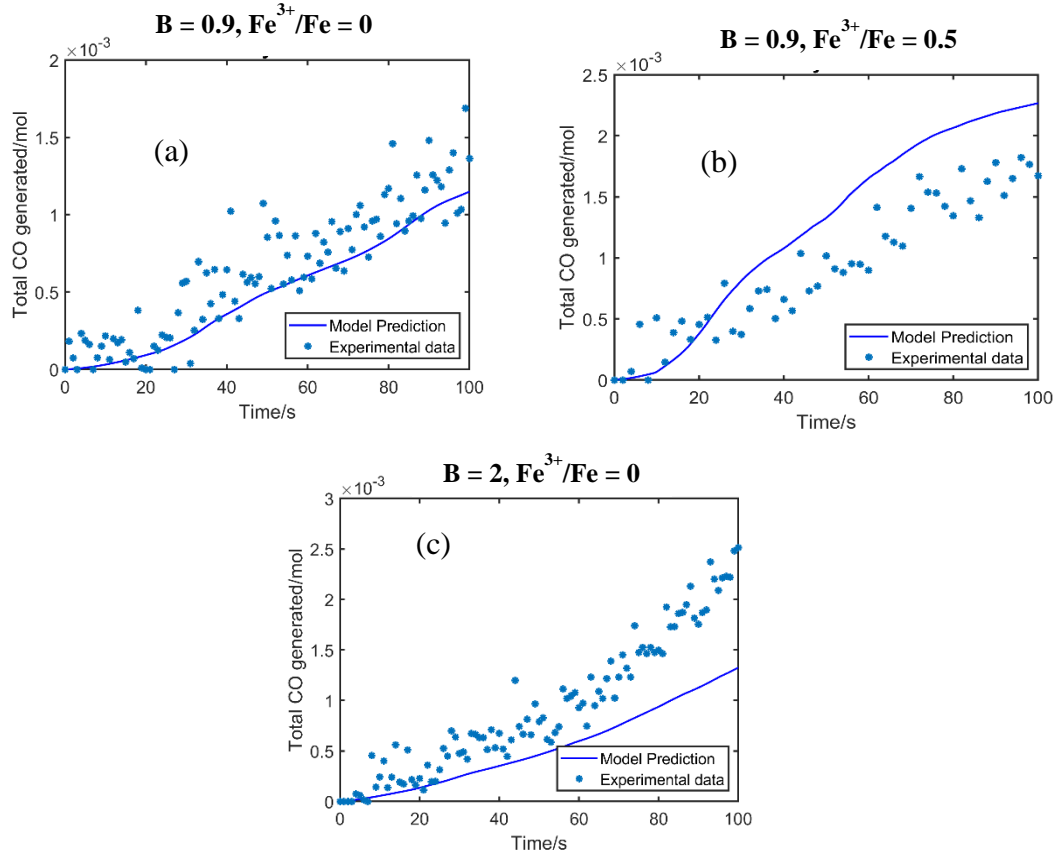


Figure 6.14: Model predicted total CO generation profile for 3.9wt%C - 0.129wt%S droplets in

(a)  $B=0.9$  and  $Fe^{3+}/Fe = 0$ , (a)  $B=0.9$  and  $Fe^{3+}/Fe = 0.5$ , (c)  $B=2.0$  and  $Fe^{3+}/Fe = 0$

The dynamic fractional coverage predicted for these three cases are presented here in Figure 6.15 showing that almost 90% of the reaction sites were blocked by sulfur irrespective of slag composition which explains the absence of bloating for low basicity  $Fe^{3+}/Fe = 0$  slag, partial bloating for low basicity  $Fe^{3+}/Fe = 0.5$  slag. For the higher basicity

(B =2)  $\text{Fe}^{3+}/\text{Fe} = 0$  slag, there was some desulfurization which is not captured in the model.

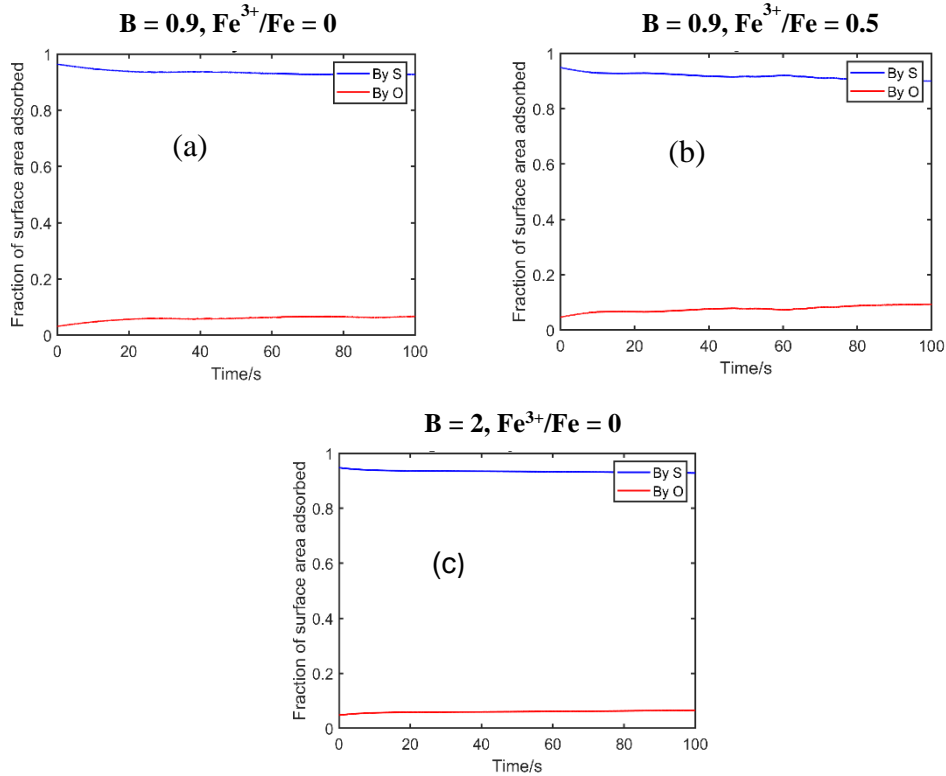


Figure 6.15: Variation of fraction of surface area covered by oxygen and sulfur with three different slags (a)  $B=0.9$  with  $\text{Fe}^{3+}/\text{Fe} = 0$ , (b)  $B=0.9$  with  $\text{Fe}^{3+}/\text{Fe} = 0.5$ , (c)  $B=2.0$  with  $\text{Fe}^{3+}/\text{Fe} =$

0

## 6.5. Conclusion

A series of experiments were performed to understand the effect of slag transport properties on the competitive adsorption between S and O at the slag/metal interface on droplet decarburization kinetics. The sulfur adsorption was altered by varying the droplet sulfur concentration, whilst the oxygen adsorption was manipulated by changing the oxygen

transport kinetics in the slag by varying the slag composition. The following conclusions can be made based on the present study.

1. At all three sulfur levels, the effect of sulfur on decarburization kinetics is diminished by increasing the oxygen transport rate in the slag, suggesting that competitive adsorption between oxygen and sulfur allows oxygen to occupy more surface sites when transport in the slag is sufficiently fast to support oxygen adsorption. This greater site occupancy by oxygen increases the number of pathways for oxygen to enter the metal.

2. The proposed mechanism is further supported when introduced into the mixed control model developed previously by the authors; the modified model offers remarkable prediction of the kinetics, including otherwise unexpected changes to the reaction trajectory, over a wide range of sulfur concentration and slag conductivity.

## References

- 1 D.. Sain and G.R. Belton: *Metall. Trans. B*, 1976, vol. 7B, pp. 235–44.
- 2 D.R. Sain and G.R. Belton: *Metall. Trans. B*, 1978, vol. 9, pp. 403–7.
- 3 F.J. Mannion and R.J. Fruehan: *Metall. Trans. B*, 1989, vol. 20, pp. 853–61.
- 4 T. Nagasaka and R.J. Fruehan: *Metall. Mater. Trans. B*, 1994, vol. 25, pp. 245–53.
- 5 H.G. Lee and Y.K. Rao: *J. Electron. Mater.*, 1991, vol. 20, pp. 403–9.
- 6 H. Gaye and P. V. Riboud: *Metall. Trans. B*, 1977, vol. 8, pp. 409–15.
- 7 D.J. Min and R.J. Fruehan: *Metall. Trans. B*, 1992, vol. 23, pp. 29–37.

- 8 T. Gare and G.S.F. Hazeldean: *Ironmak. Steelmak.*, 1981, vol. 8, pp. 169–81.
- 9 C.L. Molloseau and R.J. Fruehan: *Metall. Mater. Trans. B Process Metall. Mater. Process. Sci.*, 2002, vol. 33, pp. 335–44.
- 10 K. Gu, N. Dogan, and K.S. Coley: *Metall. Mater. Trans. B Process Metall. Mater. Process. Sci.*, 2017, vol. 48, pp. 2343–53.
- 11 K. Gu, N. Dogan, and K.S. Coley: *Metall. Mater. Trans. B Process Metall. Mater. Process. Sci.*, 2017, vol. 48, pp. 2595–606.
- 12 K. Gu, N. Dogan, and K.S. Coley: *Metall. Mater. Trans. B Process Metall. Mater. Process. Sci.*, 2017, vol. 48, pp. 2984–3001.
- 13 E. Chen and K.S. Coley: *Ironmak. Steelmak.*, 2010, vol. 37, pp. 541–5.
- 14 R.C. Urquhart and W.G. Davenport: *Can. Metall. Q.*, 1973, vol. 12, pp. 507–16.
- 15 J.K. Brimacombe: University College of London, 1970.
- 16 J.K. Brimacombe and F. Weinberg: *Metall. Trans.*, 1972, vol. 3, pp. 2298–9.
- 17 F.D. Richardson: *Trans Iron Steel Inst Jap*, 1974, vol. 14, pp. 1–8.
- 18 Y. Chung and A.W. Cramb: *Metall. Mater. Trans. B*, 2000, vol. 31B, pp. 957–71.
- 19 R.D. Phelke and J.F. Elliott: *Trans. Metall. Soc. AIME*, 1963, vol. 227, pp. 844–55.
- 20 K. Narita, S. Koyama, T. Makino, and M. Okamura: *Trans Iron Steel Inst Jap*, 1972, 12, vol. 12.



- 21 D.A. Goldstein and R.J. Fruehan: *Metall. Mater. Trans. B Process Metall. Mater. Process. Sci.*, 1999, vol. 30, pp. 945–56.
- 22 R.J. Fruehan and L.J. Martonik: *Metall. Trans. B*, 1981, vol. 12, pp. 379–84.
- 23 A.W. Cramb and G.R. Belton: *Metall. Trans. B*, 1981, vol. 12B, pp. 699–704.
- 24 J. Biswas, K. Gu, and K.S. Coley: *Decarburization of Bloated Droplets: An Experimental Study to Understand the Kinetics of Decarburization of Metallic Iron Droplets in FeO Containing CaO-SiO<sub>2</sub> Slags.*, McMaster University, Unpublished Research, 2020.
- 25 J. Biswas and K.S. Coley: *Decarburization of Iron Carbon Droplets with Oxidizing Slag: An Experimental Study to Understand the Effect of Ionic and Electronic Conductivity on Decarburization Kinetics*, 2021.
- 26 J. Biswas, K. Gu, and K.S. Coley: *Metall. Trans. B*, DOI:10.1007/s11663-021-02303-6.

## **Chapter 7**

### **7. Kinetics of Simultaneous Reactions between Fe-C-Si droplets and Oxidizing slags**

In the literature review section in Chapter 2, very few studies reported the effect of other impurity elements on decarburization kinetics. Silicon is a major impurity present in the BOF and is typically oxidized during the initial blowing period. It is very important for steelmakers to understand its effect on droplets' decarburization kinetics and the bloating behavior to control slopping. This chapter presents an experimental study of the impact of droplet silicon concentration and temperature, and its effect on bloating is discussed using mathematical model results.

The experiments for this study were performed by me and Dr. Kezhuan Gu. The original draft of this chapter was prepared by me, including analysis and then edited by Dr. Kezhuan Gu, Dr. Neslihan Dogan, and final editing was conducted by Dr. Kenneth Coley & Dr. Neslihan Dogan. The chapter will be submitted to the journal shortly.

#### **Abstract**

An experimental study was performed to investigate the simultaneous oxidation of silicon and carbon during the reaction between Fe-C-Si droplets and slags containing FeO at 1465°C and 1505°C. The experiments were carried out by employing time lapse sampling while monitoring simultaneous gas generation using a constant volume pressure increase technique (CVPI) with X-ray fluoroscopy. The desiliconization kinetics of droplets with

two different initial Si concentrations (0.5 wt pct and 0.25 wt pct), were tracked by quenching and analyzing droplets after different reaction times. Whilst the droplet decarburization kinetics were elucidated by measuring CO gas generation via CVPI along with the bloating behavior of droplet observed in-situ through X-ray fluoroscopy.

The results showed that the rate of silicon oxidation was extremely fast for all the cases where silicon in droplet decreased to 0.05 wt% or lower concentration within 5 seconds of reaction. The kinetic analysis suggested that the droplet desiliconization reaction was controlled by mass transfer in the metal phase. The metal phase mass transfer coefficients were determined to be  $1 \times 10^{-3}$  m/s at 1505°C and  $6 \times 10^{-4}$  m/s at 1465°C. The results also showed that during the desiliconization period, no significant amount of gas was observed and the onset period of was elongated as the droplet silicon concentration increased. Meanwhile, the rate and extent of droplet decarburization was found to be greater for droplets which contained silicon because the exothermic silicon oxidation increased the temperature thereby enhancing droplet decarburization. A reaction kinetic model was developed by combining the authors' previous decarburization model and the current desiliconization kinetics, to simulate the simultaneous oxidation of silicon and carbon for Fe-C-Si droplets reacting with oxidizing slags.

## **7.1. Introduction**

In the oxygen steelmaking process, a tremendous amount of metal droplets, created due to transfer of momentum from the oxygen jet to the metal bath, are ejected into the emulsion zone, where they are refined by reaction with slag during. The extent of refining of these

metal droplets before falling back into the metal bath is determined by the kinetics of decarburization which decides the residence time and slag/metal surface area of these droplets. Due to internal decarburization, droplet bloats therefore increasing both residence time and slag/metal reaction area, which in turn enhances the kinetics of the refining process. The advantageous effect of decarburization reactions over the overall refining process has motivated the authors to carry out a fundamental study of droplet reaction kinetics with oxidizing slag, which is part of a larger project for aiming to develop an advanced BOF process model in the authors' laboratory.

Over the past several decades, extensive studies<sup>[1-31]</sup> have been conducted to understand the decarburization kinetics of Fe droplets reacting with oxidizing slags from both experimental and modeling perspectives. Only the most relevant studies on droplet decarburization kinetics in FeO bearing slags are reviewed here. Mulholland *et al.*<sup>[18]</sup> first captured the dynamic nature of droplets during decarburization using X-ray fluoroscopy and confirmed the occurrence internal CO bubble nucleation. After investigating the influence of different factors on the reaction, they proposed possible rate controlling mechanism for the decarburization of droplet surrounded by a gas halo. It included oxygen transfer in slag, charge transfer, interfacial reactions at the halo/slag and halo/metal interfaces and interfacial adsorption or desorption of CO and CO<sub>2</sub>. Min & Fruehan<sup>[8]</sup> studied the decarburization kinetics in low FeO slags at which a gas halo was also present around the droplet. By calculating the overall rate constants, they proposed a mixed control rate model consisting of FeO transport in the slag, diffusion of gaseous species in the halo and a gas-metal reaction step. Considering similar rate limiting steps to other studies<sup>[8,18]</sup>,

Murthy *et al.*<sup>[23,25]</sup> suggested that the droplet decarburization involving a gas halo was controlled by slag phase mass transport and gas film diffusion, based on their experimental results on FeO reduction in oxidizing slags by Fe-C droplets. Gare and Hazeldean<sup>[32]</sup> conducted a similar study in which they also observed the presence of a gas halo. They further outlined the observed 5 stages of the reaction, including induction period, fast external decarburization, lull period, transition from external to internal nucleation period and finally a fully internal nucleation period. By measuring the rate of gas evolution and analyzing quenched samples, Gaye & Riboud<sup>[33]</sup> observed the occurrence of metal swelling although they termed wrongly as ‘emulsification’ during decarburization and proposed both slag mass transfer, interfacial reactions and gas nucleation were the possible rate determining steps for droplet decarburization. Molloseau & Fruehan<sup>[9]</sup> performed a thorough study of similar reaction over a wide range of FeO concentration from 3 to 35 wt% with the aid of X-ray fluoroscopy. The most significant result in this study was that the droplet remained intact while reacting with the slag containing 10 wt% FeO or less, whilst the droplet was believed to have been emulsified in the slag above this FeO concentration. These workers further proposed that the reaction rate was controlled by mass transfer of FeO in the slag for cases where emulsification was believed to occur, but the rate was controlled by dissociation of CO<sub>2</sub> on the metal for low FeO slags. More recently, Chen & Coley<sup>[10,34]</sup> carried out a systematic work on Fe-C-S droplet decarburization with oxidizing slags and concluded that the nucleation of CO bubbles inside droplet was the most important step in determining the CO gas evolution rate.

Regarding the influence of Si on decarburization kinetics of Fe-C droplets, an examination of the literature reveals that there is a disagreement among these limited studies. Gare & Hazeldean<sup>[32]</sup> studied the decarburization kinetics of droplets having Si, S, Mn in ferric based slag at the temperature of 1500°C, and found the initial rate of decarburization was higher when silicon was present initially. These authors claimed the presence of Si increased the carbon activity, which led to a higher decarburization rate. Sun & Pehlke<sup>[35,36]</sup> conducted a thorough study on decarburization kinetics of Fe-C-Si-Mn levitated droplets under different oxidizing gas mixtures. An interesting observation in these studies is that C was oxidized very rapidly, whilst Si and Mn concentration remained unchanged during the initial 30 seconds of reaction at reaction temperatures above 1600°C. One contributing factor to the stagnation of Si and Mn oxidation they proposed is that the carbon affinity to oxygen is higher at the temperature above 1600°C according to thermochemical calculation. By developing a kinetic model to describe the decarburization kinetics and swelling phenomenon of Fe-C droplets in FeO bearing slag, Sun<sup>[21]</sup> demonstrated the existence of a significant retardation period of decarburization because the desiliconization preferentially consumed the oxygen creating unfavorable conditions for carbon oxidation during the early stages of reaction. In the oxygen steelmaking process, it is generally accepted that Si removal starts earlier with high removal rate prior to other refining reactions. However, the time of the onset of decarburization observed in the industrial process is different from one plant to another as analyzed by Khadhraoui *et al.*<sup>[37]</sup> who summarized the reported plant trials, which were taken under somewhat similar initial conditions in terms of hot metal composition and temperature. It showed that

decarburization occurred immediately after blowing started in the trials of Van Hoorn *et al.*<sup>[38]</sup>, Asai and Muchi<sup>[39]</sup> and Chatterjee *et al.*<sup>[40]</sup>; while a significant delay in decarburization was observed in the imphos project<sup>[41]</sup> and also in the trials of Cicutti *et al.*<sup>[42,43]</sup> Khadhraoui *et al.*<sup>[37]</sup> suggested that this discrepancy could possibly have resulted from the different blowing profiles.

It can be seen that there is lack of agreement on the effect of Si on the onset of hot metal decarburization in both experimental and industrial trials. Therefore, a further detailed investigation is required to gain an insight into the factors that affect the onset of decarburization. In the current work, the authors attempt to address the disagreement in the influence of Si on droplet decarburization kinetics by carrying out a study of reaction between Fe-C-Si droplets and oxidizing slags.

## **7.2. Experimental Technique**

### **7.2.1. Experimental Setup**

The experimental procedure, identical to that used in previous work by the authors<sup>[11]</sup> is repeated here for the convenience of the reader. A resistance heated vertical tube furnace (Figure 7.1), with an 80mm inner diameter alumina working tube was used. The furnace was equipped with, X-ray imaging to observe the bloating of droplets in-situ. The pressure change inside the sealed reaction chamber caused by gas evolution from iron decarburization was instantaneously measured using a differential pressure transducer. Data from the pressure transducer was recorded by a computer software (RS232 Interface) at a selected frequency, which was 10 HZ in this study. The output data, expressed in

pounds per square inch, was converted to the number of moles of CO produced. The pressure was calibrated immediately before each experiment by introducing a fixed volume of argon gas into the furnace.

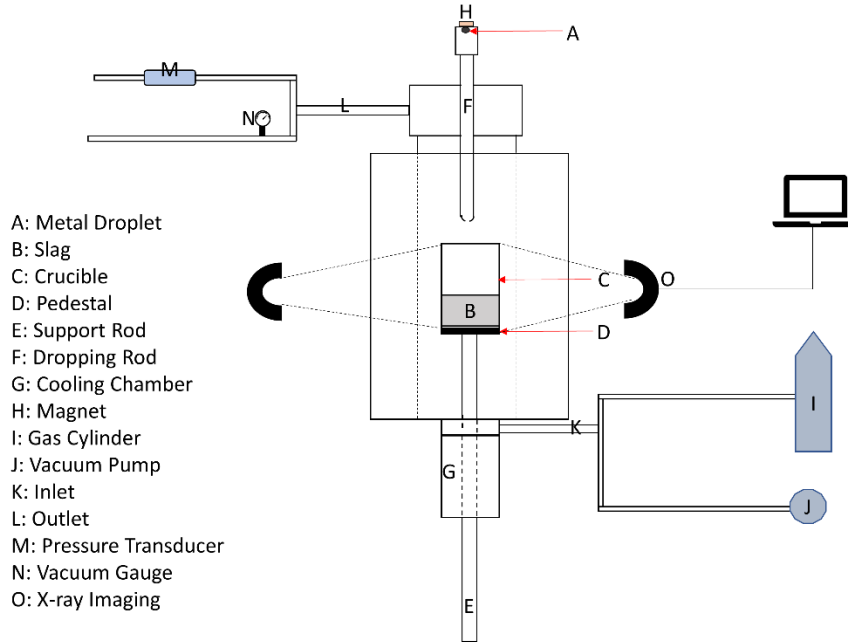


Figure 7.1: Schematic of experimental set up

### 7.2.2. Materials Preparation

Metal droplets were prepared from high purity electrolytic iron, silicon, and graphite rods. These materials were weighted according to the desired composition, mixed and melted in an alumina crucible in resistance heated furnace at 1550°C temperature. After homogenizing for 1.5 hours, cylindrical samples were pipetted out, cut into sections of specific mass and remelted in a Cu mold inside a vacuum arc melter with a high purity argon atmosphere of 0.5 atm pressure to fabricate droplets. The final composition of the



droplets were confirmed using Inductively Coupled Plasma Optical Emission Spectroscopy (ICP-OES) and LECO C & S analyzer. For slag preparation, CaO, Al<sub>2</sub>O<sub>3</sub> and SiO<sub>2</sub> powders were premelted at 1550°C, quenched, crushed and mixed together with FeO for experiments. In this study, a constant slag composition, *i.e.*, 44.7 wt%CaO-22.3 wt%SiO<sub>2</sub>-17 wt%Al<sub>2</sub>O<sub>3</sub>-16 wt%FeO, was used for all experiments. The droplet composition employed in this study was listed in Table 7.1.

Table 7.1. Metal droplet composition (wt%)

| [C] | [Si] | [S]   | Mass(g) |
|-----|------|-------|---------|
| 4.5 | 0    | 0.011 | 2.0     |
| 4.5 | 0.25 | 0.011 | 2.0     |
| 4.5 | 0.5  | 0.011 | 2.0     |

### 7.2.3. Experiment procedure

To do the experiment, first the crucible with 35 mm inner diameter containing 25 gram slag was placed in the hot zone of the furnace and the metal droplet at the top was hold using magnet. The furnace valves for inlet and outlet were closed and evacuated to 800 millitorr. Then the furnace was backfilled with argon and the flow was continued during the heating. At the desired temperature, the argon flow was stopped, all the inlet and outlet valves were closed except the one connected with the pressure transducer. The X-ray device were placed aligning with the hot zone to record the video of the crucible. The metal droplet was dropped by removing the magnet and the reaction time were started counting from the point when liquid metal droplet enters the slag, and this can be exactly pointed

from continuous X-ray video. Once the experiment was done, the support rod with the crucible (having slag and the reacted droplet) was lowered to the cooling chamber to quench and the furnace was cooled down slowly. The reacted droplets were collected and performed LECO C & S analysis to measure the final carbon concentration of the droplets. The recorded pressure transducer data were calibrated based on the final carbon concentration of the droplets. Whereas in the case of desiliconization kinetics experiments, the crucible containing the reacted slag and droplet was dropped rapidly from the hot zone into the quench chamber within 1 second to freeze the reaction. These fast quenched samples at different time intervals were analyzed for Si using ICP-OES to develop the transient behavior of the Si oxidation. Experiments were conducted only at two temperatures, *i.e.*, 1465°C and 1505°C.

## **7.3. Results**

### **7.3.1. Effect of Silicon Concentration**

A set of decarburization experiments were performed for Fe-C-Si droplets reacting with an oxidizing slag at 1505°C. The CO generation profiles along with the droplet bloating behavior for the Fe – 4.5 wt%C – 0.011 wt%S droplets with different Si concentration are presented in Figure 7.2. This figure clearly shows that the initial presence of Si had a significant effect on the droplet decarburization kinetics where the droplet decarburization experienced two distinct periods, *i.e.*, a incubation period with a much slower rate followed by a peak decarburization period for the cases of droplet containing 0.25 and 0.5 wt% Si. During the incubation period, no internal decarburization was observed as shown in Figure

7.2(b) where the volume of droplets containing Si remains unchanged. Whilst for the droplets without silicon, the decarburization starts at its peak rate from the beginning of the reaction and the droplet bloats immediately on entering the slag. It is worth noting that in the authors' previous work<sup>[44]</sup>, an incubation period for decarburization was observed when the same type of droplets with 4.5 wt% C was employed to react with a low basicity (wt%CaO/wt%SiO<sub>2</sub>=0.9) slag. The absence of an incubation period in this study for the case of Fe-4.5 wt%C droplet and a slag basicity (wt%CaO/wt%SiO<sub>2</sub>) of 2.0 slag, is attributed to the higher oxygen transport resulting from the higher basicity. Faster oxygen transport leads to a higher interfacial oxygen potential and faster transport of oxygen into the droplet, thereby eliminating the incubation period required for oxygen buildup to the threshold for internal decarburization. Figure 7.2 also shows that the incubation period for droplet decarburization increases with increasing Si concentration as expected since the Si oxidation consumes oxygen at the slag/metal interface, thereby preventing build-up in the droplet. One interesting observation presented in Figure 7.2(a) is that the peak decarburization rate was faster, and the extent of decarburization was greater for the cases of droplets which initially contained silicon; the peak decarburization rate increased from  $1.22 \times 10^{-4}$  to  $2.57 \times 10^{-4}$  mol/s as the droplet Si concentration increased from 0 to 0.5 wt%.

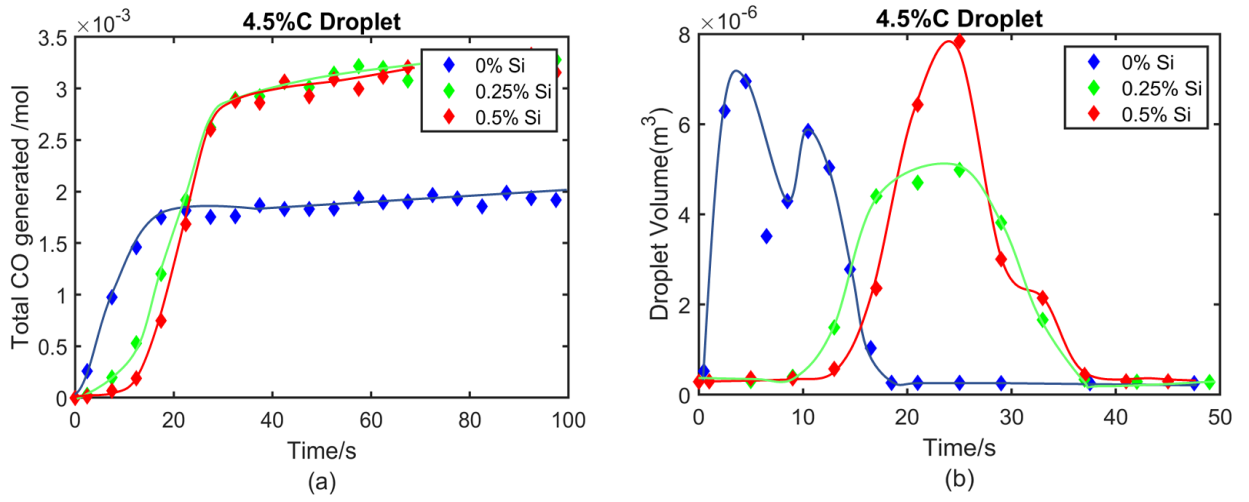


Figure 7.2: Total CO generation profile with time with varying silicon in (a) and the corresponding bloated droplet volume in (b)

The change of Si concentration in droplets with different initial Si concentration at 1505°C as a function of time is shown in Figure 7.3. The figure shows that silicon was removed very rapidly in both cases where its concentration decreased to approximately 0.01 wt% within the first 5 seconds of reaction and further decreased to a negligible level as the reaction proceeded. Combining these desiliconization data with CO generation profiles shown in Figure 7.2(a), one can determine that the onset of vigorous decarburization only occurred after Si oxidation, *i.e.*, the presence of silicon in the droplet retarded the onset of decarburization.

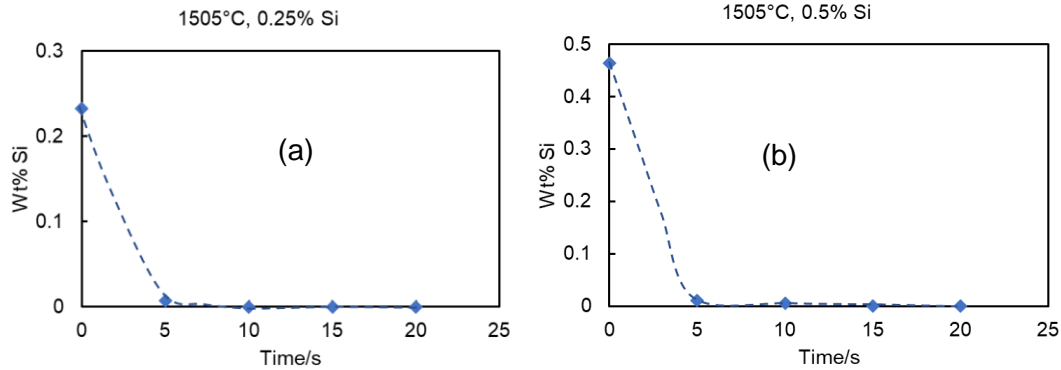


Figure 7.3: The change of Si concentration with time for droplets with different initial concentration: 0.25 wt% Si in (a) and 0.5 wt% Si in (b)

### 7.3.2. Effect of Temperature Variation

The decarburization behavior for droplets containing 0.5 wt% Si was investigated at two different temperatures, *i.e.*, 1465°C and 1505°C. The change of CO generation with time and the dynamic volume of bloated droplets over the course of reaction are presented in Figure 7.4, showing that the incubation time for droplet decarburization decreased from approximately 20 to 12 seconds as the reaction temperature increased from 1465°C to 1505°C. Figure 7.4 further shows that both the peak rate and the extent of decarburization increased with increasing temperature; the rate increased from  $1.19 \times 10^{-4}$  to  $2.57 \times 10^{-4}$  mol/s as the temperature increased from 1465°C to 1505°C.

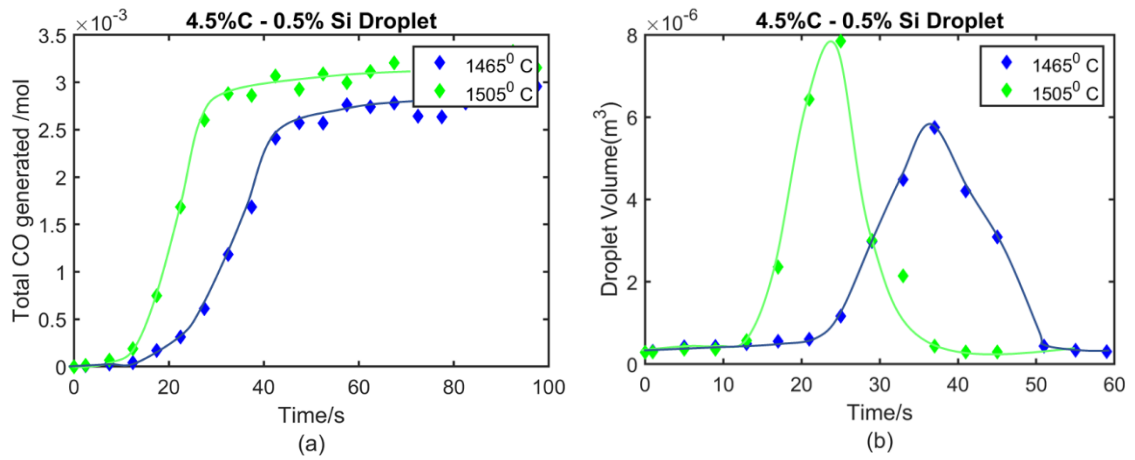


Figure 7.4: Total CO generation profile with time in (a) and the dynamic volume of bloated droplets in (b)

The change of Si concentration in droplet with time is presented in Figure 7.5 showing that Si was removed very rapidly during the initial 5 seconds, thereafter it gradually decreased for the case of 1465<sup>o</sup>C. Whereas in the case of 1505<sup>o</sup>C, silicon removal was nearly complete within the initial 5 seconds of reaction. The earlier completion of desiliconization triggered an earlier onset of decarburization, leading to a shorter incubation time as shown in Figure 7.4. This observation further echoes the point concluded in Section 7.3.1, that silicon retarded the onset of decarburization. From Figures 7.4 and 7.5, one can also recognize that the shorter incubation time for the case of 1505<sup>o</sup>C was due to the faster desiliconization reaction kinetics at higher temperature which resulted from the faster oxygen transport in the slag and the higher thermodynamic driving force.

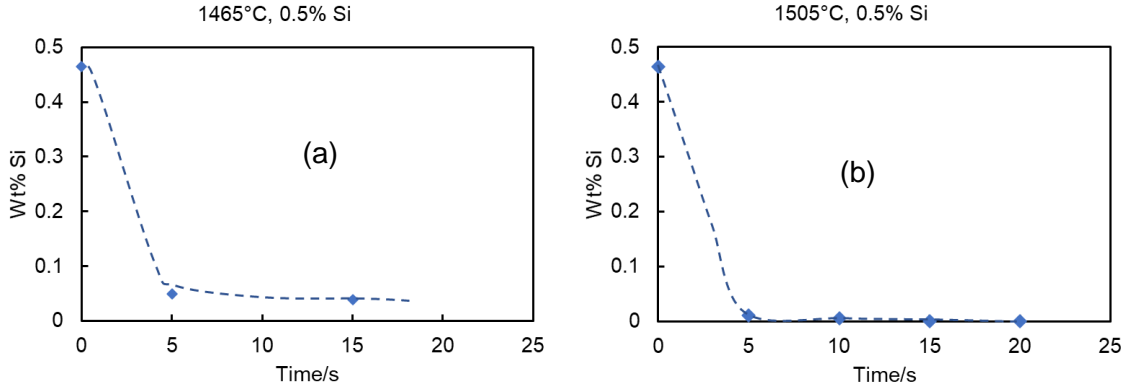


Figure 7.5: Silicon Removal Profile for Fe - 4.5%C - 0.011%S - 0.5% Si droplets with oxidizing slag at 1465°C and 1505°C in (a) and (b) respectively

## 7.4. Discussion

### 7.4.1. Desiliconization Kinetic Analysis

Given the extremely large thermodynamic driving force, it is reasonable to assume the droplet desiliconization in this study was controlled by mass transfer in metal phase. This assumption is also consistent with findings from other researchers<sup>[45,46]</sup> who studied hot metal desiliconization with oxidizing slag. The transport of silicon in the metal phase can be expressed as<sup>[45]</sup>

$$n_{Si} = -V_m \frac{dC_{Si}}{dt} = k_{Si}A(C_{Si} - C_{Si}^i) \dots \dots [7.1]$$

Where  $n_{Si}$  is the rate of transfer of silicon (mole/s),  $V_m$  is the volume of metal( $m^3$ ),  $k_{Si}$  is the mass transfer coefficient of silicon in the metal(m/s),  $C_{Si}$  and  $C_{Si}^i$  are the concentration of silicon in the bulk and at the slag/metal interface with the unit of  $m^3/s$ , respectively.  $A$  is the slag/metal interfacial area. The following Eq. [7.2] can be obtained by integrating Eq. [7.1],

$$\ln \frac{C_{Si} - C_{Si}^i}{C_{Si}^0 - C_{Si}^i} = k_{Si} \frac{A}{V_m} t \dots [7.2]$$

Rearranging this expression and converting concentration in weight percentage, Eq. [7.2] becomes

$$\frac{V_m}{A} \ln \frac{[\%Si] - [\%Si]^e}{[\%Si]^0 - [\%Si]^e} = -k_m t \dots [7.3]$$

$$Y \ln Z = -k_{Si} t \dots [7.4]$$

Where  $Y = \frac{V_m}{A}$  and  $Z = \frac{[\%Si] - [\%Si]^e}{[\%Si]^0 - [\%Si]^e}$ . Here  $Z$  represents the normalized driving force.

$[\%Si]$ ,  $[\%Si]^e$ ,  $[\%Si]^0$  are the concentration of Si at time  $t$ , at equilibrium and at the beginning of the reaction. The equilibrium concentration of silicon is very small ( $\sim 0$ ), so the normalized driving force simplifies as  $Z = \frac{[\%Si]}{[\%Si]^0}$ . The desiliconization data shown in Figure 7.3 are replotted according to Eq. [7.4] and presented in Figure 7.6 (a). For this analysis, the slag/metal interfacial area are considered to be as the initial droplet surface area  $t = 0$  since droplet only started bloating significantly after the silicon had been oxidized. Only two datapoints for each of case is presented in Figure 7.6 (b) due to the extremely fast reaction of Si oxidation, which leaves the authors no choice but to rely on those one datapoints to estimate the mass transfer coefficient calculation. The authors recognize the drawback of this analysis. However, the calculated metal phase mass transfer coefficient ( $k_{Si}$ ) of Si is 0.001 m/s at 1505°C and 0.0006 m/s 1465°C, which shows an excellent agreement with values determined by Wei *et al.*<sup>[45]</sup> and Shibata *et al.*<sup>[46]</sup>. Wei *et al.*<sup>[45]</sup> investigated the oxidation between an Fe-4.4% C-Si alloy and slags containing FeO at 1300°C determining the best fit mass transfer coefficient for Si in the metal under



different experimental conditions. The value obtained by these workers was 0.0005 m/s. By studying the kinetics of Fe-C-Si-P alloys reacting with oxidizing slag containing FeO and MnO temperature range from 1450 to 1500°C, Shibata *et al.*<sup>[46]</sup> found that the Si oxidation rate was controlled by mass transfer in metal phase and determined mass transfer coefficient in the range 0.0002 to 0.0003 m/s.

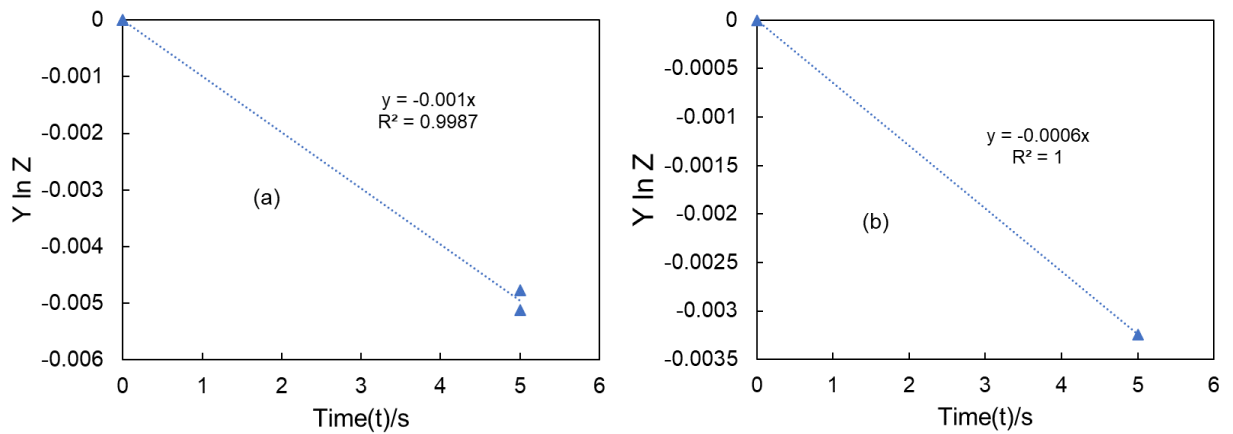


Figure 7.6: Silicon Removal data replotted according to Equation 7.4 at 1505°C in (a) and at 1465°C in (b)

The total CO generation profile in Figure 7.2(a) shows that presence of Si significantly inhibited the droplet decarburization in this case. This observation is consistent with the common recognition that the higher thermodynamic driving force is the reason for the faster Si oxidation rate prior to other refining reactions in oxygen steelmaking. It is interesting to mention that when levitated Fe-C-Si-Mn droplets were reacted in oxidizing gas at above 1600°C, Sun & Pehlke<sup>[35]</sup> observed carbon to be removed prior to the oxidation of Si and Mn in apparent contradiction to findings from this study. According to

thermodynamic calculations Si has a higher oxygen affinity at temperatures below 1600°C Which explains the discrepancy between this study and the work of Sun & Pehlke<sup>[35]</sup>.

In the current study, the length of the incubation period increased with increasing silicon concentration as shown in Figure 7.7(a) where the time at which the volume of bloating droplet reached greater than 2 times it's original droplet volume is plotted against initial silicon concentration. The peak decarburization rate was found to increase with increasing Si concentration as shown in Figure 7.7 (b). A closer examination suggests the higher decarburization rate for droplets with higher Si concentration maybe attributed to the increase of droplet temperature during Si oxidation since it is a highly exothermic reaction. A simple mathematical model is employed here to calculate the increase in temperature of the droplet during the course of exothermic silicon oxidation. It is assumed that 70% of the total heat generated from silicon oxidation is used to increase the temperature of the droplet. So, for  $n_{Si}$  moles of removal of silicon, the heat balance for the metal droplet can be written as

$$0.7 * n_{Si} * \Delta H = mC_p(T_f - T_i) \dots [7.5]$$

Where  $\Delta H$  is the enthalpy of oxidation of silicon by reducing FeO, m is the mass of the droplets,  $C_p$  is the specific heat of liquid steel,  $T_f$  and  $T_i$  are the final and initial temperature of the droplet.

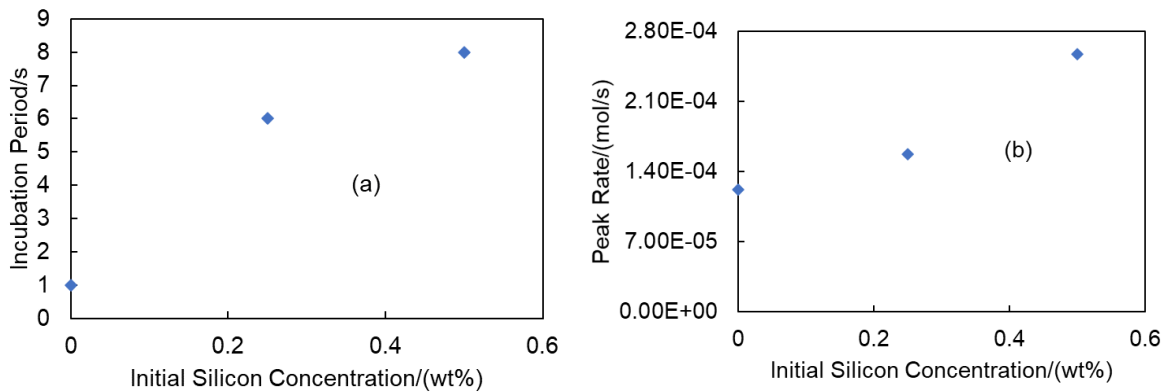


Figure 7.7: The time instant at which droplet volume is greater than 2 times of original droplet volume is plotted against the initial silicon concentration of droplets in (a) and the variation of peak rate of decarburization is plotted against initial silicon concentration in (b)

A sample calculation was carried out for Fe-C-Si droplet reacting with oxidizing slag at temperature of 1505°C. The temperature profile of the droplet is presented in Figure 7.8 for droplets with 0.5 wt% and 0.25 wt% Si concentration, respectively. This figure shows that there is approximately 80°C increase for the case of droplets with 0.5 wt% Silicon droplet, whilst around 40°C increase for the case of 0.25 wt% Silicon droplet. Higher reaction temperature leads to fast reaction kinetics. Therefore, the temperature increase caused by the exothermic silicon oxidation is the contributing factor for the higher decarburization rates for droplets with Si as presented in Figure 7.7(b).

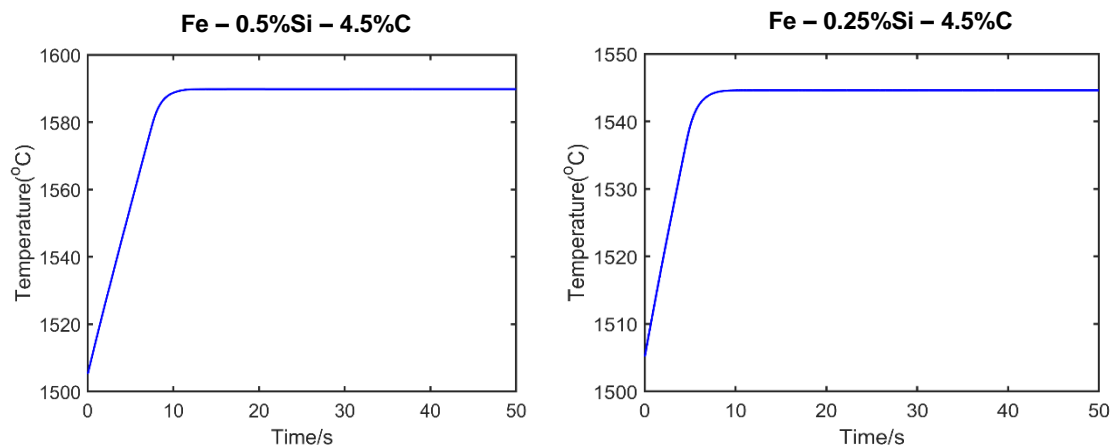


Figure 7.8: Droplet temperature profile for droplets (a) Fe - 0.5%Si - 4.5%C (b) Fe - 0.25%Si - 4.5%C in oxidizing slag

#### 7.4.2. Kinetic Model Including Multiple Reaction Steps and Reactants

The kinetics of desiliconization was incorporated into the authors' previous decarburization model <sup>[47]</sup> to predict the simultaneous oxidation of C and Si for the reaction of Fe-C-Si droplets with oxidizing slag. The desiliconization kinetics as described in Eq. [7.1] were considered in the dynamic equilibrium at the slag/metal interface. The CO generation rate and silicon removal profiles predicted from the model for droplets having 0.5 wt% and 0.25 wt% silicon at 1505°C are presented in Figure 7.9 and 7.10, respectively. The figures show that the model is able to capture the removal of silicon and the early stages of decarburization. Figure 7.9 shows that in the initial 10 seconds period, all the oxygen transported from bulk slag is consumed by silicon oxidation therefore no decarburization occurs. This is as observed in the cumulative CO profile. After 10 seconds of incubation, the depletion silicon allowed oxygen transport into the metal droplet and

when the supersaturation pressure reached the threshold value, internal decarburization initiated and droplet bloating started. Although the model over predicts the extent of decarburization, it captures the abovementioned sequence of events fairly well. It is worth noting that the poisoning effect caused by the formation of  $\text{SiO}_2$  at the slag/metal interface is not considered in this case. Whereas some other researchers<sup>[19,48]</sup> had considered this poisoning effect on slowing reaction kinetics. In this work, the model was tested incorporating the surface-active effect of  $\text{SiO}_2$  on the interfacial reaction kinetics but that didn't improve the overprediction at the end stage. Figure 7.10 shows similar results for the case of lower silicon concentration droplets (0.25 wt%), but the decarburization started earlier due to the earlier depletion of Si in this case. The overprediction at the end stage is consistent for both the silicon levels. As proposed in previous work<sup>[49]</sup> by the current authors, due to difference in rates of electron transfer reactions at the slag/metal interface and difference in rate of diffusion, there is a possibility of accumulation of charge generating a local electric field which acts as a kinetic barrier and shuts down the decarburization reaction. The presence of silicon possibly nullified the accumulated charge allowing the decarburization to continue for longer. Although this effect did not allow the reaction to continue to thermodynamic equilibrium. Unlike previous results where 2.5% C droplets reached close to thermodynamic equilibrium for  $\text{CaO/SiO}_2 = 2$ , in this study for the same slag, but with 4.5% initial carbon, the reaction stopped much earlier ( $>2\% \text{C}$ ). This means the conductivity was not high enough to dissipate the accumulated charge and avoid premature shut down of the reaction.

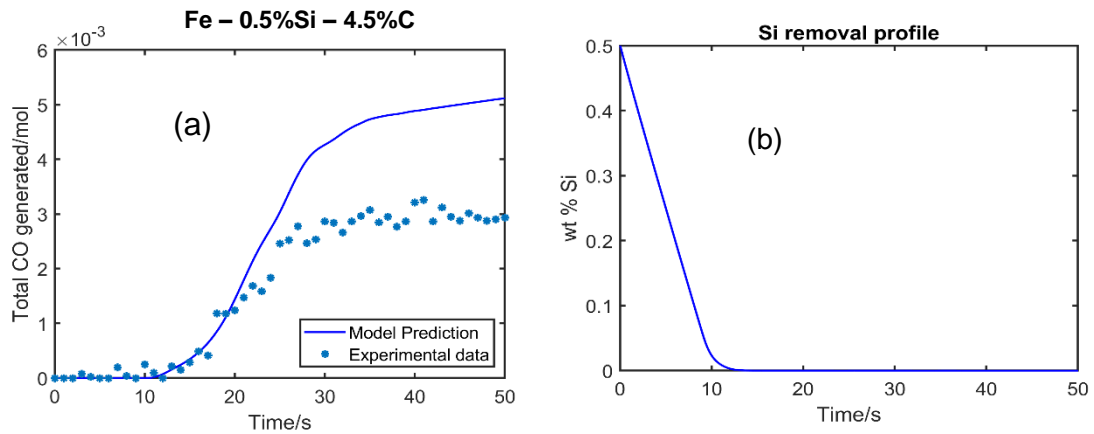


Figure 7.9: Total CO generated profile with time in (a) and the silicon removal profile in (b) for Fe - 4.5 wt%C - 0.5 wt%Si with oxidizing slag at 1505°C

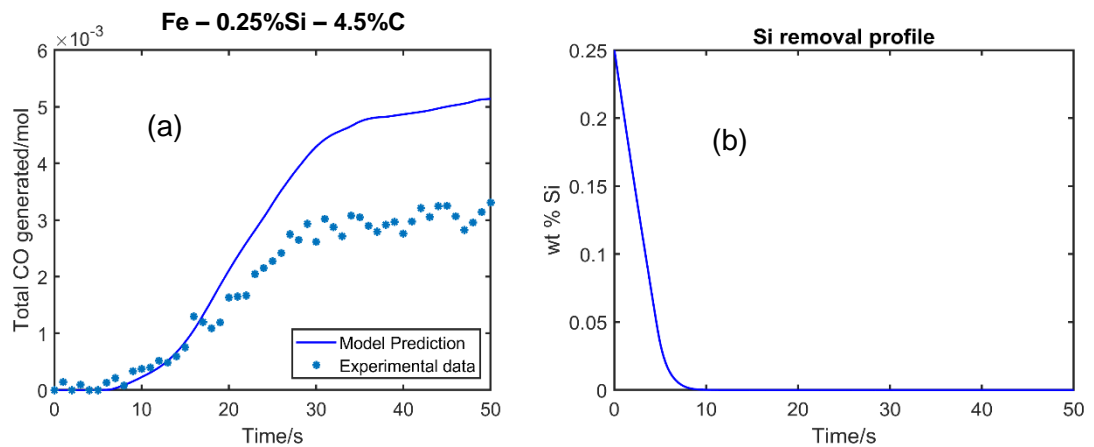


Figure 7.10: Total CO generated profile with time in (a) and the silicon removal profile in (b) for Fe - 4.5 wt%C - 0.25 wt%Si with oxidizing slag at 1505°C

### 7.4.3. Droplet Fragmentation

One interesting phenomenon came out from this experiment is that the droplets were fragmented during the peak bloating period based on the observation of X-ray video. Droplet fragmentation occurred for droplets with and without silicon. A snapshot of X-ray

images of the crucible containing slag and a metal droplet at reaction time of 1s and at 85 s are presented in Figure 7.11(a) and (b) respectively. It shows that the original droplet is fragmented into several small droplets during the course of decarburization.

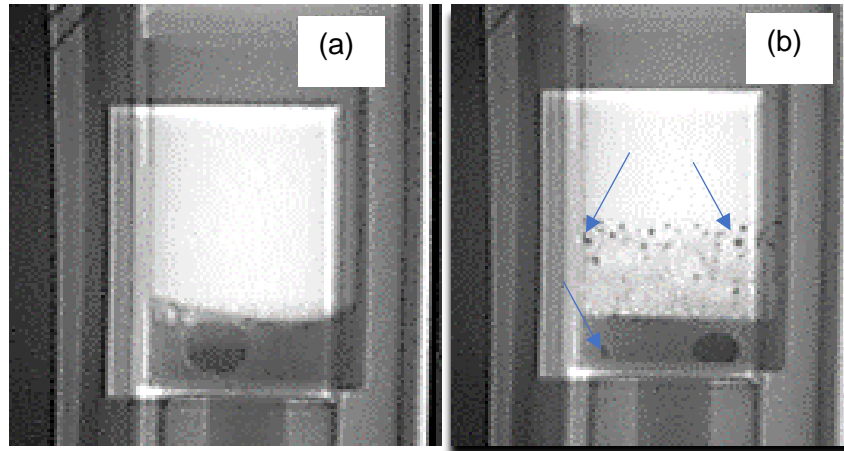


Figure 7.11: X-ray image of crucible with metal droplet and slag at reaction time 1s (a) and 85 s(b) for Fe - 4.5%C 2 g droplet in  $\text{CaO/SiO}_2 = 2$ , 16% FeO slag.

To better understand the droplet size distribution, all individual fragmented metal droplets were collected carefully from one of the quenched crucibles. The radius of the individual droplets was measured using a vernier scale. Figure 7.12 shows the fragments collected from an original droplet of 2 g and the corresponding size distribution. The most likely possibility is that caused by the bursting of CO bubbles during its escape from metal droplets. The presence of high carbon causes very high rate of generation of CO bubbles and this promotes droplet fragmentation. But it is important to mention that the mass fraction of the bigger droplets ( $>4$  mm) was  $\sim 87\%$  of the droplet mass and the remaining 13% were tiny droplets. The surface area increased by two times due to this fragmentation.

It is worth noting that when the droplets with similar carbon range were reacted with lower basicity slag ( $\text{wt\% CaO/wt\% SiO}_2 = 0.9$ ) in the authors' previous work<sup>[44]</sup>, fragmentation was not observed and the droplets remained intact throughout the reaction period. In BOF steelmaking, the slag including MgO is generally very basic therefore when the high carbon droplets reacting with it, the rate of CO generation would be very high, and those droplets would possibly be breaking into many tiny droplets as observed in this study.

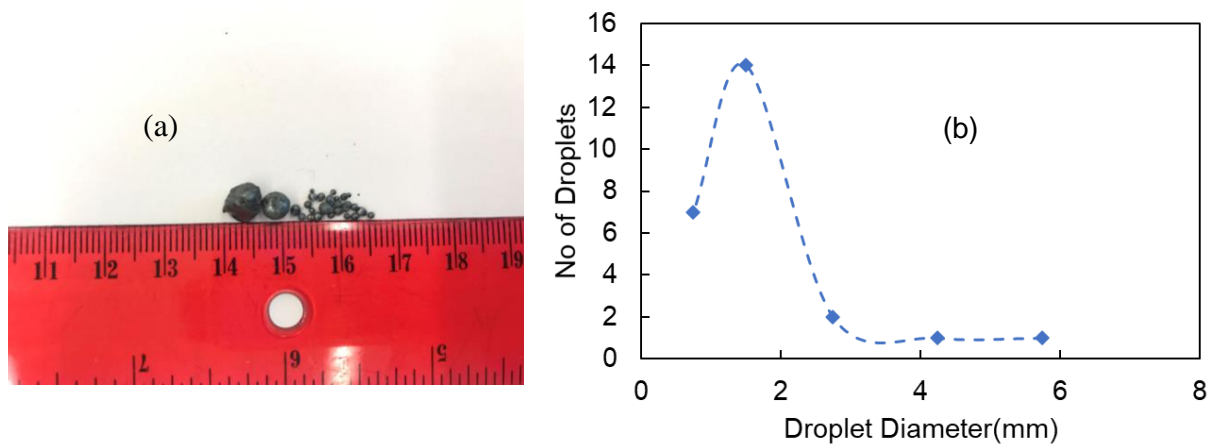


Figure 7.12: Small individual droplets separated from slag in (a) and (b) size distribution of broken droplet pieces

#### 7.4.4. Industrial Significance

A kinetic study was performed to understand the simultaneous oxidation kinetics of C and Si between Fe-C-Si droplets and oxidizing slag. In the BOF initial blow period, droplets generated by oxygen jets contain high concentration of C and Si, therefore it is important to gain insight on the kinetics of desiliconization and decarburization. Furthermore, a better understanding on the onset of decarburization is also helpful for steelmaker to employ



proper operation strategy for avoid slopping issue. This study shows that the kinetics of desiliconization is extreme fast and prior to decarburization as observed in most of BOF plants. It further shows that Si oxidation has two opposite influences on droplet decarburization, it first significantly retards the onset of decarburization, *i.e.*, vigorous decarburization only initiates after the cease of desiliconization; secondly it increases the droplet temperature because of the heat generation during the reaction, which increases the peak decarburization rate thereafter. Higher peak rate of decarburization with higher silicon concentration in droplet possibly causes slopping during decarburization period after the cease of desiliconization.

## **7.5. Conclusion**

An experimental study was performed to investigate the simultaneous oxidations of silicon and carbon by using Fe-C-Si droplets and slags containing FeO by employing time lapse sampling while monitoring simultaneous gas generation using a constant volume pressure increase technique with X-ray fluoroscopy. The desiliconization kinetics of droplets were tracked by quenching and analyzing droplets after different reaction times. Whilst the droplet decarburization kinetics were elucidated by measuring the CO gas generation via CVPI along with the bloating behavior of droplet observed in-situ through X-ray fluoroscopy. A model based on the authors' previous work was developed to describe the simultaneous reaction kinetics of C and Si oxidation. The following conclusions can be drawn based on this work.

1. The droplet desiliconization reaction is fast and the kinetic analysis suggests that the droplet desiliconization is controlled by mass transport in the metal phase.
2. This study shows that Si oxidation has two opposite influences on droplet decarburization, it first significantly retards the onset of decarburization by extending the incubation period; secondly it increases the droplet temperature due to the heat generation during the reaction thereby increasing the peak decarburization rate. Droplets with higher Si concentration experience longer incubation time but a higher peak decarburization rate.
3. A model developed for Fe-C droplets in the previous work by the current authors, modified incorporating desiliconization kinetics, describes the kinetics of desiliconization and decarburization very well in the initial stages, but overpredicts the total CO generation and the rate during the latter half of the reaction.
4. The droplets were observed to fragment during the course of decarburization in this study, and this is possibly due to high rate of generation of CO and bubble bursting which increases the total reaction surface area by two times.

## **Acknowledgement**

The authors wish to thank the member companies in McMaster Steel Research Center and Natural Science and Engineering Research Council of Canada (NSERC) for financial support.

## **References**

- 1 W.O. Philbrook and L.D. Kirkbride: *J. Met.*, 1956, vol. 8, pp. 351–6.

- 2 T.E. Dancy: *J. Iron Steel Inst.*, 1951, vol. 169, pp. 17–24.
- 3 R.S. Kaplan and W.O. Philbrook: *Metall. Trans.*, 1972, vol. 3, pp. 487–91.
- 4 P.G. Roddis: *J. Iron Steel Inst.*, 1973, vol. 211, pp. 53–8.
- 5 N.H. El Kaddah and D.G.C. Robertson: *J. Colloid Interface Sci.*, 1977, vol. 60, pp. 349–60.
- 6 N.H. El Kaddah and D.G.C. Robertson: *Metall. Mater. Trans. B*, 1988, vol. 19, pp. 831–7.
- 7 H. Gaye and Riboud.P.V: *Metall. Trans. B*, 1977, vol. 8, pp. 409–15.
- 8 D.J. Min and R.J. Fruehan: *Metall. Trans. B*, 1992, vol. 23, pp. 29–37.
- 9 C.L. Molloseau and R.J. Fruehan: *Metall. Mater. Trans. B Process Metall. Mater. Process. Sci.*, 2002, vol. 33, pp. 335–44.
- 10 E. Chen and K.S. Coley: *Ironmak. Steelmak.*, 2010, vol. 37, pp. 541–5.
- 11 K. Gu, N. Dogan, and K.S. Coley: *Metall. Mater. Trans. B Process Metall. Mater. Process. Sci.*, 2017, vol. 48, pp. 2984–3001.
- 12 Subagyo, G.A. Brooks, and K.S. Coley: *Can. Metall. Q.*, 2005, vol. 44, pp. 119–30.
- 13 B. Sarma, A.W. Cramb, and R.J. Fruehan: *Metall. Mater. Trans. B Process Metall. Mater. Process. Sci.*, 1996, vol. 27, pp. 717–30.
- 14 N. Dogan, G.A. Brooks, and M.A. Rhamdhani: *ISIJ Int.*, 2011, vol. 51, pp. 1093–

- 101.
- 15 R. Sarkar, P. Gupta, S. Basu, and B. Ballal, N: *Metall. Mater. Trans. B*, 2015, vol. 46B, pp. 961–76.
- 16 D. Dering, C. Swartz, and N. Dogan: *Processes*, 2020, vol. 8, pp. 1–23.
- 17 A. Kadrolkar and N. Dogan: *Metall. Mater. Trans. B Process Metall. Mater. Process. Sci.*, 2019, vol. 50, pp. 2912–29.
- 18 E.W. Mulholland, G.S.F. Hazeldean, and M.. Davies: *J. Iron Steel Inst.*, 1973, vol. 211, pp. 632–9.
- 19 B.K. Rout, G. Brooks, M.A. Rhamdhani, Z. Li, F.N.H. Schrama, and A. Overbosch: *Metall. Mater. Trans. B*, 2018, vol. 49B, pp. 1022–33.
- 20 B. Deo, P. Ranjan, and A. Kumar: *Steel Res.*, 1987, vol. 58, pp. 427–31.
- 21 H. Sun: *ISIJ Int.*, 2006, vol. 46, pp. 1560–9.
- 22 H. Sun, K. Gao, V. Sahajwalla, K. Mori, and R.D. Pehlke: *ISIJ Int.*, 1999, vol. 39, pp. 1125–33.
- 23 G.G.K. Murthy, A. Hasham, and U.B. Pal: *Ironmak. Steelmak.*, 1993, vol. 20, pp. 191–200.
- 24 K. ITO and K. SANO: *Tetsu-to-Hagane*, 1964, vol. 50, pp. 873–7.
- 25 G. Murthy, Krishna, G, Y. Sawada, and F. Elliot, J: *Ironmak. Steelmak.*, 1993, vol. 20, pp. 179–200.

- 26 K. ITO and K. SANO: *Tetsu-to-Hagane*, 1965, vol. 51, pp. 1252–9.
- 27 Y. NIIRI, K. ITO, and K. SANO: *Tetsu-to-Hagane*, 1969, vol. 55, pp. 437–45.
- 28 K. ITO, K. SANO, and S. ARINO: *Iron Steel Inst Japan-Trans*, 1969, vol. 9, pp. 465–71.
- 29 P.A.A. Distin, G.D.D. Hallett, and F.. D. Richardson: *J. Iron Steel Inst.*, 1968, vol. August, pp. 821–33.
- 30 L.A. Baker and R.G. Ward: *J. Iron Steel Inst*, 1967, vol. 205, pp. 714–7.
- 31 L.A. Baker, N.A. Warner, and A.E. Jenkins: *Trans. Metall. Soc.*, 1967, vol. 239, pp. 857–64.
- 32 T. Gare and G.S.F. Hazeldean: *Ironmak. Steelmak.*, 1981, vol. 8, pp. 169–81.
- 33 H. Gaye and P. V. Riboud: *Metall. Trans. B*, 1977, vol. 8, pp. 409–15.
- 34 E. Chen and K.S. Coley: McMaster University, 2010.
- 35 H. Sun and R.D. Pehlke: *Metall. Mater. Trans. B*, 1995, vol. 26, pp. 335–44.
- 36 S. Haiping and R.D. Pehlke: *Metall. Mater. Trans. B Process Metall. Mater. Process. Sci.*, 1996, vol. 27, pp. 854–64.
- 37 S. Khadhraoui, H. Odenthal, F. Krause, N. Uebber, W. Klos, P. Monheim, K. Hack, and M.T. Baben: *AISTech - Iron Steel Technol. Conf. Proc.*, 2019, vol. 2018-May, pp. 1–13.
- 38 A.I. VanHoorn, J.T. vanKonynenburg, and P.J. Kreyger: *Role Slag Basic Oxyg.*

- Steelmak. Process. McMaster Univ. Hamilton, Ontario. 1976, 26 p.*
- 39 S. Asai and I. Muchi: *Trans Iron Steel Inst Jap*, 1970, vol. 10, pp. 250–63.
- 40 A. Chatterjee, L. NO, and W. JA: *Ironmak. Steelmak.*, 1976, pp. 21–32.
- 41 M. Millman, A. Kapilashrami, M. Bramming, and D. Malmberg: *Imphos: Improving Phosphorus Refining*, 2011.
- 42 C. Cicutti, M. Valdez, T. Pérez, R. Donayo, and J. Petroni: *Lat. Am. Appl. Res.*, 2002, vol. 32, pp. 237–40.
- 43 C. Cicutti, M. Valdez, T. Perez, J. Petroni, A. Gomez, R. Donayo, and L. Ferro: in *6th International Conference on Molten Slags, Fluxes and Salts*, vol. 367, 2000.
- 44 J. Biswas, K. Gu, and K.S. Coley: *Metall. Mater. Trans. B Process Metall. Mater. Process. Sci.*, 2021, vol. 52, pp. 4215–4229.
- 45 B.P. Wei, M. Sano, M. Hirasawa, and K. Mori: *Trans. ISIJ*, 1988, vol. 28, pp. 637–44.
- 46 E. Shibata, H. Sun, and K. Mori: *Metall. Mater. Trans. B*, 1999, vol. 30, pp. 279–86.
- 47 J. Biswas, K. Gu, and K.S. Coley: *Metall. Trans. B*, 2021, vol. 52, pp. 3888–3906.
- 48 P. Wei, M. Sano, and M. Hirasawa: *ISIJ Int.*, 1991, vol. 31, pp. 358–65.
- 49 J. Biswas and K.S. Coley: *Priv. Commun. McMaster Univ.*, 2021, pp. 1–22.

## **Chapter 8**

### **8. Conclusion**

#### **8.1. Concluding Remarks**

In this chapter a summary of the research work described in the previous chapters is presented highlighting the important findings from each of the chapters followed by some overall conclusions and recommendations for future work.

The overall objective of the current work was to develop a decarburization model to quantify the decarburization behavior and the bloating kinetics of iron-carbon droplets. It was intended that the model would be able to determine the residence time and the extent of increase in slag/metal interfacial area of droplets reacting in the emulsion zone of the BOF. To better understand the decarburization kinetics, an experimental study was performed for a wide range of slag and metal compositions and a kinetic analysis was presented

Chapter 1. introduces to the motivation of this project. Chapter 2 presents a detailed research background for this decarburization study starting with a brief historical background of ironmaking and steelmaking followed by an overview of BOF steelmaking process. In the subsequent sections, two important factors: 1/ droplet generation rate, 2/ droplet residence time, which are crucial in deciding the kinetics of BOF are presented following the previous research works on decarburization kinetics of liquid metal both in slag and oxidizing gases. A brief discussion about the drawbacks of nucleation theory is presented followed by slag structure and property.

Chapter 3 introduces experimental results for decarburization of droplets and explores the effect of carbon concentration and droplet mass on the kinetics. The kinetics are discussed based on a conceptual model based on mixed control by slag mass transport, interfacial chemical reaction, nucleation and growth of bubbles within the droplet. Chapter 3 shows that the decarburization kinetics of droplets in oxidizing slag may be best represented by a mixed control model including all reaction steps and kinetic parameters and concludes that this would require a numerical model. This chapter also shows that the reaction stops suddenly before coming close to thermodynamic equilibrium. Chapter 3 suggests that the mechanism behind premature shutdown of the reaction may involve charge build up at the slag/metal interface

Based on the results from Chapter 3, Chapter 4 describes the development of a numerical model for mixed controlled decarburization of a single droplet in oxidizing slag. The parameters used in the model were determined using a single data set or were obtained directly from the published literature and Chapter 4 shows that the model developed on this basis describes results very well for a wide range of experimental conditions including significant changes in reaction behavior. A major flaw in the model is identified as its failure to predict the premature shutdown of the reaction. Chapter 5 presents an experimental study to understand the effect of the electrical conductivity of the slag on decarburization kinetics and the extent to which the reaction approaches equilibrium. This chapter confirms the hypothesis that the premature shutdown of the reaction observed in chapters 3 and 4 is related to charge build up at



the interface. In Chapter 6, model prediction shows that for high conductivity slags, where the reaction does not undergo premature shutdown, that the model developed in Chapter 4 offers a remarkable prediction of the reaction kinetics. The exception to this, is for high sulfur droplets where the surface poisoning effect is not properly captured. In an attempt to address the failure of the model to fully describe the effect of surface poisoning, Chapter 6 presents an experimental study showing the effect of competition between S and O in adsorbing at the slag/metal interface. This chapter employs the model developed to analyze the results and finds the experimentally observed behavior is described very well. Chapter 7 describes the effect of silicon on the decarburization kinetics and bloating behavior. The current work is yet to find a method to predict the premature shutdown of reaction however in the real BOF, slags are always highly basic and of high conductivity. Therefore, the model developed in this work offers excellent prediction of the different stages of decarburization for individual droplets in the emulsion zone of the BOF.

## **8.2. Overall Conclusions**

A decarburization model is developed, and an experimental study is conducted for a single Fe-C droplets in CaO-SiO<sub>2</sub>-Al<sub>2</sub>O<sub>3</sub>-FeO-Fe<sub>2</sub>O<sub>3</sub> slags. The important findings from the overall projects are as follows

a/ Based on the experimental results shown in Chapter 3 it may be concluded that although not predicted by classical nucleation, for droplets exposed to oxidizing slag, the barrier to internal nucleation and bloating is very low. These results also show that droplet decarburization shuts down prematurely, prior to exhausting either the oxidizing capacity

of the slag or the carbon in the metal. Based on the findings presented in Chapter 5, that this effect is eliminated by the use of high conductivity slags, it may be concluded that the premature shutdown is related to charge accumulation and that the effect is not of concern in real BOF slags.

b/ Chapter 4 describes the development of a decarburization model including: transport of oxygen in the slag; partitioning of oxygen at the slag/metal interface, the effect of poisoning by sulfur on the interfacial chemical reaction and the kinetics of nucleation and growth of bubbles. The model developed using just one data set was able to capture all features of the reaction over a wide range of experimental conditions, with the exception of the premature shutdown for low conductivity slags and incubation behavior for high sulfur droplets reacting with high conductivity slags. The former requires further work to be incorporated in the model although it may not matter for BOF slags, and the latter has been accommodated in the model by including the effect of competitive adsorption.

c/ Chapter 5, presents an experimental study of the effect of slag transport property showing that the premature shut down, observed for low basicity/ low conductivity slag, disappeared when the slag conductivity was increased. It is concluded from this observation that the premature shutdown is related to charge accumulation at the slag/metal interface.

d/ In chapter 6, a decarburization study at three different level of sulfur concentration in slags of varying transport property is presented. It is shown that the poisoning effect of sulfur which is observed in the current work for low basicity slags, is diminished when the slag basicity and electronic conductivity are increased. It is concluded that this observation

is due to competitive adsorption of sulfur and oxygen which comes into play when the oxygen transport in the slag is sufficiently rapid to support the role of oxygen in the competition. Under these circumstances the oxygen occupies a greater fraction of surface sites and offers “pathways” for oxidation that would not exist if sulfur occupied the vast majority of surface sites. When introduced into the model, this concept allows the model to predict behavior for high sulfur metal in high conductivity slag.

e/ Chapter 7, presents the results of an experimental study of the interplay between decarburization and desiliconization of droplets. These results show that in the presence of silicon decarburization is delayed. Because the silicon preferentially consumes oxygen that would otherwise be available for decarburization. After consumption of the silicon the resulting increase in temperature leads to a faster rate of decarburization than for a droplet that initially contained no silicon

### **8.3. Future Work**

The recommendations of future work based of the knowledge gap identified from this research are as follows

1/ For droplet decarburization, a crucial role of slag conductivity on the oxygen transport kinetics has been found. In the current work, this effect is reflected in the slag mass transfer coefficient a predictive approach relating oxygen transport directly to conductivity, would make the model more flexible for any type of slag.

2/ The importance of charge accumulation in premature shutdown of the reaction was identified in the current work However, development of a theoretical model to predict this behavior would extent the applicability of the current model.

3/ In chapter 5, a model to express the transport of oxygen in slag as a function of slag conductivity is developed and a preliminary validation is presented. It is necessary to further test this model for different slag compositions by precisely controlling the multivalent ion concentrations.

4/ In chapter 2, the lack of understanding of nucleation mechanism of bubbles in liquids was discussed. There is a need for a detailed investigation to unravel the mechanism.